UNIVERSITY OF SOUTHAMPTON

Faculty of Engineering and Physical Sciences
School of Physics with Astronomy

Constraining the Cosmological Co-Evolution of Galaxies and their Supermassive Black Holes via Cutting-Edge Jeans Modelling Techniques and Population Synthesis of Active Galactic Nuclei

DOI: 10.1002/0470841559.ch1

by

Christopher John Marsden
Msci
ORCiD: 0000-0002-7993-6228

A thesis for the degree of
Doctor of Philosophy

November 2021

University of Southampton

Abstract

Faculty of Engineering and Physical Sciences
School of Physics with Astronomy

Doctor of Philosophy

Constraining the Cosmological Co-Evolution of Galaxies and their Supermassive Black Holes via Cutting-Edge Jeans Modelling Techniques and Population Synthesis of Active Galactic Nuclei

by Christopher John Marsden

Galaxy evolution is still relatively poorly understood. Specifically, star formation, mergers and the influence of a central supermassive black hole are all thought to be key drivers in regulating galaxy formation and evolution, but their relative contributions are not well constrained. Velocity dispersion (σ), a measure of the statistical variance of stellar motions in a galaxy, is known to be a key galaxy property, effectively tracing a galaxy's gravitational potential well. The evolution of σ with cosmic time is also not well understood, despite having the potential to shed light on the relative importance of mergers versus star formation in building galaxies. σ is also known to be closely connected to the mass of the central supermassive black hole, via a tight correlation with slope of $\sim 4-6$, which theories suggest could be a result of energetic winds/jets from active galactic nuclei (AGN) impacting onto the surrounding interstellar medium. In this work, I present a comprehensive semi-empirical approach to compute σ via detailed Jeans modelling, assuming, for the first time, both a constant and scale-dependent mass-to-light ratio M^*/L. I compare with a large sample of local galaxies from the MaNGA survey and find that both models can reproduce the Faber-Jackson relation and the weak dependence of σ with bulge-to-total ratio. I also explore the dynamical-to-stellar mass ratio within $R \lesssim R_e$, and show that the full dynamical mass within the effective radius can be fully accounted for by a gradient in M^*/L or a dark matter halo with an NFW profile. I then build velocity dispersion evolutionary histories, using the average histories of main progenitor dark matter haloes, assigning stellar masses, effective radii and Sérsic indices via a variety of abundance matching and empirically motivated relations. I find clear evidence for downsizing in velocity dispersion histories along the progenitor tracks, and a steady increase in velocity dispersion at fixed stellar mass with increasing redshift. I extract comparable velocity dispersion tracks from the TNG50 hydrodynamic simulation. The relative 'flatness' of these tracks is shown to be driven by the increasing dark matter fraction within R_e, whilst showing a steeper evolution in the presence of a stellar gradient. I then show that a combination of mergers and internal star formation are likely responsible for the

constant or increasing $\sigma_{ap}[M^*, z]$ with time. I then present new evidence for the fundamental nature of the relationship between black hole mass and σ, and show that my $\sigma_{ap}[M^*, z]$ tracks are consistent with a nearly constant and steep $M_{bh} - \sigma$ relation at $z \lesssim 2$, as predicted by AGN feedback models, with black hole masses derived from the $L_X - M^*$ relation. I also show that AGN clustering can place new constraints on black hole-galaxy scaling relations, and explore the creation of AGN mock catalogs. Finally, I present an outcome of these mock catalogs, Astera, my cosmological visualization tool, which presents a real-time rendering of the large scale universe. Astera can represent an invaluable tool for survey planning and, due to its high user interactivity, also for gaming and educational and outreach activities.

When I consider your heavens,
the work of your fingers,
the moon and the stars,
which you have set in place,
What is mankind that you are mindful of them,
human beings that you care for them?
You have made them a little lower than the élöhîm,
and crowned them with glory and honor.

Psalms 8:3-5

Contents

List of Figures

List of Tables

Declaration of Authorship

I declare that this thesis and the work presented in it is my own and has been generated by me as the result of my own original research.

I confirm that:

1. This work was done wholly or mainly while in candidature for a research degree at this University;
2. Where any part of this thesis has previously been submitted for a degree or any other qualification at this University or any other institution, this has been clearly stated;
3. Where I have consulted the published work of others, this is always clearly attributed;
4. Where I have quoted from the work of others, the source is always given. With the exception of such quotations, this thesis is entirely my own work;
5. I have acknowledged all main sources of help;
6. Where the thesis is based on work done by myself jointly with others, I have made clear exactly what was done by others and what I have contributed myself;
7. Parts of this work have been published as:

Signed:..... Date:.....

Acknowledgements

- Abbey Samantha Marsden, my loving wife. Thank you for your unfailing support throughout my PhD.
- To my parents Andrew and Ros Marsden, whose support for my interest in Physics and Astronomy has been so essential. Thank you for listening to my long-winded explanations of many astronomical topics!
- To my colleagues and friends at the University of Nottingham, specifically Mike Brooks, Luke Jones, Ty Tankard and Sebastian Marriott.
- To my colleagues at the Southampton, particularly Dr Pip Grylls and Lorenzo Zanizi for your initial tuition and encouragement, and also to Hao Fu and Alba Alonso Tetilla for your enthusiasm and tireless support.
- To my co-authors, collaborators and everyone who has helped me from the scientific community for their contributions; Prof. Ravi Sheth, Prof. Mariangela Bernardi, Dr Nicola Menci, Dr Andrea Lapi, Prof. Michele Cappellari, Dr Michele Ginolfi, Dr Kastytis Zubovas and Dr Dylan Nelson.
- Special thanks to Dr Viola Allvato, with whom I co-led the creation of AGN mocks. Thank you for tolerating my continual rewrites of our code!
- Finally, and most importantly, to my PhD supervisor Prof. Francesco Shankar, whose passion for excellent astronomy has driven this project far further than it would have otherwise gone.

To Abbey

Definitions and Abbreviations

AGN	Active Galactic Nuclei
CCD	Charge Coupled Device
CMB	Cosmic Microwave Background
CPU	Central Processing Unit
DM	Dark Matter
DREAM	DiscRete semi-EmpiricAl Model
ESA	European Space Agency
FJ	Faber-Jackson [relation]
FPS	Frames Per Second
GIMP	GNU Image Manupulation Program
GPU	Graphical Processing Unit
GUI	Graphical User Interface
HMF	Halo Mass Function
HMSM	Halo Mass [to] Stellar Mass [relation]
HST	Hubble Space Telescope
IMF	Initial Mass Function
ISM	Instanced Static Mesh
LOS	Line of Sight
NASA	National Aeronautics and Space Administration
RGB	Red Green Blue
SDSS	Sloan Digital Sky Survey
SED	Spectral Energy Distribution
SHMF	Subhalo Mass Function
SMBH or BH	[Supermassive] Black Hole
SMF	Stellar Mass Function
STFC	[UK] Science and Technology Funding Council
VR	Virtual Reality
XLF	X-ray Luminosity Function [of AGN]

Chapter 1

Introduction

1.1 Overview

Galaxies are truly the most astounding places in the cosmos. Immense systems of stars (of which our sun is just one among trillions), these truly colossal objects have been dubbed 'island universes' in their own right. If you were to do the impossible and 'zoom out' your view of the universe and perceive it on the largest scales, you would see billions of galaxies scattered like glittering jewels on a pall of dark velvet. You would see the vast diversity in galaxy structure ('morphologies') with colossal, ancient elliptical galaxies and intricate, tightly wound, youthful spiral galaxies. The variation in colours would be dazzlingly beautiful, and the large-scale structures of billions of galaxies would follow the mysterious and magnificent cosmic web. Galaxies are the masterpieces of the large scale universe, havens of light and heat in the vast void of extra-galactic space, and within their gravitational cradle stars, planets and even life itself can be nurtured.

Remarkably, galaxies have only been recognized as such relatively recently in human history. Charles Messier was known to have referenced $\sim$100 luminous objects that he classified as 'spiral nebulae' (Messier, 1781), immediately recognising that these objects were different from stars due to their helical structure. A century later William Herschel (Herschel, 1864) expanded this catalog to around 5000 'nebulae' (at the time a 'nebula' being a generic term for any visibly diffuse object). However, despite this, the precise nature of these objects was not well understood, with some theories suggesting that these objects were luminous clouds within the Milky Way, or indeed true 'extra-galactic' sources, the 'island universes' of the philosopher Immanuel Kant almost a century before. This *great debate* came to a head in 1920, with a decisive conclusion provided by Hubble (1929a), who used Cepheid variable stars to calculate the distance to the Andromeda 'nebula', showing that it appeared at a distance larger than the physical size of the Milky Way itself. The universe was larger than we had imagined. Rapid

FIGURE 1.1: This image from the Hubble Space Telescope shows the spiral galaxy UGC 2885, 232 million light-years away in the constellation Perseus. Some foreground stars from the Milky Way can be seen in the image (with clear diffraction spikes). This spiral is sometimes named 'Rubin's galaxy', after astronomer Vera Rubin. Credit: HST/NASA

advances in observational techniques (specifically the development of CCDs (Charge Coupled Devices), photographic plates and other observational equipment that operates outside of the visible wavelengths) revealed thousands of galaxies in the universe around us, and a second monumental discovery by Hubble (1929b) showed via spectral analysis that the wavelength of light from a distant galaxy is shifted towards the red end of the spectrum, proportional to its distance from the observer, suggesting that distant galaxies recede faster than closer galaxies. The inevitable conclusion that was drawn from this is that the universe itself is expanding, as suggested by Hubble (1929b) and Lemaître (1927), in turn suggesting that the universe could be traced back to a single point (his so-called 'primeval atom'). This theory has now been refined into the so-called 'hot big bang' model, suggesting that the universe has expanded from a significantly hotter and denser state than we observe today. Modern cosmology, coupled with Albert Einstein's theory of General Relativity presented in 1916 (mass-energy content itself determines the structure of space-time), has been remarkably successful at explaining a broad range of observed phenomena, including the abundance of light elements, structure on large scales, the cosmic microwave background and Hubble's Law itself.

In parallel, significant progress has been made in understanding the evolution of galaxies themselves. Surveys of the nearby universe have examined millions of galaxies across the electromagnetic spectrum, capturing a wide range of galaxy masses, types and environments. Multi-wavelength coverage has also allowed for the assembly of intricate Spectral Energy Distributions (SEDs) for a large number of individual galaxies, allowing for accurate estimates of parameters such as stellar mass and star formation rate (e.g. Ahn et al., 2012). Photometry from tens of thousands of galaxies have also been acquired by medium-deep surveys (e.g. Chambers et al., 2016), and ultra-deep surveys have identified hundreds to thousands more (e.g. Lawrence et al., 2007). Remarkably, a galaxy was recently observed at redshift[1] $z = 11.06$ ($\sim$13.4 billion years ago), currently the most distant known galaxy in the observable universe (Oesch et al., 2016). Naturally, the most significant observable property used to classify galaxies was their structure or 'morphology', with Hubble (1926) presenting his now famous 'tuning fork' diagram, partitioning galaxies into ellipticals, spirals, barred spirals and irregulars. Broadly speaking however, galaxies can generally be classified into ellipticals (oblate, diffuse spheroids with randomly oriented orbits) and spirals (thin, dense disks with relatively fast rotations). It is generally agreed that each morphological type represents an evolutionary 'juncture', with most galaxies starting life as spirals (acquiring their disk shape from tidal torques and conservation of angular momentum), with major merging events or disk instabilities disrupting these relatively fragile systems and establishing elliptical galaxies. These processes, and the current 'best picture' of the evolution of galaxies in general, will be discussed at length in subsequent Sections. Galaxy evolution is still a relatively poorly understood field within astronomy and astrophysics, with no 'standard model' yet existing (unlike e.g. particle physics). The relative importance of dark matter, morphological types, star formation, galaxy-galaxy mergers etc, still remain poorly understood. Galaxies represent intensely large and complex gravitational systems, and it is still beyond the power of computational modelling to simulate them 'ab initio', leading to a variety of modelling approaches including Hydrodynamical, Semi-Analytic and Semi-Empirical models. Of central interest to this work is the understanding of a galaxy's so-called 'velocity dispersion', or a measurement of the statistical dispersion of velocities about the mean velocity of stars in a galaxy, and a key structural parameter.

Along with stars, galaxies are home to many other objects, including (arguably the most mysterious) black holes, intense gravitational singularities that maim the fabric of space-time itself. It is known that the centres of possibly all galaxies play host to a central black hole of truly epic proportions, with masses that can exceed a billion times the mass of our sun and event horizons many times larger than the solar system itself. These objects are still not well understood, and the complex interplay between these

[1] Redshift, z is a measure of increase in wavelength of light from distant objects due to the expansion of the universe, used as a distance measurement in Astronomy.

FIGURE 1.2: The Andromeda Galaxy (M31), photographed by the author using just a mobile phone and binoculars. At 2.5 million light years, Andromeda represents the closest major galaxy to the Milky Way. This photograph is the result of stacking 478 exposures of 2 seconds, taken with a Samsung Galaxy Note 10 through a pair of 7x50 binoculars, showing the remarkable sensitivity of modern mobile CMOS sensors, and the remarkable results that can be achieved with even basic astronomical equipment.

'supermassive' black holes and their host galaxies is likely to in turn strongly influence the growth and evolution of both objects. The mass of a supermassive black hole is known to be strongly linked to many of its host's properties (particularly velocity dispersion, see Ferrarese and Merritt, 2000), suggesting a close relationship. How do these black holes grow? It has long been suspected that so-called 'active' galaxies, persistently bright nuclear regions that exist within a subset of galaxies, represent actively accreting supermassive black holes. This shows that these black holes can grow by the direct accretion of matter, but it is also highly likely that these objects grow by black hole-black hole mergers following a host galaxy merger event. The relative significance of these contributions to a black hole's mass is not yet well constrained, and exploring the growth of supermassive black holes through the lens of their host galaxy is one of the key aims of this work.

This thesis for the degree of Doctor of Philosophy presents an exploration of the co-evolution of galaxies and black holes through the lens of galaxy velocity dispersion. As discussed later in the thesis, velocity dispersion is a key dynamical property of galaxies, which responds in different ways to different evolutionary channels (e.g., mergers vs gas accretion). All scaling relations, including the one with the central supermassive black hole, appear more tight when expressed in terms of velocity dispersion. The main aim of this thesis is to model, via transparent and flexible cosmological models,

the evolution of velocity dispersion, and in turn extract from them valuable information on the assembly histories of galaxies and their black holes.

In this Chapter I will start by reviewing the necessary background material required to explore galaxy evolution in a cosmological context, starting with the ΛCDM cosmology, the hierarchical growth of dark matter haloes and galaxies, and the impact these have on galaxy velocity dispersion. I will then introduce supermassive black holes, the Active Galactic Nuclei (AGN) population, and the significance of the scaling relations between black holes and their host galaxies. I will then summarize at the end of the Chapter the key questions I seek to answer in this thesis and the methods I will employ to answer them.

1.2 Background

1.2.1 ΛCDM Cosmology

The foundation of modern cosmology is based on the cosmological principle: the universe is isotropic and homogeneous on large scales. This is coupled with Einstein's theory of General Relativity (mass-energy content itself determines the structure of space-time) to provide equations that characterize the evolution of the universe. There is an abundance of observational evidence suggesting that the universe has been expanding for the past ∼13.6 billion years, from an immeasurably hot and dense state (see e.g. Mo et al., 2010). The most important event in the very early ($\sim 10^{-34}$ seconds) universe from the perspective of galaxy evolution was cosmic inflation, an extremely brief and intense period of exponential expansion. Hypothesized to have been triggered by the disconnection of the strong and electroweak interaction (Tsujikawa, 2003), cosmic inflation rapidly increased the size of the universe by a factor of at least 10^{26}. Quantum density fluctuations in the pre-inflationary epoch, 'amplified' by inflation, created the seeds for the formation of structure. These density fluctuations create (tiny) temperature fluctuations which are detectable in the Cosmic Microwave Background (CMB), dim electromagnetic radiation that is believed to be radiation released at the epoch of recombination (when protons and electrons first bound to form hydrogen), famously mapped by the COBE (Mather et al., 1994), WMAP (Bennett et al., 2013) and Planck Satellites (Ade et al., 2016).

It has long been known that a variety of astrophysical measurements point towards a vastly greater abundance of mass than can be explained by the presence of visible matter alone. This has led astronomers to hypothesize the existence of 'Dark Matter', believed to be an undiscovered type of non-baryonic subatomic particle, that makes up as much as ∼80% of the mass content of the universe. Evidence for Dark Matter comes from a variety of observations. As a first example, rotation curves of spiral

galaxies do not decrease as a function of radius as expected, but instead remain flat even at large radii, pointing towards a greater presence of mass than observed, effectively 'binding' the galaxy together when it should spread apart (Corbelli and Salucci, 2000)). Secondly, the velocity dispersions of galaxies in clusters do not match predictions derived from the observed mass distribution; this was first noticed by Zwicky (1937). Thirdly, the distortion of space-time in the presence of massive objects can be indirectly observed via gravitational lensing. The direct distortion of background light in this way is called 'strong lensing' and allows the calculation of the mass of the object (in this case a galaxy cluster) to be obtained (Taylor et al., 1998). In the same way, on larger scales the minuscule distortions of space-time caused by clusters of galaxies can infer a mass distribution; this is known as 'weak lensing' (Refregier, 2003). In both cases, the discrepancy between the observed distribution of visible matter and the calculated mass points towards a large additional presence of invisible matter. There is additional evidence in the power spectrum of the Cosmic Microwave Background (CMB) (Hinshaw et al., 2009), Dark Energy measurements (via observations of Type 1a supernovae, see (Kowalski et al., 2008), Baryon Acoustic Oscillations (Percival et al., 2007), Redshift-Space Distortions (Peacock et al., 2001) and others.

Among theorized subatomic particles there are several potential candidates for dark matter (Bergström, 2009). Regardless, the currently accepted view is the 'cold' dark matter paradigm, where dark matter particles have been moving relatively slowly since the early universe, and have little or no interaction with the electromagnetic spectrum or other types of matter (Blumenthal et al., 1984). Crucially, the gravitational interactions of dark matter wholly dominate all other interactions on large scales. The initial dark matter distribution, perturbed by the primordial density fluctuations, collapse under gravity to form the 'skeleton' of galaxy formation, upon which baryonic matter accretes, forming galaxies surrounded by dark matter 'haloes'.

On larger scales, the expansion of the universe (initially driven by radiation and matter) is now known to be accelerating (Peebles and Ratra, 2003). The exact mechanism behind this (dubbed 'Dark Energy') is unknown, but the best picture so far is drawn from Einstein's equations of General Relativity, specifically the introduction of a 'cosmological constant' Λ. Adding this to the cold dark matter picture yields the popular 'ΛCDM' model. The expanding universe on large scales leads to an ever-decreasing background density, and the accretion of dark matter into dark matter haloes leads to an increasingly 'craggy' substructure, superimposing large and small overdensities and large voids. A visualisation of this dark matter substructure is shown in Figure 1.3.

Through numerical simulations, the ΛCDM model has been notably successful in reproducing observational structure at medium to large scales (greater than a few kiloparsecs), e.g. Primack (2005). Traditionally, the dark matter substructure is simulated independently of baryonic components in a so-called 'N-body' simulation. Dark matter is predominantly thought to interact only gravitationally, so some number of dark

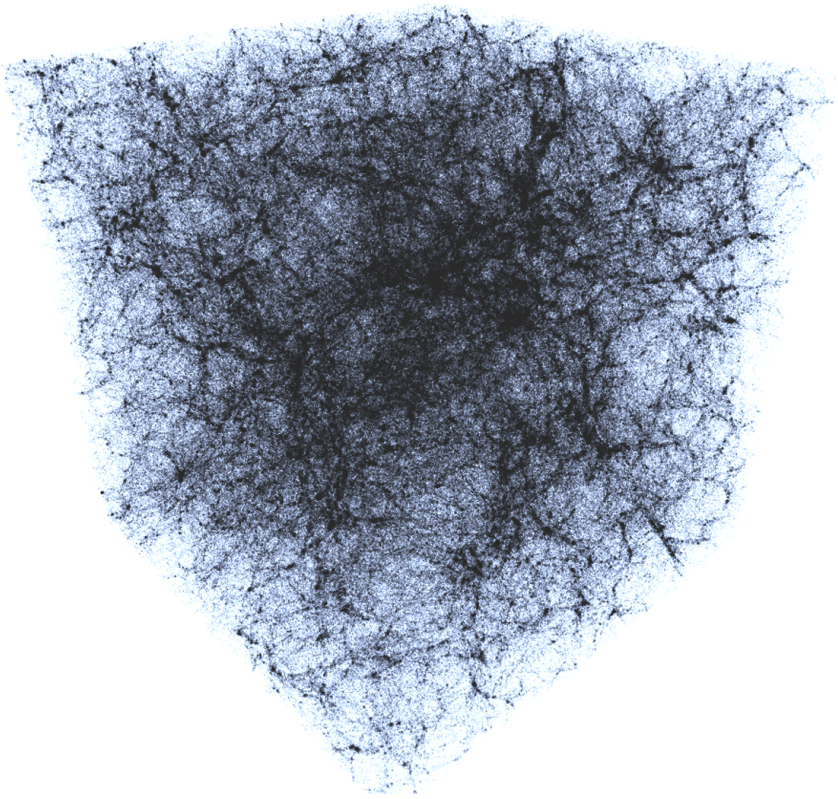

FIGURE 1.3: A visualisation of the 'cosmic web' of dark matter, created using the Bolshoi simulation data (Klypin et al., 2011b) within Unreal Engine (Astera, (Marsden and Shankar, 2020) see Chapter 5). Dark matter haloes are represented by dark points, which form filaments, clusters and voids.

matter particles can be simulated within a cosmological volume and simply evolved under their own gravity. Conceptually, this method is very simple. Some number of point particles are placed in a simulated box, and the force applied to each mass from the gravitational influence of every other particle in the simulation is calculated by solving the Poisson equation. This can then be used to calculate acceleration, and the simulation is evolved in a series of time steps. The effect of any desired cosmological expansion of space must also be considered, as must the effect of the borders of the simulation (periodic boundary conditions are often considered a reasonable approximation to a large or infinite universe).

While conceptually simple, when large numbers of particles are introduced, the calculation of a distance from each particle to every other particle becomes extremely expensive ($\mathcal{O}(n^2)$ operations for n particles), so techniques have been developed to simplify this. This includes the 'tree code' (Barnes and Hut, 1986), which only considers nearby particles individually, the 'particle mesh' approach (Hockney and Eastwood, 1988), which divides the domain into a grid and computes potential via Fourier transform, and a tree-mesh 'hybrid' approach, effectively mesh codes that use tree methods on small scales; GADGET-2 (Springel, 2005) being a popular example. Modern N-body

simulations can utilize as many as 10^{12} particles (Kim et al., 2011), and many simulations are starting to utilize technologies such as dedicated graphics (Belleman et al., 2008) for even larger potential simulations.

The behaviour of dark matter within N-body simulations follows *hierarchical assembly*. Dark matter, initially following some density field (namely the initial power spectrum), collapses into areas of greater density. Haloes of dark matter collapse further, increasing their density, and growing via the smooth accretion of dark matter particles and full mergers with other haloes, increasing their mass. The resulting structure is known as the 'cosmic web', where haloes arrange themselves into clusters, filaments and voids. A representation of this structure is shown in Figure 1.3, a rendering of the Bolshoi Simulation ($z = 0$ snapshot) Klypin et al. (2011b) using Astera (Marsden and Shankar, 2020) (see Section 5.2.3).

Once a simulation itself has been run, the opening process is to (numerically) identify the dark matter haloes where galaxy formation occurs. Because a concentration of dark matter particles is not discrete (i.e. it is not necessarily clear which halo (if any) a particle belongs to), defining the exact borders of a halo is a somewhat difficult process. The traditional method is to define a halo within a sphere which contains an average density Δ_{vir} with respect to the background density of the universe. Many groups adopt $\Delta_{vir} = 200$, which is rounded up from the approximate density perturbation in an Einstein-de Sitter Universe ($\simeq$178). Further complications arise in defining 'sub' haloes (haloes within haloes, in the process of being gravitationally stripped and merging with their host). An overview of techniques for halo and subhalo finding and consideration of their merits can be found in Klypin et al. (2011).

Once haloes and subhaloes have been identified, they are compiled into a *merger tree*; this construct records the masses of haloes at all times across the evolution of the simulation, tracing haloes as they merge to form larger haloes across the simulation. This construct can act as the foundation for the next stage of galaxy modelling, namely semi-analytic and semi-empirical modelling (as mentioned, hydrodynamical simulations simulate the baryonic and dark matter components together, so such an approach is not necessary). It is worth noting that there are other ways of generating mergers trees without the full N-body simulation, such as the Extended Press-Schechter formalism (Lacey and Cole, 1993) or the PINOCCHIO algorithm (Monaco et al., 2002).

1.2.2 Galaxies: Hierarchical Growth

The gas accreted in the deeper potential wells of the host dark matter haloes will start cooling at different rates depending on its density and initial temperatures. At 'high' temperatures ($T > 10^7$ K) the gas will cool principally via bremsstrahlung radiation, at 'medium' temperatures (in the range $T \sim 10^{4-7}$ K) by ionized electron decay and

electron recombination, and at 'low' temperatures ($T < 10^4$ K) by metal line cooling. If radiative processes are not sufficient, a so-called 'cooling flow' can form, where the central regions at higher temperatures cool faster, and the outer regions collapse (or 'flow') into the inner regions. Gas that has sufficiently collapsed will eventually become supported by its own angular momentum, obtained from tidal torques (Mo et al., 2010).

In the most central regions of a dark matter halo, gas may become dense enough to become self-gravitating. Denser regions cool faster, and some regions may reach densities sufficiently intense to kindle nuclear fusion. The processes behind which stars form is still not well understood (McKee and Ostriker, 2007). Stellar evolution is a dynamic process, and can infuse a galaxy with products such as metals and cosmic dust. Many of these features contribute to a galaxy's SED, which can be extracted via Stellar Population Synthesis techniques (Conroy, 2013). Galaxies are also known to accrete primordial hydrogen from the cosmic web, in principle leading to ongoing growth throughout a galaxy's lifetime. This 'in-situ' star formation is thought to be one of the main processes driving galaxy growth (e.g. Kennicutt, 1998).

Galaxy properties are commonly represented by expressing a comoving number density as a function of a global property; this is known as a 'distribution function'. The distribution functions of many galaxy properties commonly follow a distinguishing shape described by a 'Schechter' function (or gamma distribution) (Schechter, 1976), which can be described by a power law and an exponential fall-off at a characteristic value. Estimates of the Stellar Mass Function (SMF) over cosmic time show that galaxies also gain mass through merging ('ex-situ' growth) (Conselice et al., 2003; Somerville and Davé, 2015). The 'Hierarchical' model (see Madau and Dickinson, 2014) predicts that large structures are built from the merging of smaller structures. It is also believed that high mass galaxies formed relatively early, as the number density of higher mass galaxies increases rapidly between z$\sim$2-3 but stays predominately constant between z$\sim$2-0 (Muzzin et al., 2013). The lower mass galaxies observed today appear to have formed later and on a longer timescale (so-called 'mass assembly downsizing', see Cimatti et al. 2006). It is however unclear how the most massive galaxies have assembled their mass, as some models suggest a relatively limited role of mergers (e.g. Lapi et al., 2011), while others suggest that mergers can have a strong impact (e.g. González et al., 2011b).

Intimately connected with the growth of galaxies is the observed variations in galaxy *morphology*. Edwin Hubble, the father of extragalactic astronomy, provided the first galaxy classification scheme (the 'tuning fork' diagram) apportioning galaxies into the classifications of ellipticals, spirals (barred and non-barred) and irregulars. Although this classification has since been expanded (e.g. van der Marel et al., 1994), modern observations show that almost all galaxies generally exhibit a morphology that broadly falls into one of these categories. More generally however (for the purposes of this work) I assume galaxies can be classified as having a 'bulge' and 'disk' component

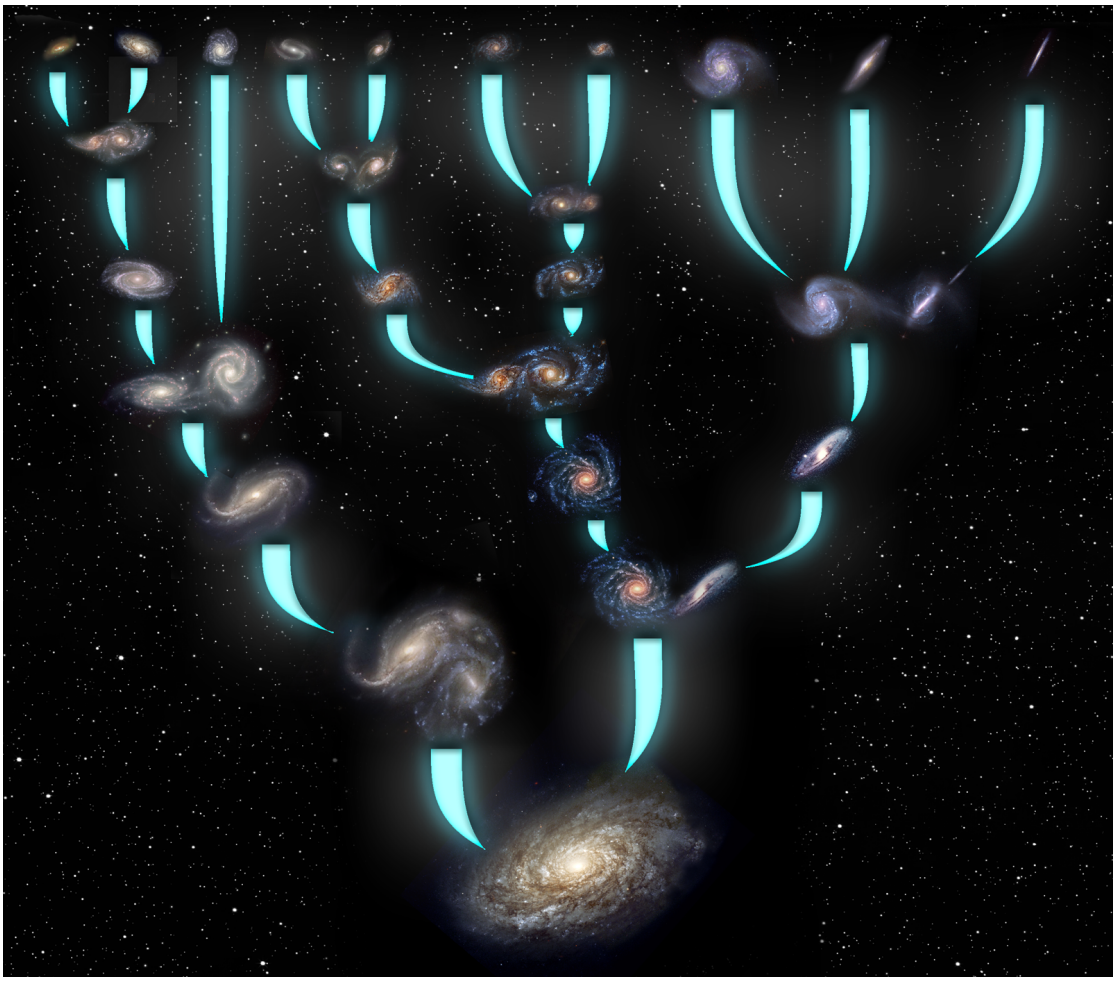

FIGURE 1.4: Cartoon image showing the hierarchical model. In this model, small galaxies form first, and their merging forms larger structures. This process is driven by the gravitational effect of the underlying dark matter substructure, which is not shown here.

in some combination (parameterised by the B/T (Bulge-to-total) ratio). The bulge is a broadly spherical, compact region of stars that are supported by random motions, and can be fitted with a Sérsic brightness profile (Sérsic, 1968). More generally, elliptical galaxies, whilst lacking a disk, follow an extremely similar brightness profile, leading to ellipticals and bulges being frequently grouped together as 'spheroids' (Caon et al., 1993; Ciotti and Bertin, 1999; Graham et al., 2001)[2]. Disks are larger, flatter and rotationally supported and commonly exhibit active star formation, and can be fitted with an exponential brightness profile (Mo et al., 2010). Figure 1.5 shows M104, the Sombrero galaxy, which is (visually) a good example of a nearby galaxy with strong bulge and disk components. The bulge is the central diffuse 'glow' (actually comprised of stars

[2]It should be noted that strictly speaking bulges should be classified into two types, *classical bulges*, with classical 'elliptical' Sérsic profiles, and *pseudobulges*, the latter of which have more 'sprial-like' mass distributions. See e.g. Kormendy (1993); Fisher and Drory (2008); Gadotti (2009); Erwin (2008). I do not consider pseudobulges in this work.

FIGURE 1.5: The Sombrero Galaxy (M104), a good example of a galaxy with prominent bulge and disk components. Image credit: HST/NASA.

with randomly oriented orbits), and the disk is the flat, almost edge-on component strongly emphasised by prominent dust lanes [3].

Spectroscopically, galaxies seem to fall into one of two persuasions; a colour-mass diagram shows a discrete 'red sequence' (typically ellipticals) and a broader 'blue cloud' (typically spirals) (Bell et al., 2004; Strateva et al., 2001; de Vaucouleurs, 1961). Spectroscopic pointers towards stellar age and photometry in the UV and IR show that the red sequence is comprised of 'quiescent', non-star forming galaxies with older stellar populations, whereas the blue cloud contains galaxies with a relatively adolescent stellar population and considerable ongoing star formation (Schiminovich et al., 2007; Baldry et al., 2004; Martin et al., 2007; Brinchmann et al., 2004; Salim et al., 2007; Noeske et al., 2007). Between these regions lies the so-called 'green-valley' (Bell et al., 2004; Martin et al., 2007; Faber et al., 2007; Fang et al., 2012; Schawinski et al., 2014). Deep surveys have shown that this bimodality exists up to at least $z{\sim}2$ (and possibly higher), and that the number of quiescent galaxies has been slowly increasing over cosmic time, whereas the number of star forming galaxies is decreasing (Muzzin et al., 2013; Brammer et al., 2011). The implication is therefore that over cosmic time there is some physical process that is 'quenching' star formation, the nature of which is not yet fully understood (Schawinski et al., 2014; Chen et al., 2020). Quenching processes can be broadly divided into two categories, processes that forcibly expel gas from the galaxy ('ejective' feedback) and processes that heat gas so that it can no longer collapse to form stars ('preventative' feedback) (Kereš et al., 2009).

[3] The B/T ratio of this galaxy is generally accepted to be ~ 0.77, although this is debated (Cohen et al., 2020).

There are several physical effects that could occur in a galaxies lifetime[4] that are regularly invoked to explain the diversity (both morphological and spectroscopic) in the galaxy population:

- *Major Mergers.* Merger events occur when two galaxies actively collide and merge together to form a more massive galaxy. Several examples of ongoing mergers have been observed. Merger events are classified according to their *merger ratio*, or ratio of the mass of the smaller galaxy to the mass of the larger. A merger event is classified as 'major' if this ratio exceeds some value, normally $\sim$0.3. Such a violent interaction will inevitably disrupt any pre-existing galactic structure, removing angular momentum from the disk (Toomre, 1977; Barnes, 1988; Barnes and Hernquist, 1992; Hernquist, 1992; Mihos and Hernquist, 1996). There is significant debate as to the role major mergers play in quenching and in building massive elliptical galaxies. While initially intense star formation is likely to be triggered, a major merger could also shock heat any gas component, potentially quenching the galaxy (Lambas et al., 2012). Stellar feedback from any star formation can also contribute (Cox et al., 2006). However, hydrodynamical simulations have shown that gas-rich mergers can instead lead to the re-formation of disks (Springel et al., 2005; Hopkins et al., 2009a; Robertson et al., 2006a). This suggests that morphological transformation must be intimately linked with quenching; some process is required to remove the gas before galaxies merge, and to prevent new gas from cooling.

- *Minor Mergers.* Minor mergers occur when there is a large difference in mass between the merging galaxies. In this case, the merging galaxy does not have enough mass to fully disrupt the parent, instead thickening disks (Moster et al., 2010a; Walker et al., 1996) and/or drawing stars out of their ordered motions in galactic disks and into the bulge component (Toomre and Toomre, 1972; Somerville and Davé, 2015, and references therin).

- *Disk instabilities.* It has also been suggested that bulges may grow 'in-situ', i.e. without outside interference. Strictly speaking there are two types of processes that can results in this, but they are collectively termed 'disk instabilities'. In the first, clumps can form in the disk, and migrate to the galaxy centre (Dekel et al., 2009; Bournaud et al., 2011; Elmegreen et al., 2008). The second method involves the formation of a bar, transferring mass into the compact core (Combes et al., 1990; Hohl, 1971; Ostriker and Peebles, 1973; Toomre, 1964).

- *Shock Heating.* A well studied mechanism for limiting the collapse of a gas cloud, the conversion of gravitational potential energy into heat can potentially result in

[4] I only consider *massive* galaxies in this paradigm, so processes that might (for example) quench small satellite galaxies (such as ram-pressure/tidal stripping) are not discussed here. See e.g. Gunn and Gott (1972); Balogh et al. (2000)

a hot halo of gas in massive galaxies (Birnboim and Dekel, 2003; Kereš et al., 2009; Dekel and Birnboim, 2006). This process alone cannot however be maintained, as the hot halo will eventually cool (on timescales of $\sim$2 Gyr), so additional feedback processes are required (Birnboim et al., 2007).

- *Feedback.* Within galaxies themselves, it is clear that at the present day only $\sim$10% of the total baryonic mass has formed stars; this is unexpected, as without some kind of feedback mechanism it is likely that almost all gas should have cooled to form stars at the current age of the universe (Krumholz et al., 2012). It is now accepted that there are several mechanisms supplying energy to interstellar gas, from radiation pressure to supernovae feedback (see Hopkins et al. (2012) for details). Externally, these processes are thought to be driving clear outflows of gas observed in star forming galaxies (Veilleux et al., 2005). AGN can theoretically deposit extremely large quantities of energy into the gas in and around galaxies. This will be discussed at length in Chapter 4, as it is of critical importance to this work.

Overall, some combination of these effects have most likely driven the evolution of the galaxies observed today. In a ΛCDM universe, mergers are expected to be ubiquitous, with major mergers providing a convincing mechanism for the formation of spheroids. Semi-analytic models of galaxy evolution have generally found that major mergers are not enough to explain the relative abundances of spheroids observed today, so disk instabilities are often invoked to explain this discrepancy (Parry et al., 2009; De Lucia and Blaizot, 2007; Guo et al., 2011; Porter et al., 2014). Reproducing the quenched fractions of galaxies has proven harder, requiring feedback mechanisms from AGN to explain even the observed colour-magnitude relations, let alone the quenched fractions (Gabor et al., 2011; Silk and Mamon, 2012; Somerville et al., 2008; Bower et al., 2006; Croton et al., 2006; Kimm et al., 2009; Somerville et al., 2008).

1.2.3 Velocity Dispersion

Galaxies are made up of stars that move in orbits. These orbits may vary substantially, with the combined orbital paths containing detailed information about the assembly history of the galaxy. This information is partially represented by galaxy's line-of-sight velocity dispersion. Absorption lines in the spectra of spheroids are broadened by the combination of this intrinsic velocity dispersion and integration along the Line of Sight (LOS). The overall integrated spectrum, weighted by brightness, will therefore be similar to that of the individual stars, but with broader absorption lines due to the motion of the stars. There are a variety of techniques used to obtain this measurement, see e.g. Burbidge et al. (1961); Minkowski (1962); Morton and Chevalier (1972); Richstone and Sargent (1972); Simkin (1974); Sargent et al. (1977); Bender and Nieto (1990); Rix

and White (1992); Barth et al. (2002); Grier et al. (2013). Velocity dispersion is normally measured within an aperture comparable to the effective radius of the galaxy $R \lesssim R_e$, denoted $\sigma_{ap}(R)$. $\sigma_{ap}(R)$ is a key property in interpreting galaxy structure and evolution. Galaxy scaling relations appear much tighter and linear when expressed in terms of $\sigma_{ap}(R)$ than, e.g., stellar mass or size (e.g., Bernardi et al., 2005, 2011a). In addition, analysis of residuals from scaling relations reveals that velocity dispersion appears as the most fundamental galaxy property linked to the mass of the central supermassive black hole (e.g., Bernardi et al., 2007; Shankar et al., 2016; Marsden et al., 2020), with a weak evolution along cosmic time (e.g., Shankar et al., 2009; Shen et al., 2015) (see Section 1.2.4). All of these pieces of observational evidence point to velocity dispersion as one of the main probes of both galaxy and supermassive black hole growth and assembly.

As discussed, galaxies appear to be progressively more compact at earlier epochs, with the more massive early-type galaxies showing the strongest evolution in their structural parameters (e.g., Trujillo et al., 2006; van Dokkum et al., 2008; Damjanov et al., 2011; Cimatti et al., 2012; Huertas-Company et al., 2013; van der Wel et al., 2014; Faisst et al., 2017; Mowla et al., 2019). One of the most popular ways to reconcile the local and high redshift observations is to invoke mergers, especially if minor and "dry" (gas-poor) mergers, which models predict to be frequent and effective enough to increase the sizes, Sérsic indices and to decrease velocity dispersions (e.g., Robertson et al., 2006b; Covington et al., 2008; van Dokkum et al., 2008; Naab et al., 2009; Nipoti et al., 2003, 2009; Oser et al., 2010; Shankar et al., 2010a,b; Covington et al., 2011; Nipoti et al., 2012; Oser et al., 2012; Shankar et al., 2013a; Lapi et al., 2018; Zanisi et al., 2021). However, additional processes can have a significant impact on modifying the structure and dynamics of galaxies, e.g., feedback from a central active galactic nuclei (AGN) and/or internal star formation (e.g., Fan et al., 2008, 2010; Ragone-Figueroa and Granato, 2011) as we have discussed, or even the appearance of newly-formed larger galaxies that may drive the observed evolution in a statistical sense (e.g., Carollo et al., 2013; Damjanov et al., 2015; Shankar et al., 2015; Fagioli et al., 2016). Indeed, velocity dispersion is predicted to grow steadily with star formation, but in a non-linear fashion in the presence of dry (gas-poor) mergers (e.g., Robertson et al., 2006b; Naab et al., 2009; Nipoti et al., 2009; Oser et al., 2012). Numerical simulations have shown that dry major mergers are expected to have a negligible impact on velocity dispersions, which are instead predicted to decrease due to the cumulative effect of minor dry mergers. Stochastic evolutionary sequences driven by strictly dry mergers are thus expected, on average, to steadily decrease velocity dispersions in galaxies with cosmic time. In Figure 1.6 I show the M^* vs σ from the SDSS (filled circles with error bars) compared to modelling presented in Bernardi et al. (2011b). A linear relation (long-dashed line) is 'bent' when velocity dispersion evolves via a sequence of (gas-poor) minor mergers. Each line represents a limit to the mass ratio ($f_{MIN} = M_{sat}/M_{cent}$) of merging satellites (at a rate predicted by numerical simulations). Setting a lower limit strongly increases the

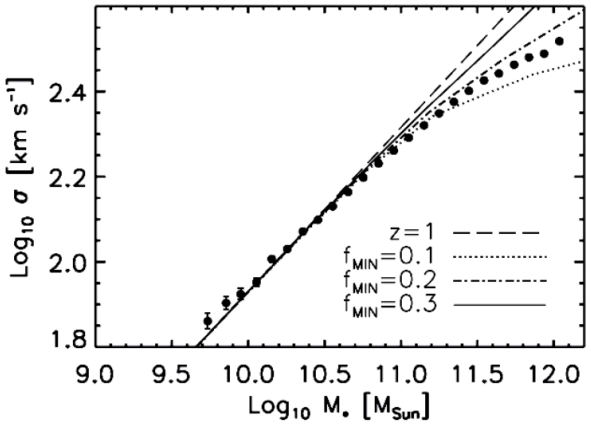

FIGURE 1.6: The Faber-Jackson relation (M^* vs σ) from the SDSS vs a merger toy model presented in Bernardi et al. (2011b).

curvature of this line, showing how sensitive velocity dispersion based observables are to the exact rate and magnitude of mergers over cosmic time. In merger-free galaxy growth histories dominated by passive or weak evolution, velocity dispersions should instead retain memory of the formation epochs of the galaxies (e.g., Granato et al., 2004; Cook et al., 2010; Lapi et al., 2018). In this framework, using an analytic model Cirasuolo et al. (2005) were able to reproduce the full local velocity dispersion function of early-type galaxies by linking velocity dispersion to the circular velocity of the halo (e.g., Ferrarese, 2002) at the epoch of the main burst of star formation. Dissecting the σ evolutionary tracks along the progenitors and/or at fixed stellar mass, which is the main aim of this thesis, can thus shed light on the different channels controlling galaxy assembly.

Velocity dispersion is also a tracer of the distribution of dark matter in the inner regions of the galaxies, via the dynamical mass $M_{dyn}(< R) \propto \sigma_{ap}(R)^2 R$, which traces the gravitational influence on test stellar or gas particles of the total mass within a certain radius R. The ratio between dynamical and stellar mass within the effective radius, $M_{dyn}/M^*(< R_e)$, appears to be increasing with stellar mass, $M_{dyn} \propto M^{*1+\alpha}$, with $\alpha \sim 0.2-0.3$ (e.g., Pahre et al., 1998; Padmanabhan et al., 2004; Gallazzi et al., 2006; Hopkins et al., 2009b), which is related to the overall "tilt" of the fundamental plane (FP) of galaxies (e.g., Djorgovski and Davis, 1987; Dressler et al., 1987), where the FP terminology is usually mostly applied to earlier type galaxies (e.g., Bernardi et al., 2020, but see also Ferrero et al. 2021). Different effects could contribute to the tilt of the FP and more specifically to the slope of the $M_{dyn}/M^*(< R_e)$ ratio, from an increasing contribution of dark matter in larger/more massive galaxies, to the effect of stellar non-homology, radial anisotropy, and/or systematic variations of the stellar population properties (e.g., Ciotti et al., 1996; Prugniel and Simien, 1997; Trujillo et al., 2004; Bertin and Lombardi, 2006; Cappellari et al., 2006; Hyde and Bernardi, 2009; Hopkins et al., 2009b; Cappellari

et al., 2013a; D'Onofrio et al., 2013; Zahid et al., 2016; Zahid and Geller, 2017; Bernardi et al., 2020; Mould, 2020; D'Eugenio et al., 2021).

In recent years it has become evident that the stellar initial mass function (IMF) may not be a universal constant. The IMF is (at its core) a distribution function that describes the inital distribution of masses for stellar populations (Mo et al., 2010). Systematic changes in the IMF, either across the population, or within a galaxy itself, can lead to changes in the stellar mass-to-light ratio. A large body of relatively recent literature argues that the systematic increase of M_{dyn}/M^* with M^* is almost entirely due to an IMF-driven M^*/L variation across the galaxy population (e.g., Cappellari et al., 2006; Conroy and van Dokkum, 2012; Cappellari et al., 2013a; Lyubenova et al., 2016; Tang and Worthey, 2017; Li et al., 2017, 2018). These studies conclude that the IMF correlates with σ_{ap}, becoming more bottom-heavy (Salpeter-like, e.g. Salpeter 1955) in galaxies with larger $\sigma_{ap}(< R_e)$, so that stellar mass estimates based on stellar population modelling which assume a universal IMF are systematically incorrect. However, these analyses assume that the IMF, and hence M^*/L within a galaxy, is constant. Recent work has shown that the IMF may, in fact, vary within a galaxy, becoming more bottom-heavy closer to the galaxy centre (e.g., Martín-Navarro et al., 2015; La Barbera et al., 2016; Lyubenova et al., 2016; van Dokkum et al., 2017; Parikh et al., 2018). This led Bernardi et al. (2018) to argue that IMF-driven M^*/L gradients within a galaxy could account for much of the perceived variation in M_{dyn}/M^*, and subsequent analyses have shown that realistic gradients may indeed reconcile the M_{dyn} and M^* estimates (Chae et al., 2018, 2019; Domínguez Sánchez et al., 2019; Bernardi et al., 2019). In this thesis I will show that mass and dynamical modelling inclusive of an IMF-driven M^*/L gradient can indeed reproduce the full systematic increase of M_{dyn}/M^* with M^* as measured by large local galaxy samples. However, I will also show that ignoring such IMF-related effects when estimating M^*, still matches some of the main sigma-related observables, which is a relevant result given that estimating IMF-related effects is costly (high S/N spectra are required).

More generally, in this thesis I will present a flexible yet accurate Jeans modelling approach developed under a variety of assumptions: the stellar profile, including wherever relevant a disk component; the inner dark matter profile; and the evolution with redshift of the galactic structural properties relevant to velocity dispersion. I will show that, whatever the exact choice of input parameters, all my models are able to reproduce the local data and make specific predictions on the relative roles of dark matter and stellar IMF, and on the evolution with redshift of $\sigma_{ap}(R)$ which are difficult to reconcile with models based solely on dry mergers.

1.2.4 Black Holes

Black Holes are arguably the most mysterious objects in the known universe. Regions of intensely curved spacetime, their gravitational influence is so intense that not even light can escape. Observational evidence suggests that galaxies host a central supermassive black hole (henceforth simply 'black hole', not to be confused with an 'ordinary' stellar mass black hole), with masses of the order of $\sim 10^{6-9} M_{\odot}$. The best evidence for the existence of these objects comes from within our own galaxy, where measurements of stellar dynamics confirmed the presence of a veiled 'leviathan' ($\sim 4.4 \times 10^{6} M_{\odot}$) designated as Sagittarius A* (Genzel et al., 1997; Ghez et al., 1998). Indeed, many nearby galaxies for which high-resolution data can be acquired show stellar kinematic patterns strongly suggesting the presence of a central massive dark object (Ferrarese and Ford, 2005; Kormendy and Ho, 2013).

The existence of massive black holes at the centre of galaxies also lends further support to the widely-accepted paradigm that quasars, and more generally AGN, are powered by matter accreting onto a central black hole. AGN are compact regions in the centres of many galaxies that exhibit terrific brightness over large portions of the electromagnetic spectrum. The release of gravitational energy from an infalling body of mass m approaching the Schwarzschild radius $R_s = 2GM/c^2$ of a compact object of mass M is possibly the most efficient energy-release process exhibited in nature. As discussed by Peterson (1997), the emission from the release of gravitational energy increases with the compactness of the source M/r. Assuming that most of the gravitational energy E powering the emission from an accreting black hole originates from within a few times R_s, say $r = 5R_s$, one could set $E = GMm/5R_s$, implying $E = 0.1mc^2$. The latter efficiency $\eta \sim 0.1$ of energy conversion in units of the rest-mass energy is an order of magnitude higher than the efficiency in stellar fusion ($\eta \sim 0.008$). Such titanic energy release provides an attractive explanation for high AGN luminosities, with theoretical models also suggesting that the energy/momentum release from the central black hole, (AGN feedback), could have profound consequences on the fate of its host galaxy, potentially driving out a galaxy's gas reservoir and quenching star formation (Silk and Rees, 1998; King, 2019). The masses of black holes within active galaxies can be estimated using a technique called 'reverberation mapping', although this requires calibration from the M_{BH}-σ relation (Bahcall et al., 1972; Peterson, 1993).

The central black hole masses, inferred from dynamical measurements of the motions of stars and/or gas in the host galaxies, appear to scale with galaxy-wide properties (or perhaps *bulge*-wide properties), such as stellar mass (Magorrian et al., 1998; Häring and Rix, 2004) and stellar velocity dispersion (Ferrarese and Merritt, 2000; Gebhardt et al., 2000; Ferrarese, 2002; Tremaine et al., 2002; Gültekin et al., 2009; McConnell and Ma, 2013; Savorgnan and Graham, 2015). The existence of such correlations is remarkable, as the black hole's (sub-parsec scale) sphere of influence is orders of magnitude

smaller than the scale of its host galaxy (kilo-parsec scale). These correlations suggest a close link (a "co-evolution") between black holes and host galaxies (Silk and Rees, 1998; Granato et al., 2004).

Modern black hole formation theories generally agree that the first black hole seeds formed at $z \gtrsim 15$. There are several possibilities for black hole seeding (Volonteri, 2010), arguably the most straightforward being the black holes formed from the remnants of the legendary 'Population III' stars (formed from ultralow-metallicity primordial gas), forming at $z \sim 20$ with masses of a few hundred $M_\odot$ ('light seeds'). This arrangement has problems explaining the high mass black holes powering AGN at $z \sim 6$ (Willott et al., 2010) without invoking accretion rates exceeding the Eddington limit[5]. An alternative model suggests that it is possible for gas clouds (of low-metallicity, with sufficient virial temperature and suppressed H_2 formation from UV background) to collapse into 'heavy seeds' of thousands to tens of thousands $M_\odot$ at $z \sim 10-15$ (Bromm and Loeb, 2003). A variation on this process include the fragmentation of gas clouds into a compact start cluster, within which stellar collisions assemble a black hole seed of a few hundred stellar masses (Devecchi and Volonteri, 2009).

Simple integral arguments (as famously suggested by Soltan 1982) suggest that black holes grow primarily through episodic accretion events. How this evolution is related to the distribution of black hole masses, the distribution of Eddington ratios, and the actual probability of a black hole being active (the 'Duty Cycle') is still a topic of much debate. It is generally agreed that a significant fraction of black hole growth is likely to happen in a 'Quasar' phase, most likely triggered by the merging of two massive galaxies. A quasar phase can grow a black hole by tens of millions to hundreds of millions $M_\odot$, making these events rare occurrences in a black hole's lifetime. Further growth is by lower luminosity accretion phases due the random accretion of cold gas (Hopkins and Hernquist, 2006).

Black hole growth is also known to occur via mergers. During a galaxy merger event, it is likely that dynamical friction will eventually bring black holes together. A binary pair is likely to be formed at a separation of a few parsecs, where the infall process has ejected sufficient matter to suppress the effects of dynamical friction. Overcoming this final distance can be problematic (the 'final parsec' problem), but solutions involving the introduction of additional matter or even a third black hole have been proposed (Merritt, 2013). Such systems are known to exist; Graham and Scott (2015) reported the observation of a binary black hole system with a separation of approximately 0.1 pc. At distances ≤ 0.01 pc, energy loss via gravitational waves can cause significant loss of orbital energy, eventually causing the black holes to merge, a significant gravitational wave event.

[5]The Eddington luminosity (or Eddington limit) is the maximum luminosity an object can achieve, balancing the outward force of radiation and the gravitational force acting inward. The luminosity of an object is sometimes expressed in terms of its *Eddington ratio*, or the ratio of its actual luminosity to its Eddington luminosity.

The most prominent and studied scaling relation relates the black hole mass $M_{\rm BH}$ to the stellar velocity dispersion σ (Ferrarese and Merritt, 2000) and the (stellar) mass of the host bulge, $M_{\rm bulge}$ (and by extension the luminosity of the bulge $L_{\rm bulge}$, see Marconi and Hunt (2003)). Other types of correlations have been proposed in the literature, such as correlations with the bulge light concentration $c_{\rm bulge}$ (Graham et al., 2001) and even the mass of the surrounding dark matter halo $M_{\rm halo}$ (Ferrarese, 2002). This work will focus on the $M_{\rm BH}$-σ relation, where σ is the stellar velocity dispersion inferred from spectral absorption lines (see Mo et al. (2010), Chapter 2).

The $M_{\rm BH}$-σ relation has attracted the attention of the astronomical community since its discovery (Ferrarese and Merritt, 2000), as it is believed to be closely connected to the galaxy/halo gravitational potential well, and thus may be related to the above-mentioned AGN feedback process (Granato et al., 2004). The relation is of the form:

$$\log \frac{M_{\rm BH}}{M_\odot} = \alpha + \beta \log \frac{\sigma_{\rm e}}{200 kms^{-1}} \,. \tag{1.1}$$

Ferrarese and Merritt (2000) initially retrieved a normalization and slope of, respectively, $\alpha = 8.14 \pm 1.80$ and $\beta = 4.80 \pm 0.54$, whereas more recent work (e.g., Tundo et al., 2007) suggests $\alpha = 8.21 \pm 0.06$ and $\beta = 3.83 \pm 0.21$. There is some debate in the literature concerning the exact shape of the $M_{\rm BH}$-σ and its dependence on, for example, morphological type or even environment (see, e.g., Lau, Wyithe (2006) and Hu (2008) for more details). It has been noted (e.g. van den Bosch et al. (2012)) that several overmassive black holes exist on this relation, hosted by galaxies that have undergone fewer than usual mergers, in tension with semi-analytic models (Savorgnan and Graham, 2015). However, these outliers could simply be the result of incorrect modelling of the galactic bulge/disk (Saglia et al., 2016).

Several groups have noted that the $M_{\rm BH}$-σ relation only weakly evolves with redshift (if at all) (e.g. Gaskell, 2009; Salviander and Shields, 2013; Shen et al., 2015). Supporting work by other groups base their conclusions on direct estimates of the $M_{\rm BH}$-σ relation on high redshift quasar samples (Woo et al., 2008), and studies based on comparing the cumulative accretion from AGN with the local black hole mass density, retrieved from assigning to all local galaxies a black hole mass via the $M_{\rm BH}$-σ relation (e.g. Shankar et al., 2009; Zhang et al., 2012).

On the assumption that all local galaxies host a central black hole, scaling relations could in principle allow us to assign black hole masses to all local galaxies without direct dynamical mass measurements, thus generating large-scale black hole mass statistical distributions such as black hole mass functions or correlation functions (see Shankar et al. (2009) and Graham and Scott (2015) for reviews on this topic). For example, a number of groups have used luminosity, as performed by Shankar et al. (2004), Salucci et al. (1999) and Marconi et al. (2004), or even Sérsic index, as performed by

Graham et al. 2007), to generate black hole mass functions. This procedure of course relies on two assumptions: firstly, that the observer has correctly identified the surrogate observable of black hole mass, and secondly that the established scaling relation is reliable. For example, the $M_{\rm BH}$-σ and $M_{\rm BH}$-$L_{\rm bulge}$, probably the most commonly used relations, have led to different black hole mass function estimates (Lau; Tundo et al., 2007).

An important question is whether the same black hole-galaxy scaling relations hold for both active and inactive galaxies. Several groups suggest that this is indeed the case (e.g. Reines and Volonteri, 2015; Caglar et al., 2019; Shankar et al., 2019b). It is important to stress that the samples of nearby (inactive) galaxies on which the black hole-host galaxy relations are based, still remain relatively small, only comprising around $\sim$ 70-80 objects. A key difficulty relies of course in acquiring sufficiently high-resolution data to allow for dynamical black hole mass measurements (see Faber (1999), Ferrarese and Ford (2005) and Kormendy and Ho (2013) for reviews of observational challenges).

Indeed, there is a growing body of work (Bernardi et al., 2007; van den Bosch et al., 2015; Shankar et al., 2016, 2017a, 2019a,b) supporting the view that current dynamical black hole mass samples may indeed be "biased-high", possibly due to angular resolution selection effects (see Merritt, 2013), with meaningful consequences for any study based on the "raw" relations. Interestingly, Shankar et al. (2016) showed that, via aimed Monte Carlo simulations, irrespective of the presence of an underlying resolution bias, the raw and "de-biased" scaling relations would still share similar slopes and overall statistical properties (e.g., very similar residuals around the mean), with (noticeable) differences arising only in the normalization between observed and de-biased scaling relations. In particular, the $M_{\rm BH}$-σ was shown to be more robust and the least affected by possible angular resolution effects.

Standard regression analyses showed that the $M_{\rm BH}$-σ has the lowest *intrinsic scatter* of any black hole scaling relation; e.g. Gültekin et al. (2009), Saglia et al. (2016) and van den Bosch (2016). This alone suggests σ is different from other variables. Beifiori et al. (2012) came to the conclusion that $M_{\rm BH}$ was fundamentally driven by σ due to its relative tightness. This work also tested the possibility of multi-dimensional relations, concluding that the introduction of additional variables barely reduced the scatter with respect to the $M_{\rm BH}$-σ, suggesting that stellar velocity dispersion remains a fundamental driving parameter. The amount of scatter characterizing diverse black hole scaling relations has been studied by several groups (Marconi and Hunt, 2003; Hopkins et al., 2007). These works also explored the addition of the effective radius $R_{\rm e}$ to σ to create a black hole 'fundamental plane' in the black hole scaling relations, further discussing in Hopkins et al. (2007). This relation naturally arises in their simulations, as a (tilted) correlation between black hole mass and bulge binding energy. This conclusion was supported by Saglia et al. (2016), who argued for a multidimensional relation deriving

from the bulge kinetic energy ($M_{\rm bulge}\sigma_{\rm e}^2$), as originally suggested by Feoli and Mele (2005).

de Nicola et al. (2019) presented a systematic study of black hole scaling relations on an improved sample of local black holes, confirming that "the correlation with the effective velocity dispersion is not significantly improved by higher dimensionality". The authors concluded that the $M_{\rm BH}$-σ is fundamental over multidimensional alternatives, independent of bulge decompositions. This is in line with van den Bosch (2016), who claimed that the $M_{\rm BH}$-$M_{\rm bulge}$ is mostly a projection of the $M_{\rm BH}$-σ relation.

As mentioned, in terms of galactic scaling relations, velocity dispersion may be statistically more significant and relevant than other galaxy observables (e.g. Bernardi et al., 2011a,b). Bernardi et al. (2005) analysed the colour-magnitude-velocity dispersion relation of an early-type galaxy sample of the Sloan Digital Sky Survey (SDSS), concluding that colour-magnitude relations are entirely a consequence of the combination of more fundamental correlations with velocity dispersion.

Bernardi et al. (2007) noted that the $M_{\rm BH}$-σ and $M_{\rm BH}$-$L_{\rm bulge}$ predict different abundances of black holes, with the former predicting a smaller number of more massive black holes. Interestingly, the combined σ-L relation (for the dynamically measured black hole sample, e.g. Yu and Tremaine 2002) is inconsistent with the same relation from the SDSS, with smaller $L_{\rm bulge}$ for given σ (regardless of the band used to estimate luminosity). This suggests that the dynamical sample of local black holes may be biased towards objects with higher velocity dispersion when compared to local galaxies of similar luminosity, which obviously calls into question the accuracy of the raw $M_{\rm BH}$-σ and $M_{\rm BH}$-$L_{\rm bulge}$ relations. While unable to identify the source of the bias, modelling of this effect by Bernardi et al. (2007) and Shankar et al. (2016) suggested that the bias in the $M_{\rm BH}$-σ is likely to be small, whereas the $M_{\rm BH}$-$L_{\rm bulge}$ is likely to predict over-massive black holes at a fixed galaxy (total) luminosity/stellar mass.

1.2.5 The main parameters controlling black hole growth: towards the creation of robust galaxy-AGN mocks

Additional and independent clues on the growth histories of supermassive black holes and on their co-evolution with their host galaxies, can be extracted from studying the statistical properties of AGN, on the common assumption that most of the past AGN emissivity is generated from gas accretion onto (central) supermassive black holes. The luminosity function of AGN represents a vital observational constraint on the growth of black holes, the shape of which is dictated by the underlying distribution of black hole masses and their Eddington ratios. For AGN samples to be used as a reliable statistical tool to probe black hole growth, they must of course be as complete as possible. X-rays (and radio) provide a highly efficient method for selecting AGN, which would

otherwise often be obscured and undetectable in other wavelength. X-Rays provide a highly efficient method for selecting AGN, especially as a fraction of the AGN population are surrounded by gas and dust that can obscure emission in some wavelengths (Obscured AGN), so sources too faint for optical detection can be identified. Intrinsic AGN X-ray emission is thought to originate from the immediate vicinity of the black hole, via Compton up-scattering in the accretion disk corona (Done, 2010; Gilfanov and Merloni, 2014). Some AGN are also known to exhibit X-ray 'jets' that can have strong links to X-ray continuum emission (e.g. Miller et al. (2010), see also Blandford et al. (2019)).

Studies of the AGN population have revealed a number of observational trends. It's known that, for example, a large proportion ($\sim$80%) of AGN are obscured, and that the obscured fraction decreases with time towards $z = 0$ (Ueda et al., 2014). Observations have allowed the X-Ray AGN luminosity function to be measured up to $z \sim 4-5$ (e.g. Georgakakis et al., 2016; Bongiorno et al., 2012, 2016; Aird et al., 2012), which has in turn revealed that AGN are a strongly evolving population. The abundance of AGN (or more accurately their spatial density) is known to peak at 'cosmic noon' of $z \simeq 1.5-2$ (Aird et al., 2010, 2015). These trends are also observed in optically selected AGN (e.g. McGreer et al., 2013; Ross et al., 2013). AGN selected using X-ray observations also tend to exhibit 'downsizing' whereby more luminous sources seem to have abundances that peak at earlier epochs (implying that more luminous sources assemble earlier, see Ebrero et al. 2009). It has also been noted that the mean mass accretion of black holes as extracted from the integral of the X-ray AGN luminosity function, closely traces the cosmological star formation density (e.g. Marconi et al., 2004; Shankar et al., 2009; Aird et al., 2015).

Much has been done to interpret these trends in a physical context. Naturally, an intuitive approach is to consider if there is any correlation between an accretion event and the properties of the host galaxy, especially it's morphological type and environment. Major galaxy mergers are tempestuous events, and provide an ideal way to bring a large supply of gas to a galaxy's nuclear regions (Sanders et al., 1988; Barnes and Hernquist, 1991). However, studies have shown that a significant fraction of AGN activity (at least since $z \sim 2$) is occurring in 'untroubled' main-sequence disk galaxies (Georgakakis et al., 2009; Kocevski et al., 2012). This suggests that the role of major mergers may be circumscribed to a specific subset of the AGN population, such as only the most luminous ones (Treister et al., 2012). In turn, the level of star formation within an AGN host can be used as a tracer of available gas, but there is debate in the literature as to whether AGN hosts exhibit atypical star formation rates or not (Santini et al., 2012; Rosario et al., 2013; Mullaney et al., 2015). Further clues may be found in the environment of AGN hosts, as their position in the cosmic web may yield important leads on the nature of AGN fuelling modes and the role of large-scale environment (Allevato et al., 2011, 2014).

The average growth of supermassive black hole growth of a given mass via gas accretion depends on a series of parameters, most notably the radiative efficiency, introduced above, the duty cycle, i.e. the fraction of active black holes of that mass active at that time, and the Eddington ratio, i.e. the rate at which these active black are accreting mass with respect to their Eddington limit. Despite intense theoretical and observational studies, these parameters are still ill-constrained.

Several semi-analytical models and hydrodynamical simulations (e.g. Springel et al., 2005; Hopkins et al., 2006; Menci et al., 2008) have been developed in recent years to describe the main mechanisms that fuel the central supermassive black holes (BHs). With suitable adjustment of parameters, these models can explain many aspects of AGN phenomenology (e.g. Hopkins et al., 2006, 2008). Often relying on a rather heavy parameterization of the physics regulating the cooling, star formation, feedback, and merging of baryons (e.g. Monaco et al., 2007), semi-analytic models of galaxy evolution can present serious degeneracies (e.g. González et al., 2011a; Lapi et al., 2011), or even significant divergences in, e.g., the adopted sub-grid physics (Scannapieco et al., 2012; Nuñez-Castiñeyra et al., 2020). Habouzit et al. (2021) present comparison of the black-hole mass host galaxy scaling relations from different simulations, finding that the chosen prescriptions for supernovae and AGN feedback can strongly affect the derived scaling relations.

Semi-empirical models (SEMs) represent an original and complementary methodology to more traditional modelling approaches (see Section 1.3.2). The application of SEMs are particularly relevant to the creation of active and normal galaxy 'mock' catalogues (e.g. Conroy and White, 2013), which are a vital component of the planning of imminent extra-galactic surveys such as Euclid (Laureijs et al., 2011) and the Vera C. Rubin Observatory Legacy Survey of Space and Time (LSST; LSST Science Collaboration et al., 2009). The first step for the creation of mocks consists in assigning galaxies to dark matter halos extracted from large cosmological N-body simulations (e.g. Riebe et al., 2013; Klypin et al., 2016), via abundance-matching techniques (e.g. Marinoni and Hudson, 2002; Kravtsov et al., 2004; Vale and Ostriker, 2004; Shankar et al., 2006; Behroozi et al., 2013; Moster et al., 2013). Despite being based on minimal assumptions, the latter are not immune to important systematics, mostly related to the input data, which propagate onto the star formation and mass assembly histories predicted by SEMs (e.g. Grylls et al., 2020a,b; O'Leary et al., 2020).

In the last few years, several studies have focused on the creation of mock catalogs specifically for AGN that can be utilized for the planning and testing of large-scale AGN-dedicated extragalactic surveys such eROSITA (e.g. Georgakakis et al., 2019; Comparat et al., 2019; Aird and Coil, 2020). These AGN mocks are built by starting from an empirical galaxy catalog and by assigning to each object a specific accretion-rate that is proportional to the quantity L_X/M^*, drawn randomly from observationally determined probability distributions $\mathrm{P_{AGN}}(L_X/M^*)$ (e.g. Bongiorno et al., 2016; Aird et al.,

2018; Aird and Coil, 2020). This quantity can be measured directly from observations and provides an estimate of X-ray emission per unit stellar mass for a galaxy.

The P_{AGN} distribution has been derived in the last decade in several studies by using X-ray selected AGN. Early observational works suggested a nearly universal shape (Aird et al., 2012; Bongiorno et al., 2012) approximated by a power-law with a slope that does not depend strongly on either redshift or host galaxy stellar mass, and a break close to the Eddington limit. More recent investigations suggest a shape of P_{AGN} similar to a Schechter function that depends on the redshift, the stellar mass and the star-formation rate of AGN hosts (e.g. Georgakakis et al., 2017; Aird et al., 2017, 2018).

The advantage of this methodology is that by using just a few input relations, namely the stellar mass-halo mass relation (from abundance matching) and the probability distribution of specific accretion-rate P_{AGN}, it is possible to create a mock catalog of AGN that – be design – reproduces the observed X-ray luminosity function (XLF) and the large-scale bias (see Appendix A.4) at a given host galaxy stellar mass. The explicit assumption in these AGN mock catalogs is that the large-scale distribution of AGN is independent of the physics of BH fueling. For example, key information such as BH mass, the AGN duty cycle (i.e. the probability for a galaxy of being active above a certain luminosity or threshold), is largely bypassed, which limits the efficacy of these models in shedding light on the processes controlling the co-evolution of BHs and their hosts. Moreover, in these models the assignment of specific accretion-rates to mock galaxies by using P_{AGN} is a stochastic process, and no distinction is made between central and satellite galaxies, implying that AGN in satellite and central halos share the same probability of being active.

In this thesis I will explore how to create AGN mock catalogs. By calibrating the AGN mocks on the bias at fixed BH mass, stellar mass, and AGN luminosity, I will show a self-consistent and robust route to break the most relevant degeneracies and narrow down the choice of input parameters. I will present this work in Chapter 5.

1.2.6 Visualization of the large scale universe

I will now explore how I can 'bring together' the science exploring galaxy and black hole evolution contained in this thesis. In this Section I will briefly review previous attempts to 'visualize' the large scale universe, and how this has guided the development of 'Astera', presented in Chapter 5.

As discussed, ΛCDM predicts that structure in the universe forms via the collapse of dark matter into distinct filaments, voids and haloes (Zel'Dovich, 1970; Peebles, 1980). This structure is notoriously difficult to visualize in two dimensions, and since the early days of cosmological research, numerous attempts have been made to visualize the ''cosmic web''. Initial attempts by, for example, Doroshkevich and Shandarin (1978)

showed a representation of the cosmic web as a simple 2D ‘‘slice”, with simple-plotted points representing the density distribution. Since then, increasing advances in digital graphics have allowed for significantly more visually impressive images (e.g. Springel et al., 2005; Abel et al., 2012). Despite the impressive quality of these images, it is clear that a 2-Dimensional projection of the large scale structure of the universe cannot capture the high complexity its full 3D structure, so more elaborate projections in pseudo-3D or utilizing iso-surface density have been developed (e.g., in Klypin and Shandarin 1983). The advent of computer graphical rendering has allowed for truly breathtaking video representations of the large scale universe in projected 3D, such as Springel et al. (2011), Klypin et al. (2011a), Illustris Collaboration (2018), and Aragon-Calvo et al. (2012).

Digital graphics can be broadly categorized into “pre-rendered” graphics and “real time” graphics. The former requires pre-processing of the digital assets (often at great computational expense, but only once) into a series of frames that are assembled into a video format that is fixed in scope but can be replayed on virtually any device. This is most commonly seen in modern digital animation, commonly used in the entertainment industry. The latter, “real time” rendering, requires digital assets to be processed ”on the fly”, and must be processed quickly enough to ensure that the image can be recreated many times a second. This requires significant computational power, but crucially allows for user interactivity, with potentially unlimited scope for the user having dynamic control over the experience. Real-time rendering has, until recently, been restricted solely to video games, with visual quality notably worse that pre-rendered graphics. However, in recent years the quality of real time graphics has notably improved, allowing for their use in a wide variety of applications, such as on virtual film sets (Farris, 2020).

Real-time rendering depicting extragalactic scales have not yet been explored with full scientific accuracy. Several projects have come close; Celestia (Laurel, 2001) is a free visualizer for many astronomical objects. Its open source nature has led to numerous extensions, including planned cosmological visualizers. There are numerous sky visualizers that offer an extragalactic view of the universe based on astronomical imagery, such as WordWide Telescope (Fay and Wong, 2008), Google Sky (Google, 2007) and others, focusing on real data. Universe Sandbox (Dixon, 2017) is an interactive educational software application that simulates gravitational effects in various scales, including interactions between pairs of galaxies. SpaceEngine (Romanyuk, 2010) is a remarkable achievement, and is capable of procedurally generating a vast universe the user can explore with scales ranging from individual planets to the extragalactic. Each of these projects, mostly focused on small-scale bodies such as planets and stars, is limited by the compelling need to simulate a vast range of length scales, understandably focusing on the solar system and similar bodies. This methodology inevitably produces a lack of accuracy when simulating the large scale structure of the Universe.

As majestic and awe-inspiring as it is, the large-scale universe is yet to capture the imagination of the general public. Visualization (and interaction) is vital for the communication of complex ideas and concepts, especially when transferring knowledge to inform and educate. People want to 'see' and interact with the universe for themselves. In this thesis I present a 'prototype' for a product that will capture the imagination of the public and inspire a new generation of astronomers. I call this project 'Astera'. Astera generates a dazzlingly beautiful, but also scientifically accurate, interactive view of the universe on cosmological scales. I will explore Astera in Chapter 5.

1.3 Tools

I have reviewed the necessary background material for this thesis in the previous Sections, but I will now review the 'Tools' that are used by astronomers to explore the areas that I have highlighted. Specifically, in this Section I will review the *computational models* that are used to explore galaxy evolution. Computational modelling has (relatively recently) emerged as a 'third pillar' of Astronomy alongside theory and observation. Simulations form a bridge between theory and observable, generating hypotheses, forecasts and predictions about the real universe. By running simulations, Astronomers can test theory against observations, and make predictions for future observations. Each theoretical component of galaxy evolution fits together to form a 'mosaic' that provides the current best picture of Galaxy Formation and Evolution. However, pieces might interact together through simulation in unexpected ways, revealing that pieces in this mosaic that are missing, incomplete or need completely remaking. A new hypothesis or technique might represent test fitting a new piece, which might be eventually accepted or rejected. The simulation itself represents the framework within which one holds these pieces, crucially allowing the modeller to predict and test the picture. In each case, one compares the output of the simulation to reality, and adjusts or modifies the parts that fit poorly, and keeps the parts that fit well.

It is clear that a large proportion of the pieces in the current best picture are oversimplified, and there is much work to be done before a full standard model of galaxy evolution can be created. Despite this, the general successes of hydrodynamic, semi-analytic and semi-empirical modelling at reproducing the observed universe are extremely encouraging, and will provide a firm foundation on which further work can be built.

1.3.1 Semi-Analytic Models

At its most basic level, a semi-analytic model treats the highly complex astrophysical processes described in Section 2 using simple analytic approximations. By design,

to reproduce the wealth of observational phenomena, this methodology necessarily requires a high number of recipes and free parameters. An example of a typical parameter is the fudge factor in the dynamical friction timescale characterizing the infall timescale of satellite haloes into more massive haloes. This factor is adjusted until the number of satellites at the present day matches the number of galaxy satellites observed in the local Universe (Grylls et al., 2019).

A semi-analytic model will (in general) include the following processes. Initially, after appropriate cosmological parameters are chosen, a N-body simulation or Extended Press Schechter formalism will be used to construct a 'merger tree' for a series of dark matter haloes. Within each halo, three mass values for the components of baryonic matter will be assigned; hot gas, cold gas and stars. The prescriptions described in the previous Section will be implemented to account for the changes in these values. Cooling processes will convert hot gas into cold, and star formation will convert cold gas into stars, as well as changing the overall metallicity of the interstellar medium. Proper prescriptions that account for the complexities of merging (e.g. triggering bursts of star formation) should also be implemented. The larger galaxy will initially become central, whilst the smaller galaxy will become a satellite that ceases to accrete gas until the galaxies are fully merged on a timescale that is set by dynamical friction. Prescriptions that affect morphology become relevant here; if there is a large size difference between galaxies, then it is likely that the larger will exhibit little morphological change. However, in the case of two similarly sized galaxies merging, two disks may be disrupted and combine to form an elliptical, for example. The remnant may then continue to accrete gas and further evolve. This procedure will be completed for a large number of haloes until the present day ($z = 0$), allowing for the global properties of the simulation to be compared to local observations.

Early semi-analytic modelling had trouble reproducing the stellar mass function at high redshifts: far too much gas collapses to form stars (e.g. White and Frenk, 1991; Blanchard et al., 1992) without some kind of additional heating, normally suggested to be supernovae heating. Other problems included reproducing the colour-magnitude relation, which was remedied by better models of dust extinction and metallicity (e.g. Cole et al. 2000). Early models also underestimated the number of large bright galaxies, which suggested that some process was suppressing star formation in massive galaxies. Various mechanisms (including AGN feedback) have been suggested, with various degrees of success (see Somerville and Davé 2015; Silk and Mamon 2012).

Despite these obstacles, semi-analytic models reproduce the observed universe reasonably well, implying that current hypotheses for galaxy evolution are generally reasonable. However, due to the large number of physical assumptions and parameters, there is still some broad disagreement among different models, and a 'standard model' for galaxy formation and evolution has not yet been achieved.

1.3.2 Semi-Empirical Models

Semi-empirical models are a relatively recent 'variation' of semi-analytic models, and aim to overcome the main disadvantages by minimizing their assumptions and parameters. This is achieved by using observational inputs instead of theoretical quantities; whilst this somewhat limits their scope, semi-empirical models are best used as a remarkably powerful complementary tool to semi-analytic and hydrodynamic modelling. Best used to investigate a specific aspect of galaxy evolution, a semi empirical model will (like a semi-analytic Model) start with a merger tree and assign a central galaxy to each dark matter halo. The properties of this galaxy will be assigned using empirical relationships; for example the stellar mass of the galaxy might be assigned using the observed Stellar Mass - Halo Mass relation at the specified redshift. This process is repeated at each timestep, so the assigned property varies as in the real universe. This approach allows the modeler to effectively test a much smaller number of assumptions (e.g. the amount of matter stripped from a satellite galaxy before merging), and compare the results to the real universe.

While this approach is still somewhat in its infancy, several successful semi-empirical models have been created. Hopkins et al. (2008) tested the ansatz that galaxy mergers trigger quasar activity, and reproduced a wide range of quasar host galaxy distribution functions at a range of redshifts. Other examples include Zavala et al. (2012), who investigated the relationship between mergers and disks, and Shankar et al. (2014), comparing semi-analytic, semi-empirical and observational catalogues.

Overall, semi-empirical models are a relatively new and unexplored approach that has the potential to overcome a lot of the limitations of semi-analytic models to focus on specific problems. This focused methodology may be limited in scope, but seems likely to yield exceptional results on the specific problems it is applied to. In this work, I will utilize techniques from semi-empirical models (e.g. empirical prescriptions) for much of my modelling of velocity dispersion and black holes, using the average evolution of dark matter haloes, combined with simple prescriptions for the evolution of galaxy properties (e.g. stellar mass, sizes etc). This approach will initially bypass the need for a full hierarchical model, but I will also use the more sophisticated model DREAM (Fu et al. in prep) to explore the effect of mergers.

1.3.3 Hydro Simulations

In brief, a hydrodynamic simulation explicitly computes the dynamics of continuum media (e.g. fluids, gases). From the perspective of a cosmological modeller, this means the simulation of the dynamics of the dark Matter, gas, stars and black holes *together*, considering not only gravitation, but also baryonic processes such as star formation,

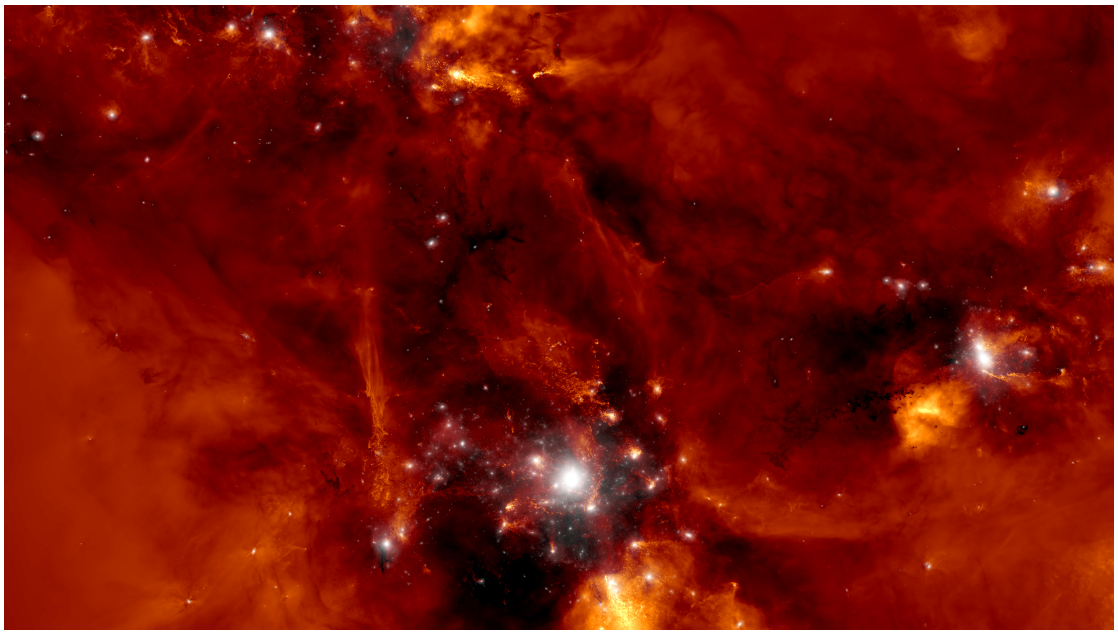

FIGURE 1.7: A proto-cluster region within the TNG50 simulation. Dark matter structures are shown in white. Vigorous feedback processes combat the inflows of cosmic gas into these gravitational potential wells, resulting in a complex interplay of gas motions. Credit: TNG

thermodynamics, etc. A hydrodynamic simulation is highly complex: it requires solving the Euler equations with conservation of mass, momentum and energy. This is typically done in one of the following three ways. Firstly, Lagrangian methods apply a smoothing kernel to the simulation particles to acquire information about the fluid (see e.g. Hernquist and Katz 1989; Read and Hayfield 2012; Hopkins 2012). Lagrangian methods are highly adaptive, can provide a broad scope given appropriate computational resources, but can struggle to effectively simulate shocks and surface instabilities. Eulerian methods, suffer from the 'reverse' problem: better modeling of surface instability and shocks at the expense of a lack of flexibility, discretizing the simulation into a (possibly adaptive) grid and compute the transmission of properties of the fluid (normally pressure) across cell boundaries (see e.g. Bryan et al. 2014). The final approach is a combination of the two (a 'Lagranian-Eulerian' method) such as AREPO (Springel, 2010), with an adaptive mesh composed of polyhedral cells. This mesh 'follows' the particles like a Lagrangian method, but also handles instabilities and shocks extremely well like a Eulerian method. In general, however, different techniques are most effective when applied to the problems they excel at, so most well-applied modern hydro methods yield effective results, making it hard to assign supremacy to any one method. For a more comprehensive overview of these topics, see Somerville and Davé (2015).

Hydro simulations appealingly fully model the spatial and time evolution of physical systems that otherwise must be treated using idealized, analytic prescriptions. The primary limitation of the hydro method is, at its core, computational resource. With the rapid evolution of this industry in recent years, such as the rise of parallel processing

and dedicated GPUs, it remains to be seen if the full potential of the hydro simulation will be able to mature (Silk and Mamon, 2012).

In this work, I will compare my results to the outputs of Hydrodynamical simulations, namely the Illustris TNG50 simulation (Nelson et al., 2019b; Pillepich et al., 2019). Illustris TNG is an ongoing series of Hydro simulations that aim to illuminate the physical processes that drive galaxy formation. TNG succeeds the original Illustris simulation, and includes three primary runs spanning a range of volumes and resolutions; TNG50, TNG100, and TNG300.

1.4 Key Questions

In this Chapter I have summarised the main processes shaping galaxy evolution, namely mergers, star formation and quenching. I have discussed the strong connection between galaxies and their central supermassive black holes. I have then highlighted that galaxy velocity dispersion is a key ingredient to unveil the assembly histories of both galaxies and supermassive black holes, and predicting its dependence on stellar mass, black hole mass and cosmic time will be the main aim of this thesis. More precisely, this thesis aims at answering the following key open questions in galaxy evolution:

- *How does velocity dispersion evolve with redshift for galaxies of different stellar mass? What ultimately drives this evolution? Is this evolution consistent with what predicted by hierarchical galaxy assembly models?* To answer this question I will first present, in Chapter 2, a semi-empirical detailed Jeans modelling technique inclusive of constant and radially-varying mass-to-light ratios, bulge-disk decompositions, halo and stellar profiles. I will show in the first part of Chapter 3 that my Jeans model is capable of reproducing all the main trends with velocity dispersion observed in large samples of local galaxies with integral field spectroscopy, with a particular focus on the role played by radially-varying mass-to-light ratios in dynamical mass estimates. Equipped with Jeans models anchored to the local Universe, in the second part of Chapter 3 I will predict the evolution of galaxy velocity dispersion along the main progenitor branches of the host dark matter haloes in a semi-empirical fashion, that is in ways independent of any specific galaxy evolution model, and I will dissect the relative role of the inner dark matter in driving velocity dispersion at high redshifts. In the final part of Chapter 3, I will compare my data-driven velocity dispersion evolutionary track with predictions from (dry) merger models (using the semi-empirical code DREAM, introduced in Chapter 2) and from the TNG50 hydrodynamic simulation.

- *Is the $M_{\rm BH}$-σ relation truly fundamental? How does the this relation evolve with redshift? Is it roughly constant in slope and normalization as predicted by AGN feedback*

models? I will address these questions in Chapter 4. In the first part of Chapter 4, I will set out detailed analysis of the residuals applied to the local sample of galaxies with dynamical measurements of their central black hole masses to show that indeed velocity dispersion seems the variable most closely correlated with black hole mass. In the second part of Chapter 4 I will couple the σ evolutionary tracks presented in Chapter 3, with black hole accretion histories independently derived from the X-ray luminosity-stellar mass relation derived from stacked X-ray AGN. My results do indeed point to a steep and constant $M_{\rm BH}$-σ relation in line with quasar-driven AGN feedback models and local data. In the last part of Chapter 4 I go a step further and show that AGN clustering at fixed black hole mass is efficient in constraining black hole-galaxy scaling relations in AGN samples in ways independent of the duty cycles and Eddington ratio distributions, thus finally providing an efficient methodology to break the degeneracies in black hole/AGN accretion models. I will show that the $M_{\rm BH}$-M^* relation of local dynamically-measured black holes is biased high and does not reproduce the clustering, while the $M_{\rm BH}$-σ relation performs much better.

Equipped with a deeper understanding of black hole-galaxy scaling relations, I will present in Chapter 5 a step-by-step methodology to build realistic mock populations of active and inactive black holes by populating dark matter haloes with galaxies and black holes in ways to avoid degeneracies in the input parameters. These type of mocks are extremely relevant to provide robust predictions for the next-generation of astronomical facilities that will observe millions of galaxies, but also for educational purposes, as described in the last part of Chapter 5 in which I will present my 3D interactive visualisation of the Universe. I will conclude the thesis in Chapter 6, in which I will discuss my main results in the context of galaxy and black hole evolution models.

Chapter 2

Methodology

2.1 Overview

In the first part of this Chapter I detail my Jeans model to compute velocity dispersions under a variety of conditions for both the stellar and dark matter profiles at both z=0 and at higher redshifts, including the methodology for handling a constant and radially-varying M*/L ratio and to incorporate redshift-dependent galactic properties (such as an increasing effective radius with cosmic time). In the second part of the Chapter I will introduce the cosmological semi-empirical DREAM (the DiscRete semi-EmpiricAl Model), which has been developed in my group in the last years and to which I substantially contributed. I will deploy DREAM to model the merger rate histories of satellite galaxies infalling on central galaxies and thus in turn model the expected evolution of velocity dispersion in hierarchical models of galaxy formation. I will finally provide an overview of the datasets I use as a reference to my models in the final part of the Chapter.

My overall methodology to compute σ is summarised in Figure 2.1. I start from an observational sample (see Section 2.4) of central galaxies with measured luminosities, stellar masses (in the case of a fixed IMF), effective radii and Sérsic indices at $z \approx 0$. I then associate to each galaxy a dark matter halo mass extracted from the (inverse) of a stellar mass-halo mass (SMHM) relation (e.g., Shankar et al., 2017b). I then follow the procedure, described in detail below, to compute velocity dispersions within an aperture for the given stellar and halo profiles. For the Sérsic-Exp fits, I include a dependence on B/T ratio. At higher redshifts, uniformly selected observational samples are scarce, so I compute velocity dispersions assuming a variety of empirically-motivated effective radii and halo masses as discussed below. From the behaviour of velocity dispersion with stellar mass, time, aperture and halo mass, I will infer some key properties on the evolution of galaxies and their central supermassive black holes.

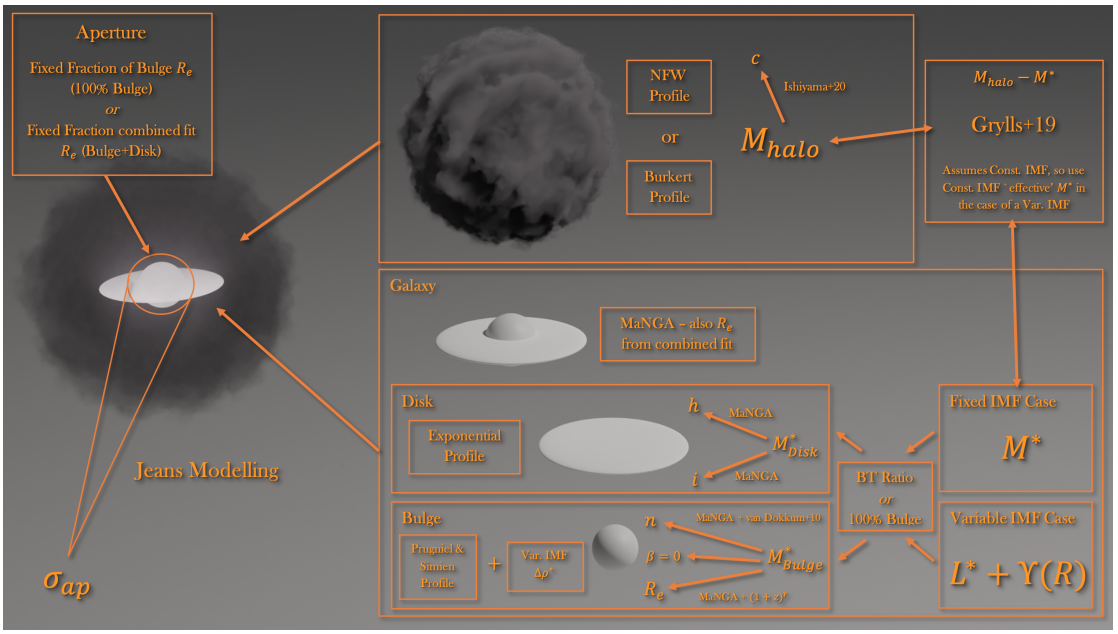

FIGURE 2.1: Cartoon image showing the contribution of the various elements of my model. Stellar masses are assigned to haloes (or vice-versa) using the relation from Grylls et al. (2019), refined by Zanisi et al. (2021), and associated disk and bulge properties are assigned using appropriate scaling relations (see text for details). The bulge, disk and dark matter components are brought together at fixed aperture size to simulate $\sigma_{ap}(R)$. This image was created using the Blender software, using assets from the Astera project (Marsden and Shankar, 2020).

2.1.1 Simulating Velocity Dispersion, σ.

I here detail my step-by-step methodology for computing the galaxy velocity dispersion $\sigma_{ap}(R)$ within a given aperture R. my method closely follows Desmond and Wechsler (2017) for models with a constant M^*/L, and Bernardi et al. (2018) for models with an IMF-driven scale-dependent M^*/L. For objects that are well described by a single-Sérsic light profile, I treat the stellar mass as a single dynamical component, whereas for two-component Sérsic+Exp models I explore what happens if I separately calculate the disk and bulge/spheroid velocity dispersion (within a given aperture) and then sum them in quadrature:

$$L_{ap,tot}\sigma^2_{ap,\,tot} = L_{ap,bulge}\sigma^2_{ap,\,bulge} + L_{ap,disk}\sigma^2_{ap,\,disk} \tag{2.1}$$

where $L_{ap} \equiv 2\pi \int_0^{R_{ap}} dR\, R\, I(R)$ and $L_{ap,tot} \equiv L_{ap,bulge} + L_{ap,disk}$. Since the bulge typically dominates on small scales, this smoothly interpolates between the bulge and disk values. I will show below that all my models, irrespective of the chosen light profile and/or M^*/L, predict a weak dependence on B/T, in excellent agreement with what is measured in the reference observational sample. In the following subsections I discuss how I model the contribution for both the bulge and the disk.

2.1.2 Spheroids/Bulges

2.1.2.1 Solving the Jeans Equations

I compute the velocity dispersion of a spheroid by solving the Jeans equation (e.g., Jeans, 1915; Binney and Tremaine, 2008) assuming spherical symmetry and no streaming motions:

$$\frac{d[\rho(r)\sigma_r^2]}{dr} + 2\frac{\beta(r)}{r}\rho(r)\sigma_r^2 = -\rho(r)\frac{GM(r)}{r^2}\,. \tag{2.2}$$

In Equation 2.2, r is the radial distance, $\rho(r)$ is the radial (mass) density of the galaxy, $M(r)$ is the total cumulative mass within r, σ_r is the radial component of the velocity dispersion, and $\beta(r)$ the radial velocity anisotropy:

$$\beta(r) = 1 - \frac{\sigma_t^2}{\sigma_r^2}\,, \tag{2.3}$$

with $\sigma_t = \sigma_\theta = \sigma_\phi$ the tangential component of σ. Assuming $\beta = 0$ corresponds to perfect isotropy, $\beta = 1$ to fully radial anisotropy and $\beta \to -\infty$ fully tangential anisotropy. Unless otherwise noted, I will assume $\beta = 0$ throughout this work, which is a good approximation to reproduce the MaNGA data at $z = 0$. I verified that none of my main results, especially the ones referring to the time evolution of velocity dispersion, change qualitatively when assuming, for example, a non-zero anisotropy $\beta \sim 0.3 - 0.4$ as often adopted in massive early-type galaxies (e.g., Mamon and Łokas, 2005; Chae et al., 2019). Note that if the two components in a SerExp fit are spheres with different dynamics (but the same β), then the result of writing equation (2.2) for each of the two components and summing the two expressions is again equation (2.2) with $\rho_{tot}\sigma^2_{r,tot} = \rho_{Ser}\sigma^2_{r,Ser} + \rho_{Exp}\sigma^2_{r,Exp}$. I discuss how I treat the possibility that the Exponential component is a rotationally supported disk shortly.

The general solution to Equation 2.2 can be written as

$$\rho(r)\sigma_r^2(r) = \frac{1}{f(r)}\int_r^\infty f(s)\rho(s)\frac{GM(s)}{s^2}ds, \tag{2.4}$$

where f is the solution to the differential equation (see, e.g., van der Marel et al., 1994)

$$\frac{d\ln f}{d\ln r} = 2\beta(r)\,. \tag{2.5}$$

Projecting the velocity ellipsoid along the line of sight, it can be shown (Binney and Mamon, 1982) that the line-of-sight velocity dispersion $\sigma_{los}(R)$ at projected radius R is

$$\frac{1}{2}I(R)\sigma^2_{los}(R) = \int_R^\infty \frac{\ell(r)\sigma_r^2 r dr}{\sqrt{r^2-R^2}} - R^2\int_R^\infty \frac{\beta\ell(r)\sigma_r^2 dr}{r\sqrt{r^2-R^2}}\,. \tag{2.6}$$

Inserting Equation 2.4 and Equation 2.5 into Equation 2.6, implies

$$\begin{aligned}\frac{I(R)\sigma_{los}^2(R)}{G} &= 2\int_R^\infty \frac{f\ell M}{s^2}ds \int_R^s \frac{1}{f}\frac{rdr}{\sqrt{r^2-R^2}} \\ &-R^2\int_R^\infty \frac{f\ell M}{s^2}ds \int_R^s \frac{df/dr}{f^2}\frac{dr}{\sqrt{r^2-R^2}}\,.\end{aligned} \tag{2.7}$$

On the assumption of constant anisotropy ($f(r) = r^{2\beta}$), it can be shown (e.g. Mamon and Łokas, 2005, Appendix A) that Equation 2.7 reduces to

$$\frac{I(R)\sigma_{los}^2(R)}{G} = 2\int_R^\infty K\left(\frac{r}{R}\right)\ell(r)M(r)\frac{dr}{r}\,, \tag{2.8}$$

where

$$\begin{aligned}K(u) \equiv \frac{1}{2}u^{2\beta-1}\Bigg[&\left(\frac{3}{2}-\beta\right)\sqrt{\pi}\frac{\Gamma(\beta-\frac{1}{2})}{\Gamma(\beta)} \\ &+\beta B\left(\frac{1}{u^2},\beta+\frac{1}{2},\frac{1}{2}\right)-B\left(\frac{1}{u^2},\beta-\frac{1}{2},\frac{1}{2}\right)\Bigg]\,.\end{aligned} \tag{2.9}$$

In Equation 2.9, B is the incomplete beta function in the format $B(z,a,b)$[1]. Various alternative expressions for $K(u)$ can be adopted, as summarised by Mamon and Łokas (2005). Finally, the aperture velocity dispersion is computed as (e.g., Mamon and Łokas, 2006; Cappellari et al., 2006; Chae et al., 2014)

$$\sigma_{ap} \equiv \sigma(R_{ap}) = \sqrt{\frac{\int_0^{R_{ap}} I(r)\sigma_{los}^2 rdr}{\int_0^{R_{ap}} I(r)rdr}}\,. \tag{2.10}$$

I adopt Equations 2.8 in the case of a constant IMF and mass-to-light ratio $\Upsilon = M^*/L$, which implies a linear and constant scaling between light and stellar mass and reduces computational cost as it does not require calculation of the radial velocity dispersion. In the case of a scale-dependent IMF and mass-to-light ratio $\Upsilon(R)$ instead (Section 2.1.3), I first numerically solve Equation 2.4 to derive $\sigma(r)$ and then "light-weight" it via Equation 2.6 to obtain the line-of-sight velocity dispersion $\sigma_{los}(R)$.

2.1.2.2 Spheroids: Mass and Stellar Profiles

Following the formalism presented in the previous Section, computing σ requires knowledge of the projected light density profile $I(R)$, of the total cumulative mass profile $M(r)$, the 3D light density profile $\ell(r)$, and the 3D stellar density profile $\rho(r)$ which, in the case of a constant M^*/L, is simply given by $\rho(r) = \Upsilon\ell(r)$. For a bulge or a spheroid, the projected light density profile $I(R)$ is well approximated by a Sérsic profile (Sérsic,

[1] In the third term of Equation 2.9, where necessary I recursively use the transformation $B(z,a,b)a = z^a(1-z)^b + (a+b)B(z,a+1,b)$.

1968)

$$I(R) = I_e \exp\left\{-b_n\left[\left(\frac{R}{R_e}\right)^{1/n} - 1\right]\right\}, \tag{2.11}$$

where n is the Sérsic index and b_n is chosen so that the luminosity within R_e is half the total luminosity. Ciotti and Bertin (1999) approximate b_n as

$$b_n \simeq 2n - \frac{1}{3} + \frac{0.09876}{n}. \tag{2.12}$$

The corresponding "deprojected" 3D light profile $\ell(r)$ is well approximated by a similar expression (Prugniel and Simien, 1997)

$$\ell(r) = \ell_0 \left(\frac{r}{R_e}\right)^{-p_n} \exp\left\{-b_n\left(\frac{r}{R_e}\right)^{1/n}\right\}, \tag{2.13}$$

where

$$\ell_0 = \frac{I_0 b_n^{n(1-p_n)}}{2\pi R_e^3} \frac{\Gamma(2n)}{\Gamma[n(3-p_n)]} \tag{2.14}$$

and

$$p_n = 1 - \frac{0.6097}{n} + \frac{0.00563}{n^2}. \tag{2.15}$$

When adopting a constant stellar mass-to-light ratio Y, both the projected and 3D stellar density profiles will be identical to the light profiles simply scaled by Y. The stellar cumulative profile $M^*(r)$ also has an analytic expression in this case which reads as

$$M^*(r) = M^* \frac{\gamma_l[n(3-p_n), b_n(r/R_e)^{1/n}]}{\Gamma[n(3-p_n)]}, \tag{2.16}$$

with γ_l the (lower) incomplete gamma function. In the case of an IMF-driven M^*/L gradient, I instead obtain $M^*(r)$ via direct integration of the 3D stellar mass density described in Section 2.1.3.

Finally, the total galaxy cumulative mass profile $M(r)$ is obtained by linear addition of the different components of stars, dark matter, gas and central black hole

$$M(r) = M^*(r) + M_{halo}(r) + M_{gas}(r) + M_{bh}. \tag{2.17}$$

In my reference model I will assume a single Sérsic light profile, and the corresponding $M^*(r)$ refers to the total stellar mass of the galaxy. In models in which I explicitly distinguish the bulge and disk components of the galaxy, I set instead $M^*(r) = M_{bulge}(r)$ in Equation 2.17. The latter approximation stems from the fact that in most cases the bulge is significantly more compact than the disk implying that the gravitational effect of the disk on the bulge is negligible at the scales of interest to this work. The dynamical effect of the disk is then added in quadrature via the circular velocity, as described in Section 2.1.4. I here adopt as a reference the Navarro, Frenk and White

(NFW) profile (Navarro et al., 1996) for the dark matter component $M_{halo}(r)$, with a concentration-halo mass relation from Ishiyama et al. (2020), although in some cases I will also show the impact of switching to a cored dark matter profile (Burkert, 1995). I assume throughout that $M_{gas}(r)$ and M_{bh} have a negligible contribution to the velocity dispersion within the central regions of the galaxy, and I checked that including them using common prescriptions as suggested in the relevant literature (e.g., Mamon and Łokas, 2005; Peeples and Shankar, 2011; Shankar et al., 2016) does not alter any of my main results to any significant degree. I further discuss the impact of black hole mass to the central velocity dispersion and of gas mass on the evolution of $\sigma_{ap}[M^*, z]$ in Section 3.2.

2.1.3 Stellar Mass-to-light ratios

The transition from stellar light to stellar mass depends on the chosen mass-to-light ratios $\Upsilon = M^*/L$ which is tightly linked to the chosen IMF. To specifically explore the impact of a scale-dependent IMF on my predicted velocity dispersions and their evolution with redshift, I follow Bernardi et al. (2018) and define a scale-dependent mass-to-light ratio $\Upsilon(R)$ of the type

$$\Upsilon(R) = \begin{cases} \Upsilon_{outer}\left(1 + \phi - \xi\frac{R}{R_e}\right) & R < R_e \\ \Upsilon_{outer} & R \geq R_e \end{cases} \tag{2.18}$$

where, for simplicity, I set $\xi = \phi$, thus ϕ becomes the only parameter controlling the gradient of the profile. Equation 2.18 states that when $R \geq R_e$, the projected stellar mass-to-light ratio reduces to a constant stellar mass-to-light ratio Υ_{outer}, whereas at $R < Re$ the stellar mass-to-light ratio increases linearly until it reaches a maximum $\Upsilon_{inner} = \Upsilon_0(1+\phi)$ at $R = 0$. In Appendix 3, I include a Table containing values for Υ_{outer} and Υ_{inner} as a function of the measured galaxy velocity dispersion and r-band absolute magnitude, as calibrated by Bernardi et al. (2019) and Domínguez Sánchez et al. (2019), which I use to calculate stellar masses in the MaNGA sample when adopting a scale-dependent M^*/L.

I can now directly multiply Equation 2.18 by the projected brightness profile (Equation 2.11) to obtain the new projected stellar mass density profile

$$J(R) \equiv I(R)\Upsilon(R)\,. \tag{2.19}$$

The corresponding deprojected stellar mass density profile can then be retrieved from the integral (Binney and Mamon, 1982)

$$\rho^*(r) = -\frac{1}{\pi}\int_r^\infty dR \frac{dJ/dR}{\sqrt{R^2 - r^2}}\,. \tag{2.20}$$

The 3D stellar mass density in Equation 2.20 can be written as a sum of two terms

$$\rho^*(r) = \rho^*_{Ser}(r) + \Delta\rho^*(r)\,, \tag{2.21}$$

where the first term represents the standard deprojected stellar density profile assuming a constant mass-to-light ratio, $\rho^*_{Ser}(r) = \Upsilon_{outer}\,\ell(r)$, and the second term represents the "extra" contribution to the stellar mass density profile. The latter can be computed as follows. The gradient in Equation 2.18 effectively adds, at each radius $R < R_e$, a projected stellar mass $\Delta\Upsilon(R) = \Upsilon_{outer}\left(\phi - \phi\frac{R}{R_e}\right)$, which can be deprojected via Equation 2.20 to yield, when adopting a Sérsic light profile as in Equation 2.11, the extra stellar mass density

$$\Delta\rho^*(r) = \frac{I_e\Upsilon_{outer}}{\pi R_e n}\int_y^1 \frac{dY}{Y\sqrt{Y^2-y^2}}\exp\left(-b_n\left[Y^{1/n}-1\right]\right)\left[n\phi Y + b_n(\phi-\phi Y)Y^{1/n}\right] \tag{2.22}$$

where $Y = R/R_e$ and $y = r/R_e$. Once the deprojected stellar mass density $\rho^*(r)$ is acquired, the cumulative stellar mass M^* can be obtained from a simple spherical integral.

I conclude this Section pointing out that so far, when computing the effect of a scale-dependent M^*/L on velocity dispersion, I have strictly followed the formulation put forward by Bernardi et al. (2018), Bernardi et al. (2019) and Domínguez Sánchez et al. (2019), i.e., I neglected any possible segregation in the phase-space distribution function of low- and high-mass stars (e.g., Caravita et al., 2021). Nevertheless, as further detailed in Appendix 4, accounting for such a segregation in the Jeans Equation leads to relatively small differences in the shape and amplitude of $\sigma_{los}(R)$ at $R < Re$. The main point is that, irrespective of the exact dynamical modelling applied via the Jeans Equation, whenever a realistic IMF-driven gradient is included in the M^*/L, the resulting velocity dispersion profile in the inner regions is rather different from the one obtained with a constant M^*/L, as emphasized by Bernardi et al. (2018).

2.1.4 The contribution from the disk component

In the models in which I adopt a Sérsic+Exponential stellar light profile, the contribution from the galaxy disk to the aperture velocity dispersion σ_{ap} is constructed as follows:

$$\sigma^2_{ap,\,disk} \equiv \sigma_{disk}(R_{ap})^2 = \frac{1}{M_{disk}(R_{ap})}\int_0^{R_{ap}} 2\pi R\,\Sigma_{disk}(R)v^2_{rot}(R)sin^2i\,dR \tag{2.23}$$

Here $M_{disk} = \Upsilon_0 L_{disk}$ is the stellar mass of the disk always computed assuming a constant mass-to-light ratio. R_{ap} is the aperture radius, $\Sigma(R)$ is the projected disk stellar mass density, $v_{rot}(R)$ the disk circular velocity, and i is the disk inclination. I assume

exponential disks of the form

$$\Sigma_{disk}(R) = \frac{M_{disk}}{2\pi h^2} \exp\left(-R/h\right) \tag{2.24}$$

where h is the disk scale length. The disk circular velocity is parameterised as follows (see e.g. Freeman 1970; Tonini et al. 2006)

$$v_{rot}(r)^2 = \frac{GM_{disk}}{2h} q^2 B\left(\frac{q}{2}\right) + v_{DM}^2 + \frac{GM_{bulge}(<r)}{r} \tag{2.25}$$

where $q = r/h$, and $B(x) = I_0K_0 - I_1K_1$, a combination of modified Bessel Functions that account for the disk asphericity. The second term is the circular velocity of the dark matter halo, and the final term represents the gravitational contribution of the bulge on the disk.

2.1.5 Effective radii and Sérsic indices

Important features to properly describe the structural properties of bulges and spheroids are effective radii and Sérsic indices. All my models start at $z = 0$ from MaNGA galaxies with already measured structural (from light profile) parameters for both the bulge and disk components. To provide a complete prediction of velocity dispersion evolution along cosmic time, I would need reliable structural parameters even at higher redshifts. However, this information becomes gradually less clear or less accessible at earlier times on a galaxy-by-galaxy basis as in the MaNGA sample, but it can be retrieved when averaged in stellar/luminosity bins (e.g., Dimauro et al., 2019). For this reason, I rely on empirically motivated analytic fits to the mean redshift evolution in effective radius R_e and Sérsic index n as a function of stellar mass as derived from a compilation of different data sets by Ricarte and Natarajan (2018, see also, e.g., Huertas-Company et al. 2013). In the Equations that follow below, stellar mass is strictly defined via a constant mass-to-light ratio, i.e. $M^* = \Upsilon_0 L$ with L the total galaxy luminosity.

Following Ricarte and Natarajan (2018), I assume a stellar mass-dependent size evolution of the type

$$R_e(M^*, z) = R_e(M^*, 0) f(M^*, z)\,. \tag{2.26}$$

The $R_e(M^*, 0)$ are the effective radii as measured in the MaNGA sample, while the evolutionary factor $f(M^*, z)$ is expressed as

$$f(M^*, z) = (1+z)^{-\gamma(M^*)}\,. \tag{2.27}$$

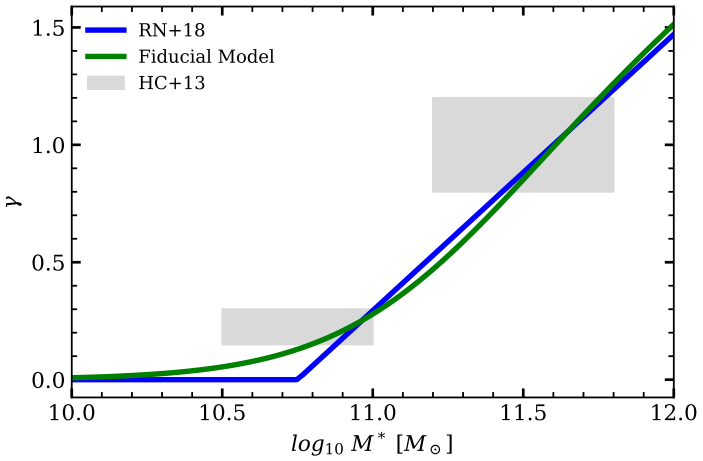

FIGURE 2.2: The effective radius evolution parameter γ versus stellar mass. The shaded regions mark the regions of observationally calibrated γ by Huertas-Company et al. (2013) in some bins of stellar mass between $0 < z < 1$. The blue line shows the prescription used by Ricarte and Natarajan (2018). The green line shows the double power law fit utilized in this thesis.

Ricarte and Natarajan (2018) assume γ to be dependent on the galaxy stellar mass at $z = 0$, but introduce a redshift dependence as

$$\gamma(M^*) = \max\left[0, \frac{1}{0.85}\left(log_{10}\, M^* - 10.75\right)\right]. \tag{2.28}$$

Equation 2.28 presents a discontinuity, which would propagate creating a visible break in velocity dispersion histories. I thus adopt a smoother dependence for γ on redshift

$$\gamma(M^*) = A \log_{10}\, M^* \left[\left(B \log_{10}\, M^*\right)^p + \left(C \log_{10}\, M^*\right)^s\right]^{-1}, \tag{2.29}$$

where $A = 3.05 \times 10^{-3}$, $B = 9.67 \times 10^{-2}$, $C = 0.204$, $p = -39.0$ and $s = -4.30$. Figure 2.2 shows that my prescription is very similar to the one adopted by Ricarte and Natarajan (2018), but allowing for a smooth variation in γ and retaining consistency with some of the available observations (Huertas-Company et al., 2013).

In a similar fashion to effective radii, Sérsic indices are assigned at any given epoch using a redshift evolution of the type

$$n(M^*, z) = n(M^*, 0)(1+z)^{-1}, \tag{2.30}$$

as suggested by van Dokkum et al. (2010, see also Shankar et al. 2017b). The local $n(M^*, 0)$ are the Sérsic indices as measured in the MaNGA sample. Both $R_e(M^*, 0)$ and $n(M^*, 0)$ from MaNGA and their associated fits are shown in Figure 2.3.

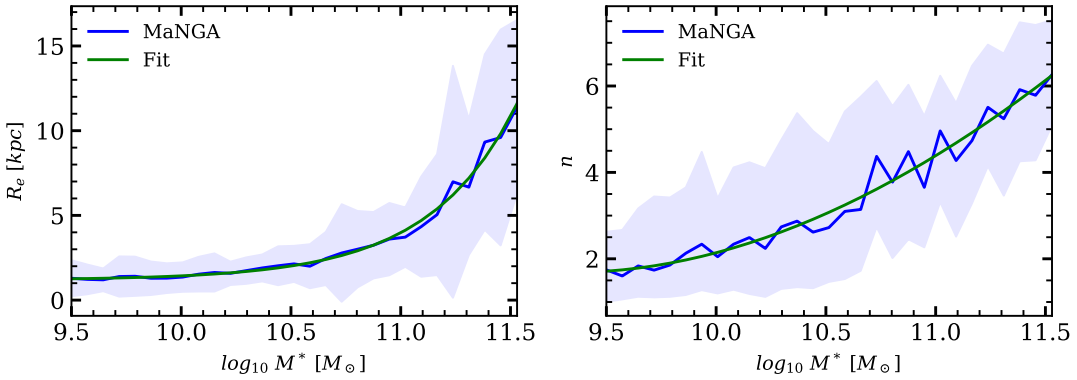

FIGURE 2.3: $R_e(M^*, 0)$ (left) and $n(M^*, 0)$ (right) for MaNGA (blue line), with shaded region representing 1σ uncertainty. Also shown are the fitting functions (green lines).

2.1.6 Implementation

The contributions from the bulge and disk (where present) are combined using Equation 2.1. The list of the parameters required by my model are shown in Table 2.1. To maintain excellent performance, I implemented my code in the C and C++ programming languages with Adaptive Richardson Extrapolation (Richardson, 1911) for fast and accurate integration, and paralleled using OpenMP. My code is available at `github.com/ChrisMarsden833/VelocityDispersion`. I also provide in Appendix A.1 a useful analytic formula to compute from my fiducial model with constant mass-to-light ratio the virial coefficient $\mathcal{F} = GM_{tot}(< R_e)/R_e\sigma^2_{ap}$, which in turn can be used to retrieve the dynamical mass, at any redshift $z \lesssim 3$, any aperture $R \lesssim R_e$, and effective radius and Sérsic index within the ranges probed in this work.

2.2 DREAM

As anticipated above, I require a fiducial model that can predict the merger rates of galaxies in a cosmological context, which I will then use to infer the expected velocity dispersion evolution under solely (gas-poor) mergers, which I will then compare with my Jeans models described in the previous Section. To reliably estimate galaxy merger rates, I adopt the semi-empirical model DREAM. In this Section, a concise summary of the methodology behind DREAM is outlined, whilst a more comprehensive overview will be published in Fu et al (in prep).

In brief, my starting point is to start from bins of dark matter halo mass at $z = 0$. To each 'typical' host halo I assign an average growth history as derived from N-body numerical simulations and analytic models (van den Bosch et al., 2005). Dark matter subhaloes infalling onto the progenitor halo are at each time step assigned via the subhalo mass function (SHMF). The latter has been recently recalibrated by Jiang and

TABLE 2.1: List of variables used in my model.

Component	Variable	Description
	R_{ap}	Aperture
Bulge, Const. M^*/L	M_{bulge}	Bulge Stellar Mass ($\Upsilon_0 L_{bulge}$)
	R_e	Half Mass Radius of the Bulge
	β	Bulge Anisotropy Parameter
	n	Sérsic Index
Bulge, Var. M^*/L	L_{bulge}	Bulge Luminosity
	R_e	Half Mass Radius of the Bulge
	β	Bulge Anisotropy Parameter
	n	Sérsic Index
	Υ_0	Mass-to-light ratio at R_e
	ϕ	Mass-to-light ratio gradient
Disk	M_{disk}	Disk Stellar Mass ($\Upsilon_0 L_{disk}$)
	i	inclination
	h	Disk Scale length
Halo	M_{halo}	Halo Mass
	c	Halo Concentration
Black Hole	M_{BH}	Black Hole Mass

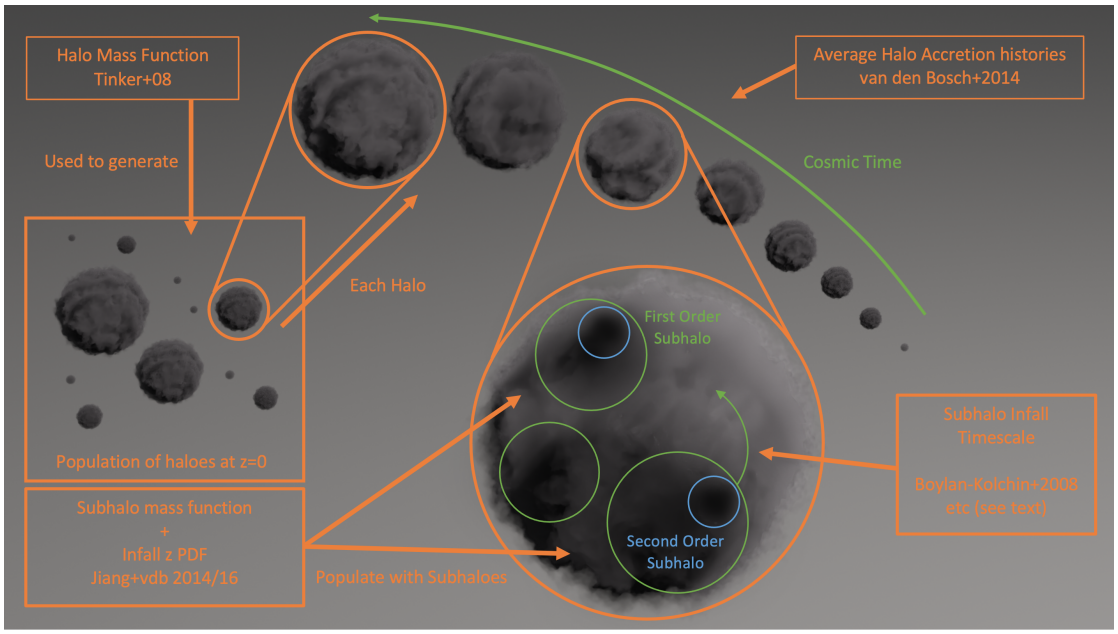

FIGURE 2.4: Cartoon depiction of DREAM. The halo mass function is used to generate a catalogue of central haloes (left). A mean accretion history is assigned to each. I compute the SHMF for all subhaloes as well as for each order, and use it as probability density distribution for generating the subhaloes population. Finally, the redshift of infall is assigned to subhaloes via fitted analytical equations, depending on their order and mass.

van den Bosch (2014, 2016) who found a universal fit for the distribution of subhalo (unstripped or "unevolved") mass independent of host halo mass and redshift. The unevolved subhalo mass function is distinguished by 'order' of accretion in the merger tree, with first order subhaloes being the ones falling directly onto the main branch, and second order subhaloes the ones already satellites in first-order subhaloes at the time of accretion onto the main branch (see centre right of Figure 2.4). I neglect any higher order of accretion as their contribution to galaxy growth is minimal. Once a subhalo first falls into its host halo, it is affected by tidal stripping and dynamical friction. The typical timescale that a subhalo needs in order to fully merge with its progenitor from the time they first accreted is well described by the merging timescale formula given by Equation (5) of Boylan-Kolchin et al. (2008):

$$\tau_{\rm merge} = \tau_{\rm dyn} A \frac{(M_{\rm h,host}/M_{\rm h,sub})^b}{\ln(1+M_{\rm h,host}/M_{\rm h,sub})} \exp\left[c\frac{J}{J_c(E)}\right]\left[\frac{r_c(E)}{R_{\rm vir}}\right]^d \tag{2.31}$$

where $J/J_c(E)$ the orbital energy and (A, b, c, d) are parameters taken from McCavana et al. (2012) that govern the dependence of the merging timescale on the mass ratio. For further details, I direct the reader to Grylls et al. (2019) and Fu et al. (in prep). Galaxies are assigned to central and infalling satellite haloes via abundance matching techniques. I note that, although DREAM can also work on object-specific assembly histories, in this thesis I only consider in the average evolution of stellar mass (and velocity dispersion) and thus I only follow in time average quantities in terms of halo mass, central galaxy mass, and subhalo masses. The key advantage of DREAM over conventional N-body derived merger trees to calculate average galaxy assembly histories, is that the poor statistics that arise from mass resolution and/or volume limitations within N-body simulations is entirely avoided, allowing the average properties of even the largest mass haloes to be explored without limitation. My methodology is also much faster, more flexible, and it naturally incorporates all subhaloes down to the chosen resolution limit, as detailed below. DREAM is consistent with the halo accretion histories as extracted from the Millennium simulation, as well as with the satellite richness and mean star formation rates from the latest observations (see details in Grylls et al. (2019, 2020a,b), Fu et al. in prep.).

2.3 Abundance Matching

An underpinning technique used throughout this work is that of abundance matching, so I will briefly discuss it here. Abundance matching is explained by Figure 2.5, where the relative abundances of haloes (parameterized by the halo mass function, top panel) are compared to the relative abundance of galaxies of a particular stellar mass (right

TABLE 2.2: Parameters for equation 2.32.

	M_n	N	β	λ	σ
Central, $z = 0.1$	11.95	0.032	1.61	0.54	0.11
Total, $z = 0.1$	11.89	0.031	1.77	0.52	0.10
Evolution, $z > 0.1$	0.4	-0.02	-0.6	-0.1	N/A

panel). The corresponding number densities define which haloes host galaxies, defining the halo mass - stellar mass relationship. This must be done at multiple redshifts. I use the results from Grylls et al. (2019), who use a multi-epoch approach without satellite evolution to fit the evolution parameters, before adding a satellite SMF and comparing to the total SMF from the data minimizing the sum of the root mean squares error over eight redshift steps.

I here briefly recall the parameterization of this halo mass - stellar mass relation, including the correction from Zanisi et al. (2021), which I use as a reference throughout the work. The analytic formula is

$$\begin{aligned} M^*(M_{halo}, z) &= 2\frac{M_{halo}N(z)}{10^{0.1}}\left[\left(\frac{M_{halo}}{M_n(z)}\right)^{-\beta(z)} + \left(\frac{M_{halo}}{M_n(z)}\right)^{\gamma(z)}\right]^{-1} \\ N(z) &= N_{0.1} + N_z\left(\tfrac{z-0.1}{z+1}\right) \\ M_n(z) &= M_{n,0.1} + M_{n,z}\left(\tfrac{z-0.1}{z+1}\right) \\ \beta(z) &= \beta_{0.1} + \beta_z\left(\tfrac{z-0.1}{z+1}\right) \\ \gamma(z) &= \gamma_{0.1} + \gamma_z\left(\tfrac{z-0.1}{z+1}\right) . \end{aligned} \tag{2.32}$$

Here M^* represents the stellar mass of the galaxy and M_{halo} represents the host halo mass. The values of the parameters N, M_n, β and γ are given in Table 2.2 (the subscript 0.1 refers to the value of the parameters at $z = 0.1$). The Grylls et al. (2019) relation is mostly valid in the redshift range $0.1 < z < 4$. For an overview of how this relation is derived, and more information on abundance matching in general, see Grylls et al. (2019).

2.4 Observational and numerical comparison data

Here I briefly discuss the datasets that I use to compare to my modelling. In what follows, I will compare my numerical models for galaxy velocity dispersions with both *simulated* and *observed* samples. The former comes from the TNG50 hydrodynamical simulation (Pillepich et al., 2019; Nelson et al., 2019a,b) developed in a 50 Mpc box, resolved down to a baryonic mass of $8 \times 10^4\, M_\odot$. As detailed below, from TNG50 I select a variety of central galaxies of different stellar masses at $z = 0$, follow their evolution along their main progenitor branches, and at each timestep compute their

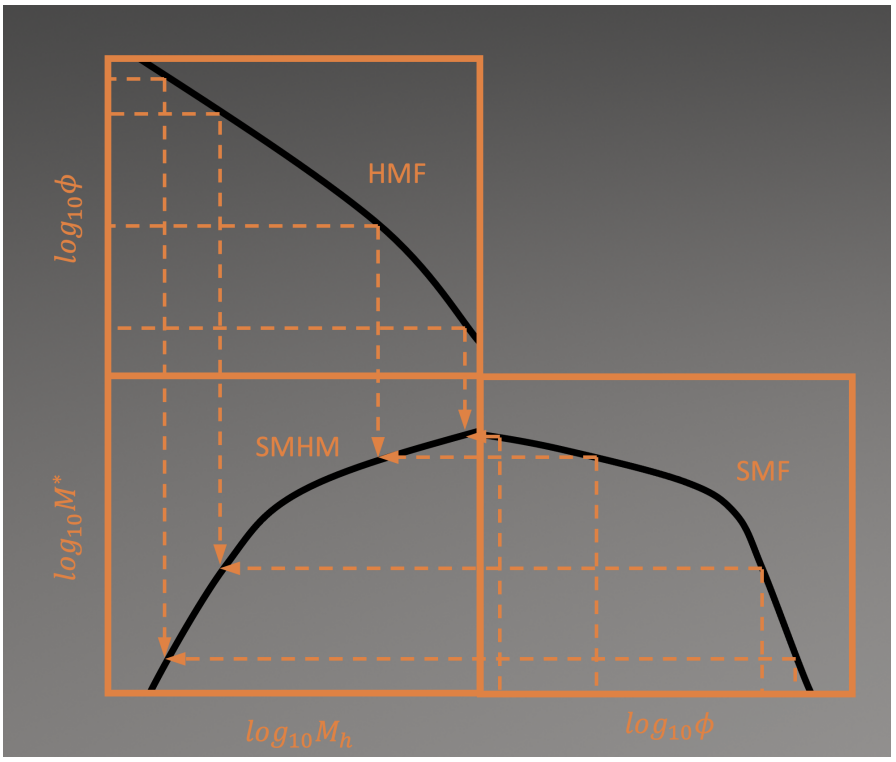

FIGURE 2.5: Cartoon image showing the principles behind abundance matching. The HMF (top left panel) and SMF (right lower panel) are matched by abundance. The combined mapping allows halo mass and stellar mass to be connected, the SMHM relation (left lower panel).

(stellar) velocity dispersions (within the specified aperture) directly from the available stellar particle data, as described below.

The latter consists of a large sample of galaxies published by Fischer et al. (2019) which was part of an early release (SDSS-DR15, Aguado et al. 2019) of the MaNGA (Mapping Nearby Galaxies at Apache Point Observatory; Bundy et al. 2015) Survey. MaNGA provides integral field unit spectroscopy and accurate kinematic maps (stellar rotation velocity and velocity dispersion) for each galaxy. The photometric parameters and bulge-to-total (B/T) decompositions are from Fischer et al. (2019) based on single component Sérsic (e.g., Sérsic, 1968) or two-component Sérsic+Exponential light profiles, with additional morphological properties derived from supervised Deep Learning algorithms based on Convolutional Neural Networks (Domínguez Sánchez et al., 2018a). I restrict the observational sample to only those galaxies with a reliable fit to a single Sérsic profile (*flag_fit=1*, 1402 galaxies) or to a Sérsic+Exponential profile (*flag_fit=0 or 2*, 1516 galaxies) . I will sometimes refer to the two components as the bulge and disk components, even if there is no hint of a disk in the imaging. For each object, I consider two definitions of stellar masses: one is based on the total stellar mass-to-light ratio from Mendel et al. (2014), which assumes a Chabrier (Chabrier, 2003) stellar initial mass function (IMF) for all galaxies; the other allows for a gradient in M^*/L which is driven by an IMF gradient in each object, as described in Section 2.1.3.

2.4.1 Determination of Stellar Velocity Dispersion from TNG

Here I briefly describe the process of extracting velocity dispersions from the TNG galaxies, as projected velocity dispersions within an aperture are not available in the provided datasets (or even just *stellar* velocity dispersions, as the current catalogs seem to focus on the velocity dispersion of all member particles, including dark matter, gas etc). Firstly I select the main progenitor history of all galaxies within an appropriate mass bin, and at each snapshot calculate σ as follows. I first project the stellar particles belonging to the galaxy (determined using a FOF method, see the TNG documentation for more details) along an arbitrary direction. Next, to obtain realistic values for R_e (and also n, although I do not utilize this in this thesis), I fit a Sérsic profile to the projected density of these particles. Next, I eliminate all particles that are not within my projected aperture size. I then calculate the velocity dispersion of the remaining stellar particles in the projected dimension, weighted by their masses

$$\sigma_x = \sqrt{\frac{N}{N-1}} \sqrt{\frac{\sum m_i (v_{i,x} - \bar{v}_x)^2}{m_i}}, \tag{2.33}$$

where (given N particles) for particle i, x is the projected direction (hence $v_{i,x}$ is the component of the velocity in direction x). $\bar{v}_x$ is the average (component of) velocity of all the particles, again weighed by the mass[2]. Discounting the projection and aperture, this process is identical to how the velocity dispersion of all particles identified as members of the halo, not just stellar particles are calculated in the TNG Group Catalogues (variable 'SubhaloVelDisp'). I compute the projected velocity dispersion for each galaxy three times, projecting in the directions x, y and z (in the simulation coordinate system), and take the mean of these values to minimize any bias due to the projection axis.

[2]Additional corrections must naturally be applied for the periodicity of the box, cosmology etc, as described in the TNG documentation.

Chapter 3

Results: Velocity Dispersion

In this Chapter I present the main outputs of my modelling of velocity dispersion detailed in Chapter 2. I will first show in Section 3.1 that my models provide a good match to the data from MaNGA in the local Universe. Anchoring my model at $z = 0$ allows us to make predictions at higher redshifts, which I present in Section 3.2, based on empirically informed recipes for the evolution of the stellar mass and structural parameters of galaxies with redshift. For each of my most relevant steps, I will present results adopting both a constant and radially varying mass-to-light ratio. I will also include an extended discussion Section at the end of this Chapter.

3.1 The Low Redshift Universe

Before providing a detailed comparison of my models with the low redshift data, it is informative to first describe the overall behaviour of my Jeans modelling against all the main input parameters (Figure 3.1). Here I simply show the case with a constant M^*/L, as labelled, though the trends are similar for a radially-dependent mass-to-light ratio. The upper left panel of Figure 3.1 shows the velocity dispersion $\sigma_{ap}(R)$ as a function of aperture[1] normalised to the effective radius R_e, whilst the other panels show the dependence of $\sigma_{ap}(R)$, calculated within an aperture of $R = R_e/8$, on several different quantities, from left to right and from bottom to top, the effective radius, the Sérsic index n, the orbital anisotropy parameter β, the host halo mass M_h, the host halo scale radius R_s, the host halo concentration c, the central black hole mass M_{bh}. The different coloured lines are for different galaxy stellar masses, as labelled in the top, left panel. The solid circles in different panels mark the mean velocity dispersion in MaNGA that corresponds to that stellar mass. The most striking feature apparent from

[1]The profile for $\sigma_{ap}(R)$ as a function of aperture is consistent with the usual formula (e.g., Equation A2 in Shankar et al. 2019b) for transforming $\sigma_{ap}(R)$ between different aperture sizes.

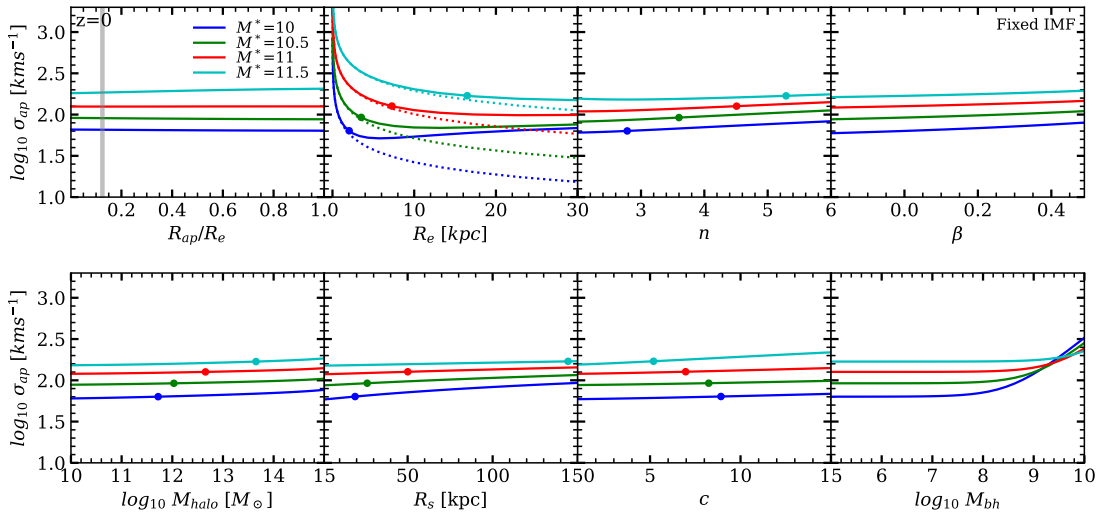

FIGURE 3.1: Dependence of (single-Sérsic profile) velocity dispersion σ_{ap} on all main input parameters. Each coloured line represents a galaxy of fixed stellar mass at $z = 0$, with all non-varying parameters in each panel assigned following the fiducial model ($ap = R_e/8$, except in panel 1). Solid circles show the typical values of some galaxy parameters for the chosen stellar mass bins. Dotted lines show the calculated velocity dispersion when the dark matter component is neglected; except for the largest masses, the dark matter contribution within R_e is negligible

.

all panels is that my models predict velocity dispersions with extremely weak dependence on almost all input parameters, with only two possible exceptions, very small effective radii (upper middle left panel) and/or very large black hole masses (bottom right panel). The flatness of these curves strongly suggests that varying, e.g., the mapping between stellar mass and halo mass, and/or details on the structure of the stellar or the dark matter component would not significantly alter the velocity dispersion at fixed stellar mass (at least in the local Universe, I will show in the next Section that this is not strictly true at higher redshifts). This weak dependence on the input parameters could in turn explain the tight correlation of velocity dispersion as a function of stellar mass, as anticipated by, e.g., Bernardi et al. (2010), and further discussed below.

Equipped with a clearer understanding of the dependencies of velocity dispersion on input parameters, I can now move to a close comparison to the observational data sets, most notably MaNGA (Section 2.4). To this purpose, to each MaNGA galaxy with a measured velocity dispersion and luminosity profile, I assign a halo mass via abundance matching techniques. More specifically, I make use of the *inverse* of the stellar mass-halo mass relation (SMHM hereafter)[2], and then apply the formalism discussed above to predict its velocity dispersion within a given aperture $\sigma_{ap}(R)$ which I then

[2]The latter is computed by first generating a large catalogue of host halo masses from the Tinker et al. (2010) halo mass function, assigning stellar masses via the (direct) stellar mass-halo mass relation, inclusive of normal scatter in stellar mass at fixed halo mass, then binning in stellar mass and finally computing the mean halo mass and scatter around the mean.

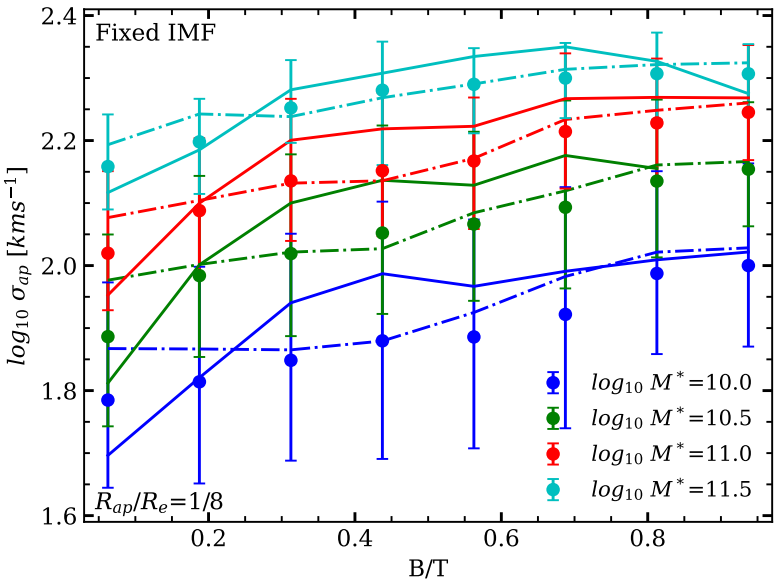

FIGURE 3.2: Coloured circles with error bars show the mean (with 1σ spread) σ_{ap} versus B/T for MANGa galaxies of different stellar mass of width 0.5 dex, as labelled. The solid and dot-dashed lines show the predictions of models with single-Sérsic and Sérsic+Exponential light profiles when I ignore M^*/L gradients.

compare with the measured one. Here stellar mass is again intended to be the one computed at fixed mass-to-light ratio, $M^* = \Upsilon_0 L$. When adopting a gradient in the M^*/L, I still assign halo masses to galaxies of a given luminosity L using the Grylls et al. (2019) relation based on stellar masses derived from a constant $\Upsilon_0 = M^*/L$. In other words, a SMHM relation derived with constant $M^*/L = \Upsilon_0$ can actually be considered, on average, a mapping between galaxy *luminosity* and host halos mass, though the relation between stellar mass and halo mass when adopting a gradient will be different, in fact steeper, than the case with constant M^*/L (see, e.g., Shankar et al., 2017b).

Figure 3.2 shows velocity dispersion computed within an aperture of $R_{ap} = R_e/8$ as a function of bulge-to-total (B/T) ratio as measured in the MaNGA sample (filled circles) for different stellar bins, as labelled, and assuming a constant M^*/L. It is clear from the data that, for all stellar mass bins, velocity dispersion decreases as B/T decreases, but it flattens out at $B/T \gtrsim 0.25$. This remains true for larger apertures $R_{ap} \lesssim R_e$ and when I consider models with scale-dependent M^*/L. I compare the MaNGA data with my predicted velocity dispersions – computed following the methodology outlined previously, using both the full bulge-to-disk decomposition (solid lines) and the single Sérsic profile with zero anisotropy (dotted lines), assuming a constant M^*/L. The two component SerExp-based model predicts an initial increase of $\sigma_{ap}(R)$ with B/T and then a flattening above $B/T \gtrsim 0.3$, while the single-Sérsic model is overall flatter, especially at low B/T, but still very much consistent with the data, implying that modelling velocity dispersion adopting spherical symmetry is still a good approximation for a wide range

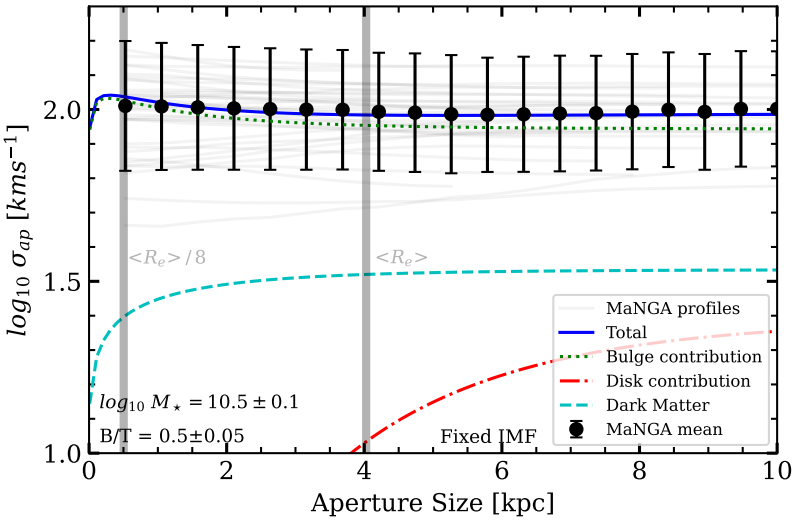

FIGURE 3.3: σ_{ap} as a function of aperture size for a subset of galaxies within the MaNGA sample (faint grey lines, solid markers with error bars show the mean and 1σ spread), compared to the theoretical prediction (blue line) of my model for a galaxy with properties equal to the average properties of the galaxies from the selected MaNGA sample. Also shown are the corresponding bulge, disk and dark matter contributions to the total $\sigma_{ap}(R)$.

of galaxy morphologies, as long as appropriate galaxy luminosity-dependent effective radii and Sérsic indices are included in the model. In my models, the weak dependence of velocity dispersion on B/T is just a reflection of the virial theorem – velocity dispersion depends more on the total mass within an aperture and less on how this mass is distributed in it. This may partly explain the similarity in the scaling relations of early and late-type galaxies (e.g., Bernardi et al., 2011a; Ferrero et al., 2021), as well as the universality of the $M_{bh} - \sigma$ relation (e.g., Ferrarese and Merritt, 2000; Shankar et al., 2016).

The main reason behind the weak dependence of velocity dispersion on B/T in Figure 3.2 can be ascribed to the dominance of the bulge component to the dynamics in the inner regions. I would expect a progressively larger contribution of the disk when considering larger apertures. Figure 3.3 compares the (mean) predicted velocity dispersion $\sigma_{ap}(R)$ as a function of aperture size for galaxies with $B/T = 0.50 \pm 0.05$, and $\log_{10} M^*/M_\odot = 10.5 \pm 0.1$ dex (solid blue line), with the mean velocity dispersion profile (solid circles) extracted from 25 galaxies (light gray lines) in the MaNGA sample in the same range of stellar and bulge masses (constant M^*/L). The model very well aligns with the data (solid blue line), and it shows that the total velocity dispersion is vastly dominated by the bulge (dotted green line). The relative dynamical contributions of the disk itself on the rotational velocity and thus on the velocity dispersion (dot-dashed red line) is relatively minor even up to the effective radius ($\lesssim 40\%$ at $R = R_e$). Similarly, even the contribution of the dark matter component (dashed cyan

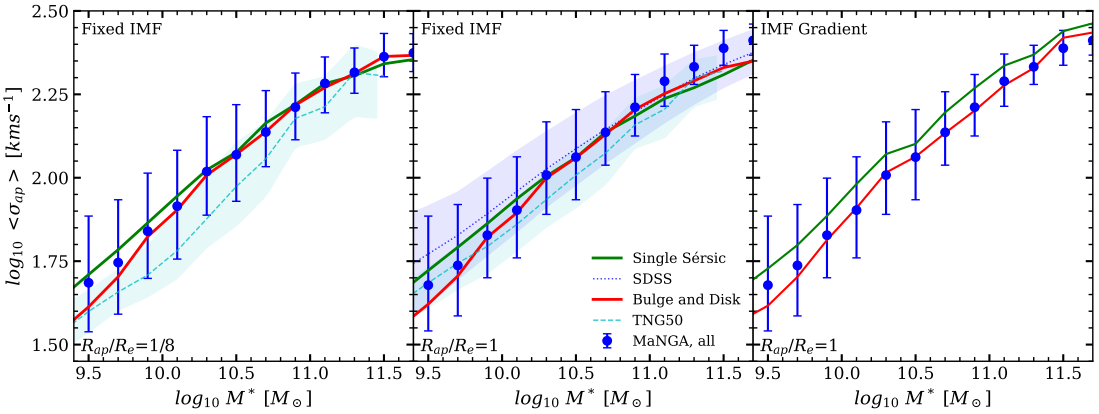

FIGURE 3.4: Predicted Faber-Jackson relation, σ_{ap} versus stellar mass, for a single-Sérsic and two-component Sérsic+Exponential light profiles (green and red solid lines) with constant (left and middle panels) and scale-dependent (right panel) M^*/L. Blue filled circles show the mean FJ relation measured in MaNGA (in all three panels, the x-axis uses the Mendel et al. (2014) stellar masses), blue dotted line shows that in the SDSS and cyan dashed lines show the relation in the TNG50 simulation.

line) is contained in the inner regions, reaching $\sim 30\%$ at $R_e \sim 8$ kpc, though I will see dark matter fractions are relevant in shaping the evolution of velocity dispersion with cosmic time. Once again, both data and models in Figure 3.3 highlight an extremely flat velocity dispersion as a function of aperture size.

To further validate my modelling, in Figure 3.4 I compare my predicted mean velocity dispersion-stellar mass relation, also known as the Faber-Jackson (FJ) relation (Faber and Jackson, 1976), with the one measured in MaNGA (filled blue circles). The left panel shows that my predicted σ_{ap} calculated at an aperture of $R = R_e/8$ for both models with a single-Sérsic and Sérsic+Exponential light profiles (solid green and red lines, respectively) and constant M^*/L are very similar to each other and to the MaNGA data. This very good match with the data extends up to the effective radius, as shown in the middle panel of Figure 3.4, in which I also include the FJ from the SDSS data[3] as calibrated by Shankar et al. (2019b, dotted blue line and purple region). Both data sets are in very good agreement with each other despite the significant differences in galaxy selections and velocity dispersion measurements.

The right panel of Figure 3.4 shows the FJ relation at an aperture of $R = R_e$ with the same MaNGA data as before, only now the model curves result from including the IMF-driven M^*/L gradient as described in Section 2.1.3.

It is interesting to compare the curves in this panel with those in the middle one (the symbols are the same but the stellar masses somewhat different due to the inclusion of the IMF-driven M^*/L gradient). I have already made the point that the two-component

[3]I apply a constant horizontal shift of -0.05 dex to the $\sigma_{ap} - M^*$ SDSS relation by Shankar et al. (2019b) who increased all their stellar masses by an average 0.05 dex to account for the relatively small difference between the Mendel et al. (2014) and Bell et al. (2003) mass-to-light ratios following Bernardi et al. (2017).

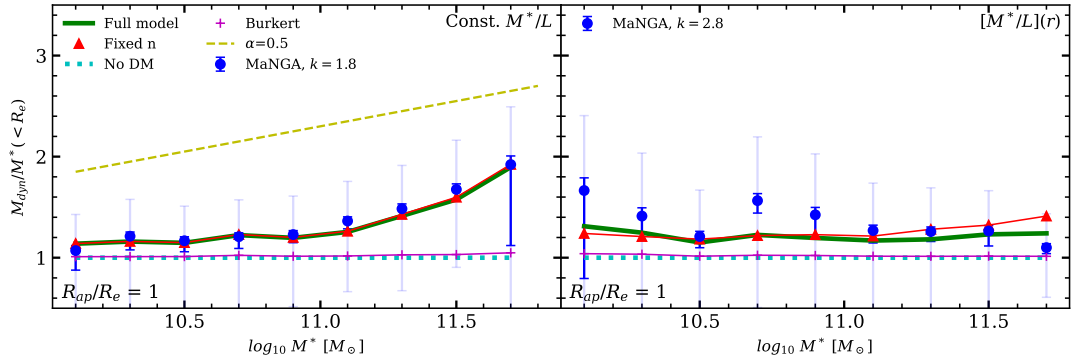

FIGURE 3.5: Dynamical-to-stellar mass ratio as a function of stellar mass for a model with constant (left) and scale-dependent (right) M^*/L. Blue points represent mean values derived from the velocity dispersion from the MaNGA sample, with faint error bars showing the associated 1σ uncertainty, and solid bars showing the error on the mean. The green line, red triangles, cyan dotted line and purple crosses represent the predicted values from my fiducial model, my fiducial model at fixed Sérsic index, no dark matter and with a Burkert DM profile respectively. Accounting for an IMF-driven M^*/L gradient makes $M_{dyn} \propto M^*$ within the effective radius. The dashed yellow line in the left panel indicated a slope of $\alpha = 0.5$ to guide the eye.

Sérsic+Exponential models (red) are more accurate. In the middle panel, these models systematically underestimate the measurements at large masses; this is the difference that is usually explained by assuming that the IMF becomes bottom heavy at large masses. In contrast, the panel on the right, which includes an IMF-driven M^*/L gradient in the Jeans equation analysis – shows no such systematic underestimate. Thus, the price I pay for ignoring IMF-related effects altogether is the small deficit between the red curves and the measurements in the middle panel.

For completeness, in both the left and middle panels of Figure 3.4 I also include the FJ relation derived from the TNG50 simulation (I discuss below and in Appendix 2.4.1 how I extract velocity dispersions in TNG50), which is also remarkably close to the data at high masses and only slightly below them at $\log_{10}\ M^*/M_\odot \lesssim 11$.

Figure 3.5 shows with filled blue circles the ratio between dynamical mass and stellar mass both as measured in MaNGA within an aperture equal to the effective radius $R = R_e$ for a constant (left panel) and scale-dependent M^*/L (right panel) with superposed errors on the mean (thick lines) and variance (shaded lines). In this plot I retain all galaxies irrespective of their morphological types though, interestingly, very similar results are found when limiting the analysis to only early-type or elliptical galaxies.[4] The dynamical masses are simply computed as

$$M_{dyn} = k\sigma^2 R_e/G, \tag{3.1}$$

[4]In this plot I limit the analysis to galaxies with Sérsic index $n > 1.8$ to avoid the inclusion of noisy velocity dispersions.

with $k = 1.8$ and 2.8 in the left and right panels. These constant 'virial' coefficients k are simply chosen to normalise the M_{dyn}/M^* ratio towards unity at low stellar masses, and thus differ from the more accurate values computed in Appendix A.1, which include the effects of, e.g., stellar profile and anisotropy. When assuming a constant IMF (left panel), the measurements (symbols) show evidence for a "slope" in the dynamical-to-stellar mass ratio especially at $R = R_e$. (The slope is shallower at $R_e/8$.) This trend of increasing M_{dyn}/M^* with stellar mass is reproduced by my fixed IMF models, without any extra fine-tuning. In these models it is mainly the fraction of dark matter within the effective radius which drives this trend: if I assume there is no dark matter (dotted cyan line), then my models return no trend. In fact, switching to a Burkert (1995) dark matter profile generates a flat M_{dyn}/M^* ratio (purple line with cross markers). In addition, structural parameters tend to play a secondary role in shaping the M_{dyn}/M^* ratio. For example, setting Sérsic index $n = 4$ for all galaxies yields nearly identical results to my base model (red line with triangular markers).

It is interesting that my fixed IMF model seems to be in good agreement with the data, despite the large body of literature arguing that the IMF must change across the population (if, as I have done here, one assumes there are no M^*/L gradients). In fact, if I plot M_{dyn}/M^* versus σ instead, then the models significantly underpredict the measurements as σ increases, in good agreement with the literature (e.g. Cappellari et al., 2013a). The agreement in the left hand panels of Figure 3.5 must result from the fact that the scatter between σ and M^* is large enough to hide the problems at large σ.

For completeness, the right panel of Figure 3.5 shows M_{dyn}/M^* after assuming an IMF-driven M^*/L gradient (this changes the denominator of the data, and both numerator and denominator of the model) as described in Section 2.1.3. In this case the resulting M_{dyn}/M^* ratio is flat as a function of stellar mass both in the MaNGA data (blue filled circles) as well as in the models. (The ratio is also flat when plotted as a function of σ.) Reducing the fraction of dark matter (purple line with cross markers) or setting $n = 4$ for all objects (solid red line with triangles) has negligible impact on the predicted ratio. All in all, my results show that when an IMF-driven gradient in M^*/L is included in the Jeans analysis, then $M_{dyn} \propto M^*$ within R_e, in agreement with Bernardi et al. (2020).

3.2 The high redshift Universe

I showed in Section 3.1 that my model to build velocity dispersion profiles for galaxies of different stellar masses is successful in matching the local data. In particular, I showed that the models can reproduce the weak dependence on B/T ratio, as well as the full velocity dispersion profile, FJ relation and dynamical-to-stellar mass ratio, irrespective of the exact (constant or spatially varying) M^*/L. In this Section 3.2 I make

predictions on the velocity dispersion $\sigma_{ap}[M^*, z]$ evolutionary tracks, and their implications for the evolution of the FJ relation and of the dynamical-to-stellar mass ratio. To generate the $\sigma_{ap}[M^*, z]$ tracks I adopt the following strategy:

- I consider stellar masses defined by a constant M^*/L in the MaNGA data set. I then select a stellar mass bin and compute its mean effective radius and Sérsic index which I choose as my starting point in Equations 2.26 and 2.30.
- I compute the mean host halo mass competing to the chosen bin of galaxy stellar mass at $z = 0$ via the inverse of the SMHM relation, and then follow backwards in time the mean halo assembly history $\langle M_{halo}(z) \rangle$ competing to that halo. I use the halo growth histories from van den Bosch et al. (2014), which were derived from detailed analytic recipes tested against N-body dark matter simulations.
- I then evolve at each time step the (mean) effective radius via Equations 2.26, 2.27 and 2.29, and the Sérsic index via Equation 2.30.
- At each time step I then apply my numerical formalism to derive the velocity dispersion. In my reference/fiducial model I adopt the Grylls et al. (2019) (inverted) SMHM relation and assume a NFW profile for the dark matter component.

I will further discuss below that the main trends in my output $\sigma_{ap}[M^*, z]$ are qualitatively unchanged when varying, within reason, any of the input parameters or their exact evolution with redshift. In what follows, I rely only on single-Sérsic profiles for two reasons: 1) I do not need to assume any time evolution in the B/T along the main progenitors, which is still debated (and in any case not too relevant to velocity dispersion as emphasized in, e.g., Figure 3.2); 2) I decrease the number of parameters to only the redshift evolution in effective radius and Sérsic index. All the predictions on the $\sigma_{ap}[M^*, z]$ presented in this Section 3.2 are calculated, unless otherwise noted, within an aperture of $R = R_e/8$. Although $R_e/8$ is difficult to resolve at higher z, this choice is mostly driven by the comparison with the TNG50 simulation. Increasing the aperture to $R = R_e$, for example, would significantly increase the computational cost of extracting and computing TNG50 velocity dispersions on a galaxy-by-galaxy basis. In addition, larger apertures tend to give more noisy results from TNG50. I note, however, that my predicted $\sigma_{ap}[M^*, z]$ evolutionary tracks are very similar in shape when adopting an aperture equal to the effective radius, they only slightly reduce in normalization. As discussed in Section 3.1, the choice of a constant or scale-dependent M^*/L produces different outputs in the dynamical-to-stellar mass ratio within the effective radius (Figure 3.5), which could be controlled by either the fraction of inner dark matter mass and/or by a larger amount of low-mass stars (bottom-heavy IMF, Equation 2.18). Therefore, in what follows, I will present results on the evolution of $\sigma_{ap}[M^*, z]$ with both a fixed IMF and IMF-gradient driven $M^*/L[r]$. Since there is no consensus on how IMF-driven gradients evolve, I include them using a very simplified

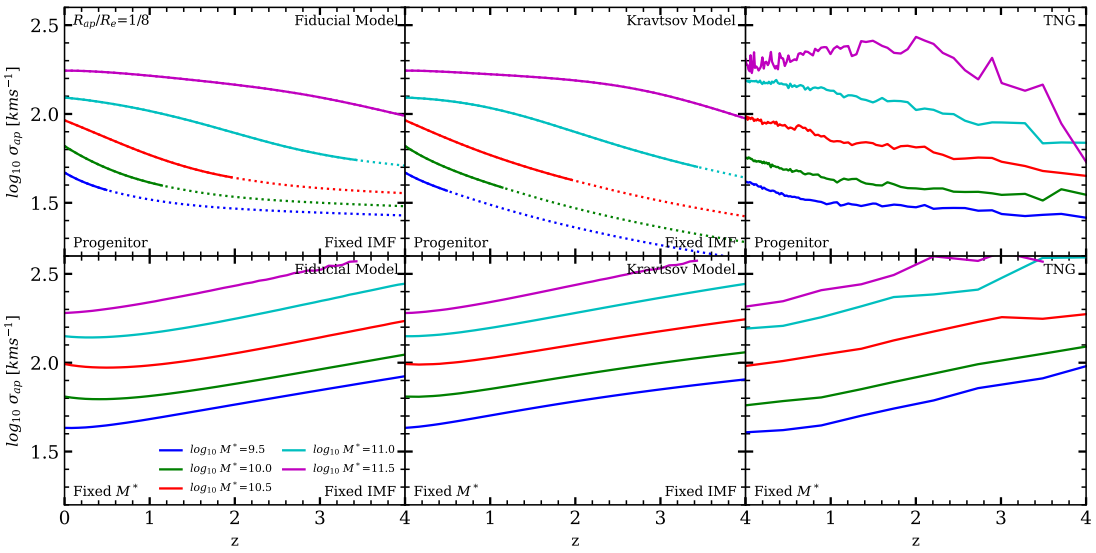

FIGURE 3.6: Predicted $\sigma_{ap}[M^*, z]$ evolutionary tracks for models with constant M^*/L along the progenitors (top panels) and at fixed stellar mass (bottom panels) for different stellar masses, as labelled. The left column shows my fiducial model. The central column shows the fiducial model with effective radii computed via the Kravtsov (2013) relation. The right column shows σ_{ap} for galaxies within the same mass bins extracted from the TNG50 simulation. Dotted lines mark the region where the input empirical scaling relations fall outside the observational parameter space in which they were calibrated (see text for details).

model: I simply set $\Upsilon_0 = 4$ and $\phi = \xi = 1$ in equation (2.18) for all the galaxies in my higher z runs.

Figure 3.6 shows my predicted velocity dispersion evolutionary tracks $\sigma_{ap}[M^*, z]$ at an aperture of $R_{ap} = R_e/8$, for different stellar masses, as labelled, along the main dark matter progenitors (top panels) and at fixed stellar mass (bottom panels). The left panels report the results of my fiducial model, the middle panels contain outputs of a model that replaces my empirical relations for effective radii (Equation 2.26) with an empirical linear and tight relation between effective radius and halo virial radius $R_e \propto R_{vir}$ (e.g., Kravtsov, 2013; Stringer et al., 2014; Huang et al., 2017; Zanisi et al., 2020, 2021), and the right panels show the results extracted from the TNG50 hydrodynamical simulation, for the same bins of stellar mass, with stellar velocity dispersions computed as described in Appendix 2 and averaged within the same aperture as in my semi-empirical models. The point to note is that all models show a similar imprint of "downsizing" in the predicted $\sigma_{ap}[M^*, z]$, with the more massive galaxies approaching the local value of $\sigma_{ap}[M^*, z]$ at earlier epochs, comparably to what observed in the relative mass growth histories of central galaxies along their main progenitor tracks (e.g., Moster et al., 2013; Behroozi et al., 2019; Grylls et al., 2019; Shankar et al., 2020a). Ricarte and Natarajan (2018) also found a clear sign of downsizing in their velocity dispersion evolutionary tracks.

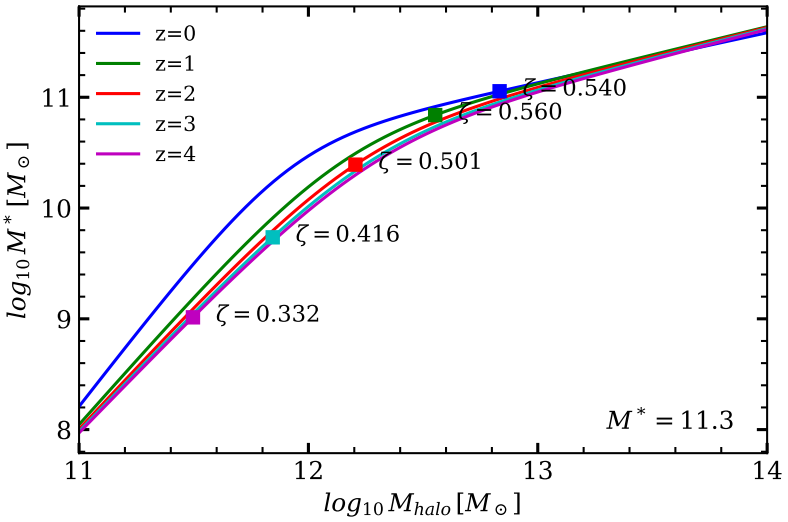

FIGURE 3.7: The Grylls et al. (2019) stellar mass-halo mass (SMHM) relation at different cosmic epochs, as labelled. The coloured squares mark the value of ζ for a galaxy of final ($z = 0$) mass $log_{10}\ M^* = 11.3\ [M_\odot]$ at $z = 0$, at the different redshift steps listed in the legend. The parameter ζ is the stellar-mass-to-total-mass ratio within R_e ($\zeta = M^*(< R_e)/(M_{halo}(< R_e) + M^*(< R_e))$). ζ has a weak evolution above the knee but drops significantly when below the knee of the SMHM relation.

Interestingly, I do not find the downsizing in $\sigma_{ap}[M^*, z]$ to be strongly dependent on the exact choice of my model for the effective radius. For example, computing the $\sigma_{ap}[M^*, z]$ in my fiducial model assuming no redshift evolution in effective radii ($\gamma = 0$ in Equation 2.29), would yield similar results. In addition, the close similarity between the fiducial model and the Kravtsov model in the predicted $\sigma_{ap}[M^*, z]$ tracks opens up the possibility of computing reliable galaxy velocity dispersion in semi-analytic and semi-empirical models via the use of only the virial radius of the host dark matter halo (see also Zanisi et al., 2021). The $\sigma_{ap}[M^*, z]$ evolutionary tracks in Figure 3.6 are shown down to a minimum stellar mass of $\log M^*/M_\odot = 9$, below this threshold I do not have data to calibrate the SMHM relation, nor sufficient velocity dispersion measurements in MaNGA, and also the $R_e \propto R_{vir}$ relation has not been well constrained below $R_e \lesssim 0.5$ kpc (e.g., Kravtsov, 2013; Somerville et al., 2018), which are the typical scales of galaxies with $M^* \lesssim 10^9\ M_\odot$. I therefore mark with dotted lines in Figure 3.6 all extrapolations in my data-driven models below this mass threshold of $\log_{10} M^*/M_\odot = 9$.

Instead, the downsizing in $\sigma_{ap}[M^*, z]$ appears to be largely driven by the shape of the input stellar mass-halo mass (SMHM) relation. The different lines in Figure 3.7 show the SMHM relation at different redshifts, as labelled, as derived by Grylls et al. (2019) and updated in Zanisi et al. (2020). The results show a weak evolution of the SMHM relation, especially at $z \gtrsim 1$ and at higher stellar masses, a conclusion shared by several previous works (e.g., Shankar et al., 2006; Moster et al., 2010b). The constant double power-law shape of the SMHM relation inevitably implies a varying fraction of stellar

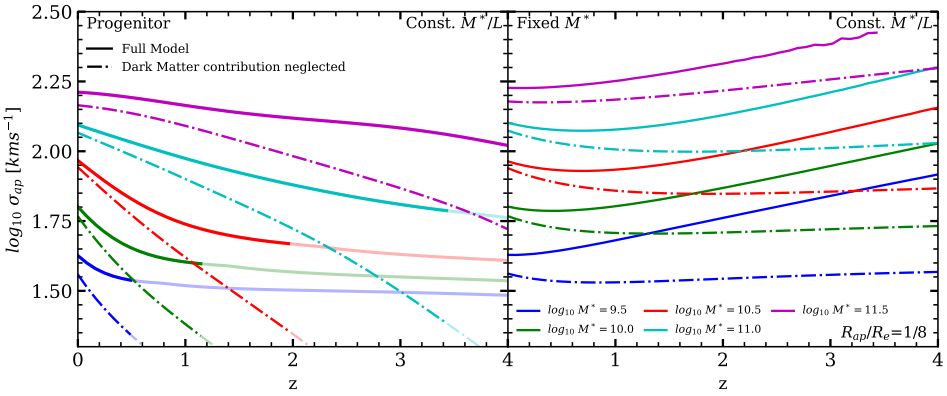

FIGURE 3.8: The average velocity dispersion for galaxies of fixed stellar mass (at $z = 0$) vs redshift for a fixed IMF (and no M^*/L gradient). The solid lines show the fiducial model, whereas the dot-dashed lines are without the dark matter component. The faint lines show the extrapolations of these models in the regions where the input scaling relations exceed the parameter space of the MaNGA catalogue. Neglecting the dark matter component produces a much steeper evolution of σ.

mass across different halo masses (e.g., Kravtsov et al., 2004; Vale and Ostriker, 2004; Shankar et al., 2006). In particular, when a halo crosses the threshold of $M_h \sim 10^{12}\ M_\odot$, marking the "knee" of the SMHM relation, the amount of stellar mass assigned to the central halo rapidly drops more steeply than in the host halo, in turn significantly reducing the central velocity dispersion. To illustrate this effect, I mark with filled squares the evolution along the SMHM relation of the ratio $\zeta = M^*(R_e)/[M^*(R_e) + M_{halo}(R_e)]$ for a galaxy with stellar mass of $M^* = 10^{11.3}\ M_\odot$ at $z = 0$. It is apparent that, whilst the ratio ζ remains similar when the galaxy resides above the knee of the SMHM relation (in this specific case $\zeta \sim 0.55$), it rapidly drops (in this case by up to $\sim 40\%$ at $1 < z < 4$) when the galaxy crosses the knee of the SMHM relation. A similar behaviour in ζ is observed for all galaxy masses of interest here. When the stellar mass $M^*(< R)$ drops sufficiently, a condition that is more easily met below the knee of the SMHM relation, the dark matter "takes over" in controlling the velocity dispersion within the aperture R. It is then natural to expect a flattening in the $\sigma_{ap}[M^*, z]$ tracks as the evolution in $M_{halo}[< R_e, z]$ is relatively weak along the progenitor tracks. In summary, the top panels of Figure 3.6 point to a pivotal role of the SMHM relation, and in particular of the location of its knee, in shaping the downsizing in the $\sigma_{ap}[M^*, z]$ evolutionary tracks, at least in models with no M^*/L gradient.

The bottom panels of Figure 3.6 present the $\sigma_{ap}[M^*, z]$ at *fixed* stellar mass for the same models as in the corresponding top panels and for the same stellar masses at $z = 0$. To generate these plots I build a mock catalogue of central galaxies and parent dark matter haloes at each redshift of interest and then bin in stellar mass. In this case the velocity dispersions are predicted to steadily increase at earlier epochs in a nearly parallel fashion. This behaviour could also be ascribed to the role of dark matter in the inner regions. Given the weak redshift evolution of the input SMHM relation (e.g., Moster

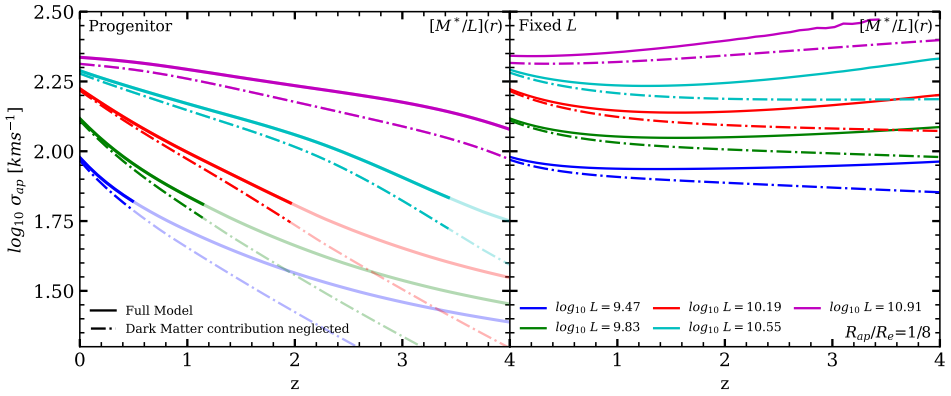

FIGURE 3.9: Average velocity dispersion histories for my fiducial model with an IMF driven M^*/L gradient. Colours correspond to the galaxies with total luminosities that would correspond to the usual bins of stellar mass (e.g. Figure 3.8) if the constant M^*/L model is assumed.

et al., 2010b), when moving backwards in time at fixed stellar mass implies retaining a similar host halo mass and thus an increasing central dark matter mass density induced by progressively smaller virial radii and increasing background densities. Our fixed IMF models (which ignore M^*/L gradients) predict an evolution of velocity dispersion at fixed stellar mass of the type $\sigma_{ap}[M^*, z] \propto (1+z)^{0.3}$, irrespective of the details of the stellar mass/dark matter profile or of the exact evolution in effective radius. The exception to this general trend is when a Burkert (1995) (rather than NFW) profile is used for the dark matter: in this case, a result similar to the no dark matter model (see Figure 3.8 and following discussion) is obtained, due to the lower dark matter density in the central regions of the galaxy predicted by the Burkert (1995) profile. My predicted evolution in velocity dispersion agrees well with the observational findings of Mason et al. (2015, see also Gargiulo et al. 2016), who find $\sigma_{ap}(R) \propto (1+z)^{0.20\pm0.07}$, and also consistent with van de Sande et al. (2011) and Cannarozzo et al. (2020), who found $\sigma_{ap}(R) \propto (1+z)^{0.4}$. Some previous semi-empirical models (e.g., Hopkins et al., 2009b) predicted a very similar evolution in velocity dispersion at fixed stellar mass to my no-M^*/L-gradient models.

To further highlight the significant role of dark matter in shaping the velocity dispersion evolutionary tracks, Figure 3.8 compares the $\sigma_{ap}[M^*, z]$ for different stellar masses along the progenitors (left panel) and at fixed stellar mass (right) with and without the contribution of dark matter in the mass budget (Equation 2.17, solid and dotted lines, respectively). Of course, in this exercise I can only rely on my analytic semi-empirical models and cannot compare with the TNG50 hydrodynamic simulation, as in the latter it is not possible to remove the dark matter contribution from the gravitational potential and from the stellar particles' velocities (Equation 2.33), once more proving the flexibility and usefulness of semi-empirical models as exploratory tools. Velocity dispersions are predicted to rapidly drop along the main progenitors in a nearly parallel

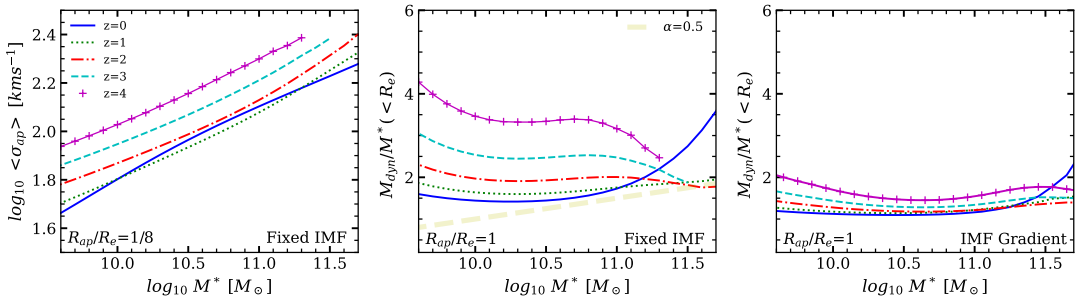

FIGURE 3.10: Predictions derived from my fiducial model of the evolution of the Faber-Jackson relation and the M_{dyn}/M^* ratio as a function of stellar mass and redshift for a fixed IMF and no M^*/L gradients (left and middle panels) and an IMF driven M^*/L gradient (right panel). In the central panel, the faint yellow dashed line shows a slop of $\alpha = 0.5$ to guide the eye. In both models I find an increase of velocity dispersion at fixed stellar mass which is however less pronounced when there is an M^*/L gradient.

fashion when dark matter is removed (dot-dashed lines, left panel), at least for galaxies with $\log_{10} M^*/M_\odot \lesssim 10^{11}$. More massive galaxies tend to retain their weak evolution with redshift as the stellar component dominates the inner dynamics for longer periods of time before it crosses the knee of the SMHM relation. Removing the dark matter component also flattens out the $\sigma_{ap}[M^*, z]$ at fixed stellar mass (dot-dashed lines, right panel). As expected, when dark matter is not considered in the mass budget (Equation 2.17), a steady decrease of stellar mass naturally implies a constant decrease in the corresponding velocity dispersion. Equivalently, at fixed stellar mass the model predicts an approximately constant velocity dispersion, further proving the relatively weak roles of effective radius and Sérsic index in determining central velocity dispersions. I note that I have neglected the contribution of gas in the computation of velocity dispersions throughout, also given the sparsity of available data. Nevertheless, gas fractions in galaxies are predicted and observed to increase at higher redshifts (e.g., Stewart et al., 2009, and references thereafter), thus possibly promoting an even weaker evolution of velocity dispersions along the progenitors and an even steeper evolution at fixed stellar mass than the trends reported in Figure 3.8.

Figure 3.9 shows the analogue $\sigma_{ap}[M^*, z]$ evolutionary tracks along the progenitors (left) and at fixed stellar mass (right) for models with an IMF driven M^*/L gradient, for different bins of galaxy luminosity L, as labelled. Similarly to when M^*/L gradients are ignored, the $\sigma_{ap}[M^*, z]$ continue to present a marked downsizing, but their evolution is similar with (solid lines) and without (dot-dashed lines) dark matter at least up to $z \sim 1-2$ before diverging from one another at higher redshifts. This behaviour is expected from my discussion of Figure 3.5, which supports the fact that a significant gradient in M^*/L could account for the full dynamical mass within R_e. Therefore, in the case of a variable IMF, the stellar mass tends to dominate over dark matter for a longer time before the dark matter is able to take over the gravitational budget of the

central regions of the galaxy. The evolution of $\sigma_{ap}[M^*, z]$ at fixed stellar mass is also similar to the case with no M^*/L gradients, but is somewhat weaker, roughly described by the scaling $\sigma_{ap}[M^*, z] \propto (1+z)^{0.2}$, which is, interestingly, in even better agreement with the observational results by Mason et al. (2015).

The behaviour of $\sigma_{ap}[M^*, z]$ with redshift summarised in Figure 3.8 helps to make solid predictions on other relevant galaxy probes which I introduced in Section 3.1. The left panel of Figure 3.10 shows the predicted FJ relation at different redshifts. As velocity dispersion increases at fixed stellar mass, the FJ will in turn increase in normalization, consequent to the increasing central dark matter mass density. More specifically, the evolution in normalization is relatively weak up to $z \sim 1$, in agreement with some observational data (e.g., Zahid et al., 2016), and then it starts increasing at a rate of $\propto (1+z)^{0.3}$, faithfully mirroring the evolution in $\sigma_{ap}[M^*, z]$ at fixed stellar mass shown, e.g., in the right panel of Figure 3.8. I confirm that I observe a similar redshift evolution in the FJ relation extracted from the TNG simulation. The middle panel of Figure 3.10 reports the predicted evolution of the ratio between dynamical mass and stellar mass within the effective radius R_e, i.e. $M_{dyn}(< R_e) \propto M^*(R_e)^{1+\alpha}$, in the same format as in Figure 3.5. It is first of all evident that the normalization of the $M_{dyn}(< R_e)/M^*(R_e)$ ratio increases with redshift consequent to the increase in the inner dark matter density which drives the increase in velocity dispersion. More interestingly, the initial tilt of $\alpha \sim 0.5$ at $z = 0$ (as shown in Figure 3.5) rapidly drops, and in fact α becomes negative at higher stellar masses and at high redshift. The main reason behind this strong and rapid evolution in this ratio has to be mostly ascribed, in my models, to the steady decrease in effective radii with redshift which is more pronounced in more massive galaxies, as parameterised in Equations 2.26 and 2.29 (see Figures 3.4 and 2.2). As the galaxy effective radii gradually shrink at earlier epochs, the contribution of dark matter becomes proportionally less relevant in massive galaxies. A similar trend in the shape of the $M_{dyn}(< R_e)/M^*(R_e)$ ratio with time is predicted also in the presence of a variable IMF (right panel), though the normalization has a much weaker evolution in this instance, a trend once more mainly induced by the dominance of the stellar mass within R_e.

3.3 Discussion

By using a semi-empirical approach, following dark matter assembly histories and making use of an input SMHM relation, I have built a flexible model to predict the velocity dispersion evolutionary tracks $\sigma_{ap}[M^*, z]$ of galaxies in the stellar mass range $9 < \log M^*/M_\odot < 11.5$. I showed that, in models with no M^*/L gradient, which appear very similar to the predictions of the TNG50 hydrodynamic simulation (Figure 3.8), the inner relative fraction of dark matter with respect to stars regulates the

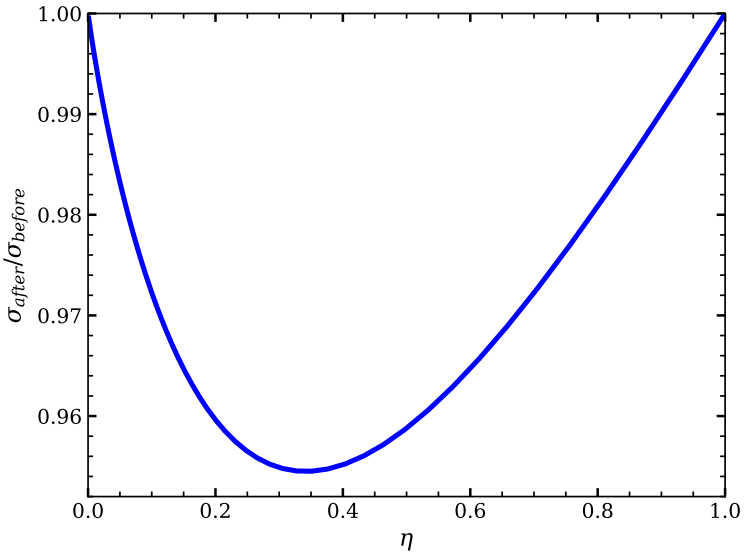

FIGURE 3.11: Graphical representation of equation 3.2, showing the (theoretical) change in σ under a merger of ratio $\eta = M^*_{sat}/M^*_{cent}$, assuming basic energy conservation arguments. This plot sets $\delta = 0.6$, as in the text. Note that while the fractional change appears small, the cumulative effect of many mergers is significant.

$\sigma_{ap}[M^*, z]$ tracks, although its role becomes less prominent in the presence of sufficiently steep (IMF driven) gradients in M^*/L. In this Section I discuss my findings of $\sigma_{ap}[M^*, z]$ evolutionary tracks that are constant or increasing with time, in light of galaxy evolutionary models, in particular focusing on role of "dry" (gas-poor) mergers, and on the link between velocity dispersion and central black hole mass.

3.4 The role of (dry) mergers

One of the key predictions from all hierarchical models of galaxy formation is that velocity dispersion should *decrease* with cosmic time in the presence of minor, dry mergers (see Chapter 1.2.4). A simple approximation to velocity dispersion evolution under dry mergers, derived from basic energy conservation arguments, can be written as (e.g., Naab et al., 2009; Fan et al., 2010; Nipoti et al., 2012; Lapi et al., 2018)

$$\sigma^2_{after} = \sigma^2_{before} \frac{1 + \eta^{2-\delta}}{1 + \eta}, \tag{3.2}$$

where σ_{before} and σ_{after} are, respectively, the velocity dispersions of the central galaxy before and after a merger, η is the stellar mass ratio between the infalling and central galaxy, and δ is the exponent of the radius-mass relation $r \propto M^\delta$ (which I set to a reference value of $\delta = 0.6$ following Shankar et al. 2014). This relation is represented graphically in Figure 3.11. In all cases, the final velocity dispersion is expected to decrease by a small amount, with a maximum decrease predicted at $\eta \sim 0.3$.

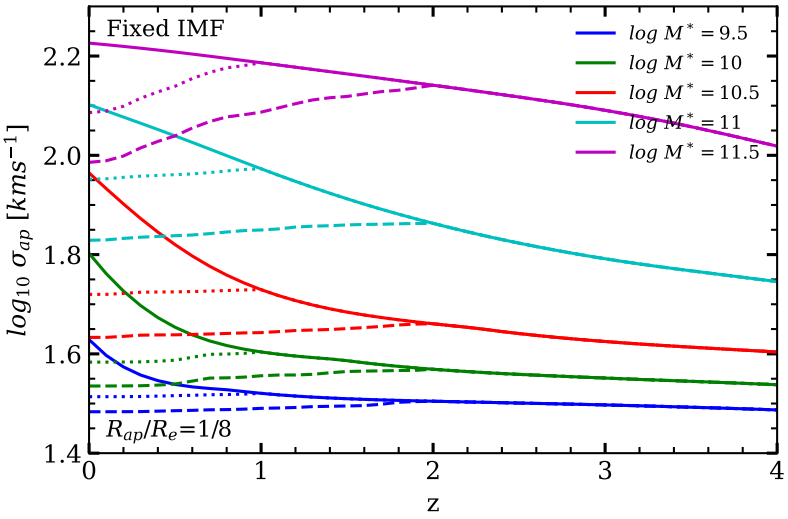

FIGURE 3.12: Average σ for galaxies of fixed mass at $z = 0$, showing the effect of multiple repeated mergers on the evolution of σ commencing at $z = 2$ (dashed lines) and $z = 1$ (dotted lines). Solid lines show the original tracks. Velocity dispersion drops unreasonably quickly under repeated mergers, suggesting other processes are at work.

To simulate the cumulative impact of mergers on velocity dispersions, I apply Equation 3.2 to the mergers occurring along the dark matter main progenitor branches of the stellar mass accretion tracks that I generated as the baseline for my $\sigma_{ap}[M^*, z]$ evolutionary tracks (Figure 3.8). More specifically, I follow the methodology put forward by Grylls et al. (2019, 2020b,a), and further developed and refined by Fu et al. (in prep.), in which infalling dark matter subhaloes at each interval dz are extracted from the unevolved (i.e., unstripped), subhalo mass function (e.g., Hopkins et al., 2009b; Jiang and van den Bosch, 2016). Galaxy stellar masses are assigned to both central and satellite dark matter haloes via a SMHM relation, and are then assumed to be "frozen" after infall, i.e. with negligible stripping and star formation once they cross the virial radius, which Grylls et al. (2019) showed to be a very good approximation for reproducing the local satellite stellar mass function above $M^* \gtrsim 10^{10}\,M_\odot$, the range of mass of interest here. I stress that none of the conclusions discussed below will be qualitatively altered by allowing for some late evolution in the infalling satellites or by varying the rate of galaxy mergers via, e.g., the adoption a different input SMHM relation (e.g., Grylls et al., 2020a). My aim here is to check whether a sequence of repeated dry mergers, at the rate predicted by a ΛCDM Universe, induces a (late) σ evolution roughly consistent with the one inferred by my semi-empirical models.

The solid lines in Figure 3.12 correspond to my $\sigma_{ap}[M^*, z]$ evolutionary tracks in my fiducial model with a constant M^*/L for different stellar masses at $z = 0$, as labelled. I assume that the galaxy undergoes a two-phase evolution (e.g., Oser et al., 2010; Lapi et al., 2018), comprising of an early in-situ growth followed by a sequence of mostly

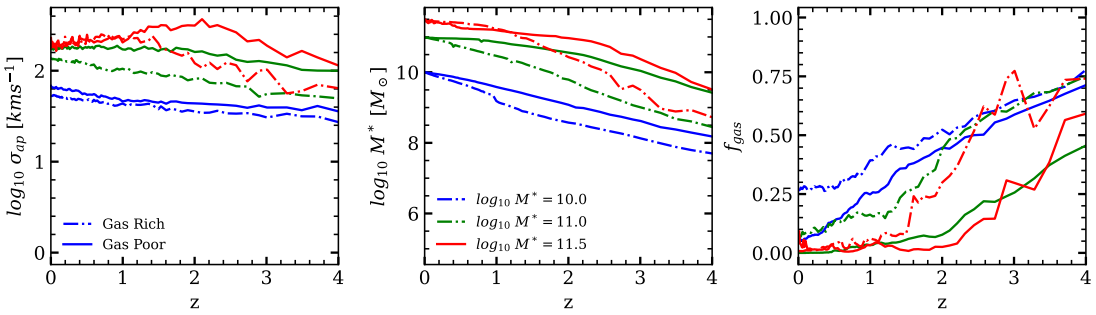

FIGURE 3.13: Velocity Dispersion, M^* and f_{gas} histories from galaxies defined as Gas Rich and Gas Poor within TNG50. Galaxies are selected in mass bins of 0.1 dex (at $z = 0$) and for each the ratio of gas to stellar mass within the half mass radius is computed. The upper and lower quartiles of this distribution are plotted here, as 'Gas Rich' and 'Gas Poor' respectively.

dry mergers. I choose the latter phase to kick in either at $z = 1$ or at $z = 2$, and thus from that redshift onwards, for each of my evolutionary tracks, I update the velocity dispersion following each merger event via Equation 3.2. The result is shown with dotted and dashed lines, respectively. For galaxies with stellar mass $M^* \lesssim 10^{11}\,M_\odot$, the evolution of $\sigma_{ap}[M^*, z]$ is predicted to be approximately flat from $z = 1 - 2$, as naturally expected from Equation 3.2 as galaxy mergers are progressively less relevant at lower stellar masses (e.g., De Lucia et al., 2006; Hopkins et al., 2010; Shankar et al., 2013a). Such a flat trend is in tension with the increasing $\sigma_{ap}[M^*, z]$ at $z \sim 0.5 - 1$, suggesting that in-situ growth is a dominant component for the mass and dynamical evolution of lower mass galaxies. More massive galaxies with $M^* \gtrsim 10^{11}\,M_\odot$ instead show relatively flat $\sigma_{ap}[M^*, z]$ at $z \sim 1 - 2$, which however are still in tension with the evolution via Equation 3.2 which predicts velocity dispersions steadily decreasing with cosmic time, especially for galaxies $M^* \gtrsim 2 \times 10^{11}\,M_\odot$. I note that adopting a gradient in M^*/L would induce even steeper evolution in the predicted $\sigma_{ap}[M^*, z]$ at all epochs (Figure 3.9), thus exacerbating the tensions with pure dry merger models. I thus conclude that completely dry mergers cannot dominate the late evolution of galaxies, and that additional in-situ stellar mass growth, even in the most massive galaxies, should occur during and/or in between mergers to maintain a flat or increasing $\sigma_{ap}[M^*, z]$. This conclusion is consistent with the declining, but still non-zero, star formation histories inferred in massive galaxies (e.g., Buchan and Shankar, 2016; Leja et al., 2019; Grylls et al., 2020b, and references therein) and with the presence of substantial amounts of gas in massive galaxies at intermediate epochs (e.g., Gobat et al., 2018, 2020).

To further probe the role of gas richness in shaping the evolutionary histories of $\sigma_{ap}[M^*, z]$, I dissect the velocity dispersion evolutionary tracks in the TNG50 simulation for different gas fractions and stellar masses. The left panel of Figure 3.13 plots the $\sigma_{ap}[M^*, z]$ of galaxies of equal stellar mass at $z = 0$ (middle panel), but distinct gas fractions at all relevant epochs (right panel), namely the 95% percentile above and below the mean gas fractions for galaxies of the selected stellar mass bin (dot-dashed lines and solid lines,

respectively). I find clear evidence that gas-richer galaxies, as expected, have a significantly steeper evolution in both stellar mass and velocity dispersion, whilst gas-poorer galaxies tend to have a flatter evolution in stellar mass, and a flat or even decreasing velocity dispersion at late epochs, consistently with what predicted from my toy models in Figure 3.12 (dashed lines). Interestingly, the most massive and gas-poor galaxies in the TNG50 simulation tend to show a decreasing velocity dispersion at late times $z \lesssim 2$ (solid red line in the left panel of Figure 3.13), which is what it would be expected in the presence of repeated dry mergers. In order to reproduce this trend in $\sigma_{ap}[M^*, z]$ in my semi-empirical model I would require an input SMHM relation that steepens at earlier epochs, in a way to keep the $\zeta = M^*(R_e)/[M^*(R_e) + M_{halo}(R_e)]$ ratio (Figure 3.7) increasing at earlier epochs along the halo progenitor track, a trend that is however not favoured by current estimates of the stellar mass function at high redshifts (e.g., Kawinwanichakij et al., 2020). My conclusions agree with previous analytic and numerical work suggesting that dry mergers alone cannot entirely account for the behaviour of velocity dispersion at late epochs (e.g., Nipoti et al., 2012).

Chapter 4

Results: Black Hole Scaling Relations

In this Chapter I firstly present analysis of the residuals around the scaling relations of the local sample of galaxies with dynamically measured supermassive black hole mass. I will show that the analysis strongly suggests that velocity dispersion is more fundamental than other galaxy properties, most notably stellar mass (additional residuals test performed on other galaxy properties such as Sérsic index, and other samples such as active galaxies, are presented in Shankar et al. 2017a and Shankar et al. 2019b). In the second part of the Chapter I will connect the evolutionary tracks in velocity dispersions derived in Chapter 3 with those independently derived for supermassive black holes from stacked X-ray AGN, to build a $M_{\rm BH}$-σ relation at all redshifts. Finally, I will show how I can place additional constraints on black hole scaling relations using AGN clustering.

4.1 Fundamental $M_{\rm BH}-\sigma$ - Residuals analysis

In this section I now consider additional evidence that the $M_{\rm BH}-\sigma$ may be the most fundamental scaling relation. I start by revisiting the residual analysis on the black hole scaling relations following the method outlined in Shankar et al. (2016), Shankar et al. (2017a) and Shankar et al. (2019b). Residuals in pairwise correlations (Sheth and Bernardi, 2012) allow for a statistically sound approach to probe the relative importance among variables in the scaling with black hole mass. Residuals are computed as

$$\Delta(Y|X) \equiv \log Y - \langle \log Y | \log X \rangle \tag{4.1}$$

where the residual is computed in the Y variable (at fixed X) from the log-log-linear fit of $Y(X)$ vs X, i.e. $\langle \log Y | \log X \rangle$. For each pair of variables, each residual is computed 200 times, and at each iteration five objects at random are removed from the original sample. From the full ensemble of realizations, I then measure the mean slope and its 1σ uncertainty.

My results are shown in Figures 4.1 and 4.2, which show the residuals extracted from the recent homogeneous sample calibrated by de Nicola et al. (2019). This sample consists of 109 black holes compiled from several sources, with masses measured using spatially resolved kinematics (a combination of stellar, gas dynamics and astrophysical masers (see Kormendy and Ho, 2013)). This sample does not include black hole masses derived from reverberation mapping or virial methods, as such techniques must be calibrated using black hole - galaxy scaling relations[1].

Figure 4.1 shows that black hole mass strongly correlates with velocity dispersion at fixed galaxy luminosity with a Pearson coefficient $r \sim 0.7$ (top left panel), and even more so at fixed effective radius with $r \sim 0.8$ (bottom left panel), while the corresponding correlations with stellar luminosity or effective radius are significantly less strong with $r \sim 0.4$ at fixed velocity dispersion (right panels). Figure 4.2 shows the residuals restricting the analysis to only early type galaxies (red circles). The residuals appear quite similar in both slopes and related Pearson coefficients. These results further support the findings by Shankar et al. (2016) (shown, for comparison, in Figure 4.3) that velocity dispersion is more fundamental than effective radius and stellar mass, and that even disc-dominated galaxies follow similar scaling relations[2].

The total slope of the $M_{\rm BH}$-σ relation can be estimated as $M_{\rm BH} \propto \sigma^{\beta} M_*^{\alpha} \propto \sigma^{\beta+\alpha\,\gamma}$, where γ comes from $M_* \propto \sigma^{\gamma}$. Since SDSS galaxies tend towards $\gamma \approx 2.2$ (Shankar et al., 2017b), and the residuals in Figure 4.1 yield $\beta \sim 3$ and $\alpha \sim 0.4$, one obtains a total dependence of $M_{\rm BH} \propto \sigma^5$, consistent with models of black hole growth being regulated by AGN feedback, as further discussed in Section 4.2 (e.g. Silk and Rees, 1998; Fabian, 1999; King, 2003; Granato et al., 2004).

4.2 Discussion: Fundamental $M_{\rm BH} - \sigma$

As I have briefly discussed, a growing body of work is pointing to the fundamental importance of the $M_{\rm BH}$-σ. A key perspective that I have so far neglected in regards to

[1] This sample itself is indeed highly likely be suffer from selection bias, as discussed in Chapter 1, as larger black holes are more likely to be kinematically resolved. While this has important implications for the determination of correct galaxy-black hole scaling relations, we must assume here that the relative importance of the scaling relations is not sample dependant.

[2] In Shankar et al. (2016), we show additional correlation coefficients. They are however not very informative, so are not included in this work.

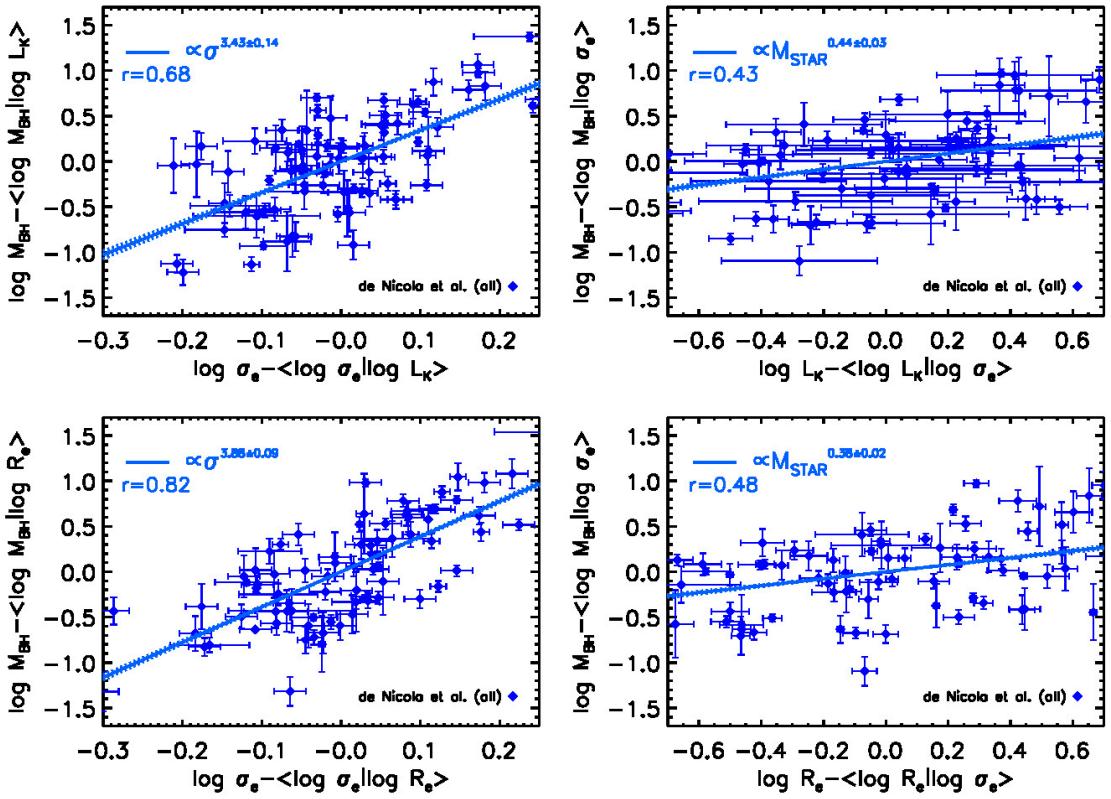

FIGURE 4.1: Correlations between residuals from the observed scaling relations, as indicated. The residuals are extracted from the recent homogeneous sample calibrated by de Nicola et al. (2019). It can be clearly seen that black hole mass is strongly correlated with velocity dispersion at fixed galaxy luminosity with a Pearson coefficient $r \sim 0.7$ (top left panel), and even more so at fixed effective radius with $r \sim 0.8$ (bottom left panel). Correlations with other relations appear less strong (right panels)

.

black hole scaling relations is that of the *theoretical modeller*, which I will explore in this section before considering further applications of this relation as the most fundamental.

The parameters of the galaxy that correlate with $M_{\rm BH}$ tell us which physical processes are most important in setting the black hole mass. Each parameter is related to certain physical quantities. For example, velocity dispersion is naturally related to the mass of the galaxy's spheroidal component, and by extension to its gravitational potential. In the simplest case, modelling the bulge as an isothermal density profile, gas density is $\rho \propto \sigma^2$ and its weight (the product of the gas mass and gravitational acceleration) is $W \propto \sigma^4$. Therefore, modelling a connection between the upper limit of the black hole mass and the weight of the gas surrounding it may indeed be a good starting point to explaining the correlation. Alternatively, if the SMBH mass were controlled by stellar processes, such as turbulence driven by stellar feedback, I would expect a strong correlation between $M_{\rm BH}$ and stellar mass. Similarly, if the rate of SMBH feeding from large-scale reservoirs were an important constraint, a correlation with the bulge size R or dynamical timescale $t_{\rm dyn} \simeq R/\sigma$ might emerge. The fact that such correlations are

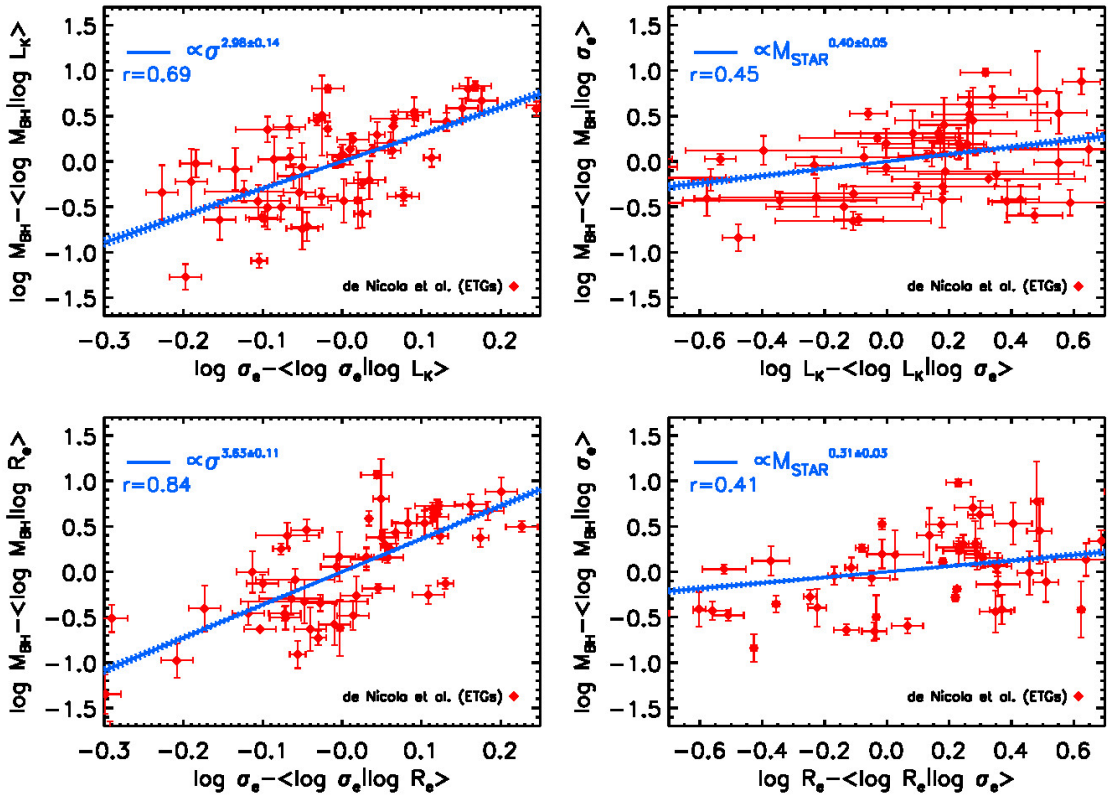

FIGURE 4.2: Identical analysis to Figure 4.1, but only early type galaxies. Correlations with velocity dispersion are comparable.

not seen suggests that these processes are secondary to the host's gravitational potential.

A very promising group of models that have emerged over the past two decades are those based on AGN feedback (Silk and Rees, 1998; Granato et al., 2004; Harrison, 2017; Morganti, 2017). The common argument is that AGN luminosity transfers energy to the surrounding gas and at some point drives it away, quenching further black hole growth. These models are generally capable of explaining not only the $M_{\rm BH}$-σ relation, but also the presence of quasi-relativistic nuclear winds and large-scale massive outflows observed in many active galaxies. Other models that presume either no causal connection between galaxy and black hole growth (Peng, 2007; Jahnke and Macciò, 2011) or those that claim the black hole to be merely a passive recipient of a fraction of the gas used to build up the bulge (Haan et al., 2009; Anglés-Alcázar et al., 2013, 2015) make no predictions regarding outflows and generally connect the black hole mass to the mass, rather than velocity dispersion, of the galaxy bulge.

There are several ways of transferring AGN power to the surrounding gas, e.g. radiation, winds and/or jets (Morganti, 2017). Jets are typically efficient on galaxy cluster scales, heating intergalactic gas and prevent it from falling back into the galaxy (McNamara and Nulsen, 2007). This process, referred to as "maintenance mode" of feedback,

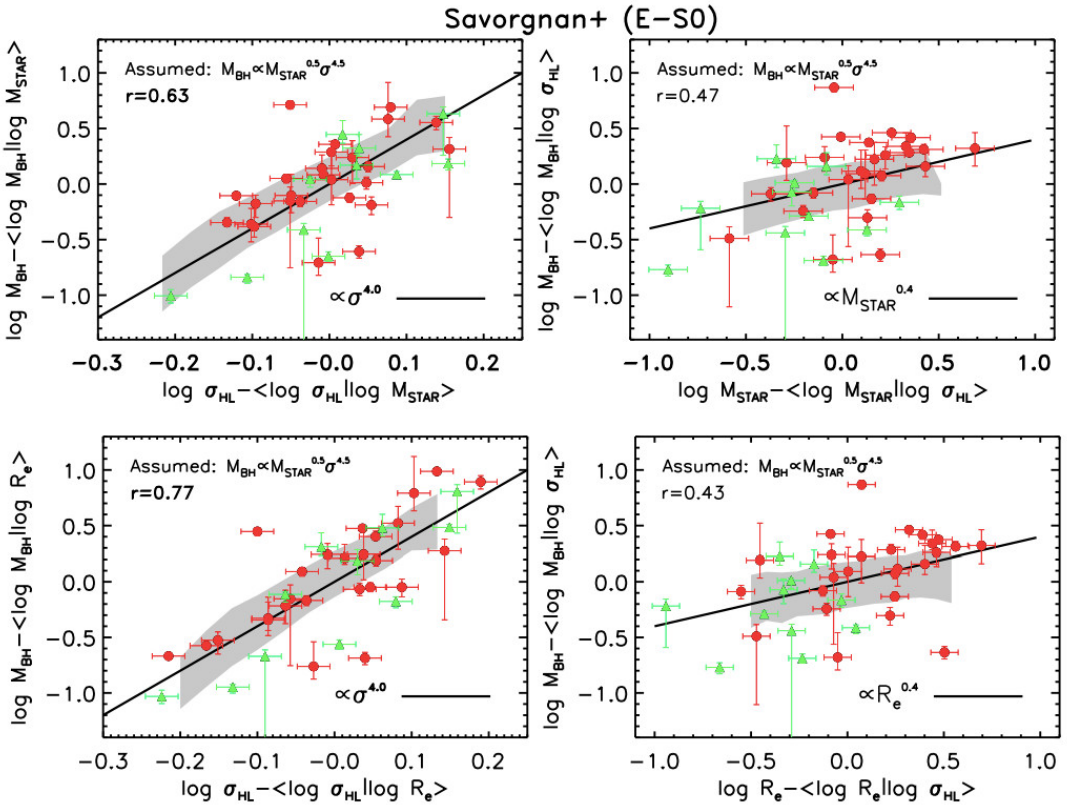

FIGURE 4.3: Figure 5 from Shankar et al. (2016) showing correlations between residuals. Correlations with velocity dispersion (left panels) appear to be stronger than other relations. The data is from the sample of Savorgnan and Graham (2016).

prevents the SMBH mass from growing above the limit established by the M_{BH}-σ relation. Jets are considered to be the primary form of feedback in AGN that accrete at low rates and have luminosities $L < 0.01 L_{AGN}$ (Merloni and Heinz, 2007). The opposite type of feedback is known as "quasar mode", and it is believed to be most efficient in more luminous AGN. Here, again, there are two possibilities in which energy can be transferred. Directly coupling AGN luminosity to the gas in the interstellar medium is possible if the gas is dusty (due to a very high opacity, see Fabian et al. 2008). On the other hand, dust evaporates when shocked to the temperatures expected within AGN outflows (Barnes et al., 2018), potentially limiting the impact of radiation-driven outflows. A much more promising avenue is to connect the AGN with the surrounding gas via a quasi-relativistic wind (King and Pounds, 2015). Such a model naturally produces both a M_{BH}-σ relation similar to the observed one, and outflow properties in excellent agreement with observations, both within galaxies (Zubovas and King, 2012a; Cicone et al., 2014; Menci et al., 2019) and on intergalactic scales in galaxy groups (Lapi et al., 2005).

4.2.1 AGN wind-driven feedback

AGN are highly variable on essentially all timescales and are known to occasionally reach the Eddington luminosity

$$L_{\rm Edd} = \frac{4\pi G M_{\rm BH} c}{\kappa_{\rm e.s.}}, \tag{4.2}$$

where $\kappa_{\rm e.s} \simeq 0.346\ {\rm cm^2\ g^{-1}}$ is the electron scattering opacity. Under such circumstances, the geometrically thin accretion disc produces a quasi-spherical wind that self-regulates to an optical depth $\tau \sim 1$ (King and Pounds, 2003). Therefore each photon emitted by the AGN will, on average, scatter only once before escaping to infinity, and the wind carries a momentum rate

$$\dot{M}_{\rm w} v_{\rm w} = \tau \frac{L_{\rm AGN}}{c}, \tag{4.3}$$

where $\dot{M}_{\rm w}$ is the wind mass flow rate, $v_{\rm w}$ is the wind velocity and $L_{\rm AGN} \equiv l L_{\rm Edd}$ is the AGN luminosity, where l is the Eddington ratio. By writing $L_{\rm AGN} = \eta \dot{M}_{\rm BH} c^2$, the wind velocity can be shown to be

$$v_{\rm w} = \frac{\tau \eta}{\dot{m}} c, \tag{4.4}$$

where $\dot{m} \equiv \dot{M}_{\rm w} / \dot{M}_{\rm BH}$. The value of $\dot{m}$ is highly uncertain, but should not be extremely different from unity. To see this, consider the extreme ends of the possible range of $\dot{M}_{\rm BH}$. If the accretion rate on to the accretion disc is significantly below Eddington, no wind is produced, while if the accretion rate rises above the Eddington limit, the wind moderates the accretion flow. Overall, the highest possible average accretion rate is the dynamical rate:

$$\dot{M}_{\rm dyn} = f_{\rm g} \frac{\sigma^3}{G} \simeq \frac{64}{\sigma_{200}} \dot{M}_{\rm Edd}, \tag{4.5}$$

where $f_{\rm g} \simeq 0.16$ is the cosmological gas fraction, $\sigma \equiv 200 \sigma_{200}$ km s^{-1} is the velocity dispersion in the galaxy (King, 2010b; King and Pounds, 2015), and $\dot{M}_{\rm Edd} = L_{\rm Edd} / \eta c^2$ is the mass flow rate corresponding to the Eddington Ratio. In deriving the second equality, I used the $M_{\rm BH} - \sigma$ relation that is derived below, in eq. 4.10. Therefore, in most cases, the SMBH feeding rate is not significantly higher than the Eddington rate, unless $M_{\rm BH}$ is well below the observed relation. As a result, I take $\dot{m} \sim 1$ for the rest of this section. This leads to the final expression for the AGN wind velocity

$$v_{\rm w} \simeq \eta c \simeq 0.1 c, \tag{4.6}$$

which is very close to the average velocity in observed winds (Tombesi et al., 2010a,b). The kinetic power of the wind is

$$\dot{E}_{\rm w} = \frac{\dot{M}_{\rm w} v_{\rm w}^2}{2} \simeq \frac{\eta}{2} L_{\rm AGN} \simeq 0.05 L_{\rm AGN}. \tag{4.7}$$

The wind rapidly reaches the interstellar medium (ISM) surrounding the AGN and shocks against it. The shock is strong, since $v_{\rm w}/\sigma \gg 1$, and the wind heats up to a temperature

$$T_{\rm sh} = \frac{3m_{\rm p}v_{\rm w}^2}{16k_{\rm b}} \simeq 10^{10}{\rm K}, \tag{4.8}$$

where $m_{\rm p}$ is the proton mass, and $k_{\rm b}$ is the Boltzmann constant. The most efficient cooling process at this temperature is Inverse Compton (IC) cooling via interaction with AGN photons (King, 2003; Faucher-Giguère and Quataert, 2012). Most of the photons interact with electrons in the shocked wind, and a two-temperature plasma develops (Faucher-Giguère and Quataert, 2012). The actual cooling timescale then depends on the timescale for energy equilibration between electrons and protons. As a result, cooling is highly inefficient and the shocked wind can expand as an approximately adiabatic bubble.

The subsequent evolution of the expanding bubble depends on the density structure of the ISM. Most of the energy stored in the hot wind bubble escapes through the low-density channels and creates a large-scale outflow (Zubovas and Nayakshin, 2014). Denser clouds, however, remain and are mainly affected by the direct push of the wind material. These two situations create two kinds of outflow, known as energy-driven and momentum-driven, respectively. The latter kind is responsible for establishing the $M_{\rm BH}-\sigma$ relation.

4.2.2 The predicted relation

Momentum-driven outflows push against the dense clouds surrounding the black hole. These clouds are the most likely sources of subsequent black hole feeding, therefore their removal quenches further black hole growth for a significant time and establishes the $M_{\rm BH}$-σ relation (King, 2003; Murray et al., 2005; King, 2010a). Considering the balance between AGN wind momentum and the weight of the gas $W_{\rm gas}$ leads to a critical AGN luminosity required for clearing the dense gas:

$$L_{\rm crit} = W_{\rm gas}c \simeq \frac{4f_{\rm g}\sigma^4 c}{G}, \tag{4.9}$$

where the second equality assumes that the gas distribution and the background gravitational potential are isothermal, i.e. $\rho = \sigma^2/\left(2\pi G R^2\right)$ (Murray et al., 2005). Equating this critical luminosity with the Eddington luminosity of the black hole allows us to derive a critical mass (King, 2010a):

$$M_{\rm crit} \simeq \frac{f_{\rm g}\kappa_{\rm e.s.}\sigma^4}{\pi G^2} \simeq 3.2\times10^8\frac{f_{\rm g}}{0.16}\sigma_{200}^4\,M_\odot. \tag{4.10}$$

This value is very close to the observed one, although it has a slightly shallower slope. This discrepancy may be explained by the fact that the black hole still grows during

the time while it drives the gas away (Zubovas and King, 2012b). As the gas is pushed away, it joins the energy-driven outflow. This outflow coasts for approximately an order of magnitude longer than the AGN phase inflating it and stalls at a distance (King et al., 2011)

$$R_{\rm stall} \simeq \frac{v^2}{\sigma} t_{\rm AGN}, \tag{4.11}$$

where $t_{\rm AGN}$ is the duration of the driving phase and the energy-driven outflow velocity is (King, 2005; Zubovas and King, 2012a)

$$v = \left(\frac{2\eta c}{3\sigma}\frac{0.16}{f_{\rm g}}\right)^{1/3} \simeq 925\sigma_{200}^{2/3}\left(\frac{0.16}{f_{\rm g}}\right)^{1/3} {\rm kms}^{-1}. \tag{4.12}$$

By equating $R_{\rm stall}$ with either the bulge radius or the virial radius of the galaxy, one obtains the time $t_{\rm AGN}$ for which the galaxy must be active in order to quench further accretion on to the black hole and find $t_{\rm AGN} \propto R\sigma^{-1/3} \propto \sigma^{2/3}$, since $R \propto \sigma$ on average (this relation arises from the Fundamental plane of galaxies, see Djorgovski and Davis, 1987; Cappellari et al., 2013b). Note that this growth does not need to happen all at once: as long as the outflow is still progressing by the time the next episode begins, the system behaves as if it was powered by a continuously shining AGN (Zubovas, 2019).

This extra growth steepens the $M_{\rm BH}$-σ relation beyond the simpler analytical prediction and brings it more in line with observations (Zubovas and King, 2012b). Furthermore, it shows that galaxy radius may be an important secondary parameter determining the final black hole mass.

As a final note, the extra black hole growth while clearing the galaxy also depends on its spin. Since a rapidly spinning black hole produces more luminosity and drives a faster outflow than a slow-spinning one, the latter has to be active for longer and grow more before it clears the gas from the galaxy. Although present-day estimates of black hole spins are not robust or numerous enough to test this prediction in detail, this might become possible in the near future (Zubovas and King, 2019).

In general, theoretical models based on momentum-driven outflows are capable of naturally explaining the relationship between black hole mass and velocity dispersion, primarily due to the latter acting as a tracer of the host's gravitational potential well. In addition, these models could account for *secondary*, weaker dependencies on, e.g., galaxy stellar mass or size, which may still be allowed by current data as discussed above (Figure 4.1).

4.3 σ modelling - Implications for black hole scaling relations

I have seen how the $M_{\rm BH}$-σ is likely to be the most fundamental scaling relation, and I now consider how I can apply my σ modelling to reveal more about this relation,

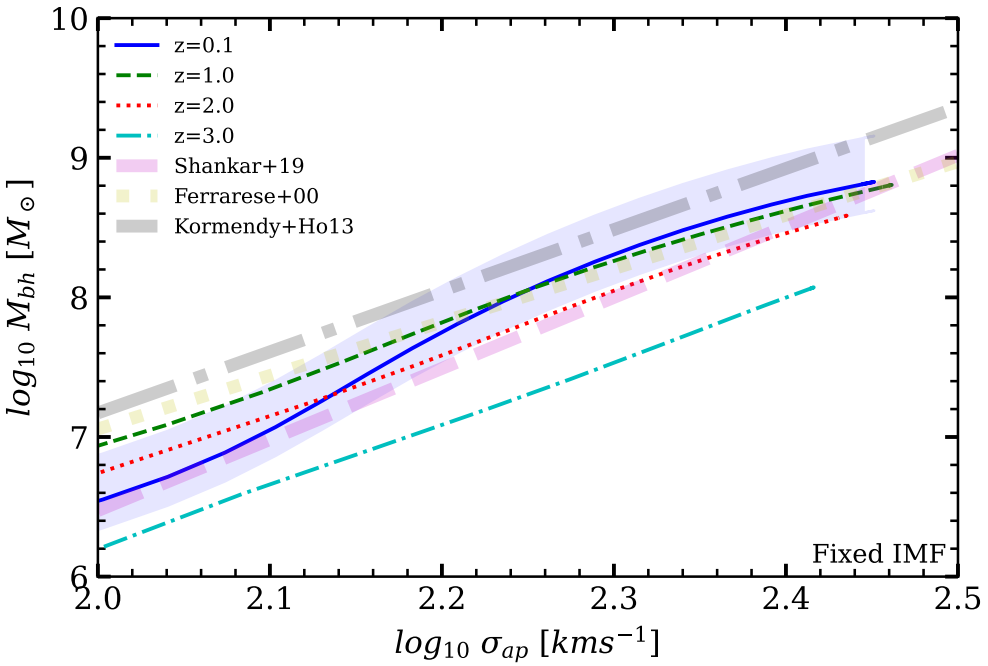

FIGURE 4.4: The $M_{\rm BH}-\sigma$ relation as predicted by my model at different redshifts and compared with various relations at $z = 0$ from the literature. The blue shaded region shows the effect of varying the radiative efficiency ϵ (at $z = 0$) by ± 0.05.

particularly at high redshift.

In this Section I attempt to derive the $M_{\rm BH}$-σ at different redshifts following a methodology similar to the one put forward by other groups in the context of the $M_{\rm BH}$-M^* relation (e.g., Yang et al., 2018; Carraro et al., 2020; Shankar et al., 2020a). I calculate the black hole accretion rate $\dot{M}_{\rm BH}[z, M^*]$ integrating at each time step the probability $P(z, L_X|M^*)$ of having a certain X-ray AGN luminosity for a given stellar mass and converting to an accretion rate via the equation,

$$\dot{M}_{\rm BH}(M^*, z) = \int_{-2}^{\infty} P(L_{SX}|M^*, z) \frac{(1-\epsilon-\epsilon_{kin}) k_{bol}(M^* L_{SX}) M^* L_{SX}}{\epsilon c^2} d\log L_{SX} \tag{4.13}$$

where $P(L_{SX}|M^*, z)$ is the probability distribution of specific X-ray luminosity, ϵ is the mean radiative efficiency (I set this to a nominal value of 0.1), ϵ_{kin} is the kinetic efficiency (I set this to 0.15, see, e.g., Shankar et al. 2009 and references therein), and k_{bol} is the bolometric correction. In Equation 4.13, the (specific) X-ray luminosity is defined in units of host stellar mass, hence the lower limit of integration, -2, corresponds to $L_X \sim 2 \times 10^{41}$ ergs^{-1}. For the functions P and k_{bol}, I use the definitions described in Yang et al. (2019). I then integrate in time the black hole accretion rate derived from Equation 4.13 along each $\sigma_{ap}[M^*, z]$ evolutionary track, which corresponds to a given

stellar mass growth history $M^*[z]$, to generate a corresponding $M_{\rm BH}[z, M^*]$ and thus ultimately build an $M_{\rm BH}[z]-\sigma[z]$ relation.

My result is shown in Figure 4.4 for different redshifts, as labelled. I find an $M_{\rm BH}-\sigma_{ap}$ relation that is roughly constant in both slope (which is around a value of 5) and normalization up to $z\sim 2$, and possibly decreasing in normalization only beyond this epoch, in good agreement with available observations up to $z\sim 1-2$ (e.g., Shankar et al., 2009; Salviander and Shields, 2013; Shen et al., 2015). When adopting reference values of $\epsilon = 0.1$ and $\epsilon_{\rm kin} = 0.15$ (e.g., Shankar et al., 2020b, and references therein), my predicted $M_{\rm BH}-\sigma$ relation at $z = 0$ is in the ballpark of the one calibrated in the local Universe from the available sample of supermassive black holes with dynamical mass measurements (e.g., Ferrarese and Merritt, 2000; Kormendy and Ho, 2013). I note that the local data are less dispersed in the $M_{\rm BH}-\sigma$ plane than in the $M_{\rm BH}-M^*$ one (e.g., Shankar et al., 2020b), thus pointing to the former as a stronger constraint for galaxy evolution models (e.g., Lapi et al., 2018; Li et al., 2020). The modelling of the black hole accretion tracks $M_{\rm BH}[z]$ via Equation 4.13 generates a downsizing in black hole growth, as already found by Shankar et al. (2020a), which mimics the one found here in velocity dispersion, further suggesting a close link between galaxies and their central black holes.

In more general terms, the black hole accretion rate could be written as (e.g., Aller and Richstone, 2002; Marconi et al., 2004; Shankar et al., 2004)

$$\left\langle \frac{dM_{\rm BH}}{dz} \right\rangle (M_{\rm BH}, z) = \frac{U(M_{\rm BH}, z)\lambda(M_{\rm BH}, z)M_{\rm BH}(z)}{t_{ef}} \frac{dt}{dz} \tag{4.14}$$

in terms of the duty cycle $U(M_{\rm BH}, z)$, i.e. the associated probability of a black hole of being active, and an Eddington ratio distribution $\lambda(M_{\rm BH}, z)$ which, together with the e-folding time

$$t_{ef} = \frac{\epsilon}{(1-\epsilon)} 4\times 10^8\, yr\,, \tag{4.15}$$

controls the average growth rate of a black hole at a given epoch. Equation 4.14 clearly highlights the degeneracy between duty cycle and Eddington rate in shaping black hole growth (e.g., Shankar et al., 2013a; Aversa et al., 2015b; Allevato et al., 2021). If I adopt an average duty cycle $U(M_{\rm BH}, z)$ as suggested by Aversa et al. (2015b, their Figure 7), in turn derived by continuity equation arguments and physically motivated black hole light curves, I find that in order for the black holes to remain on a non-evolving $M_{\rm BH}-\sigma$, they must steadily reduce their Eddington ratios with cosmic time, in line with a number of independent measurements and observations (e.g., Shankar et al., 2013a, and references therein).

In summary, its fundamental nature and lower inclination towards selection biases (in comparison to other scaling relations, e.g. Shankar et al. 2016) make the $M_{\rm BH}$-σ relation the ideal benchmark for statistical studies of black holes in a variety of contexts. The

$M_{\rm BH}$-σ relation should always be the one adopted to constrain the $f_{\rm vir}$ factor used in reverberation mapping studies (see e.g. Shankar et al. 2019b). The $M_{\rm BH}$-σ relation also provides more robust large-scale clustering predictions in black hole mock catalogues (Shankar et al., 2019a). Furthermore, pulsar timing array predictions of the gravitational wave background (e.g. Kramer and Champion (2013)) are strongly dependent on the normalization of the black hole scaling relations (Sesana et al., 2008; Shankar et al., 2016), but they should be based on the $M_{\rm BH}$-σ rather than on the $M_{\rm BH}$-M_* relation (see Rosado et al. 2015).

4.4 AGN Clustering as a probe of scaling relations

In this Chapter I have shown that there is strong evidence that the $M_{\rm BH}-\sigma$ is the most fundamental black hole scaling relation, and I have examined the results of my modelling to explore how the $M_{\rm BH}-\sigma$ could plausibly evolve with redshift. In the next Chapter, I will explore the idea of creating mock catalogs of AGN using appropriate scaling relations, but before this I will conclude this Chapter by exploring additional constraints on black hole scaling relations, namely by using the *clustering* of AGN. In Shankar et al. (2019a), we present a methodology that uses AGN clustering to set new and valuable *independent* constraints on the overall shape of the local black hole scaling relations. As discussed in Chapter 1, different host galaxy morphology, observational biases and selection effects all tend to result in different black hole mass–host galaxy scaling relations. To make progress, an independent constraint on these scaling relations is needed, which is obtained as follows.

Within the framework of a cold dark matter Universe, more massive host dark matter haloes appear progressively more strongly clustered, i.e., their spatial distribution shows more marked departures from an underlying random distribution (Cooray and Sheth, 2002). Galaxies and black holes residing in more massive dark matter haloes are thus naturally expected to appear more clustered. This methodology builds on this basic notion of galaxy clustering and it can be briefly outlined as follows:

At any redshift of interest z, we first create large catalogues of host dark matter haloes from the halo mass function $n(M_{\rm halo})$. To each dark matter halo we then assign a central galaxy with stellar mass given the SMHM relation (Grylls et al., 2019). To each mock galaxy we then assign a central supermassive black hole given by the Shankar et al. (2016) $M_{\rm BH}[z]-M^*[z]$ empirical relation. we also explore a model in which we bypass the $M_{\rm BH}[z]-M^*[z]$ relation assigning black holes via the $M_{\rm BH}-\sigma$ relation. The combination between black-hole and galaxy property (stellar mass or velocity dispersion), and galaxy property with host halo mass effectively predicts a $M_{\rm BH}[z]-M_{\rm halo}[z]$ relation. More massive haloes are more strongly clustered, and their (large-scale) clustering strength is encoded in the bias parameter (b). The bias parameter and how we

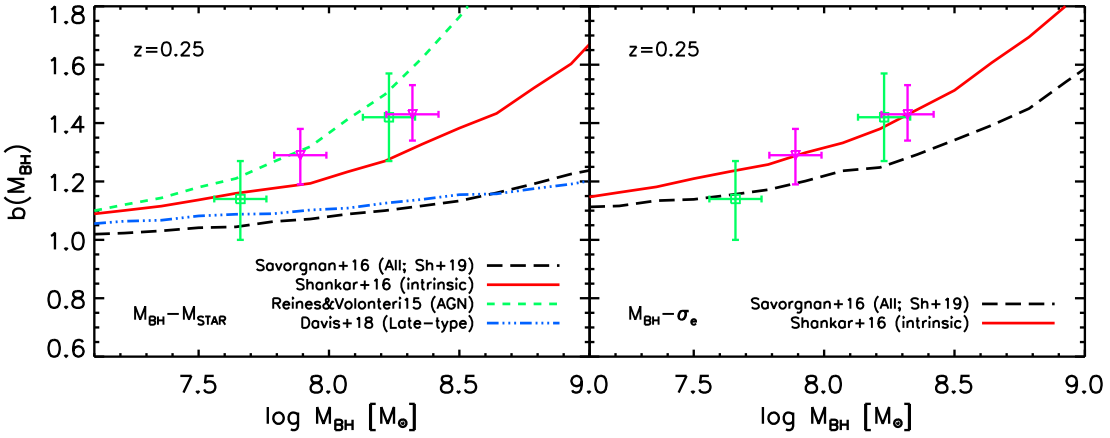

FIGURE 4.5: Predicted bias as a function of black hole mass. Left: Results for the mean large-scale clustering are shown at $z = 0.25$ for unbiased and observed (red solid and long-dashed black lines, respectively), the Reines and Volonteri (2015) (dashed green line), and the (late-type) Davis et al. (2018) (blue triple-dot-dashed line) $M_{\rm BH}$-M^* relations, as labelled. The data Krumpe et al. (2015) (green squares and purple triangles are X-ray and optical AGN, respectively) are extracted from the clustering properties of AGN identified in ROSAT and SDSS in the redshift range $0.16 < z < 0.36$. The models with the unbiased/lower normalization $M_{\rm BH}$-M^* relation are favoured by current data. Right: Similar to left hand panel, but now showing $b(M_{\rm BH})$ expected from the observed/biased (dashed) and intrinsic (solid) $M_{\rm BH}$-σ scaling relations.

calculate it is explained in appendix A.4, but I note here that this methodology does not depend on duty cycles or Eddington ratio distributions. More massive haloes are on average characterized by larger b-values. For a given input $M_{\rm BH}[z] - M^*[z]$ relation, we compute the implied $M_{\rm BH}[z] - M_{\rm halo}[z]$ relation, and finally the predicted large-scale clustering of black holes, encoded in the $b - M_{\rm BH}$ relation. The higher the normalization in the $M_{\rm BH}[z] - M_{\rm halo}[z]$ relation, the lower is the $M_{\rm halo}$ that hosts a given $M_{\rm BH}$, and so the weaker is the expected clustering strength of black holes at fixed black hole mass (and dispersion around the mean). The $M_{\rm BH}[z] - M_{\rm halo}[z]$ relation(s) that provide the closest match to the AGN clustering measurements, will set key constraints on, most noticeably, the most appropriate input $M_{\rm BH}[z] - M^*[z]$ relation.

The results are presented in Figure 4.5. The data (Krumpe et al., 2015) is represented by two green squares with error bars (same in both panels) showing the large-scale bias factors for two samples of low- and high-mass active supermassive black holes observed in X-ray band. Similarly, the two magenta triangles show the bias factor b in a low- and high-mass sample of optically-selected AGN. The inferred bias factors b appear to be rather independent of wavelength, and indeed larger for the samples with larger black hole mass $M_{\rm BH}$. The curves in the left-hand panel of 4.5 show the expected large-scale bias from my model, assuming black hole masses are assigned via the observed/biased (long-dashed black) or intrinsic/unbiased (solid red) $M_{\rm BH}$-M^* scaling relations Shankar et al. (2016). The predicted bias parameter b based on the observed/biased scaling relations is too low and is ruled out at high confidence ($\gtrsim 3\sigma$), whilst that based on the intrinsic/unbiased scaling relations provides a good match to

the data. The agreement is remarkable, given that there are no free parameters to fit. The dashed green curve shows that the Reines and Volonteri (2015) $M_{\rm BH}$-M^* scaling relation also yields a good match to the clustering measurements, implying that the AGN clustering measurements are still consistent with $M_{\rm BH}$-M^* relations that are even lower in normalization than Shankar et al.'s intrinsic relation.

It has been argued that host galaxy morphology may play a substantial role in creating the systematic offset between black hole scaling relations of active and quiescent galaxies. In fact the former active black holes could be mostly hosted in later-type galaxies, which are expected to allegedly be hosting lower black hole masses at fixed stellar mass, while the latter quiescent samples with larger black hole masses tend to inhabit earlier-type galaxies Reines and Volonteri (2015). However, the Davis et al. (2018) steep relation of dynamically-measured quiescent black holes in late-type galaxies (blue triple dot-dashed line), tends to still fall substantially below the bias data at high $M_{\rm BH}$. The latter result clearly supports the view of a bias in the observed $M_{\rm BH}$-M^* relation which is independent of galaxy morphology or AGN type. We also expect the Krumpe et al. (2015) AGN clustering measurements, based on large, serendipitous samples, to be representative of a variety of host galaxy morphologies and not just late types. We finally note that all of the data in Figure 4.5 mostly corresponds to Type 1 AGN. Observationally, Type 2/obscured AGN have been measured to cluster at a comparable or even higher level, at least at $z < 1$ (DiPompeo et al., 2016; Jiang and van den Bosch, 2016), which would further strengthen my results in favour of lower normalizations in the $M_{\rm BH}$-M^* intrinsic relation.

In summary, the low-redshift AGN clustering measurements considered here favour considerably *lower* normalizations of the $M_{\rm BH}$-M^* relation. Scalings in $M_{\rm BH}$-M^* with high normalizations such as the observed/biased one characterizing quiescent galaxies (black long-dashed line), tend to map black holes to lower stellar masses and thus to lower host halo masses, significantly decreasing the predicted clustering signal. AGN clustering thus provides additional, independent evidence for the presence of a bias in the observed $M_{\rm BH}$-M^* relation, at least for quiescent black holes with $M_{\rm BH} \gtrsim 3 \times 10^7\ M_\odot$. At lower black hole masses, AGN clustering data is not currently available and thus loses its constraining power. For example, for $M_{\rm BH} \lesssim 3 \times 10^7\ M_\odot$, AGN clustering data are not able to distinguish between the steep (late-type) relation of Davis et al. (2018) or the flatter one of Reines and Volonteri (2015). This loss in constraining power is a consequence of the fact that $b(M_{halo})$ becomes nearly constant at low masses (Sheth and Tormen, 1999).

For completeness, the right-hand panel of Figure 4.5 shows the bias parameter $b(M_{\rm BH})$ expected from the $M_{\rm BH}$-σ scaling relation. Measuring the clustering strength implied by the $M_{\rm BH}$-σ relation represents an additional independent test to the overall reliability of the black hole scaling relations. This test is also particularly valuable as it

circumvents the use of M^* by directly applying abundance matching between the velocity dispersion-based local black hole mass function and halo (plus subhalo) mass functions. Moreover, it has been claimed that the $M_{\rm BH}$-σ relation is less biased than the $M_{\rm BH}$-M^* relation, implying that the former should be closer to the "intrinsic" relation, in terms of normalization, slope, dispersion around the mean (Bernardi et al., 2007; Shankar et al., 2016, 2019b). It is thus expected that the related (large-scale) clustering properties should be less sensitive to observational biases. Indeed, when adopting reasonable scatter ($\sim$ 0.3 dex) around the mean $M_{\rm BH}$-M_{halo} relation (Shankar et al., 2010a; Aversa et al., 2015a), when adopting the observed (dashed black) and intrinsic (solid red) $M_{\rm BH}$-σ relations, in both cases we find mean b-$M_{\rm BH}$ relations broadly consistent with the data, with the former only slightly disfavoured at the highest black hole masses.

In summary, I have shown in this section how clustering can be used to place strong constraints on black hole scaling relations. With this tool at my disposal, I can explore the creation of mock catalogs, which I will discuss in the next Chapter.

Chapter 5

Wider Applications: Mock Catalogs

In this Chapter, I will present two further applications of the techniques used in this work. The first is in the development of AGN mock catalogs, the second is the real-time visualization of mock catalogs through my cosmological visualization tool Astera. The background for these applications is discussed in Chapter 1, but the motivation will be briefly discussed here.

The European Space Agency's 'Euclid' space telescope is scheduled for launch in 2020, and will capture images and SEDs for millions of galaxies. Although Euclid's primary aim is an accurate investigation of Dark Energy, the data will be of truly paramount importance to numerous other sub-fields within Astronomy. Vital to the preparation behind the processing of this data will be the development of mock datasets that match the complexity of the real data; this is required mainly for testing and calibration of the pipelines prepared to process the vast amount of data that Euclid will generate. Recently a team of scientists within the Euclid Consortium have worked to produce the largest simulated galaxy catalogue yet produced, the so-called 'Flagship' Mock. The underlying merger trees are based on a 2^{12} particle dark matter simulation (run at the Swiss National Supercomputing Center), the largest to date (Potter et al., 2017). Atop this, the full galaxy catalogue is being constructed using halo occupation and abundance matching techniques. Notably absent from the current catalogue are SMBHs and AGN; the author and several collaborators have been working with the Galaxy Mock Production Work Package Team to add AGN and SMBHs into the flagship mock, using the semi-analytic and semi-empirical techniques discussed in this work. Adding SMBHs/AGN into an existing galaxy catalogue has not been done before, and a tool would be required that can be applied to any catalogue, and construct several SMBH/AGN properties and observables.

As mentioned in the previous Chapters, building reliable mock catalogues of galaxies and supermassive black holes is a vital exercise not only to provide robust predictions for the next-generation of extra-galactic missions such as Euclid, but equally important

for educational and outreach purposes, to create visible and realistic Universes that can be accessed by the general public and inspire the next-generation of scientists. For this purpose in this Chapter I will discuss my 3D interactive rendition of the Universe "Astera" which is built adopting the same semi-empirical routines described in the next sections.

5.1 How to build realistic AGN mocks?

In this section, I seek to answer the questions: can one create mock catalogs of AGN by using semi-empirical relations, starting from samples of dark matter halos from large N-body simulations, to test the effect of different input model parameters? Given this, can one reveal the right observables that one should focus on to break degeneracies in the input model parameters, providing a complete framework to build a robust and realistic AGN mock catalog? In Allevato et al. (2021) we showed how observables depend on the input model parameters (Figure 5.1) and how to build step-by-step robust mock catalogs of AGN that minimize the danger of inner degeneracies and include knowledge of the underlying black hole mass and Eddington ratio distributions (Figure 5.2). I will present the outcomes of this work in this section.

The first observable we considered was the specific accretion-rate distribution P_{AGN}, defined as the convolution of the input AGN duty cycle U and specific Eddington ratio distribution $P(\lambda)$:

$$P_{AGN}(\lambda \propto L_X/M^*) = \int_{log\lambda_{min}} P(\lambda \propto L_X/M^*)U(M^*)dlog(\lambda) \tag{5.1}$$

where $\lambda \propto L_X/M^*$ describes the rate of accretion relative to the stellar mass of the host galaxy. P_{AGN} describes the probability of a galaxy hosting an AGN of a given L_X/M^* at a specific redshift[1]. The P_{AGN} distribution has been intensively studied in the last decade, mostly in X-ray selected AGN samples (e.g. Bongiorno et al., 2016; Aird et al., 2017, 2018; Georgakakis et al., 2017) and it has been extensively used as the main key observable to generate data-driven AGN mock catalogs (e.g. Comparat et al., 2019; Aird and Coil, 2020). However, when using models uniquely tuned on the measured P_{AGN}, we miss info on individual input parameters, such as the AGN duty cycle U, the Eddington ratio distribution and the BH mass – stellar mass relation. We showed that for a fixed $M^* - M_{BH}$ relation, widely different combinations of U and $P(\lambda)$ can provide very similar specific accretion-rate distributions and AGN XLFs consistent with the data. Additionally, any specific accretion-rate distribution P_{AGN} that reproduces the AGN XLF does not affect the AGN large-scale bias at a given stellar mass, an observable which is usually adopted as a "success" feature of a given model.

[1]Note that this convolution also appears in equation 4.13

Thus the P_{AGN} distribution and the AGN XLF are not suited to constrain the input model parameters when used in isolation.

We explicitly considered the AGN duty cycle, $P(\lambda)$ and the BH mass–stellar mass relation as distinct input model parameters, which we tested against several independent observables, including the large-scale bias as a function of stellar/BH mass and X-ray luminosity. In particular, we found that the comparison of observationally derived P_{AGN} with the predictions of AGN mock catalogs are in better agreement with models that assume an input BH mass–stellar mass relation lower in normalization with respect to what is usually inferred in the local Universe from early-type galaxies with dynamically measured BHs. My mock also prefers AGN duty cycle decreasing with BH mass (Schulze and Wisotzki, 2010), consistent with what is also derived from continuity equation arguments (e.g. Shankar et al., 2013b). The agreement with the data, and in particular with the measured P_{AGN} function, further improves when the input Eddington ratio $P(\lambda)$ includes a long tail of high Eddington ratio values, as for example in a broad Gaussian or in a double power law distribution (e.g. Yang et al., 2019). It is worth noticing that, when considered in isolation, the P_{AGN} distribution can be also reproduced, at least at lower luminosities/stellar masses ($\log\lambda \leq 33$), by using in input the *raw* BH mass–stellar mass relation and a duty cycle that increases or is constant with the BH/stellar mass (for both a Gaussian or a Schechter $P(\lambda)$). This degeneracy can be broken by testing the model against additional independent observable, most notably the AGN large-scale clustering.

The second key observable to consider is indeed the AGN large-scale bias as a function of both stellar mass and BH mass, which is not affected by the input AGN duty cycle and $P(\lambda)$. As shown in Shankar et al. (2020b), the AGN large-scale bias as a function of BH mass can in fact effectively be used to put constraints on the BH mass–stellar mass relation and the parameter Q, the ratio of satellite to central active galaxies/BHs. In Chapter 4 (originally presented in Shankar et al., 2020b) we found that the observed bias of AGN at $z = 0.25$ (Krumpe et al., 2015) can be reproduced by assuming a *debiased*[2] $M_{BH} - M^*$ relation and $Q \leq 2$, which corresponds to satellite AGN fractions $f_{sat}^{AGN} \leq 0.15$. A similar value ($f_{sat}^{AGN} \sim 0.18$) has been suggested by Leauthaud et al. (2015) for COSMOS AGN at $z < 1$. Allevato et al. (2012) performed a direct measurement of the HOD for COSMOS AGN based on the mass function of galaxy groups hosting AGN and found that the duty cycle of satellite AGN is comparable or even larger than that of central AGN, i.e. $Q \geq 1$. A very low value of the Q parameter would be in line with quasars hosted in central galaxies that more frequently undergo mergers with other galaxies (Hopkins et al., 2008). On the other hand, a relatively high value of Q would suggest that other triggering mechanisms other than mergers, such as secular processes and bar instabilities, are equally, or even more efficient, in producing luminous AGN (e.g. Georgakakis et al., 2009; Allevato et al., 2011; Gatti et al., 2016).

[2]I define 'raw' and 'debiased' relations in section 1.2.5

We find that a model with an input *debiased* $M_{\rm BH} - M^*$ relation and $Q \leq 2$ would better match the large-scale bias as a function of the BH mass of X-ray AGN at z < 0.1 (Powell et al., 2018), further extending the results of Shankar et al. (2020b) even at lower redshifts[3]. Additionally, the same model is in better agreement with observationally inferred $\rm P_{AGN}$ distributions. This model also assumes: (i) A stellar mass – halo mass relation as derived in Grylls et al. (2019), which reproduces the most recent estimates of the local galaxy stellar mass function by Bernardi et al. (2017), the large-scale clustering in stellar mass bins of SDSS AGN (Zhang et al., 2020) and galaxies (Domínguez Sánchez et al., 2018b) (ii) A parameter $Q \leq 2$ as suggested by observations of the AGN satellite fraction at low z (e.g. Allevato et al., 2012; Leauthaud et al., 2015). A *raw* $M^* - M_{\rm BH}$ relation with an increasing or constant duty cycle as a function of the stellar mass would instead require high Q values (> 2) and/or an input stellar mass – halo mass relation as derived by Moster et al. (2013). More importantly, the latter model is inconsistent with the large-scale bias versus X-ray luminosity inferred for X-ray AGN at similar redshift (e.g. Krumpe et al., 2018; Powell et al., 2018), independently of the choice of the input P(λ) distribution.

The large-scale AGN bias as a function of X-ray luminosity thus represents an additional crucial and powerful diagnostic to constrain the viable models, being in fact strongly dependent on the input AGN duty cycle, but weakly dependent on the input stellar mass - halo mass relation of the P(λ) distribution. Measurements of the bias dependence on L_X for X-ray selected AGN at z ≤ 0.1 (e.g. Krumpe et al., 2018; Powell et al., 2018) can be reproduced by models assuming (i) an input decreasing duty cycle with the BH mass (Schulze and Wisotzki, 2010), and a *debiased* $M^* - M_{\rm BH}$ relation with $Q \leq 2$; (ii) or a *raw* relation with $Q > 2$ (for both a Schechter or Gaussian P(λ)). However in the latter case, the corresponding specific accretion-rate distribution $\rm P_{AGN}$ would be almost one order of magnitude higher than observations. As discussed in the previous section, the combination of all the observables, namely the AGN XLF, the $\rm P_{AGN}$ distribution, the AGN large-scale bias as a function of stellar/BH mass and L_X can break the degeneracy in the input model parameters and ensure the creation of realistic AGN mock catalogs.

Given this, we know that models of mock AGN with *any* $M^* - M_{\rm BH}$ relation and a chosen specific accretion-rate distribution $\rm P_{AGN}$ (obtained as convolution of the input P(λ) with the AGN duty cycle U) can create mock AGN matching the observed AGN XLF. In addition, the corresponding large-scale bias at a given stellar mass of mock AGN is independent of $\rm P_{AGN}$ and the $M^* - M_{\rm BH}$ relation, simply because the bias only depends on the parameter Q (ratio of duty cycles between black holes hosted in satellite and central galaxies) and the input $M^* - M_h$ relation. Thus, having characterised a given $\rm P_{AGN}$ that, by design, observationally fits the AGN XLF, is not a guarantee for a

[3]Specifically, Figure 7 (right panels) of Allevato et al. (2021) proves this, and is further confirmed by Shankar et al. (2020b) at $z = 0.55$ and Viitanen et al. (2021) at z=1.2.

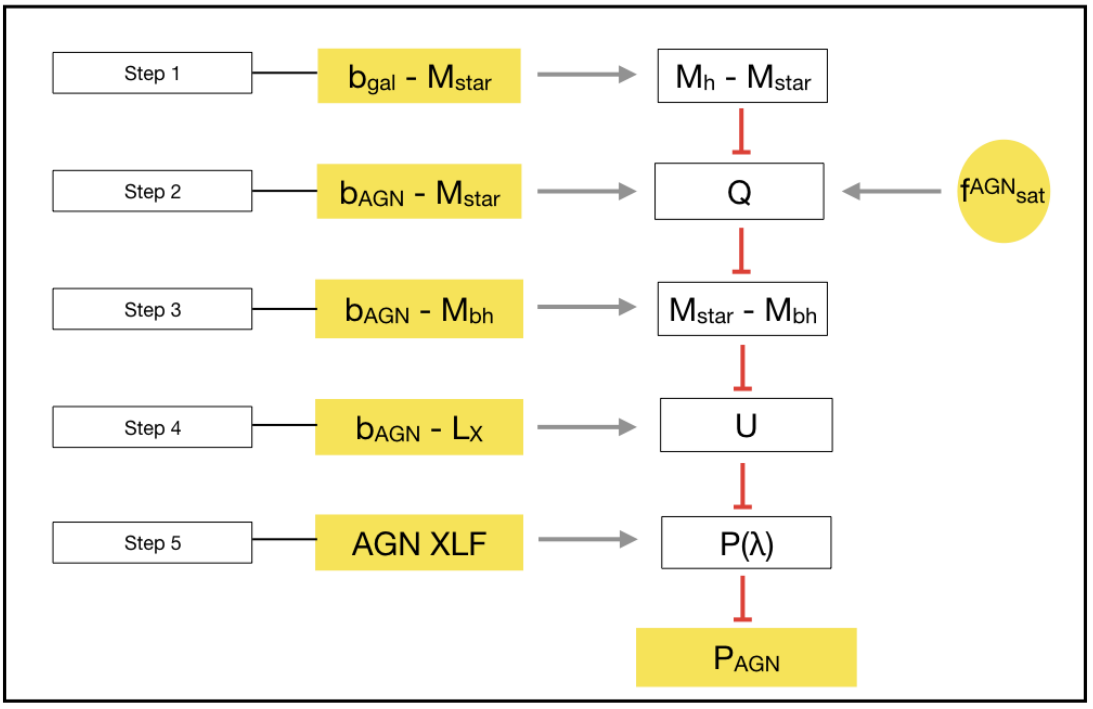

FIGURE 5.1: Sketch of how to build realistic AGN mocks. Full yellow boxes refer to the observables considered in this work (b_x represents the bias of property x. M_{star}, M_{bh}, L_X and AGN XLF represent the stellar mass, black hole mass, X-ray luminosity and AGN X-ray luminosity function respectively). The dependence of each observable on one or few input model parameters (empty boxes) is shown as red lines (M_h represents the halo mass, Q is the Q-parameter, U is the duty cycle and $P(\lambda)$ represents the distribution of λ, as explained in the text.). From the comparison of observationally derived relations and the AGN mock catalog predictions we can constrain (grey row) the input parameters. Additional observables, such as the fraction of satellite AGN (full yellow circle) can help in breaking the degeneracies among the input model parameters.

unique and valid model to create AGN mocks even when we consider the clustering at fixed stellar mass, simply because the latter is not affected by the P_{AGN} distribution and the stellar-BH mass relation.

These results imply a strong degeneracy among the input parameters used to create mock catalogs of AGN. Only considering all the observables, in particular the AGN large-scale bias as a function of BH mass and as a function of X-ray luminosity we can break the degeneracy in the input model parameters. In the following, we provide the different steps to create a robust and realist mock catalog of AGN. As sketched in Figure 5.1, the stellar - halo mass relation and the Q parameter can be constrained by combining the large-scale clustering as a function of stellar mass for both galaxies and AGN. In particular, my results suggest a model with an input $M^* - M_{halo}$ relation as described in Grylls et al. (2019) and $Q \leq 2$ (Figure 5.1, first two rows). At fixed input stellar - halo mass relation and Q, the AGN large-scale bias as a function of the

	Input Parameter				
Observable	P(λ)	U	M_{star} - M_h	M_{star} - M_{bh}	Q
AGN XLF	✓	✓	✓	✓	
P_{AGN}	✓	✓	✓	✓	
b_{gal} - M_{star}			✓		
b_{AGN} - M_{star}			✓		✓
b_{AGN} - M_{bh}			✓	✓	✓
b_{AGN} - L_X	✓	✓		✓	✓
f_{AGNsat}					✓

FIGURE 5.2: Dependence of the observables on the input model parameters.

BH mass can be used to derive the input $M^* - M_{BH}$ relation. As already discussed in Chapter 4 (originally in Shankar et al. 2020b) we found that a model with an input *debiased* $M^* - M_{BH}$ relation (with $Q \leq 2$) provides a better match to the bias estimates as a function of the BH mass of X-ray selected AGN (third row). Observational constraints on the AGN duty cycle can then be derived from the comparison of the model predictions with the measured AGN large-scale bias as a function of the luminosity (fourth row). A model with an input *debiased* $M^* - M_{BH}$ relation, $Q \leq 2$ and a duty cycle that decreases with BH mass is able to reproduce the AGN bias as a function of L_X, for both a Gaussian or Schechter P(λ). Finally, fixing the stellar - halo mass relation (Grylls et al., 2019), the *debiased* $M^* - M_{BH}$ relation, $Q \leq 2$ and a duty cycle that decreases with BH mass, the combination of the AGN XLF and the specific accretion-rate distribution P_{AGN} will allow us to derive the free parameters of the input Eddington ratio distribution, independently of the choice of a Gaussian or Schechter shape of $P(\lambda)$ (final row).

Estimates of the fraction of active satellites in groups and clusters at the redshift of interest (e.g. Allevato et al., 2012; Leauthaud et al., 2015) can further help to independently constrain the Q parameter. Additional observables can be considered, such as the average L_X-SFR/M^* relation that mostly depends on P(λ) and on the M^*-M_{BH} relation (Carraro et al., submitted). This work thus reveals the right observables that we should focus on to break degeneracies in the model input parameters and provide the steps to have a complete framework to build a robust and realistic AGN mock that is consistent with many different observables, is physically based, born out of the scaling relation between galaxies and dark matter halos.

5.2 Astera

In this section I seek to answer the following questions: Is it possible to digitally render, in *real time*, a large cosmological volume, given the performance constraints of real time rendering? Can such a rendering be set up to reveal the large scale structure of the universe in a user accessable way? My answer to these questions is 'Astera', my cosmological visualization tool. I will discuss Astera as follows: In section 5.2.1 I discuss the 'assets' required for this task, which pertains to the creation of the underlying example galaxy catalogue that forms the theoretical foundation of Astera, and the astronomical images used to represent galaxies. This is followed (Section 5.2.2) by a description of the technical implementation of Astera itself within Unreal Engine 4. In Section 5.2.3 I present the 'results' of this work, namely the 3D universe that Astera creates.

5.2.1 Assets

Assets, as mentioned previously, are the reusable and replaceable components of a digital project. It is worth emphasizing that these components are able to be changed with a minimum of effort, so although integral parts of the experience they are not fixed parts of the software. This includes the underlying galaxy catalogue, and the astronomical images used to represent galaxies.

5.2.1.1 Galaxy Catalog

In the case of Astera, I am interested in (at least initially) creating a catalogue that can be "explored" by the user in real time, imitating non-physical superluminal speeds (or a universe "frozen" with no relative motions of galaxies, no cosmological expansion, etc). Therefore, the creation of a light cone is not necessary, and a simple cosmological volume will suffice. It should be noted that Astera itself is Cosmology independent, as it simply presents coordinates and galaxy imagery. In this section, I describe a very simple "recipe" that produces what the authors consider to be a reasonable mock catalogue for showcasing Astera using the techniques described in this thesis, but in principle any catalogue could be used.

As appropriate for the ΛCDM paradigm, the foundation of my catalogue is a Dark Matter N-Body simulation. I use both the Bolshoi Klypin et al. (2011b) $(500h^{-1}Mpc)^3$ and the Multi-Dark (Klypin et al., 2016) $(1000h^{-1}Mpc)^3$ simulation catalogues, depending on the volume desired (as larger volumes require more powerful hardware, although it should be noted that volumes can also be ''cropped" to manage performance). The most important variables in this catalogue are naturally the 3D coordinates (x, y, z), as they dictate the 3D positions of the haloes in the virtual world, but also vitally important are the virial masses of the haloes, upon which I use statistical ''empirical"

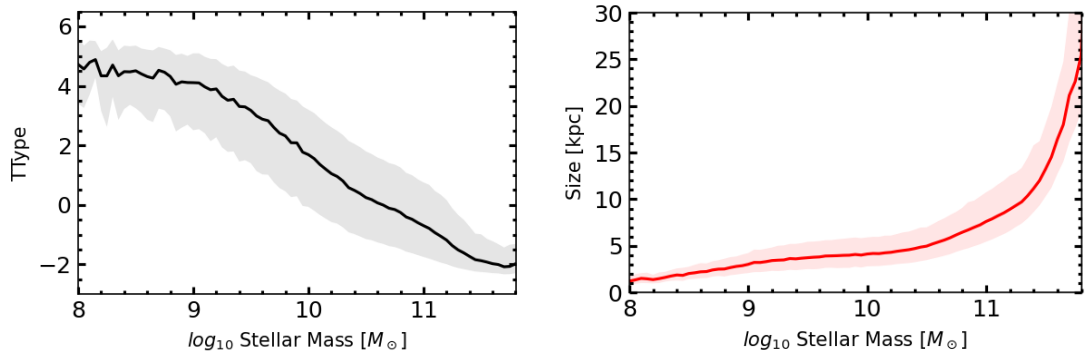

(A) TType (B) Size

FIGURE 5.3: (a) Morphological type (TType) and (b) Size vs Stellar Mass relations within the SDSS, used to assign the respective parameters to the catalogue. The shaded regions show the 1σ uncertainty in these parameters.

relations to construct my model. I therefore assume that a galaxy exists at the centre of every dark matter halo resolved within the catalogue, and assign the stellar mass.

Assigning stellar mass allows for a robust foundation upon which further properties can be built. Aside from 3D distribution, the most obvious property required for a visually realistic galaxy catalogue is obviously morphological classification. This was assigned using phenomenological relations derived from the Sloan Digital Sky Survey (SDSS) data Blanton et al. (2017). Binning the SDSS by stellar mass allows for an approximate Stellar Mass-morphological type (TType) relation (see Figure 5.3 (a)). In short, the catalogue of galaxies is binned in appropriately sized bins of stellar mass, and the mean TType and scatter for each bin are recorded, producing an (average) relation allowing transformation from stellar mass to TType. With the associated scatter, this relation can be applied to the simulation catalogue for a statistically comparable distribution of morphological types to the real universe. Each galaxy is therefore assigned a TType representing its morphological classification based on its stellar mass. A caveat here is that this distribution is only valid at low redshifts, limiting this technique to catalogues representing the universe in the "present day". This limitation is not insurmountable, as numerous semi-analytic models and semi-empirical models are capable of predicting morphological abundances at varying redshifts, and their datasets could be easily be used in Astera.

A galaxy's physical size (parametrised by the effective radius R_{eff}) is also naturally important for visual realism. These were assigned in identical fashion to morphological types, using the mean relations from the SDSS (again see Figure 5.3 (b)).

A simple validation to show that these components are "working together" as expected is shown in Figure 5.4, where I show the average predicted 3D mass density profile for elliptical galaxies of stellar mass $11.3 < \log_{10} M^*/M_\odot < 11.7$. Each elliptical galaxy in this mass range is additionally assigned a Sérsic index (again according to the mean

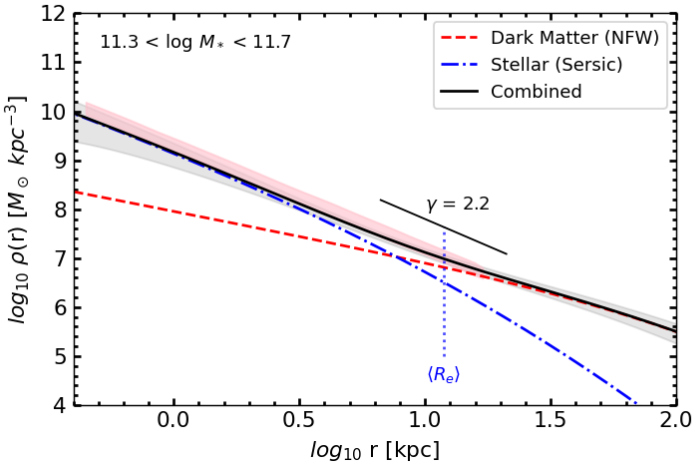

FIGURE 5.4: Predicted (average) 3D density profile haloes hosting elliptical galaxies of mass $11.3 < \log_{10} M^*/M_\odot < 11.7$ for the sample catalogue. The solid black line represents the combined density, whilst the blue (dot-dashed) and red (dashed) lines represents the average stellar (Sérsic) and dark matter (NFW) components, respectively. The pink shaded region represents the empirical fit from Cappellari et al. (2015). The grey shaded region shows the 1σ dispersion of the total density. The vertical blue dotted line shows the average half light radius, and the solid short black line shows (for comparison) the established slope of $\gamma = 2.2$ at this radius.

relation in the SDSS), a de-projected stellar mass density profile according to the prescription of Prugniel and Simien (1997), and an NFW profile (Navarro et al., 1996) with halo concentrations according to the model of Diemer and Joyce (2019). Finally, the average mass density per bin of radius is calculated for the sample. This result is compared to the pure power law model of Cappellari et al. (2015) $\rho(r) \propto r^{-\gamma}$, where $\gamma = 2.2$ at $r \sim R_e$, derived from 2D stellar kinematics and strong lensing measurements. Specifically, Cappellari et al. (2015) inferred that $\langle\gamma\rangle = 2.19 \pm 0.03$, valid in the range $0.1Re$ to $4Re$ and $10.2 < \log_{10} M^*/M_\odot < 11.7$. This result is shown as the pink stripe in Figure 5.4, showing good agreement with the model at $\langle R_e \rangle$. The slopes at low radii were found to be very sensitive to the definition of R_e, in this case showing a slight divergence from the data.

Finally, active galaxies were also considered. The central supermassive black hole mass was assigned from the stellar mass using the 'de-bias' relation from Shankar et al. (2016), with appropriate Eddington ratios and X-Ray luminosity assigned using a Schechter function with values chosen to fit the known X-Ray luminosity function and Eddington ratio distribution. The "Duty Cycle" U or associated probability of a Supermassive Black Hole being active, was for now set to $U \sim 0.1$. We note that this methodology is somewhat simplified compared to the description at the start of this Chapter, due to the different timeframes for these projects.

5.2.1.2 Galaxy Imagery

An obviously vital part of Astera is the galaxies. I elected to use actual astronomical imagery. For now, I discuss the images themselves. Getting both good quality and a large variation in galaxy images will contribute greatly to the user experience, so various approaches were considered. There are relatively few high resolution images from the Hubble Space Telescope (HST), but much more diverse but lower resolution images from the Sloan Digital Sky Survey (SDSS), which may be more appropriate. Further work was also put into investigating the feasibility of creating my own artificial images based on a relatively small number of starting parameters; this is known as "procedural generation". This has been done before using Neural Networks and Hydrodynamical simulations (Nguyen et al., 2016), but a considerably simpler (at least initially) approach was desired here. I therefore focused on acquiring actual astronomical imagery.

The actual astronomical imagery from the SDSS is available on their website[4]. Properly identifying likely target galaxies is challenging. A list of targets, identified by Meert et al. (2014), was processed into a list of likely candidates. The most promising targets had a large angular diameter, allowing the most high quality galaxies to be quickly identified. Creating a visually appealing astronomical image from the data acquired in the appropriate bands is a somewhat subjective process. Of vital importance is the "stretch function" applied to the data, which applies a mathematical transformation to the pixel values to (ideally) enhance brighter areas and saturate darker areas, eliminating noise. In this project, the stretch function was applied using the "FITS Liberator" Christense et al. (2019) software, which offers a GUI to allow the user to select and tweak the stretch function parameters on the fly. The FITS Liberator can also export the image into the GIMP (The GIMP Development Team, 1996) image manipulation software as Red, Green and Blue (RGB) components, creating the image. Some additional tweaking was required at this point. Background stars and galaxies have to be carefully erased (GIMP offers many tools to do this, the best of which are actually designed to interpolate out blemishes from images of human skin, but equally applicable to "blemishes" in the sky), and cubic interpolation to re-scale all the images to the same size.

Finally, one of the most important steps is the construction of an "alpha" channel. This image layer contains values that dictate the transparency of the corresponding pixel in the image; an alpha value of one would signify a fully opaque pixel, whereas an alpha value of zero would be fully transparent. Setting this up properly is vital for Astera, as the transparency is the property that will "soften" a geometric mesh into a believable diffuse galaxy. The alpha channel was assigned in this case using the sum of the RGB

[4] http://skyserver.sdss.org/

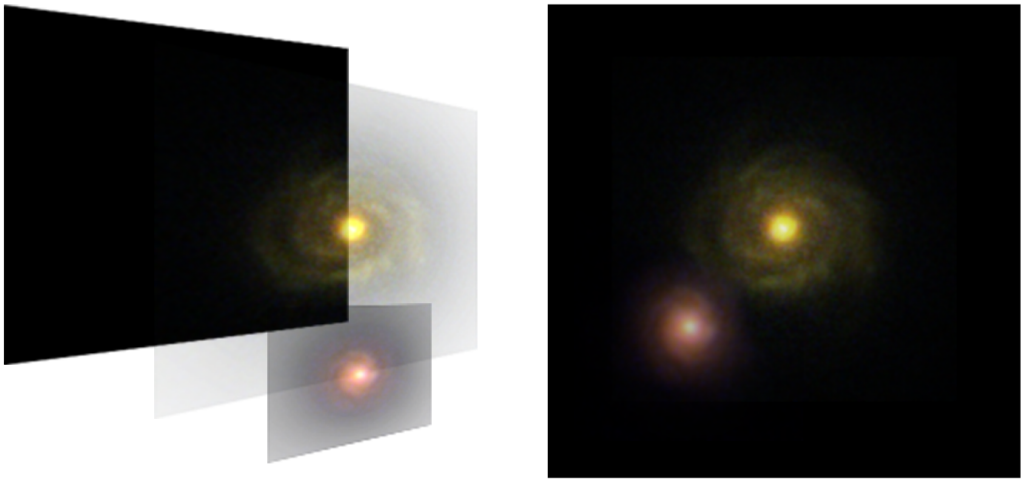

FIGURE 5.5: Example depiction of the importance of the alpha channel. When projected onto each other, the alpha channel allows the galaxies to appear as diffuse objects, hiding the sharp edges.

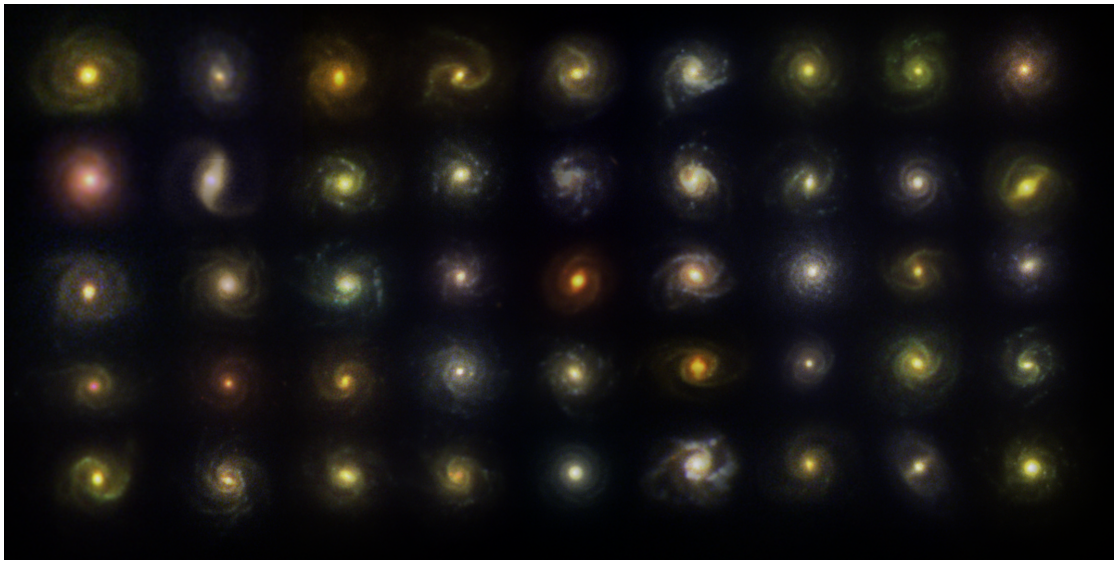

FIGURE 5.6: Composite images of 45 spiral galaxies extracted from the SDSS, processed to be visually pleasing.

layers, appropriately normalized "by eye" to appear visually realistic. The importance of this channel is demonstrated in Figure 5.5.

Using this method, a few hundred distinct galaxies were extracted and processed from the SDSS dataset. Some examples are shown in Figure 5.6. While these galaxies are not as high resolution as HST images, their diversity allows for a wide range of galaxy types and morphological classifications. The Stellar Mass and Morphological types of each galaxy was also recorded for later use.

5.2.2 Unreal Engine

The Unreal Engine is a game creation engine. Technically, a complete suite of creation tools, Unreal is best known as a package containing a rendering engine, sound engine, physics engine, gameplay framework, animation, artificial intelligence, networking, memory management and parallel processing support. These reusable software components act like a vast library of tools that can be utilized by the game developer to assemble their game. Strictly speaking, references to Unreal Engine in this thesis indicate Unreal Engine 4 (sometimes referred to as "UE4"), the fourth release of the software. Unreal Engine 4 significantly overhauled many of the features of Unreal Engine 3 when it was released in 2014, so many of the tools and features discussed and utilized as part of this project may not be available in earlier versions of the software. Unreal is freely available for non-commercial use.

There are various possible approaches to render galaxies in the Unreal Engine. It is possible to render galaxies in real time as a system of diffuse particles. These systems are often both computationally expensive and visually unrealistic, so a different approach was considered in the development of Astera. Because each galaxy will be relatively small on the scales that I are interested in viewing, a single geometric object with an applied material (sampling a texture based on actual astronomical imagery) will suffice, and free up resources to show a greater quantity of galaxies in the game world.

This is done as follows. Spiral galaxies are generally disc-shaped, and ellipticals are vaguely spherical. Although it is possible to construct 3D versions of these shapes, a more geometrically complex shape is both more expensive to render in bulk and harder to properly configure with a material. galaxies are diffuse objects, but a simple approximation allows for a "Static Mesh" object that defines the geometric shape of the galaxy to be used as a visual proxy. A static mesh will have a "material" applied to it, which can contain colours and textures (in this case, the galaxy image), but also a large amount of additional complexity (such as transparency or varying textures in time, used for AGN activity). Based on this, every galaxy in Astera is based on a simple two polygon plane to keep the geometry simple (see Figure 5.7, with additional "work" being done by the material applied to it). As the galaxies will be kept relatively small with respect to the camera, this should not be problematic.

This is a fair approximation for spiral galaxies. On the other hand, elliptical galaxies are spheroids, so must be represented differently. The obvious choice would, therefore, be a spheroidal mesh. However, this does not correctly represent the diffuse nature of an elliptical. A far more realistic choice requires some visual trickery; if the elliptical mesh always appears "face on", then a moving camera will always perceive the object as a diffuse sphere. This requires all elliptical galaxies to (for now) be essentially spherical, but this is an acceptable limitation. It may be possible in the future to dynamically

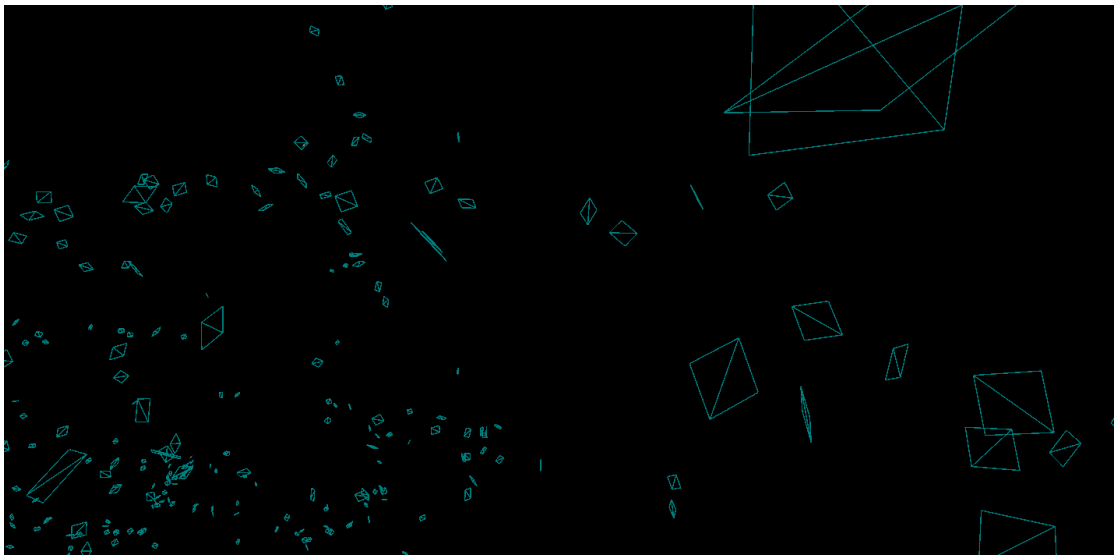

FIGURE 5.7: A wireframe view of a small area with Astera. The instanced static mesh objects used in Astera to represent galaxies can be seen.

change the scaling of the mesh to a greater extent on one axis based on the camera's position, thereby enabling more irregular ellipticals. Lenticular galaxies are problematic (as they require a combination of these effects) and are therefore structurally treated as spirals. Unreal Engine's material system is powerful enough to allow this modification to take place within the material itself.

Rendering a large number of objects inevitably leads to a performance penalty. It should be noted at this point that performance in real time rendering, although measurable in many ways, is generally parametrised using "Frames Per Second" (FPS), a number representing the mean number of updates to the screen per second (higher is better). Values between 30–60 FPS are generally considered acceptable. Naturally, a more complex scene requires more computational resources, and may therefore result in a lower FPS.

Extraordinary care must be therefore taken when rendering large numbers of distinct mesh objects in Unreal. The best approach in this case requires careful thought. Graphical Processing Units (GPUs) are very efficient at drawing polygons, but need to be "fed" these data by the (comparatively slow) CPU. Whenever a new object is "drawn" to the screen, it requires a separate CPU call (going through the graphics driver). An alternative is to combine these objects into a single mesh; requiring only one draw call. The only disadvantage to this approach is it requires all objects to have the same material and textures. As the galaxies are "duplicated" anyway, this is not a problem; I simply create one object per available galaxy image asset. Although there are more draw calls, the overall number of CPU calls is still significantly lower (hundreds as opposed to millions), so the performance is still excellent. A mesh created in this way is called an "instanced" static mesh (ISM), and is the technology that makes a universe as large as Astera's possible.

Based on this technology, spawning the objects takes place as follows (this process is implemented in C++, using Unreal Engine's Application Programming Interface). For each galaxy image extracted for the SDSS, a parent unreal actor (with no mesh of its own) is spawned and the image and the properties of the imaged galaxy are assigned to it. Next, each galaxy in the catalogue is assigned to the object with its "nearest" properties in TType-Stellar Mass space. Practically, this means that the galaxy is assigned to the object that minimizes A in the following relation:

$$A^2 = \alpha \Delta T_{type}^2 + \beta \Delta M_*^2 \tag{5.2}$$

where ΔT_{type} is the difference in TType between the galaxy and the object, ΔM^* is the difference in stellar mass. The constants α and β are adjustable normalization factors to ensure the relative weighting is appropriate. If ΔM_* was in units of $\log_{10} M_\odot$, then $\alpha = \beta = 1$ was found to be a reasonable choice. The end result is that there will, of course, be many duplicates; individually assigning unique galaxy images to every galaxy in the catalogue is computationally unfeasible, and the aforementioned ISM technology requires duplicates. The aim here is to have a sufficient number of unique galaxies so that duplicates are not noticeable to the user, but sufficiently few to preserve performance. An appropriate compromise was a few hundred unique galaxy images, compared to the millions of galaxies in the catalogue.

Next, each object spawns its galaxies, each represented by a mesh with its galaxy image applied as a material. Spiral galaxies are assigned random orientations. At this point, different features can be activated, such as the technology to make the mesh follow the camera, approximating an elliptical. All galaxies have the capability to be AGN, where a central oscillating bright source was added with an active period equal to its duty cycle. The light curve of an AGN is not yet well constrained—e.g., in (Hopkins and Hernquist, 2009)—so the shape of the curve is approximated by the peak of a sine wave to give smooth variation in brightness. Naturally the period of this oscillation requires some level of approximation as to the ''rate of time" at which the user perceives the universe, but keeping this period reasonably long ($\sim$ 60 seconds) presented a visually pleasing result. Note that this is not entirely realistic, as on the timescales of AGN phases galaxies will themselves have moved and evolved. This is not something that Astera (yet) considers.

5.2.3 Results

Screenshots from Astera are shown in Figures 5.8, 5.9, 5.10, 5.11 and 5.12. Note that, in these images, galaxy brightness has been enhanced to improve visual clarity. Nonetheless, the experience Astera offers is hard to communicate in a document such as this. I

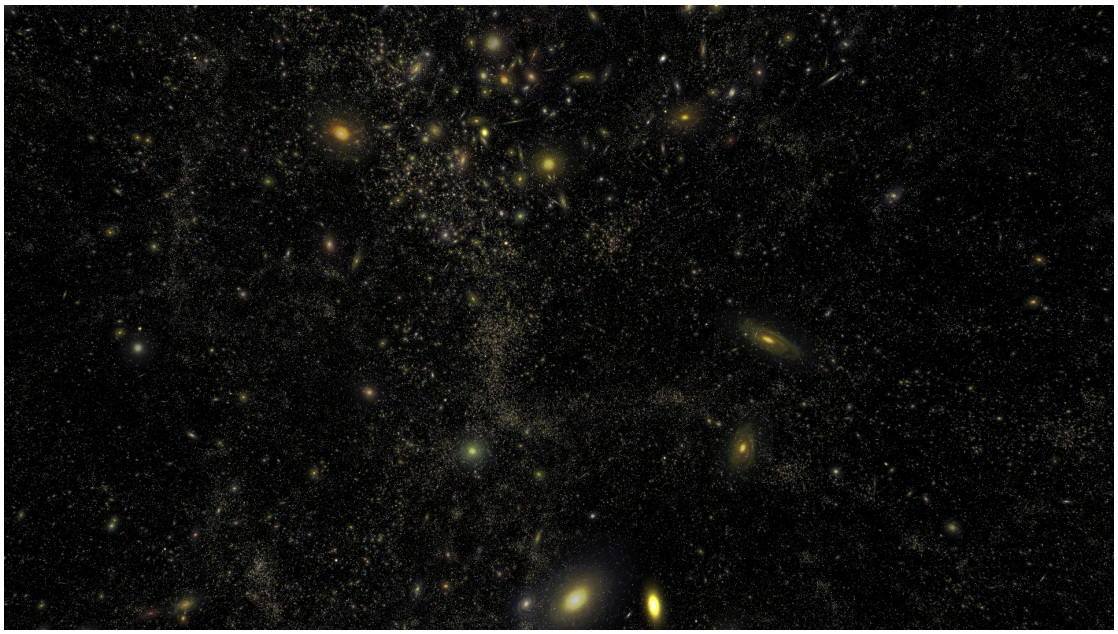

FIGURE 5.8: A screenshot from Astera, showing some nearby galaxies in the foreground and a dense cluster/filament in the background.

strongly encourage the reader to watch the video available at https://astera.soton.ac.uk/AsteraVid.mp4[5], to get a full experience of what Astera can offer.

Astera is capable of displaying the entire galaxy catalogue with volume (1000 h^{-1} Mpc)^3 at 60 FPS (on a NVidia Titan GPU), with each galaxy represented by a static mesh containing a galaxy image, effectively creating a ''universe" for the user to explore. The player has control of the camera facing, position and movement in real time. The finite nature of the catalogue means that a user can exit the cube and view it from the ''outside" (see Figure 5.12).

Astera has also received preliminary adaption for Virtual Reality using the Unreal Engine virtual reality tools, which ports Astera from projected 2D to simulated 3D when viewed through a VR headset. This is an entirely visual effect, but allows for some level of binocular vision, enabling the 3D large scale structure of the universe to be experienced in binocular 3D for the first time.

5.2.4 Discussion

This project's objective was to create a visualization of a mock galaxy catalogue, rendered in real time. This would one of the first attempts to execute a fully realized real time rendering of the large scale universe. To power this project, the Unreal Engine 4 game engine was selected. A framework was constructed using C++ to read the

[5]Due to the difficulty video streaming compression algorithms have with many small moving objects, it is recommended the reader download this video and play it locally.

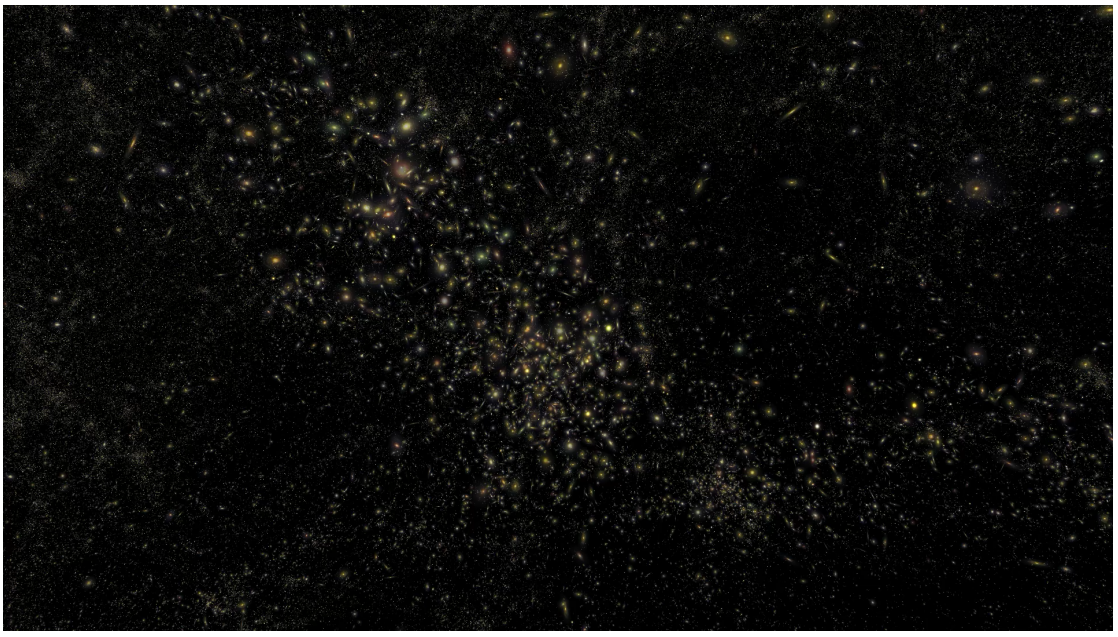

FIGURE 5.9: A screenshot of Astera showing a relatively dense region. The structure of the cosmic web is just visible.

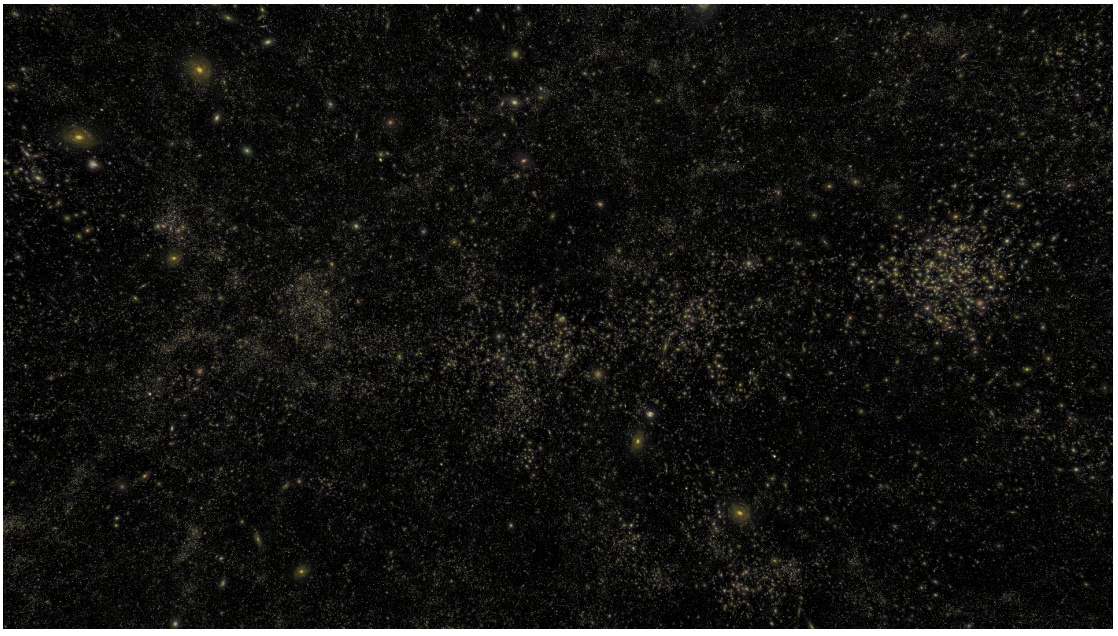

FIGURE 5.10: A screenshot showing a distant view of four clusters joined by a filament.

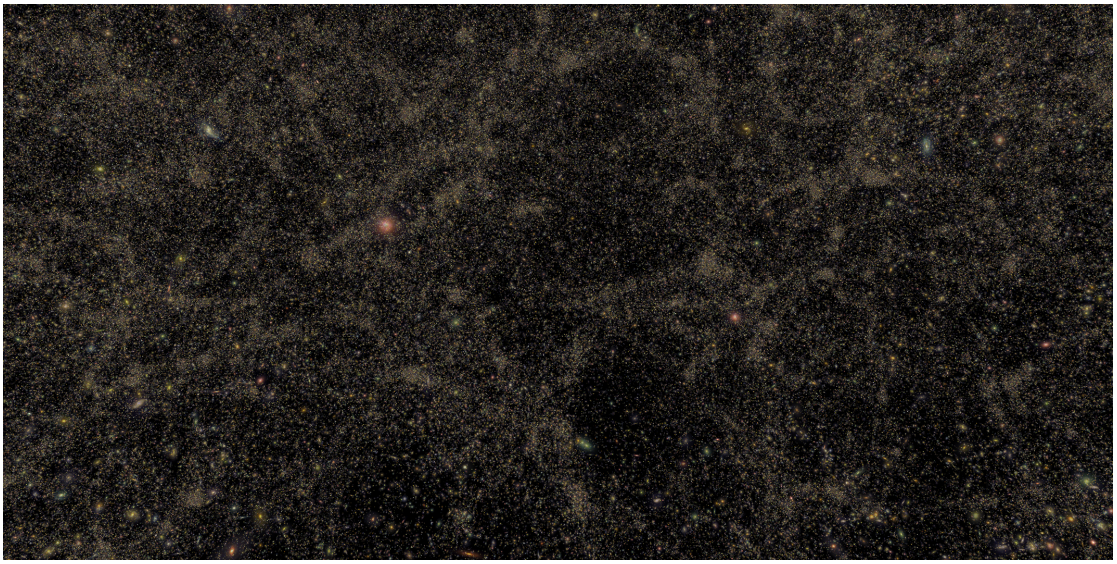

FIGURE 5.11: A large scale screenshot showing many millions of galaxies within Astera.

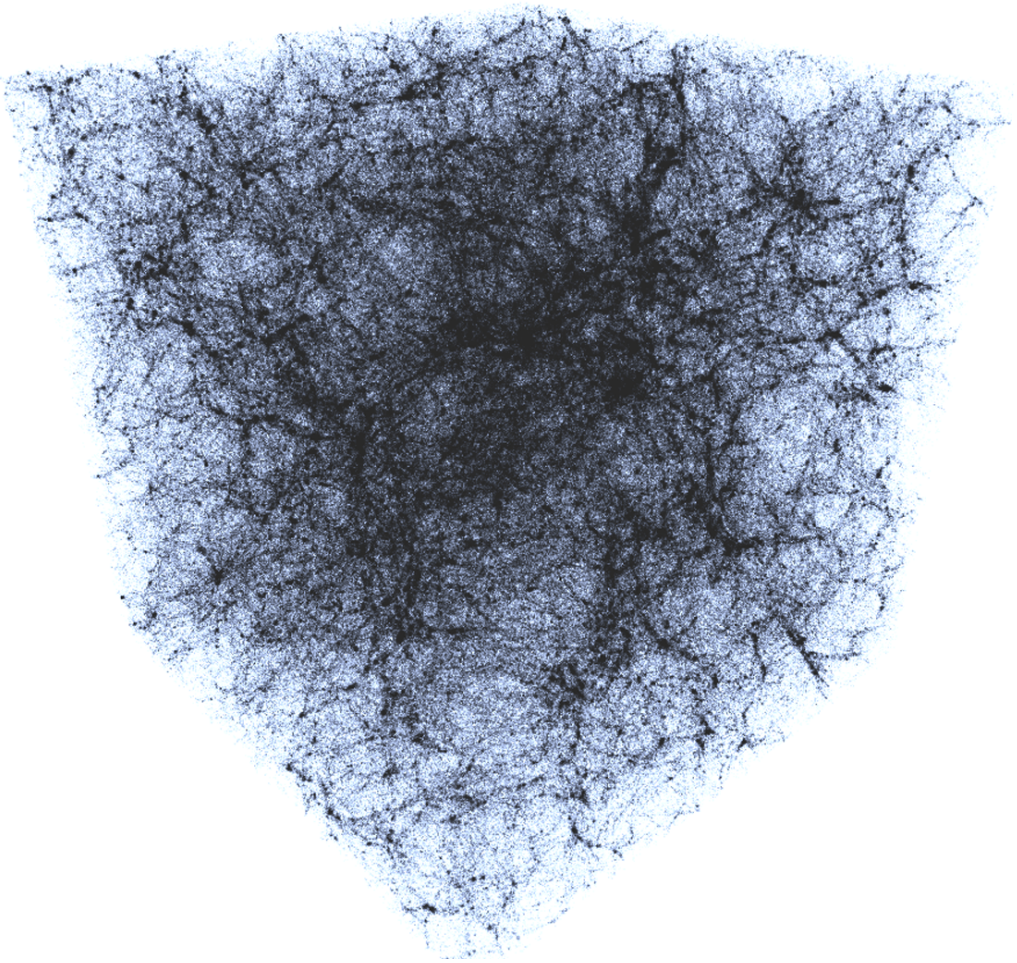

FIGURE 5.12: A colour-inverted view of the full simulation volume. The large scale cosmic web is clearly visible. This image is also shown in Chapter 1, but I repeat it here to illustrate Astera's capabilities.

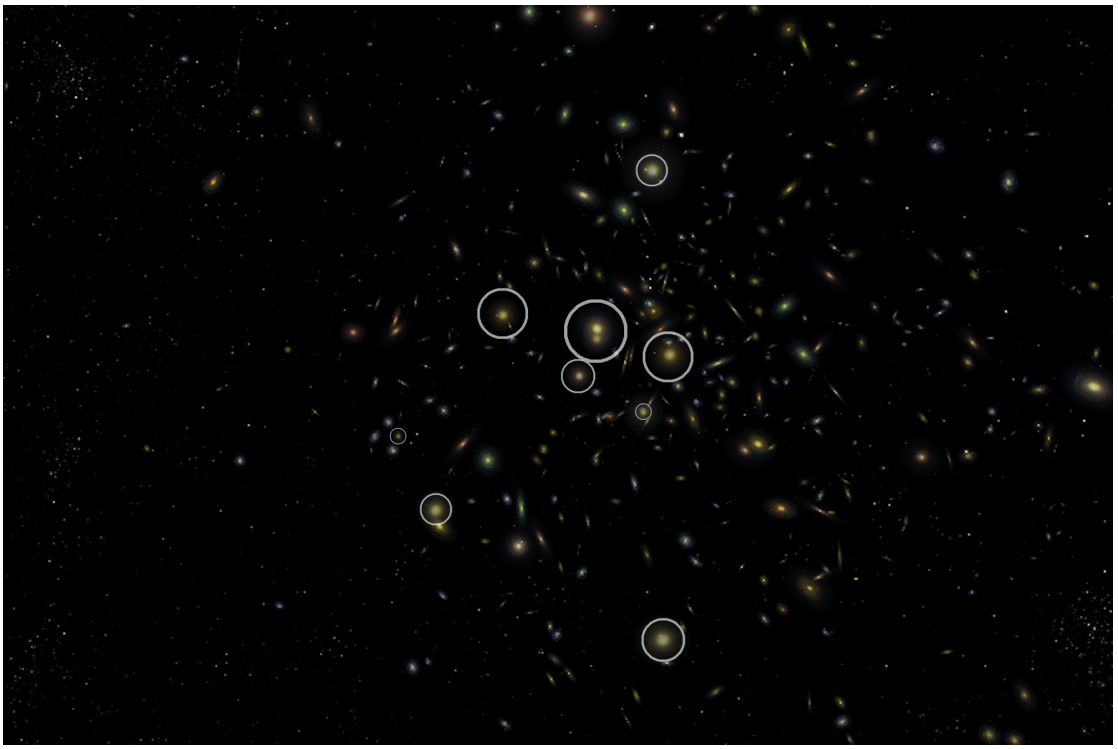

FIGURE 5.13: A cluster of galaxies within Astera, where the large elliptical galaxies have been circled. The elliptical galaxies preferentially occupy the centre of the cluster, in line with observations.

data, create mesh instances and place the galaxies. The primary problem behind this task was performance; how many static mesh objects (representing galaxies) could be drawn to the screen at an acceptable frame rate. Remarkably, through the use of Unreal Engine's Instanced Static Mesh Technology, this was achieved to the extent that every galaxy in a full frame of a catalogue representing a $(1000\ h^{-1}\text{Mpc})^3$ box could be shown simultaneously on hardware running a NVidia Titan GPU at a full 60 FPS. Less powerful hardware can still run large volumes, with a NVidia GTX 760 rendering a $(300\ h^{-1}\ \text{Mpc})^3$ box at 60 FPS.

This was attained through intelligent use of Unreal's powerful and efficient Instanced Static Mesh Technology. Another success of Astera is its compatibility with any dataset. Any galaxy catalogue could easily be imported (within hardware constraints), a feature that could allow a researcher to replace the default data and explore their own universe. Exploring the universe within Astera reveals the large scale cosmic structure in a way that is vastly easier to understand than a 2D image or even potentially a video. The author noted that several ''wall" like structures become visible in the cosmic web, which are not apparent in 2D imagery, in agreement with Diemer and Facio (2017). The distribution of galaxy mythologies also seem to follow established trends (see Figure 5.13), such as elliptical galaxies occupying the central regions of clusters—e.g., in (De Lucia et al., 2011).

From an academic perspective, there are unique advantages to creating a mock universe that is rendered in real time. The first is simply the visual examination of Mock Galaxy catalogues (e.g., in preparation for large surveys); while not necessarily statistically robust, a quick visual examination can often reveal issues that would not otherwise be easy to detect. A more nuanced approach could be to reproduce the effects of a program, such as SkyMaker (Bertin, 2009), where a mock galaxy catalogue is used to create a simulated astronomical image. Crucially, Astera would render this in real time, allowing for alternative images to be rapidly explored, or even a simulated sequence of images over a period of time, which could simulate data from time-variable objects, such as AGN.

Future "features' that the authors are exploring include:

- Dark Matter Viewer. The conspicuous absence of Dark Matter in Astera would be remedied by a view mode that would show the dark matter substructure.
- Time Evolution. An exciting option which would essentially integrate Astera with a semi-analytic model, the motions and evolution of galaxies would be visible in (accelerated) real time. The user would be able to, at the press of a button, watch the universe evolve in front of them. This would dramatically increase the strain on the hardware to perform this on real time, so the volume of this universe might be limited.
- Gravitational Lensing. An ambitious proposal, where the weak gravitational lensing of large clusters could be visually shown. Obviously solving the full equations from General Relativity would not be viable, but it might be possible to develop a ''lens" object that acts as a close approximation.
- Gamification. As previously mentioned, Astera is a potentially invaluable outreach tool for increasing public awareness of the large scale universe. Gamifying Astera by introducing elements that make exploring the cosmological volume fun and educational could increase this value even further.

Commercially, I believe that Astera has a bright future, specifically having the potential to become a product that defines the awareness of the large-scale universe in the public consciousness. My 'endgame' is therefore a digital product that presents a fully mature software experience that both educates the user about the large-scale universe but also presents a thrilling gaming experience that will keep players coming back for more.

With a global market value of $151.55 billion in 2019 that is expected to reach a value of 256.97 billion by 2025, the gaming industry is surprisingly the most valuable entertainment industry (outstripping even Hollywood), and has the potential for the most growth. Despite strong competition, there have been recent examples of games

that have met significant commercial success by defy the norm and utilizing complex and unusual principles derived from physics, mathematics and computer science. In Astera, I plan to engage the player with the advanced concepts of galaxy evolution, presented intuitively. A player could, for example, control the evolution of a galaxy over its lifetime, perhaps choosing when star formation will occur, or when a galaxy will merge, witnessing first-hand the consequences of these processes on shape and evolution of galaxies. The player will thus be able to enjoy, visualize and at the same time learn about the main physical events in the lives of galaxies, a fundamental scientific topic that would otherwise remain largely inaccessible to the general public. I plan to develop Astera into a product that can 1) return significant economic benefit as a popular video game 2) return significant societal benefit through dramatically improving public participation withing otherwise inaccessible research field.

More information, visual materials and videos can be found on the Astera website https://astera.soton.ac.uk. I will also update this website with any future details of Astera's public release.

At the time of writing, Astera has received major investment to achieve these goals. Astera has received investment from NVidia, in the form of a GPU grant. The STFC Impact Innovation Fund has provided funding for Astera to be installed as a dedicated exhibit at a local attraction in Southampton, the Winchester Science Centre, with upgrades to "gamify" the experience to allow the user to scan and classify galaxies to gain points, with the aim of attracting a new generation to extra-galactic astronomy. I have also received support for the ongoing development of bespoke audio effects[6], and most significantly investment from the STFC Follow-on-Fund for a 10 months of full time development work for the development of a fully prototyped version of Astera.

[6]With samples available at https://youtube.com/channel/UCQVFE8MezthphL5PhJa6NxA

Chapter 6

Conclusions

In this thesis I have first reviewed the main processes shaping galaxy evolution, the connections between black holes and galaxies and the importance of galaxy velocity dispersion (Chapter 1). I have created a semi-empirical Jeans modelling technique to predict galaxy velocity dispersions, inclusive of bulge/disk decompositions and radially varying M^*/L ratios (Chapter 2). Next, I showed that this model reproduces the local scaling relations, and predicts the evolution of σ in a semi-empirical fashion, showing consistency with TNG50, but not with purely dry merger models of galaxy evolution (Chapter 2). Following this, I set out a detailed analysis of the residuals of the scaling relations with black hole masses, utilized the sigma evolutionary tracks computed in Chapter 3 to predict the evolution in the $M_{\rm BH}$-σ relation, and showed that clustering can break difficult degeneracies in black hole accretion models (Chapter 4). Finally, I presented a step-by-step methodology for creating realistic mock populations of active and inactive black holes, and presented my application of these mock catalogs for educational purposes and survey planning (Astera). In this Chapter, I will conclude by providing some relevant answers to the questions posed in Chapter 1.

6.1 Velocity Dispersion

How does velocity dispersion evolve with redshift for galaxies of different stellar mass? What ultimately drives this evolution? Is this evolution consistent with what predicted by hierarchical galaxy assembly models?

In this work I have presented a comprehensive analytic Jeans modelling to probe the galaxy scaling relations involving velocity dispersion $\sigma_{ap}(R)$ in the local Universe, as well as making valuable predictions for the evolutionary tracks $\sigma_{ap}[M^*, z]$ along the progenitors and at fixed stellar mass. I compared my model predictions with a large sample of local MaNGA galaxies with spatially resolved velocity dispersions, and also

with the outputs of the TNG50 hydrodynamic simulation. When including both a bulge and a disk component in my models, I find that, in agreement with what measured in MaNGA, at fixed stellar mass velocity dispersions are relatively flat (Figure 3.3) and become largely independent of the bulge-to-total ratio B/T for $B/T \gtrsim 0.25$, irrespective of the exact stellar mass bin or aperture considered (Figure 3.2), or whether or not a gradient in M^*/L is included. The dynamical-to-stellar mass ratio $M_{dyn}/M^* \sim M^{*\alpha}$ can be fully accounted for by a sufficiently steep gradient in the stellar M^*/L ratio (Figure 3.5). When a flat M^*/L is assumed, the full dependence of the dynamical-to-stellar mass ratio on stellar mass can be reproduced by assuming a power-law mass density profile (Figure 3.5, right), showing almost perfect degeneracy between a gradient in M^*/L and dark matter. The predicted $\sigma_{ap}[M^*, z]$ evolutionary tracks show, irrespective of the exact input parameters, a clear sign of downsizing, with more massive galaxies reaching their final $\sigma_{ap}(R)$ value at earlier epochs, whilst $\sigma_{ap}[M^*, z]$ steeply increases approximately as $\sigma_{ap} \propto (1+z)^{0.3}$ at fixed stellar mass at constant M^*/L. Very similar results are found when extracting velocity dispersions from the TNG50 simulation (Figure 3.6). I interpret the behaviour of $\sigma_{ap}[M^*, z]$ in light of the ratio between stellar mass to dark matter mass in the inner regions. When a galaxy falls below the knee of the stellar mass–halo mass relation, a decrease in halo mass implies a stronger decrease in stellar mass, thus the dark matter component becomes the dominant factor in controlling sigma (Figure 3.7). The inclusion of a gradient in M^*/L maintains the downsizing in $\sigma_{ap}[M^*, z]$, but the single evolutionary tracks along the progenitors are steeper, whilst the ones at fixed stellar mass/galaxy luminosity evolve more slowly as $\sigma_{ap} \propto (1+z)^{0.2}$ or less (Figure 3.9). Furthermore, the FJ relation is seen to increase in normalization as redshift increases, but not to change in slope, at the same pace as the dynamical-to-stellar mass ratio, closely following the degree of evolution of σ_{ap} at fixed stellar mass (Figure 3.10). I show that pure dry merger models are inconsistent with my retrieved $\sigma_{ap}[M^*, z]$ evolutionary tracks (Figure 3.12), calling for additional processes, most probably residual star formation, as an important ingredient in shaping velocity dispersion through time. Indeed, I find that in the TNG50 simulation gas-rich galaxies at fixed stellar mass have a much steeper evolution in $\sigma_{ap}[M^*, z]$ than counterpart galaxies with the same stellar mass (Figure 3.13). All in all, my results point to a complex interplay between mergers and gas accretion in keeping velocity dispersion evolutionary tracks relatively flat or even increasing with cosmic time, a condition that supports the view in which velocity dispersions may retain memory of the initial stages of galaxy evolution. Our methodology (presented in Shankar et al., 2020b; Allevato et al., 2011) proves the usefulness of data-driven semi-empirical models as *complementary* tools to provide fast and robust predictions on galaxy properties and to probe the interplay of the different components (e.g., dark matter versus baryonic matter), something that would be difficult to disentangle in, e.g., hydrodynamic simulations.

6.2 Black Holes

Is the $M_{\rm BH}$-σ relation truly fundamental? How does the this relation evolve with redshift? Is it roughly constant in slope and normalization as predicted by AGN feedback models?

I first review previous evidence for the $M_{\rm BH}$-σ being the most fundamental of all black hole-host galaxy scaling relations (among those discovered so far) and I have presented new evidence based on the statistical analysis of the sample recently compiled by de Nicola et al. (2019). Analysis of residuals (e.g., Shankar et al. 2016) point to σ being more fundamental than both stellar luminosity/mass or effective radius in their correlation to central black hole mass. Theoretically, as reviewed by King and Pounds (2015), the $M_{\rm BH}$-σ arises as a consequence of AGN feedback. In short, the black hole in these models is expected to grow until it becomes massive enough to drive energetic/high-momentum large-scale winds that can potentially remove residual gas, inhibiting further star formation and black hole growth. The limiting mass reached by the black hole, which ultimately depends on the potential well of the host, naturally provides an explanation for the existence of the $M_{\rm BH}$-σ relation. For each $\sigma_{ap}[M^*, z]$ I compute the growth of the central supermassive black hole derived from the $L_X - M^*$ relation of stacked X-ray AGN. My resulting $M_{\rm BH} - \sigma_{ap}(R)$ relation appears to be nearly independent of redshift, at least up to $z \lesssim 2$, with a constant slope of ~ 5 (Figure 4.4).

I have also described in Chapter 4 how flexible and transparent semi-empirical models of AGN clustering can be used to place strong constraints on the normalization and shape of different black hole scaling relations. In particular, I discussed how current AGN clustering data favour lower normalizations of the $M_{\rm BH}$-M^* relation (labelled by Shankar et al. (2016) as 'de-biased'), and highlighted how once more the $M_{\rm BH}$-σ relation produces a good match to the data

6.3 Wider Applications: Mock catalogs

In this thesis I described a step-by-step methodology to create robust, transparent and physically motivated AGN mock catalogs that can be safely used for extra-galactic large-scale surveys and as a testbed for cosmological models of BH and galaxy co-evolution. My methodology, summarized in Figure 5.2, allows to minimise the danger of degeneracies and to pin down the underlying physical properties of BHs in terms of their accretion distributions and links to their host galaxies. The AGN XLF and the specific accretion-rate distribution $\rm P_{AGN}$ depend on the input M^*-M_{BH} and M^*-M_{halo} relations, Eddington ratio distribution P(λ) and AGN duty cycle U; and are independent of the particular choice of Q. Any input stellar-BH mass relation and specific accretion-rate distribution $\rm P_{AGN}$ (defined as convolution of the Eddington ratio distribution P(λ) and the AGN duty cycle U) produce mock AGN that match the observed

AGN XLF and large-scale bias at a given stellar mass. Only the combination with additional observables, namely the AGN large-scale bias as a function of the BH mass and X-ray luminosity can break the degeneracy in the input model parameters. I have succeeded in creating what is most likely the first attempt to execute a fully realized real time rendering of the large scale universe. This project was powered by Unreal Engine 4, and a framework was constructed to read in data, create object instances and place galaxies. The most difficult challenge was performance; how many galaxies could be simultaneously rendered at an acceptable frame rate. This was achieved to the extent that every object in a full frame of a catalogue derived from the MultiDark simulation (Klypin et al., 2016) could be shown simultaneously a full 60 FPS, on powerful (but consumer-grade) hardware. The software was also designed to be compatible with any dataset, a feature that could allow anyone to replace the default data with their own. Exploring Astera reveals the large scale cosmic structure in a way that is significantly easier to understand than a 2D image or even a video.

6.4 Closing Remarks

In this thesis, I have explored several key areas within galaxy evolution. I first developed a set of flexible and accurate tools for the simulation of σ, which can unveil patterns in galaxy evolution as they are data-driven and thus independent of any specific model of galaxy formation and assembly. I have also revealed several key aspects of velocity dispersion that have been hitherto unexplored, such as the role of dark matter in driving velocity dispersion at high redshift and the effect of a radially varying M^*/L. I have also explored black holes and their mysterious links to galaxies, providing meaningful contributions to black hole scaling relations and AGN mock catalogs. Finally, I have developed my cosmological visualization tool Astera, which provides the first real-time rendering of the large scale universe. I hope that Astera, which arguably has the most potential of all these works, will take on a life of its own through data planning, visualization and maybe one day inspire a future generation of astronomers to explore the large-scale universe.

List of papers

The list of the authors papers in support of this thesis are as follows:

1. **Marsden** et al (submitted)
2. **Marsden** et al 2020a
3. **Marsden** et al 2020b
4. Allevato, Shankar, **Marsden** et al 2021
5. Shankar, Weinberg, **Marsden** et al 2021
6. Shankar, Bernardi, Richardson, **Marsden** 2019a
7. Shankar, Alleato, Bernardi, **Marsden** et al 2019b
8. Carraro, Shankar, Allevato, **Marsden** et al (submitted)
9. Viitanen, Allevato, Finoguenov, Shankar, **Marsden** (submitted)
10. Fu,Shankar, Ayromlou, Dickson, **Marsden** et al (in prep)

List of material

Much of the material within this thesis is also presented elsewhere. The following is a breakdown of how this material has been distributed throughout this work:

1. Chapter 1: Marsden et al (submitted), Marsden et al. (2020), Marsden and Shankar (2020), Fu et al (in prep): Allevato et al. (2021).
2. Chapter 2: Marsden et al (submitted), Fu et al (in prep).
3. Chapter 3: Marsden et al (submitted).
4. Chapter 4: Marsden et al (submitted), Marsden et al. (2020), Shankar et al. (2020a).
5. Chapter 5: Allevato et al. (2021), Marsden and Shankar (2020).
6. Chapter 6: Marsden et al (submitted), Marsden et al. (2020), Marsden and Shankar (2020), Allevato et al. (2021).

Additional Comments and Acknowledgements

The author would like to acknowledge that sections of this 4.2.1 and 4.2.2 were originally written by Dr Kastytis Zubovas for Marsden et al. (2020), before being modified by the author for this work. Additionally, Figures 4.1 and 4.2 were co-produced by the author and Dr Francesco Shankar.

Appendix A

Additional Material

A.1 Virial coefficients

In this thesis, I have presented a comprehensive methodology for computing velocity dispersion. Our source code is publicly available at `github.com/ChrisMarsden833/VelocityDispersion`, along with the associated documentation. In addition, I here provide a convenient and comprehensive look-up Table of virial coefficients that can be used to compute the total dynamical mass within the effective radius for a constant M^*/L.

The velocity dispersion of a spheroid within an arbitrary aperture can be well represented by the following relation

$$\frac{GM(<R_e)}{R_e} = \mathcal{F}\sigma_{ap}^2 \tag{A.1}$$

where G is the gravitational constant, R_e is the scale radius, $M(<R_e)$ is the total mass within R_e and σ_{ap} is the velocity dispersion within the aperture. While some approximations for $\mathcal{F}$ already exist (e.g. Bernardi et al., 2018), a more comprehensive approximation that also takes into account the roles of dark matter and velocity anisotropy β can be expressed as

$$\mathcal{F} = \zeta\mathcal{K}\left(\frac{R_{ap}}{R_e}, n\right) + \zeta_{halo}\mathcal{L}\left(\frac{R_{ap}}{R_e}, n, c\right) + \mathcal{N}\left(\frac{R_{ap}}{R_e}, n, \beta\right) \tag{A.2}$$

where $\zeta = M^*(<R_e)/M(<R_e)$ is the ratio of stellar mass to total mass within R_e (see Figure 3.7), and $\zeta_{halo} = M_{halo}(<R_e)/M(<R_e)$ is the ratio of dark matter mass to total mass within R_e, which is simply $\zeta_{halo} = 1-\zeta$ when neglecting gas and black hole masses. The functions $\mathcal{K}$, $\mathcal{L}$ and $\mathcal{N}$ are represented by numerical approximations. I present some example values in Table A.1, but I also include a code in the aforementioned repository to numerically generate these Tables over arbitrary domains at the

TABLE A.1: Table containing numerical values for approximation of equation A.2. n is the Sérsic index, c is the halo concentration parameter, and β is the anisotropy parameter.

R_{ap}/R_e	$\mathcal{K}$		$\mathcal{L}$				$\mathcal{N}$				
	n	$\mathcal{K}$		c				β				
				5	7	10	14	−0.15	0.0	0.1	0.25	0.4
1/8	2	2.79	2	3.99	4.0	4.02	4.03	0.42	0.0	−0.28	−0.7	−1.12
	3	2.35	3	4.01	4.05	4.12	4.22	0.25	0.0	−0.17	−0.45	−0.74
	4	1.94	n 4	3.58	3.64	3.73	3.86	0.15	0.0	−0.11	−0.28	−0.48
	5	1.63	5	3.12	3.18	3.27	3.41	0.1	0.0	−0.07	−0.19	−0.32
	6	1.38	6	2.72	2.77	2.86	2.99	0.07	0.0	−0.05	−0.13	−0.22
	n	$\mathcal{K}$		c				β				
				5	7	10	14	−0.15	0.0	0.1	0.25	0.4
1	2	2.83	2	2.53	2.57	2.61	2.66	0.09	0.0	−0.06	−0.16	−0.28
	3	2.71	3	2.86	2.89	2.94	2.98	0.07	0.0	−0.05	−0.14	−0.23
	4	2.51	n 4	3.03	3.06	3.1	3.15	0.06	0.0	−0.04	−0.11	−0.19
	5	2.29	5	3.06	3.09	3.14	3.19	0.04	0.0	−0.03	−0.09	−0.15
	6	2.07	6	2.99	3.03	3.08	3.15	0.04	0.0	−0.03	−0.07	−0.12

TABLE A.2: Table containing numerical values of ζ based on our model, as a function of stellar mass and effective radius. Stellar Mass (M^*) is listed in units of log_{10} solar masses $[M_\odot]$, and R_e is listed in kiloparsecs $[kpc]$.

		R_e											
		1.0	3.0	5.0	7.0	9.0	11.0	13.0	15.0	17.0	19.0	21.0	23.0
	9.0	0.5	0.12	0.05	0.03	0.02	0.02	0.01	0.01	0.01	0.01	0.01	0.01
	9.5	0.75	0.28	0.14	0.09	0.06	0.05	0.04	0.03	0.03	0.02	0.02	0.02
	10.0	0.9	0.53	0.31	0.21	0.15	0.11	0.09	0.08	0.06	0.06	0.05	0.05
M^*	10.5	0.96	0.75	0.55	0.4	0.31	0.24	0.2	0.16	0.14	0.12	0.11	0.1
	11.0	0.98	0.88	0.73	0.6	0.48	0.4	0.33	0.28	0.24	0.21	0.18	0.16
	11.5	0.99	0.94	0.85	0.74	0.64	0.55	0.47	0.41	0.35	0.31	0.27	0.24
	12.0	1.0	0.97	0.92	0.86	0.78	0.71	0.64	0.57	0.51	0.46	0.41	0.37

desired resolution. Each function depends on the ratio of the aperture size ap to R_e. $\mathcal{K}$ additionally depends on the Sérsic index n and R_e, $\mathcal{L}$ depends on n and the halo concentration c, $\mathcal{N}$ depends on β, the anisotropy parameter. If dark matter and anisotropy are neglected, the functions $\mathcal{L}$ and $\mathcal{N}$ (respectively) can be set to zero. In this case Equation A.2 reduces to the form presented in Bernardi et al. (2018, see their Equation 2). Note that there is a subtle difference between their Equation and ours (when neglecting dark matter and anisotropy), as the left hand side of our Equation requires the mass within R_e rather than the total stellar mass. In Table A.2 I also include some useful tabulated values of ζ as a function of stellar mass and effective radius, which are strictly valid for stellar and dark matter mass profiles from, respectively, Prugniel and Simien (1997) and Navarro et al. (1996), and halo concentrations from Ishiyama et al. (2020), as discussed in Chapter 2. In table A.1, I show the dynamical mass ratio vs radius for several of the galaxies from my model, showing that ζ has a strong dependence on radius.

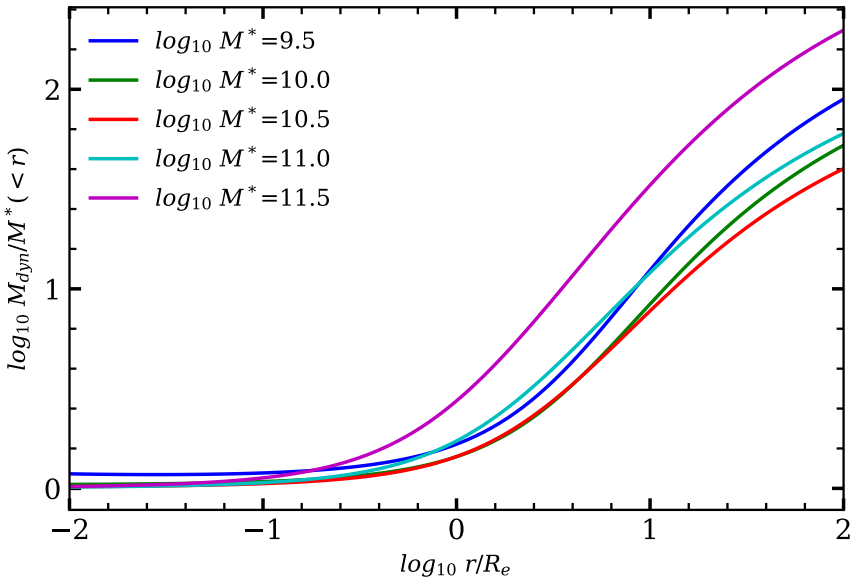

FIGURE A.1: The dynamical to stellar mass ratio as a function of radius for the average (single-Sérsic) galaxies in my model.

TABLE A.3: Table of the extreme values of the mass-to-light ratios values for galaxies of different absolute magnitudes and measured velocity dispersion.

Absolute magnitude (r-band)	$log_{10}\,\sigma\,[kms^{-1}]$	Υ_{inner}	Υ_{outer}
Ellipticals			
$-22.5 > M_r > -23.5$	$2.4-2.5$	8.0	3.5
	$2.3-2.4$	7.0	3.0
$-21.5 > M_r > -22.5$	$2.3-2.4$	5.0	3.0
	$2.2-2.3$	5.0	2.5
$-20.5 > M_r > -21.5$	$2.2-2.3$	5.0	3.0
	$2.1-2.2$	3.0	2.0
S0s			
$-21.5 > M_r > -22.5$	$2.3-2.4$	6.5	4.5
	$2.2-2.3$	5.0	2.0
	$2.1-2.1$	2.0	1.0
$-20.5 > M_r > -21.5$	$2.2-2.3$	5.5	2.0
	$2.1-2.2$	3.0	1.5
	$2.0-2.1$	2.0	1.5
$-19.5 > M_r > -20.5$	$2.1-2.2$	4.0	3.0
	$2.0-2.1$	4.0	3.0
	$1.9-2.0$	1.5	1.5

A.2 Extreme values of Υ(R)

I provide in Table A.3 the values of the scale-dependent mass-to-light ratio at R_e (Υ_{outer}) and at the centre (Υ_{inner}) for galaxies of different absolute magnitudes and measured velocity dispersion. As described in Chapter 2, I assume the M^*/L varies linearly between these two extreme values and it is constant, equal to Υ_{outer}, at radii $R > R_e$.

A.3 The impact of segregation in the SSP phase-space distribution functions

The formulation in Bernardi et al. (2018), which I followed in Chapter 2 to compute the radial profile and velocity dispersion, assumes that the objects (low mass stars) which cause the IMF gradient are not dynamically different from the others (e.g., if stars always form in clusters, but the stellar IMF in the clusters depends on how far the cluster is from the centre of the galaxy). In this case, ignoring dark matter for the time being, Equation 2.4 would read as

$$\rho^*(r)\sigma_r^2(r) = \frac{1}{f(r)}\int_r^\infty f(s)\rho^*(s)\frac{GM^*(s)}{s^2}ds \tag{A.3}$$

with $\rho^*(r) = \rho^*_{Ser}(r) + \Delta\rho^*(r)$ and $M^*(r) = M^*_{Ser}(r) + \Delta M^*(r)$. Instead, if one thinks of a galaxy as being a linear combination of simple stellar populations (SSPs), each having its own M^*/L ratio, and that each SSP is described by its own *distinct* phase-space distribution function, then one would rearrange the Jeans Equation in Equation A.3 in the following way

$$\rho^*_{Ser}(r)\sigma_r^2(r) = \frac{1}{f(r)}\int_r^\infty f(s)\rho^*_{Ser}(s)\frac{GM^*(s)}{s^2}ds\,, \tag{A.4}$$

where the low mass stars, similarly to a dark matter component, would not significantly contribute to the total luminosity but only to the total mass and thus would appear only on the right-hand side of Equation A.4 (see Caravita et al., 2021). Our simple test shown in Figure A.2 for a given galaxy of with $\phi = 1.3$, $\Upsilon_0 = 3$, $\log L/L_\odot = 11$, indicates that, for M^*/L gradients of current interest, the two formulations only lead to relatively small differences in the $\sigma_{los}(R)$ profiles at $R \lesssim R_e$. I hope that future datasets will have sufficient signal-to-noise to determine which of the two formulations of the dynamics of the stars giving rise to IMF gradients is more realistic.

A.4 Computing large-scale bias

It has long been known that the spatial clustering of observable galaxies does not necessarily mirror the clustering of dark matter in the Universe. Most generally, the galaxy density can be some function of the underlying dark matter density. This galaxy 'bias', the relationship between the spatial distribution of galaxies and the underlying density field. Bias is a result of the complex physics of galaxy formation and evolution which can result in the distribution of baryonic matter being different to that of dark matter. The abundance of haloes themselves can also be represented by the he bias factor (b) that represents the overabundance of haloes with respect to the underlying mass density. For a detailed overview of bias, see Mo et al. (2010).

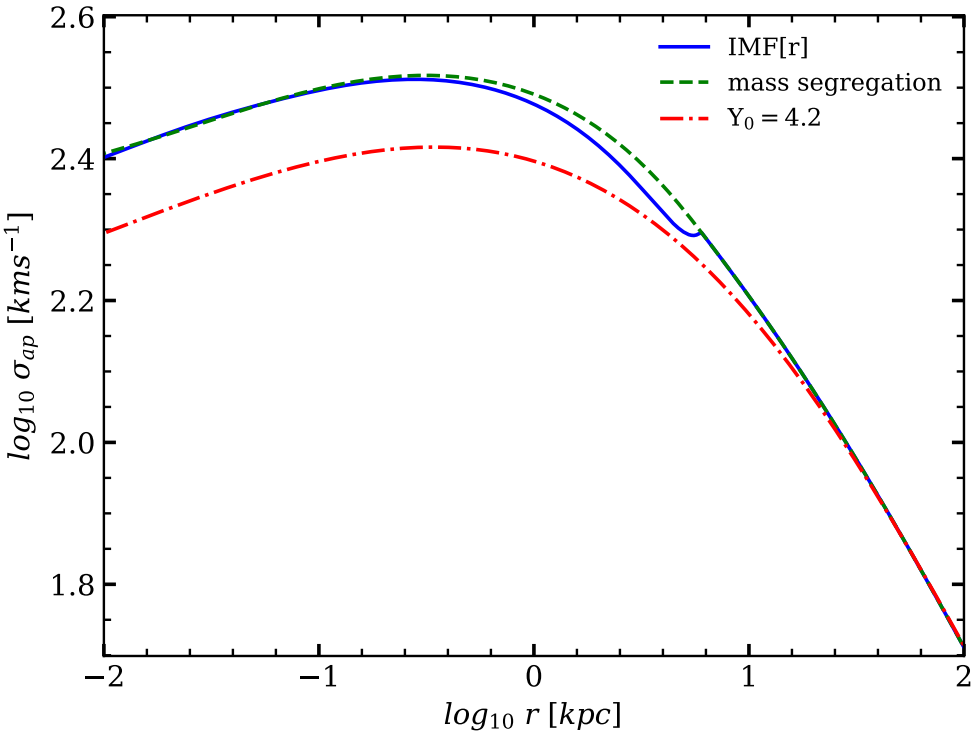

FIGURE A.2: $\sigma_{los}(R)$ radial profiles for a typical galaxy in our MaNGA sample with $\phi = 1.3$, $Y_0 = 3$, $\log L/L_\odot = 11$, computed via Equation A.3 assuming both a constant M^*/L (red dot-dashed line) and a scale-dependent M^*/L as given in Equation 2.18 (blue solid line), and via Equation A.4 with the same scale-dependent M^*/L (green dashed line).

To compare models to clustering data, we first perform abundance matching at the average redshift of $z = 0.25$. We then extract large host halo catalogues from the halo (plus subhalo) mass function and assign galaxies to haloes via the M^*-M_{halo} relation as described in Chapter 4. On the general assumption that black hole scaling relations do not depend on environment/host halo mass, to each mock galaxy in the catalogue we assign a black hole mass adopting an input $M_{\rm BH}$-M^* relation inclusive of scatter. In principle, the mean large-scale bias for black holes with mass in the range $M_{\rm BH}$ and $M_{\rm BH} + dM_{\rm BH}$ could be straightforwardly estimated as

$$b(M_{\rm BH}) = \frac{1}{N_{\rm bin}} \sum_{i=1}^{N_{\rm bin}} b_h \left[M_{\rm halo,i}(M_{\rm BH})\right] , \tag{A.5}$$

where the sum runs over the total number $N_{\rm bin}$ of (central and satellite) parent haloes hosting central black holes with mass in the range $M_{\rm BH}$ and $M_{\rm BH} + dM_{\rm BH}$.

However, A.5 neglects the probabilities for central and satellite black holes to be active. In the case of AGN in fact, not all galaxies in a given host halo mass bin necessarily

contribute to the same clustering signal, and A.5 should be modified to include the duty cycles, or probabilities, $U_{\rm cen}(M_{\rm BH})$ and $U_{\rm sat}(M_{\rm BH})$ of, respectively, central and satellite black holes of mass $M_{\rm BH}$ to be active at a given cosmic epoch. We here follow the same convention as in Shankar et al. (2013b) and denote the duty cycles at fixed black hole mass $M_{\rm BH}$ at a given redshift z as $U(M_{\rm BH}, z)$. As in this work we only focus on the specific redshift of $z = 0.25$, we will drop the redshift dependence in the duty cycles from here onwards. Generalising A.5 to include the central/satellite probabilities of being active we obtain

$$b(M_{\rm BH}) = \frac{\left[\sum_{i=1}^{N_{\rm cen}(M_{\rm BH})} U_{\rm cen,i}(M_{\rm BH})(M_{\rm BH}) b_{\rm cen,i}(M_{\rm BH}) + \sum_{i=1}^{N_{\rm sat}(M_{\rm BH})} U_{\rm sat,i}(M_{\rm BH}) b_{\rm sat,i}(M_{\rm BH})\right]}{\left[\sum_{i=1}^{N_{\rm cen}(M_{\rm BH})} U_{\rm cen,i}(M_{\rm BH}) + \sum_{i=1}^{N_{\rm sat}(M_{\rm BH})} U_{\rm sat,i}(M_{\rm BH})\right]}, \tag{A.6}$$

where both $U_{\rm cen}(M_{\rm BH})$ and $U_{\rm sat}(M_{\rm BH})$ are related to the total duty cycle of active black holes by the relation $N_{\rm AGN}(M_{\rm BH}) = U(M_{\rm BH})N(M_{\rm BH}) = U_{\rm cen}(M_{\rm BH})N_{\rm cen}(M_{\rm BH}) + U_{\rm sat}(M_{\rm BH})N_{\rm sat}(M_{\rm BH})$, with $N(M_{\rm BH}) = N_{\rm cen}(M_{\rm BH}) + N_{\rm sat}(M_{\rm BH})$ the number of central and satellite black holes in the mass bin $M_{\rm BH}$ and $M_{\rm BH} + dM_{\rm BH}$. In the limit in which all central and satellite black holes are active or share equal probabilities to be active, i.e., $U_{\rm cen}(M_{\rm BH}) = U_{\rm sat}(M_{\rm BH})$, then A.6 reduces to the special case of A.5.

Throughout this work we adopt as a reference the total duty cycle $U(M_{\rm BH})$ in A.6 as derived from the continuity equation model by Shankar et al. (2013b), with constant lognormal Eddington ratio distribution. The exact normalization and shape of the total duty cycle $U(M_{\rm BH})$ depends on the minimum luminosity threshold considered and input Eddington ratio distributions $P(\lambda)$, as anticipated in the previous . As extensively discussed by, e.g., Shankar et al. (2013b), continuity equation models generally tend to generate duty cycles decreasing with increasing black hole mass, as also retrieved by direct data modelling by other groups (Shankar et al., 2013b). The latter trend would then imply that active lower mass black holes would have a larger weight on the bias. However, when computing the mean bias in narrow bins of black hole mass, the exact shape or normalization of the assumed total duty cycle $U(M_{\rm BH})$ are irrelevant. It is in fact clear from A.6 that, in a relatively small bin of black hole mass, what contributes to the mean bias is not the total duty cycle $U(M_{\rm BH})$, rather the *relative* probabilities for central and satellite black holes to be active, i.e., the ratio $Q_{\rm bh}(M_{\rm BH}) = U_{\rm sat}(M_{\rm BH})/U_{\rm cen}(M_{\rm BH})$.

For further details, I direct the reader to Shankar et al. (2020a).

References

Jose Luis Sérsic *Atlas de Galaxias Australes*. 1968.

Tom Abel, Oliver Hahn, and Ralf Kaehler. Tracing the dark matter sheet in phase space. *Monthly Notices of the Royal Astronomical Society*, 427(1):61–76, November 2012. .

Peter AR Ade, N Aghanim, M Arnaud, M Ashdown, J Aumont, C Baccigalupi, AJ Banday, RB Barreiro, JG Bartlett, N Bartolo, et al. Planck 2015 results-xiii. cosmological parameters. *Astronomy & Astrophysics*, 594:A13, 2016.

D. S. Aguado, Romina Ahumada, Andrés Almeida, Scott F. Anderson, Brett H. Andrews, Borja Anguiano, Erik Aquino Ortíz, Alfonso Aragón-Salamanca, Maria Argudo-Fernández, Marie Aubert, Vladimir Avila-Reese, Carles Badenes, Sandro Barboza Rembold, Kat Barger, Jorge Barrera-Ballesteros, Dominic Bates, Julian Bautista, Rachael L. Beaton, Timothy C. Beers, Francesco Belfiore, Mariangela Bernardi, Matthew Bershady, Florian Beutler, Jonathan Bird, Dmitry Bizyaev, Guillermo A. Blanc, Michael R. Blanton, Michael Blomqvist, Adam S. Bolton, Médéric Boquien, Jura Borissova, Jo Bovy, William Nielsen Brandt, Jonathan Brinkmann, Joel R. Brownstein, Kevin Bundy, Adam Burgasser, Nell Byler, Mariana Cano Diaz, Michele Cappellari, Ricardo Carrera, Bernardo Cervantes Sodi, Yanping Chen, Brian Cherinka, Peter Doohyun Choi, Haeun Chung, Damien Coffey, Julia M. Comerford, Johan Comparat, Kevin Covey, Gabriele da Silva Ilha, Luiz da Costa, Yu Sophia Dai, Guillermo Damke, Jeremy Darling, Roger Davies, Kyle Dawson, Victoria de Sainte Agathe, Alice Deconto Machado, Agnese Del Moro, Nathan De Lee, Aleksandar M. Diamond-Stanic, Helena Domínguez Sánchez, John Donor, Niv Drory, Hélion du Mas des Bourboux, Chris Duckworth, Tom Dwelly, Garrett Ebelke, Eric Emsellem, Stephanie Escoffier, José G. Fernández-Trincado, Diane Feuillet, Johanna-Laina Fischer, Scott W. Fleming, Amelia Fraser-McKelvie, Gordon Freischlad, Peter M. Frinchaboy, Hai Fu, Lluís Galbany, Rafael Garcia-Dias, D. A. García-Hernández, Luis Alberto Garma Oehmichen, Marcio Antonio Geimba Maia, Héctor Gil-Marín, Kathleen Grabowski, Meng Gu, Hong Guo, Jaewon Ha, Emily

Harrington, Sten Hasselquist, Christian R. Hayes, Fred Hearty, Hector Hernandez Toledo, Harry Hicks, David W. Hogg, Kelly Holley-Bockelmann, Jon A. Holtzman, Bau-Ching Hsieh, Jason A. S. Hunt, Ho Seong Hwang, Héctor J. Ibarra-Medel, Camilo Eduardo Jimenez Angel, Jennifer Johnson, Amy Jones, Henrik Jönsson, Karen Kinemuchi, Juna Kollmeier, Coleman Krawczyk, Kathryn Kreckel, Sandor Kruk, Ivan Lacerna, Ting-Wen Lan, Richard R. Lane, David R. Law, Young-Bae Lee, Cheng Li, Jianhui Lian, Lihwai Lin, Yen-Ting Lin, Chris Lintott, Dan Long, Penélope Longa-Peña, J. Ted Mackereth, Axel de la Macorra, Steven R. Majewski, Olena Malanushenko, Arturo Manchado, Claudia Maraston, Vivek Mariappan, Mariarosa Marinelli, Rui Marques-Chaves, Thomas Masseron, Karen L. Masters, Richard M. McDermid, Nicolás Medina Peña, Sofia Meneses-Goytia, Andrea Merloni, Michael Merrifield, Szabolcs Meszaros, Dante Minniti, Rebecca Minsley, Demitri Muna, Adam D. Myers, Preethi Nair, Janaina Correa do Nascimento, Jeffrey A. Newman, Christian Nitschelm, Matthew D. Olmstead, Audrey Oravetz, Daniel Oravetz, René A. Ortega Minakata, Zach Pace, Nelson Padilla, Pedro A. Palicio, Kaike Pan, Hsi-An Pan, Taniya Parikh, III Parker, James, Sebastien Peirani, Samantha Penny, Will J. Percival, Ismael Perez-Fournon, Thomas Peterken, Marc H. Pinsonneault, Abhishek Prakash, M. Jordan Raddick, Anand Raichoor, Rogemar A. Riffel, Rogério Riffel, Hans-Walter Rix, Annie C. Robin, Alexandre Roman-Lopes, Benjamin Rose, Ashley J. Ross, Graziano Rossi, Kate Rowlands, Kate H. R. Rubin, Sebastián F. Sánchez, José R. Sánchez-Gallego, Conor Sayres, Adam Schaefer, Ricardo P. Schiavon, Jaderson S. Schimoia, Edward Schlafly, David Schlegel, Donald P. Schneider, Mathias Schultheis, Hee-Jong Seo, Shoaib J. Shamsi, Zhengyi Shao, Shiyin Shen, Shravan Shetty, Gregory Simonian, Rebecca J. Smethurst, Jennifer Sobeck, Barbara J. Souter, Ashley Spindler, David V. Stark, Keivan G. Stassun, Matthias Steinmetz, Thaisa Storchi-Bergmann, Guy S. Stringfellow, Genaro Suárez, Jing Sun, Manuchehr Taghizadeh-Popp, Michael S. Talbot, Jamie Tayar, Aniruddha R. Thakar, Daniel Thomas, Patricia Tissera, Rita Tojeiro, Nicholas W. Troup, Eduardo Unda-Sanzana, Octavio Valenzuela, Mariana Vargas-Magaña, José Antonio Vázquez-Mata, David Wake, Benjamin Alan Weaver, Anne-Marie Weijmans, Kyle B. Westfall, Vivienne Wild, John Wilson, Emily Woods, Renbin Yan, Meng Yang, Olga Zamora, Gail Zasowski, Kai Zhang, Zheng Zheng, Zheng Zheng, Guangtun Zhu, Joel C. Zinn, and Hu Zou. The Fifteenth Data Release of the Sloan Digital Sky Surveys: First Release of MaNGA-derived Quantities, Data Visualization Tools, and Stellar Library. *ApJ Supplement*, 240(2):23, February 2019. .

Christopher P Ahn, Rachael Alexandroff, Carlos Allende Prieto, Scott F Anderson, Timothy Anderton, Brett H Andrews, Eric Aubourg, Stephen Bailey, Eduardo Balbinot, Rory Barnes, and Others. The ninth data release of the sloan digital sky survey: First spectroscopic data from the sdss-iii baryon oscillation spectroscopic survey. *Astrophysical Journal, Supplement Series*, 203(2):21, 7 2012.

J. Aird, K. Nandra, E. S. Laird, A. Georgakakis, M. L. N. Ashby, P. Barmby, A. L. Coil, J. S. Huang, A. M. Koekemoer, C. C. Steidel, and C. N. A. Willmer. The evolution of the hard X-ray luminosity function of AGN. *MNRAS*, 401(4):2531–2551, February 2010. .

J. Aird, A. L. Coil, A. Georgakakis, K. Nandra, G. Barro, and P. G. Pérez-González. The evolution of the X-ray luminosity functions of unabsorbed and absorbed AGNs out to z$\sim$ 5. *MNRAS*, 451(2):1892–1927, August 2015. .

J. Aird, A. L. Coil, and A. Georgakakis. X-rays across the galaxy population - I. Tracing the main sequence of star formation. *MNRAS*, 465(3):3390–3415, March 2017. .

J. Aird, A. L. Coil, and A. Georgakakis. X-rays across the galaxy population - II. The distribution of AGN accretion rates as a function of stellar mass and redshift. *MNRAS*, 474:1225–1249, January 2018. .

James Aird and Alison L. Coil. The AGN-galaxy-halo connection: The distribution of AGN host halo masses to z=2.5. *arXiv e-prints*, art. arXiv:2010.02957, October 2020.

James Aird, Alison L. Coil, John Moustakas, Michael R. Blanton, Scott M. Burles, Richard J. Cool, Daniel J. Eisenstein, M. Stephen M. Smith, Kenneth C. Wong, and Guangtun Zhu. PRIMUS: The Dependence of AGN Accretion on Host Stellar Mass and Color. *ApJ*, 746(1):90, February 2012. .

M. C. Aller and D. Richstone. The Cosmic Density of Massive Black Holes from Galaxy Velocity Dispersions. *Astronomical Jmynal*, 124(6):3035–3041, December 2002. .

V. Allevato, A. Finoguenov, N. Cappelluti, T. Miyaji, G. Hasinger, M. Salvato, M. Brusa, R. Gilli, G. Zamorani, F. Shankar, J. B. James, H. J. McCracken, A. Bongiorno, A. Merloni, J. A. Peacock, J. Silverman, and A. Comastri. The XMM-Newton Wide Field Survey in the COSMOS Field: Redshift Evolution of AGN Bias and Subdominant Role of Mergers in Triggering Moderate-luminosity AGNs at Redshifts up to 2.2. *ApJ*, 736(2):99, August 2011. .

V. Allevato, A. Finoguenov, G. Hasinger, T. Miyaji, N. Cappelluti, M. Salvato, G. Zamorani, R. Gilli, M. R. George, M. Tanaka, M. Brusa, J. Silverman, F. Civano, M. Elvis, and F. Shankar. Occupation of X-Ray-selected Galaxy Groups by X-Ray Active Galactic Nuclei. *ApJ*, 758(1):47, October 2012. .

V. Allevato, A. Finoguenov, F. Civano, N. Cappelluti, F. Shankar, T. Miyaji, G. Hasinger, R. Gilli, G. Zamorani, G. Lanzuisi, M. Salvato, M. Elvis, A. Comastri, and J. Silverman. Clustering of Moderate Luminosity X-Ray-selected Type 1 and Type 2 AGNS at Z ~3. *ApJ*, 796(1):4, November 2014. .

Viola Allevato, Francesco Shankar, Christopher Marsden, Uluk Rasulov, Akke Viitanen, Antonis Georgakakis, Andrea Ferrara, and Alexis Finoguenov. Building robust

AGN mock catalogs to unveil black hole evolution and for survey planning. *arXiv e-prints*, art. arXiv:2105.02883, May 2021.

D. Anglés-Alcázar, F. Özel, and R. Davé. Black Hole-Galaxy Correlations without Self-regulation. *ApJ*, 770:5, June 2013. .

D. Anglés-Alcázar, F. Özel, R. Davé, N. Katz, J. A. Kollmeier, and B. D. Oppenheimer. Torque-limited Growth of Massive Black Holes in Galaxies across Cosmic Time. *ApJ*, 800:127, February 2015. .

Miguel Aragon-Calvo, Mark Subbarao, and Alex Szalay. A Flight through the Universe, by the Sloan Digital Sky Survey, 2012. URL https://www.youtube.com/watch?v=08LBltePDZw. [Online; accessed 30-August-2020].

R. Aversa, A. Lapi, G. de Zotti, F. Shankar, and L. Danese. Black Hole and Galaxy Coevolution from Continuity Equation and Abundance Matching. *ApJ*, 810(1):74, September 2015a. .

R. Aversa, A. Lapi, G. de Zotti, F. Shankar, and L. Danese. Black Hole and Galaxy Coevolution from Continuity Equation and Abundance Matching. *ApJ*, 810(1):74, September 2015b. .

John N. Bahcall, Ben-Zion Kozlovsky, and E. E. Salpeter. On the Time Dependence of Emission-Line Strengths from a Photoionized Nebula. *ApJ*, 171:467, February 1972. .

Ivan K. Baldry, Karl Glazebrook, Jon Brinkmann, Željko Ivezić, Robert H. Lupton, Robert C. Nichol, and Alexander S. Szalay. Quantifying the Bimodal Color-Magnitude Distribution of Galaxies. *ApJ*, 600(2):681–694, January 2004. .

Michael L. Balogh, Julio F. Navarro, and Simon L. Morris. The Origin of Star Formation Gradients in Rich Galaxy Clusters. *ApJ*, 540(1):113–121, September 2000. .

D. J. Barnes, R. Kannan, M. Vogelsberger, and F. Marinacci. Radiative AGN feedback on a moving mesh: the impact of the galactic disc and dust physics on outflow properties. *arXiv e-prints*, December 2018.

Josh Barnes and Piet Hut. A hierarchical o (n log n) force-calculation algorithm. *nature*, 324(6096):446, 1986.

Joshua E. Barnes. Encounters of Disk/Halo Galaxies. *ApJ*, 331:699, August 1988. .

Joshua E. Barnes and Lars Hernquist. Dynamics of interacting galaxies. *Annual Review of Astron and Astrophys*, 30:705–742, January 1992. .

Joshua E. Barnes and Lars E. Hernquist. Fueling Starburst Galaxies with Gas-rich Mergers. *Apj Letters*, 370:L65, April 1991. .

Aaron J. Barth, Luis C. Ho, and Wallace L. W. Sargent. A Study of the Direct Fitting Method for Measurement of Galaxy Velocity Dispersions. *Astronomical Jmynal*, 124 (5):2607–2614, November 2002. .

Peter Behroozi, Risa H. Wechsler, Andrew P. Hearin, and Charlie Conroy. UNIVERSEMACHINE: The correlation between galaxy growth and dark matter halo assembly from z = 0-10. *MNRAS*, 488(3):3143–3194, September 2019. .

Peter S. Behroozi, Risa H. Wechsler, and Charlie Conroy. The Average Star Formation Histories of Galaxies in Dark Matter Halos from z = 0-8. *ApJ*, 770(1):57, June 2013. .

A. Beifiori, S. Courteau, E. M. Corsini, and Y. Zhu. On the correlations between galaxy properties and supermassive black hole mass. *MNRAS*, 419(3):2497–2528, Jan 2012. .

Eric F. Bell, Daniel H. McIntosh, Neal Katz, and Martin D. Weinberg. The Optical and Near-Infrared Properties of Galaxies. I. Luminosity and Stellar Mass Functions. *ApJ Supplement*, 149(2):289–312, December 2003. .

Eric F. Bell, Christian Wolf, Klaus Meisenheimer, Hans-Walter Rix, Andrea Borch, Simon Dye, Martina Kleinheinrich, Lutz Wisotzki, and Daniel H. McIntosh. Nearly 5000 Distant Early-Type Galaxies in COMBO-17: A Red Sequence and Its Evolution since z~1. *ApJ*, 608(2):752–767, June 2004. .

Robert G Belleman, Jeroen Bédorf, and Simon F Portegies Zwart. High performance direct gravitational n-body simulations on graphics processing units ii: An implementation in cuda. *New Astronomy*, 13(2):103–112, 2008.

R. Bender and J. L. Nieto. Internal kinematics of low-luminosity ellipsoidal galaxies. *A&A*, 239:97–112, November 1990.

CL Bennett, D Larson, JL Weiland, N Jarosik, G Hinshaw, N Odegard, KM Smith, RS Hill, B Gold, M Halpern, et al. Nine-year wilkinson microwave anisotropy probe (wmap) observations: final maps and results. *The Astrophysical Journal Supplement Series*, 208(2):20, 2013.

Lars Bergström. Dark matter candidates. *New Journal of Physics*, 11(10):105006, 2009.

M. Bernardi, F. Shankar, J. B. Hyde, S. Mei, F. Marulli, and R. K. Sheth. Galaxy luminosities, stellar masses, sizes, velocity dispersions as a function of morphological type. *MNRAS*, 404(4):2087–2122, June 2010. .

M. Bernardi, A. Meert, R. K. Sheth, J. L. Fischer, M. Huertas-Company, C. Maraston, F. Shankar, and V. Vikram. The high mass end of the stellar mass function: Dependence on stellar population models and agreement between fits to the light profile. *MNRAS*, 467(2):2217–2233, May 2017. .

M. Bernardi, R. K. Sheth, J. L. Fischer, A. Meert, K. H. Chae, H. Dominguez-Sanchez, M. Huertas-Company, F. Shankar, and V. Vikram. Stellar mass functions and implications for a variable IMF. *MNRAS*, 475(1):757–771, March 2018. .

M. Bernardi, H. Domínguez Sánchez, J. R. Brownstein, N. Drory, and R. K. Sheth. Galaxy properties as revealed by MaNGA - II. Differences in stellar populations of slow and fast rotator ellipticals and dependence on environment. *MNRAS*, 489(4): 5633–5652, November 2019. .

M. Bernardi, H. Domínguez Sánchez, B. Margalef-Bentabol, F. Nikakhtar, and R. K. Sheth. The stellar mass Fundamental Plane: the virial relation and a very thin plane for slow rotators. *MNRAS*, 494(4):5148–5160, June 2020. .

Mariangela Bernardi, Ravi K. Sheth, Robert C. Nichol, D. P. Schneider, and J. Brinkmann. Colors, Magnitudes, and Velocity Dispersions in Early-Type Galaxies: Implications for Galaxy Ages and Metallicities. *Astronomical Jmynal*, 129(1):61–72, Jan 2005. .

Mariangela Bernardi, Ravi K. Sheth, Elena Tundo, and Joseph B. Hyde. Selection Bias in the $M_\bullet$-σ and $M_\bullet$-L Correlations and Its Consequences. *ApJ*, 660(1):267–275, May 2007. .

Mariangela Bernardi, Nathan Roche, Francesco Shankar, and Ravi K. Sheth. Curvature in the colour-magnitude relation but not in colour-σ: major dry mergers at M_* > 2 $\times$ 10^{11} $M_\odot$? *MNRAS*, 412(1):684–704, Mar 2011a. .

Mariangela Bernardi, Nathan Roche, Francesco Shankar, and Ravi K. Sheth. *MNRAS*, 412(1):L6–L10, Mar 2011b. .

E. Bertin. SkyMaker: astronomical image simulations made easy. *Memorie della Società Astronomica Italiana*, 80:422, January 2009.

G. Bertin and M. Lombardi. Looking at the Fundamental Plane through a Gravitational Lens. *Apj Letters*, 648(1):L17–L20, September 2006. .

J. Binney and G. A. Mamon. M/L and velocity anisotropy from observations of spherical galaxies, of must M 87 have a massive black hole ? *MNRAS*, 200:361–375, July 1982. .

James Binney and Scott Tremaine. *Galactic Dynamics: Second Edition*. 2008.

Yuval Birnboim and Avishai Dekel. Virial shocks in galactic haloes? *MNRAS*, 345(1): 349–364, October 2003. .

Yuval Birnboim, Avishai Dekel, and Eyal Neistein. Bursting and quenching in massive galaxies without major mergers or AGNs. *MNRAS*, 380(1):339–352, September 2007. .

A. Blanchard, D. Valls-Gabaud, and G. A. Mamon. The origin of the galaxy luminosity function and the thermal evolution of the intergalactic medium. *A&A*, 264:365–378, October 1992.

Roger Blandford, David Meier, and Anthony Readhead. Relativistic jets from active galactic nuclei. *Annual Review of Astronomy and Astrophysics*, 57(1): 467–509, Aug 2019. ISSN 1545-4282. . URL http://dx.doi.org/10.1146/annurev-astro-081817-051948.

Michael R. Blanton, Matthew A. Bershady, Bela Abolfathi, Franco D. Albareti, Carlos Allende Prieto, Andres Almeida, Javier Alonso-García, Friedrich Anders, Scott F. Anderson, Brett Andrews, Erik Aquino-Ortíz, Alfonso Aragón-Salamanca, Maria Argudo-Fernández, Eric Armengaud, Eric Aubourg, Vladimir Avila-Reese, Carles Badenes, Stephen Bailey, Kathleen A. Barger, Jorge Barrera-Ballesteros, Curtis Bartosz, Dominic Bates, Falk Baumgarten, Julian Bautista, Rachael Beaton, Timothy C. Beers, Francesco Belfiore, Chad F. Bender, Andreas A. Berlind, Mariangela Bernardi, Florian Beutler, Jonathan C. Bird, Dmitry Bizyaev, Guillermo A. Blanc, Michael Blomqvist, Adam S. Bolton, Médéric Boquien, Jura Borissova, Remco van den Bosch, Jo Bovy, William N. Brandt, Jonathan Brinkmann, Joel R. Brownstein, Kevin Bundy, Adam J. Burgasser, Etienne Burtin, Nicolás G. Busca, Michele Cappellari, Maria Leticia Delgado Carigi, Joleen K. Carlberg, Aurelio Carnero Rosell, Ricardo Carrera, Nancy J. Chanover, Brian Cherinka, Edmond Cheung, Yilen Gómez Maqueo Chew, Cristina Chiappini, Peter Doohyun Choi, Drew Chojnowski, Chia-Hsun Chuang, Haeun Chung, Rafael Fernando Cirolini, Nicolas Clerc, Roger E. Cohen, Johan Comparat, Luiz da Costa, Marie-Claude Cousinou, Kevin Covey, Jeffrey D. Crane, Rupert A. C. Croft, Irene Cruz-Gonzalez, Daniel Garrido Cuadra, Katia Cunha, Guillermo J. Damke, Jeremy Darling, Roger Davies, Kyle Dawson, Axel de la Macorra, Flavia Dell'Agli, Nathan De Lee, Timothée Delubac, Francesco Di Mille, Aleks Diamond-Stanic, Mariana Cano-Díaz, John Donor, Juan José Downes, Niv Drory, Hélion du Mas des Bourboux, Christopher J. Duckworth, Tom Dwelly, Jamie Dyer, Garrett Ebelke, Arthur D. Eigenbrot, Daniel J. Eisenstein, Eric Emsellem, Mike Eracleous, Stephanie Escoffier, Michael L. Evans, Xiaohui Fan, Emma Fernández-Alvar, J. G. Fernandez-Trincado, Diane K. Feuillet, Alexis Finoguenov, Scott W. Fleming, Andreu Font-Ribera, Alexander Fredrickson, Gordon Freischlad, Peter M. Frinchaboy, Carla E. Fuentes, Lluís Galbany, R. Garcia-Dias, D. A. García-Hernández, Patrick Gaulme, Doug Geisler, Joseph D. Gelfand, Héctor Gil-Marín, Bruce A. Gillespie, Daniel Goddard, Violeta Gonzalez-Perez, Kathleen Grabowski, Paul J. Green, Catherine J. Grier, James E. Gunn, Hong Guo, Julien Guy, Alex Hagen, ChangHoon Hahn, Matthew Hall, Paul Harding, Sten Hasselquist, Suzanne L. Hawley, Fred Hearty, Jonay I. Gonzalez Hernández, Shirley Ho, David W. Hogg, Kelly Holley-Bockelmann, Jon A. Holtzman, Parker H. Holzer, Joseph Huehnerhoff, Timothy A. Hutchinson, Ho Seong Hwang, Héctor J. Ibarra-Medel, Gabriele

da Silva Ilha, Inese I. Ivans, KeShawn Ivory, Kelly Jackson, Trey W. Jensen, Jennifer A. Johnson, Amy Jones, Henrik Jönsson, Eric Jullo, Vikrant Kamble, Karen Kinemuchi, David Kirkby, Francisco-Shu Kitaura, Mark Klaene, Gillian R. Knapp, Jean-Paul Kneib, Juna A. Kollmeier, Ivan Lacerna, Richard R. Lane, Dustin Lang, David R. Law, Daniel Lazarz, Youngbae Lee, Jean-Marc Le Goff, Fu-Heng Liang, Cheng Li, Hongyu Li, Jianhui Lian, Marcos Lima, Lihwai Lin, Yen-Ting Lin, Sara Bertran de Lis, Chao Liu, Miguel Angel C. de Icaza Lizaola, Dan Long, Sara Lucatello, Britt Lundgren, Nicholas K. MacDonald, Alice Deconto Machado, Chelsea L. MacLeod, Suvrath Mahadevan, Marcio Antonio Geimba Maia, Roberto Maiolino, Steven R. Majewski, Elena Malanushenko, Viktor Malanushenko, Arturo Manchado, Shude Mao, Claudia Maraston, Rui Marques-Chaves, Thomas Masseron, Karen L. Masters, Cameron K. McBride, Richard M. McDermid, Brianne McGrath, Ian D. McGreer, Nicolás Medina Peña, Matthew Melendez, Andrea Merloni, Michael R. Merrifield, Szabolcs Meszaros, Andres Meza, Ivan Minchev, Dante Minniti, Takamitsu Miyaji, Surhud More, John Mulchaey, Francisco Müller-Sánchez, Demitri Muna, Ricardo R. Munoz, Adam D. Myers, Preethi Nair, Kirpal Nandra, Janaina Correa do Nascimento, Alenka Negrete, Melissa Ness, Jeffrey A. Newman, Robert C. Nichol, David L. Nidever, Christian Nitschelm, Pierros Ntelis, Julia E. O'Connell, Ryan J. Oelkers, Audrey Oravetz, Daniel Oravetz, Zach Pace, Nelson Padilla, Nathalie Palanque-Delabrouille, Pedro Alonso Palicio, Kaike Pan, John K. Parejko, Taniya Parikh, Isabelle Pâris, Changbom Park, Alim Y. Patten, Sebastien Peirani, Marcos Pellejero-Ibanez, Samantha Penny, Will J. Percival, Ismael Perez-Fournon, Patrick Petitjean, Matthew M. Pieri, Marc Pinsonneault, Alice Pisani, Radosław Poleski, Francisco Prada, Abhishek Prakash, Anna Bárbara de Andrade Queiroz, M. Jordan Raddick, Anand Raichoor, Sand ro Barboza Rembold, Hannah Richstein, Rogemar A. Riffel, Rogério Riffel, Hans-Walter Rix, Annie C. Robin, Constance M. Rockosi, Sergio Rodríguez-Torres, A. Roman-Lopes, Carlos Román-Zúñiga, Margarita Rosado, Ashley J. Ross, Graziano Rossi, John Ruan, Rossana Ruggeri, Eli S. Rykoff, Salvador Salazar-Albornoz, Mara Salvato, Ariel G. Sánchez, D. S. Aguado, José R. Sánchez-Gallego, Felipe A. Santana, Basílio Xavier Santiago, Conor Sayres, Ricardo P. Schiavon, Jaderson da Silva Schimoia, Edward F. Schlafly, David J. Schlegel, Donald P. Schneider, Mathias Schultheis, William J. Schuster, Axel Schwope, Hee-Jong Seo, Zhengyi Shao, Shiyin Shen, Matthew Shetrone, Michael Shull, Joshua D. Simon, Danielle Skinner, M. F. Skrutskie, Anže Slosar, Verne V. Smith, Jennifer S. Sobeck, Flavia Sobreira, Garrett Somers, Diogo Souto, David V. Stark, Keivan Stassun, Fritz Stauffer, Matthias Steinmetz, Thaisa Storchi-Bergmann, Alina Streblyanska, Guy S. Stringfellow, Genaro Suárez, Jing Sun, Nao Suzuki, Laszlo Szigeti, Manuchehr Taghizadeh-Popp, Baitian Tang, Charling Tao, Jamie Tayar, Mita Tembe, Johanna Teske, Aniruddha R. Thakar, Daniel Thomas, Benjamin A. Thompson, Jeremy L. Tinker, Patricia Tissera, Rita Tojeiro, Hector Hernandez Toledo, Sylvain de la Torre, Christy Tremonti, Nicholas W. Troup, Octavio Valenzuela, Inma Martinez

Valpuesta, Jaime Vargas-González, Mariana Vargas-Magaña, Jose Alberto Vazquez, Sandro Villanova, M. Vivek, Nicole Vogt, David Wake, Rene Walterbos, Yuting Wang, Benjamin Alan Weaver, Anne-Marie Weijmans, David H. Weinberg, Kyle B. Westfall, David G. Whelan, Vivienne Wild, John Wilson, W. M. Wood-Vasey, Dominika Wylezalek, Ting Xiao, Renbin Yan, Meng Yang, Jason E. Ybarra, Christophe Yèche, Nadia Zakamska, Olga Zamora, Pauline Zarrouk, Gail Zasowski, Kai Zhang, Gong-Bo Zhao, Zheng Zheng, Zheng Zheng, Xu Zhou, Zhi-Min Zhou, Guangtun B. Zhu, Manuela Zoccali, and Hu Zou. Sloan Digital Sky Survey IV: Mapping the Milky Way, Nearby Galaxies, and the Distant Universe. *Astronomical Journal*, 154(1):28, July 2017. .

George R Blumenthal, SM Faber, Joel R Primack, and Martin J Rees. Formation of galaxies and large-scale structure with cold dark matter. *Nature*, 311(5986):517, 1984.

A. Bongiorno, A. Merloni, M. Brusa, B. Magnelli, M. Salvato, M. Mignoli, G. Zamorani, F. Fiore, D. Rosario, V. Mainieri, H. Hao, A. Comastri, C. Vignali, I. Balestra, S. Bardelli, S. Berta, F. Civano, P. Kampczyk, E. Le Floc'h, E. Lusso, D. Lutz, L. Pozzetti, F. Pozzi, L. Riguccini, F. Shankar, and J. Silverman. Accreting supermassive black holes in the COSMOS field and the connection to their host galaxies. *MNRAS*, 427(4):3103–3133, December 2012. .

A. Bongiorno, A. Schulze, A. Merloni, G. Zamorani, O. Ilbert, F. La Franca, Y. Peng, E. Piconcelli, V. Mainieri, J. D. Silverman, M. Brusa, F. Fiore, M. Salvato, and N. Scoville. AGN host galaxy mass function in COSMOS. Is AGN feedback responsible for the mass-quenching of galaxies? *A&A*, 588:A78, April 2016. .

Frédéric Bournaud, Avishai Dekel, Romain Teyssier, Marcello Cacciato, Emanuele Daddi, Stéphanie Juneau, and Francesco Shankar. Black Hole Growth and Active Galactic Nuclei Obscuration by Instability-driven Inflows in High-redshift Disk Galaxies Fed by Cold Streams. *Apj Letters*, 741(2):L33, November 2011. .

R. G. Bower, A. J. Benson, R. Malbon, J. C. Helly, C. S. Frenk, C. M. Baugh, S. Cole, and C. G. Lacey. Breaking the hierarchy of galaxy formation. *MNRAS*, 370(2):645–655, August 2006. .

Michael Boylan-Kolchin, Chung-Pei Ma, and Eliot Quataert. Dynamical friction and galaxy merging time-scales. *MNRAS*, 383(1):93–101, January 2008. .

Gabriel B. Brammer, K. E. Whitaker, P. G. van Dokkum, D. Marchesini, M. Franx, M. Kriek, I. Labbé, K. S. Lee, A. Muzzin, R. F. Quadri, G. Rudnick, and R. Williams. The Number Density and Mass Density of Star-forming and Quiescent Galaxies at 0.4 ¡= z ¡= 2.2. *ApJ*, 739(1):24, September 2011. .

J. Brinchmann, S. Charlot, S. D. M. White, C. Tremonti, G. Kauffmann, T. Heckman, and J. Brinkmann. The physical properties of star-forming galaxies in the low-redshift Universe. *MNRAS*, 351(4):1151–1179, July 2004. .

Volker Bromm and Abraham Loeb. Formation of the First Supermassive Black Holes. *ApJ*, 596(1):34–46, October 2003. .

Greg L Bryan, Michael L Norman, Brian W O'Shea, Tom Abel, John H Wise, Matthew J Turk, Daniel R Reynolds, David C Collins, Peng Wang, Samuel W Skillman, et al. Enzo: An adaptive mesh refinement code for astrophysics. *The Astrophysical Journal Supplement Series*, 211(2):19, 2014.

Stewart Buchan and Francesco Shankar. Setting firmer constraints on the evolution of the most massive, central galaxies from their local abundances and ages. *MNRAS*, 462(2):2001–2010, October 2016. .

Kevin Bundy, Matthew A. Bershady, David R. Law, Renbin Yan, Niv Drory, Nicholas MacDonald, David A. Wake, Brian Cherinka, José R. Sánchez-Gallego, Anne-Marie Weijmans, Daniel Thomas, Christy Tremonti, Karen Masters, Lodovico Coccato, Aleksandar M. Diamond-Stanic, Alfonso Aragón-Salamanca, Vladimir Avila-Reese, Carles Badenes, Jésus Falcón-Barroso, Francesco Belfiore, Dmitry Bizyaev, Guillermo A. Blanc, Joss Bland-Hawthorn, Michael R. Blanton, Joel R. Brownstein, Nell Byler, Michele Cappellari, Charlie Conroy, Aaron A. Dutton, Eric Emsellem, James Etherington, Peter M. Frinchaboy, Hai Fu, James E. Gunn, Paul Harding, Evelyn J. Johnston, Guinevere Kauffmann, Karen Kinemuchi, Mark A. Klaene, Johan H. Knapen, Alexie Leauthaud, Cheng Li, Lihwai Lin, Roberto Maiolino, Viktor Malanushenko, Elena Malanushenko, Shude Mao, Claudia Maraston, Richard M. McDermid, Michael R. Merrifield, Robert C. Nichol, Daniel Oravetz, Kaike Pan, John K. Parejko, Sebastian F. Sanchez, David Schlegel, Audrey Simmons, Oliver Steele, Matthias Steinmetz, Karun Thanjavur, Benjamin A. Thompson, Jeremy L. Tinker, Remco C. E. van den Bosch, Kyle B. Westfall, David Wilkinson, Shelley Wright, Ting Xiao, and Kai Zhang. Overview of the SDSS-IV MaNGA Survey: Mapping nearby Galaxies at Apache Point Observatory. *ApJ*, 798(1):7, January 2015. .

E. Margaret Burbidge, G. R. Burbidge, and R. A. Fish. The Masses of Elliptical Galaxies. I. a Redetermination of the Mass of M32. *ApJ*, 133:393, March 1961. .

A. Burkert. The Structure of Dark Matter Halos in Dwarf Galaxies. *Apj Letters*, 447: L25–L28, July 1995. .

Turgay Caglar, Leonard Burtscher, Bernhard Brand, Jarle Brinchmann, Richard I. Davies, Erin K. S. Hicks, Michael Koss, Ming-Yi Lin, Witold Maciejewski, Francisco Müller-Sánchez, Rogemar A. Riffel, Rogério Riffel, David J. Rosario, Marc Schartmann, Allan Schnorr-Müller, T. Taro Shimizu, Thaisa Storchi-Bergmann, Sylvain Veilleux, Gilles O. de Xivry, and Vardha N. Bennert. Llama: The m_{BH} - $\sigma_\star$ relation of the most luminous local agns, 2019.

Carlo Cannarozzo, Alessandro Sonnenfeld, and Carlo Nipoti. The cosmic evolution of the stellar mass-velocity dispersion relation of early-type galaxies. *MNRAS*, 498(1): 1101–1120, October 2020. .

N. Caon, M. Capaccioli, and M. D'Onofrio. On the shape of the light profiles of early-type galaxies. *MNRAS*, 265:1013–1021, December 1993. .

Michele Cappellari, R. Bacon, M. Bureau, M. C. Damen, Roger L. Davies, P. T. de Zeeuw, Eric Emsellem, Jesús Falcón-Barroso, Davor Krajnović, Harald Kuntschner, Richard M. McDermid, Reynier F. Peletier, Marc Sarzi, Remco C. E. van den Bosch, and Glenn van de Ven. The SAURON project - IV. The mass-to-light ratio, the virial mass estimator and the Fundamental Plane of elliptical and lenticular galaxies. *MNRAS*, 366(4):1126–1150, March 2006. .

Michele Cappellari, Nicholas Scott, Katherine Alatalo, Leo Blitz, Maxime Bois, Frédéric Bournaud, M. Bureau, Alison F. Crocker, Roger L. Davies, Timothy A. Davis, P. T. de Zeeuw, Pierre-Alain Duc, Eric Emsellem, Sadegh Khochfar, Davor Krajnović, Harald Kuntschner, Richard M. McDermid, Raffaella Morganti, Thorsten Naab, Tom Oosterloo, Marc Sarzi, Paolo Serra, Anne-Marie Weijmans, and Lisa M. Young. The ATLAS^{3D} project - XV. Benchmark for early-type galaxies scaling relations from 260 dynamical models: mass-to-light ratio, dark matter, Fundamental Plane and Mass Plane. *MNRAS*, 432(3):1709–1741, July 2013a. .

Michele Cappellari, Nicholas Scott, Katherine Alatalo, Leo Blitz, Maxime Bois, Frédéric Bournaud, M. Bureau, Alison F. Crocker, and et al. The ATLAS^{3D} project - XV. Benchmark for early-type galaxies scaling relations from 260 dynamical models: mass-to-light ratio, dark matter, Fundamental Plane and Mass Plane. *MNRAS*, 432(3):1709–1741, Jul 2013b. .

Michele Cappellari, Aaron J. Romanowsky, Jean P. Brodie, Duncan A. Forbes, Jay Strader, Caroline Foster, Sreeja S. Kartha, Nicola Pastorello, Vincenzo Pota, Lee R. Spitler, Christopher Usher, and Jacob A. Arnold. Small Scatter and Nearly Isothermal Mass Profiles to Four Half-light Radii from Two-dimensional Stellar Dynamics of Early-type Galaxies. *Astrophysical Journall*, 804(1):L21, May 2015. .

Caterina Caravita, Luca Ciotti, and Silvia Pellegrini. Jeans modelling of axisymmetric galaxies with multiple stellar populations. *MNRAS*, 506(1):1480–1497, September 2021. .

C. M. Carollo, T. J. Bschorr, A. Renzini, S. J. Lilly, P. Capak, A. Cibinel, O. Ilbert, M. Onodera, N. Scoville, E. Cameron, B. Mobasher, D. Sanders, and Y. Taniguchi. Newly Quenched Galaxies as the Cause for the Apparent Evolution in Average Size of the Population. *ApJ*, 773(2):112, August 2013. .

R. Carraro, G. Rodighiero, P. Cassata, M. Brusa, F. Shankar, I. Baronchelli, E. Daddi, I. Delvecchio, A. Franceschini, R. Griffiths, C. Gruppioni, E. López-Navas,

C. Mancini, S. Marchesi, M. Negrello, A. Puglisi, E. Sani, and H. Suh. Coevolution of black hole accretion and star formation in galaxies up to z = 3.5. *A&A*, 642:A65, October 2020. .

Gilles Chabrier. Galactic Stellar and Substellar Initial Mass Function. *Publications of the ASP*, 115(809):763–795, July 2003. .

Kyu-Hyun Chae, Mariangela Bernardi, and Andrey V. Kravtsov. Modelling mass distribution in elliptical galaxies: mass profiles and their correlation with velocity dispersion profiles. *MNRAS*, 437(4):3670–3687, February 2014. .

Kyu-Hyun Chae, Mariangela Bernardi, and Ravi K. Sheth. Modeling Nearly Spherical Pure-bulge Galaxies with a Stellar Mass-to-light Ratio Gradient under the ΛCDM and MOND Paradigms. I. Methodology, Dynamical Stellar Mass, and Fundamental Mass Plane. *ApJ*, 860(1):81, June 2018. .

Kyu-Hyun Chae, Mariangela Bernardi, and Ravi K. Sheth. Modeling Nearly Spherical Pure-bulge Galaxies with a Stellar Mass-to-light Ratio Gradient under the ΛCDM and MOND Paradigms. II. The Orbital Anisotropy of Slow Rotators within the Effective Radius. *ApJ*, 874(1):41, March 2019. .

Kenneth C Chambers, EA Magnier, N Metcalfe, HA Flewelling, ME Huber, CZ Waters, L Denneau, PW Draper, D Farrow, DP Finkbeiner, et al. The pan-starrs1 surveys. *arXiv preprint arXiv:1612.05560*, 2016.

Zhu Chen, S. M. Faber, David C. Koo, Rachel S. Somerville, Joel R. Primack, Avishai Dekel, Aldo Rodríguez-Puebla, Yicheng Guo, Guillermo Barro, Dale D. Kocevski, and et al. Quenching as a contest between galaxy halos and their central black holes. *The Astrophysical Journal*, 897(1):102, Jul 2020. ISSN 1538-4357. . URL http://dx.doi.org/10.3847/1538-4357/ab9633.

Lars Lindberg Christense, Lars Holm Nielsen, Kaspar K. Nielsen, and Teis Johansen. The ESA/ESO/NASA fits liberator 3 [Software Application]. 2019. [Online; accessed 04-August-2020].

C. Cicone, R. Maiolino, E. Sturm, J. Graciá-Carpio, C. Feruglio, R. Neri, S. Aalto, R. Davies, and et al. Massive molecular outflows and evidence for AGN feedback from CO observations. *A&A*, 562:A21, February 2014. .

A. Cimatti, C. Nipoti, and P. Cassata. Fast evolving size of early-type galaxies at ¿z ¿ 2 and the role of dissipationless (dry) merging. *MNRAS*, 422(1):L62–L66, May 2012. .

Andrea Cimatti, E Daddi, and A Renzini. Mass downsizing and "top-down" assembly of early-type galaxies. *Astronomy & Astrophysics*, 453(2):L29–L33, 2006.

L. Ciotti and G. Bertin. Analytical properties of the $R^{1/m}$ law. *A&A*, 352:447–451, December 1999.

L. Ciotti, B. Lanzoni, and A. Renzini. The tilt of the fundamental plane of elliptical galaxies - I. Exploring dynamical and structural effects. *MNRAS*, 282(1):1–12, September 1996. .

Michele Cirasuolo, Francesco Shankar, Gian Luigi Granato, Gianfranco De Zotti, and Luigi Danese. Dynamical and Photometric Imprints of Feedback Processes on the Formation and Evolution of E/S0 Galaxies. *ApJ*, 629(2):816–824, August 2005. .

Roger E. Cohen, Paul Goudfrooij, Matteo Correnti, Oleg Y. Gnedin, William E. Harris, Rupali Chandar, Thomas H. Puzia, and Rubén Sánchez-Janssen. The Strikingly Metal-rich Halo of the Sombrero Galaxy. *ApJ*, 890(1):52, February 2020. .

Shaun Cole, Cedric G Lacey, Carlton M Baugh, and Carlos S Frenk. Hierarchical galaxy formation. *Monthly Notices of the Royal Astronomical Society*, 319(1):168–204, 2000.

F. Combes, F. Debbasch, D. Friedli, and D. Pfenniger. Box and peanut shapes generated by stellar bars. *A&A*, 233:82, July 1990.

J. Comparat, A. Merloni, M. Salvato, K. Nandra, T. Boller, A. Georgakakis, A. Finoguenov, T. Dwelly, J. Buchner, A. Del Moro, N. Clerc, Y. Wang, G. Zhao, F. Prada, G. Yepes, M. Brusa, M. Krumpe, and T. Liu. Active galactic nuclei and their large-scale structure: an eROSITA mock catalogue. *MNRAS*, 487(2):2005–2029, August 2019. .

Charlie Conroy. Modeling the panchromatic spectral energy distributions of galaxies. *Annual Review of Astronomy and Astrophysics*, 51:393–455, 2013.

Charlie Conroy and Pieter G. van Dokkum. The Stellar Initial Mass Function in Early-type Galaxies From Absorption Line Spectroscopy. II. Results. *ApJ*, 760(1):71, November 2012. .

Charlie Conroy and Martin White. A Simple Model for Quasar Demographics. *ApJ*, 762(2):70, January 2013. .

Christopher J. Conselice, Matthew A. Bershady, Mark Dickinson, and Casey Papovich. A Direct Measurement of Major Galaxy Mergers at z¡˜3. *Astronomical Jmynal*, 126(3): 1183–1207, September 2003. .

M. Cook, E. Barausse, C. Evoli, A. Lapi, and G. L. Granato. Two-phase galaxy formation: the evolutionary properties of galaxies. *MNRAS*, 402(4):2113–2126, March 2010. .

Asantha Cooray and Ravi Sheth. Halo models of large scale structure. *Physics Reports*, 372(1):1–129, December 2002. .

Edvige Corbelli and Paolo Salucci. The extended rotation curve and the dark matter halo of m33. *Monthly Notices of the Royal Astronomical Society*, 311(2):441–447, 2000.

M. Covington, A. Dekel, T. J. Cox, P. Jonsson, and J. R. Primack. Predicting the properties of the remnants of dissipative galaxy mergers. *MNRAS*, 384(1):94–106, February 2008. .

M. D. Covington, J. R. Primack, L. A. Porter, D. J. Croton, R. S. Somerville, and A. Dekel. The role of dissipation in the scaling relations of cosmological merger remnants. *MNRAS*, 415(4):3135–3152, August 2011. .

T. J. Cox, Patrik Jonsson, Joel R. Primack, and Rachel S. Somerville. Feedback in simulations of disc-galaxy major mergers. *MNRAS*, 373(3):1013–1038, December 2006. .

Darren J Croton, Volker Springel, Simon DM White, Gabriella De Lucia, Carlos S Frenk, Liang Gao, Adrian Jenkins, Guinevere Kauffmann, JF Navarro, and Naoki Yoshida. The many lives of active galactic nuclei: cooling flows, black holes and the luminosities and colours of galaxies. *Monthly Notices of the Royal Astronomical Society*, 365(1): 11–28, 2006.

Ivana Damjanov, Roberto G. Abraham, Karl Glazebrook, Patrick J. McCarthy, Evelyn Caris, Raymond G. Carlberg, Hsiao-Wen Chen, David Crampton, Andrew W. Green, Inger Jørgensen, Stéphanie Juneau, Damien Le Borgne, Ronald O. Marzke, Erin Mentuch, Richard Murowinski, Kathy Roth, Sandra Savaglio, and Haojing Yan. Red Nuggets at High Redshift: Structural Evolution of Quiescent Galaxies Over 10 Gyr of Cosmic History. *Apj Letters*, 739(2):L44, October 2011. .

Ivana Damjanov, Margaret J. Geller, H. Jabran Zahid, and Ho Seong Hwang. Quiescent Compact Galaxies at Intermediate Redshift in the COSMOS Field. The Number Density. *ApJ*, 806(2):158, June 2015. .

Benjamin L. Davis, Alister W. Graham, and Ewan Cameron. Black Hole Mass Scaling Relations for Spiral Galaxies. II. M $_{BH}$-M $_{*,tot}$ and M $_{BH}$-M $_{*,disk}$. *ApJ*, 869(2):113, December 2018. .

Gabriella De Lucia and Jérémy Blaizot. The hierarchical formation of the brightest cluster galaxies. *MNRAS*, 375(1):2–14, February 2007. .

Gabriella De Lucia, Volker Springel, Simon D. M. White, Darren Croton, and Guinevere Kauffmann. The formation history of elliptical galaxies. *MNRAS*, 366(2):499–509, February 2006. .

Gabriella De Lucia, Fabio Fontanot, and David Wilman. What determines the fraction of elliptical galaxies in clusters? *Monthly Notices of the Royal Astronomical Society*, 419(2):1324–1330, 12 2011. ISSN 0035-8711. . URL https://doi.org/10.1111/j.1365-2966.2011.19789.x.

Stefano de Nicola, Alessandro Marconi, and Giuseppe Longo. The fundamental relation between supermassive black holes and their host galaxies. *MNRAS*, 490(1): 600–612, Nov 2019. .

Gerard de Vaucouleurs. Integrated Colors of Bright Galaxies in the u, b, V System. *ApJ Supplement*, 5:233, January 1961. .

Avishai Dekel and Yuval Birnboim. Galaxy bimodality due to cold flows and shock heating. *MNRAS*, 368(1):2–20, May 2006. .

Avishai Dekel, Re'em Sari, and Daniel Ceverino. Formation of Massive Galaxies at High Redshift: Cold Streams, Clumpy Disks, and Compact Spheroids. *ApJ*, 703(1): 785–801, September 2009. .

Harry Desmond and Risa H. Wechsler. The Faber-Jackson relation and Fundamental Plane from halo abundance matching. *MNRAS*, 465(1):820–833, February 2017. .

Francesco D'Eugenio, Matthew Colless, Nicholas Scott, Arjen van der Wel, Roger L. Davies, Jesse van de Sande, Sarah M. Sweet, Sree Oh, Brent Groves, Rob Sharp, Matt S. Owers, Joss Bland-Hawthorn, Scott M. Croom, Sarah Brough, Julia J. Bryant, Michael Goodwin, Jon S. Lawrence, Nuria P. F. Lorente, and Samuel N. Richards. The SAMI Galaxy Survey: stellar population and structural trends across the Fundamental Plane. *MNRAS*, 504(4):5098–5130, July 2021. .

B. Devecchi and M. Volonteri. Formation of the First Nuclear Clusters and Massive Black Holes at High Redshift. *ApJ*, 694(1):302–313, March 2009. .

Benedikt Diemer and Isaac Facio. The fabric of the universe: Exploring the cosmic web in 3d prints and woven textiles. *Publications of the Astronomical Society of the Pacific*, 129(975):058013, Apr 2017. ISSN 1538-3873. . URL http://dx.doi.org/10.1088/1538-3873/aa6a46.

Benedikt Diemer and Michael Joyce. An Accurate Physical Model for Halo Concentrations. *Astrophysical Journal*, 871(2):168, February 2019. .

Paola Dimauro, Marc Huertas-Company, Emanuele Daddi, Pablo G. Pérez-González, Mariangela Bernardi, Fernando Caro, Andrea Cattaneo, Boris Häußler, Ulrike Kuchner, Francesco Shankar, Guillermo Barro, Fernando Buitrago, Sandra M. Faber, Dale D. Kocevski, Anton M. Koekemoer, David C. Koo, Simona Mei, Reynier Peletier, Joel Primack, Aldo Rodriguez-Puebla, Mara Salvato, and Diego Tuccillo. The structural properties of classical bulges and discs from z ˜ 2. *MNRAS*, 489(3):4135–4154, November 2019. .

M. A. DiPompeo, J. C. Runnoe, R. C. Hickox, A. D. Myers, and J. E. Geach. The impact of the dusty torus on obscured quasar halo mass measurements. *MNRAS*, 460(1): 175–186, July 2016. .

Daniel Dixon. Universe Sandbox 2 [Software Application]. *Seattle: Giant Army LLC*, 2017. [Online; accessed 04-August-2020].

S. Djorgovski and Marc Davis. Fundamental Properties of Elliptical Galaxies. *ApJ*, 313: 59, February 1987. .

H. Domínguez Sánchez, M. Huertas-Company, M. Bernardi, D. Tuccillo, and J. L. Fischer. Improving galaxy morphologies for SDSS with Deep Learning. *MNRAS*, 476 (3):3661–3676, February 2018a. .

H. Domínguez Sánchez, M. Huertas-Company, M. Bernardi, D. Tuccillo, and J. L. Fischer. Improving galaxy morphologies for SDSS with Deep Learning. *MNRAS*, 476 (3):3661–3676, February 2018b. .

H. Domínguez Sánchez, M. Bernardi, J. R. Brownstein, N. Drory, and R. K. Sheth. Galaxy properties as revealed by MaNGA - I. Constraints on IMF and M_*/L gradients in ellipticals. *MNRAS*, 489(4):5612–5632, November 2019. .

Chris Done. Observational characteristics of accretion onto black holes. *arXiv e-prints*, art. arXiv:1008.2287, August 2010.

M. D'Onofrio, G. Fasano, A. Moretti, P. Marziani, D. Bindoni, J. Fritz, J. Varela, D. Bettoni, A. Cava, B. Poggianti, M. Gullieuszik, P. Kjærgaard, M. Moles, B. Vulcani, A. Omizzolo, W. J. Couch, and A. Dressler. The hybrid solution for the Fundamental Plane. *MNRAS*, 435(1):45–63, October 2013. .

A. G. Doroshkevich and S. F. Shandarin. A statistical approach to the theory of galaxy formation. *Soviet Astronomy*, 22:653–660, December 1978.

Alan Dressler, Donald Lynden-Bell, David Burstein, Roger L. Davies, S. M. Faber, Roberto Terlevich, and Gary Wegner. Spectroscopy and Photometry of Elliptical Galaxies. I. New Distance Estimator. *ApJ*, 313:42, February 1987. .

J. Ebrero, F. J. Carrera, M. J. Page, J. D. Silverman, X. Barcons, M. T. Ceballos, A. Corral, R. Della Ceca, and M. G. Watson. The XMM-Newton serendipitous survey. VI. The X-ray luminosity function. *A&A*, 493(1):55–69, January 2009. .

Bruce G. Elmegreen, Frédéric Bournaud, and Debra Meloy Elmegreen. Bulge Formation by the Coalescence of Giant Clumps in Primordial Disk Galaxies. *ApJ*, 688(1): 67–77, November 2008. .

Peter Erwin. The coexistence of classical bulges and disky pseudobulges in early-type disk galaxies. In Martin Bureau, E. Athanassoula, and Beatriz Barbuy, editors, *Formation and Evolution of Galaxy Bulges*, volume 245, pages 113–116, July 2008. .

S. M. Faber. The demography of massive galactic black holes. *Advances in Space Research*, 23(5-6):925–936, Jan 1999. .

S. M. Faber and R. E. Jackson. Velocity dispersions and mass-to-light ratios for elliptical galaxies. *ApJ*, 204:668–683, March 1976. .

S. M. Faber, C. N. A. Willmer, C. Wolf, D. C. Koo, B. J. Weiner, J. A. Newman, M. Im, A. L. Coil, C. Conroy, M. C. Cooper, M. Davis, D. P. Finkbeiner, B. F. Gerke, K. Gebhardt, E. J. Groth, P. Guhathakurta, J. Harker, N. Kaiser, S. Kassin, M. Kleinheinrich, N. P. Konidaris, R. G. Kron, L. Lin, G. Luppino, D. S. Madgwick, K. Meisenheimer, K. G. Noeske, A. C. Phillips, V. L. Sarajedini, R. P. Schiavon, L. Simard, A. S. Szalay, N. P. Vogt, and R. Yan. Galaxy Luminosity Functions to z~1 from DEEP2 and COMBO-17: Implications for Red Galaxy Formation. *ApJ*, 665(1):265–294, August 2007. .

A. C. Fabian. The obscured growth of massive black holes. *MNRAS*, 308(4):L39–L43, Oct 1999. .

A. C. Fabian, R. V. Vasudevan, and P. Gandhi. The effect of radiation pressure on dusty absorbing gas around active galactic nuclei. *MNRAS*, 385:L43–L47, March 2008. .

Martina Fagioli, C. Marcella Carollo, Alvio Renzini, Simon J. Lilly, Masato Onodera, and Sandro Tacchella. Minor Mergers or Progenitor Bias? The Stellar Ages of Small and Large Quenched Galaxies. *ApJ*, 831(2):173, November 2016. .

A. L. Faisst, C. M. Carollo, P. L. Capak, S. Tacchella, A. Renzini, O. Ilbert, H. J. McCracken, and N. Z. Scoville. Constraints on Quenching of Z $\lesssim$ 2 Massive Galaxies from the Evolution of the Average Sizes of Star-forming and Quenched Populations in COSMOS. *ApJ*, 839(2):71, April 2017. .

L. Fan, A. Lapi, G. De Zotti, and L. Danese. The Dramatic Size Evolution of Elliptical Galaxies and the Quasar Feedback. *Apj Letters*, 689(2):L101, December 2008. .

L. Fan, A. Lapi, A. Bressan, M. Bernardi, G. De Zotti, and L. Danese. Cosmic Evolution of Size and Velocity Dispersion for Early-type Galaxies. *ApJ*, 718(2):1460–1475, August 2010. .

Jerome J. Fang, S. M. Faber, Samir Salim, Genevieve J. Graves, and R. Michael Rich. The Slow Death (Or Rebirth?) of Extended Star Formation in z ~0.1 Green Valley Early-type Galaxies. *ApJ*, 761(1):23, December 2012. .

Jeff Farris. Forging new paths for filmmakers on "The Mandalorian, 2020. URL https://www.unrealengine.com/en-US/blog/forging-new-paths-for-filmmakers-on-the-mandalorian. [Online; accessed 04-August-2020].

C.-A. Faucher-Giguère and E. Quataert. The physics of galactic winds driven by active galactic nuclei. *MNRAS*, 425:605–622, September 2012. .

Jonathan Fay and Curtis Wong. Worldwide telescope, 2008. URL http://worldwidetelescope.org. [Online; accessed 04-August-2020].

A. Feoli and D. Mele. Is There a Relationship Between the Mass of a Smbh and the Kinetic Energy of its Host Elliptical Galaxy? *International Journal of Modern Physics D*, 14(11):1861–1872, Jan 2005. .

Laura Ferrarese. Beyond the Bulge: A Fundamental Relation between Supermassive Black Holes and Dark Matter Halos. *ApJ*, 578(1):90–97, Oct 2002. .

Laura Ferrarese and Holland Ford. Supermassive Black Holes in Galactic Nuclei: Past, Present and Future Research. *Space Science Reviews*, 116(3-4):523–624, Feb 2005. .

Laura Ferrarese and David Merritt. A Fundamental Relation between Supermassive Black Holes and Their Host Galaxies. *Apj Letters*, 539(1):L9–L12, Aug 2000. .

Ismael Ferrero, Julio F. Navarro, Mario G. Abadi, José A. Benavides, and Damián Mast. A unified scenario for the origin of spiral and elliptical galaxy structural scaling laws. *A&A*, 648:A124, April 2021. .

J. L. Fischer, H. Domínguez Sánchez, and M. Bernardi. SDSS-IV MaNGA PyMorph Photometric and Deep Learning Morphological Catalogues and implications for bulge properties and stellar angular momentum. *MNRAS*, 483(2):2057–2077, February 2019. .

David B. Fisher and Niv Drory. The Structure of Classical Bulges and Pseudobulges: the Link Between Pseudobulges and SÉRSIC Index. *Astronomical Jmynal*, 136(2):773–839, August 2008. .

K. C. Freeman. On the Disks of Spiral and S0 Galaxies. *ApJ*, 160:811, June 1970. .

J. M. Gabor, R. Davé, B. D. Oppenheimer, and K. Finlator. Quenching massive galaxies with on-the-fly feedback in cosmological hydrodynamic simulations. *MNRAS*, 417 (4):2676–2695, November 2011. .

Dimitri A. Gadotti. Structural properties of pseudo-bulges, classical bulges and elliptical galaxies: a Sloan Digital Sky Survey perspective. *MNRAS*, 393(4):1531–1552, March 2009. .

Anna Gallazzi, Stéphane Charlot, Jarle Brinchmann, and Simon D. M. White. Ages and metallicities of early-type galaxies in the Sloan Digital Sky Survey: new insight into the physical origin of the colour-magnitude and the Mg_2-σ_V relations. *MNRAS*, 370 (3):1106–1124, August 2006. .

A. Gargiulo, P. Saracco, S. Tamburri, I. Lonoce, and F. Ciocca. Ultramassive dense early-type galaxies: Velocity dispersions and number density evolution since z = 1.6. *A&A*, 592:A132, August 2016. .

C. Martin Gaskell. An Improved [O III] Line Width to Stellar Velocity Dispersion Calibration: Curvature, Scatter, and Lack of Evolution in the Black-Hole Mass Versus Stellar Velocity Dispersion Relationship. *arXiv e-prints*, art. arXiv:0908.0328, Aug 2009.

M. Gatti, F. Shankar, V. Bouillot, N. Menci, A. Lamastra, M. Hirschmann, and F. Fiore. Constraining AGN triggering mechanisms through the clustering analysis of active black holes. *MNRAS*, 456(1):1073–1092, February 2016. .

Karl Gebhardt, Ralf Bender, Gary Bower, Alan Dressler, S. M. Faber, Alexei V. Filippenko, Richard Green, Carl Grillmair, Luis C. Ho, John Kormendy, Tod R. Lauer, John Magorrian, Jason Pinkney, Douglas Richstone, and Scott Tremaine. A Relationship between Nuclear Black Hole Mass and Galaxy Velocity Dispersion. *Apj Letters*, 539(1):L13–L16, Aug 2000. .

R. Genzel, A. Eckart, T. Ott, and F. Eisenhauer. On the nature of the dark mass in the centre of the Milky Way. *MNRAS*, 291(1):219–234, October 1997. .

A. Georgakakis, A. L. Coil, E. S. Laird, R. L. Griffith, K. Nandra, J. M. Lotz, C. M. Pierce, M. C. Cooper, J. A. Newman, and A. M. Koekemoer. Host galaxy morphologies of X-ray selected AGN: assessing the significance of different black hole fuelling mechanisms to the accretion density of the Universe at z ~1. *MNRAS*, 397(2):623–633, August 2009. .

A. Georgakakis, J. Aird, A. Schulze, T. Dwelly, M. Salvato, K. Nandra, A. Merloni, and D. P. Schneider. Observational constraints on the specific accretion-rate distribution of X-ray-selected AGNs. *MNRAS*, 471(2):1976–2001, October 2016. .

A. Georgakakis, J. Aird, A. Schulze, T. Dwelly, M. Salvato, K. Nandra, A. Merloni, and D. P. Schneider. Observational constraints on the specific accretion-rate distribution of X-ray-selected AGNs. *MNRAS*, 471(2):1976–2001, October 2017. .

A. Georgakakis, J. Comparat, A. Merloni, L. Ciesla, J. Aird, and A. Finoguenov. Exploring the halo occupation of AGN using dark-matter cosmological simulations. *MNRAS*, 487(1):275–295, July 2019. .

A. M. Ghez, B. L. Klein, M. Morris, and E. E. Becklin. High Proper-Motion Stars in the Vicinity of Sagittarius A*: Evidence for a Supermassive Black Hole at the Center of Our Galaxy. *ApJ*, 509(2):678–686, December 1998. .

Marat Gilfanov and Andrea Merloni. Observational Appearance of Black Holes in X-Ray Binaries and AGN. *Space Science Reviews*, 183(1-4):121–148, September 2014. .

R. Gobat, E. Daddi, G. Magdis, F. Bournaud, M. Sargent, M. Martig, S. Jin, A. Finoguenov, M. Béthermin, H. S. Hwang, A. Renzini, G. W. Wilson, I. Aretxaga, M. Yun, V. Strazzullo, and F. Valentino. The unexpectedly large dust and gas content of quiescent galaxies at z ¿ 1.4. *Nature Astronomy*, 2:239–246, January 2018. .

R. Gobat, G. Magdis, C. D'Eugenio, and F. Valentino. The evolution of the gas fraction of quiescent galaxies modeled as a consequence of their creation rate. *A&A*, 644:L7, December 2020. .

Juan E. González, C. G. Lacey, C. M. Baugh, and C. S. Frenk. The role of submillimetre galaxies in hierarchical galaxy formation. *MNRAS*, 413(2):749–762, May 2011a. .

Juan E. González, C. G. Lacey, C. M. Baugh, and C. S. Frenk. The role of submillimetre galaxies in hierarchical galaxy formation. *MNRAS*, 413(2):749–762, May 2011b. .

Google. Google sky, 2007. URL https://www.google.com/sky/. [Online; accessed 04-August-2020].

Alister W. Graham and Nicholas Scott. The (Black Hole)-bulge Mass Scaling Relation at Low Masses. *ApJ*, 798(1):54, Jan 2015. .

Alister W. Graham, Peter Erwin, N. Caon, and I. Trujillo. A Correlation between Galaxy Light Concentration and Supermassive Black Hole Mass. *Apj Letters*, 563(1):L11–L14, Dec 2001. .

Alister W. Graham, Simon P. Driver, Paul D. Allen, and Jochen Liske. The Millennium Galaxy Catalogue: the local supermassive black hole mass function in early- and late-type galaxies. *MNRAS*, 378(1):198–210, Jun 2007. .

Gian Luigi Granato, Gianfranco De Zotti, Laura Silva, Alessandro Bressan, and Luigi Danese. A Physical Model for the Coevolution of QSOs and Their Spheroidal Hosts. *ApJ*, 600(2):580–594, Jan 2004. .

C. J. Grier, P. Martini, L. C. Watson, B. M. Peterson, M. C. Bentz, K. M. Dasyra, M. Dietrich, L. Ferrarese, R. W. Pogge, and Y. Zu. Stellar Velocity Dispersion Measurements in High-luminosity Quasar Hosts and Implications for the AGN Black Hole Mass Scale. *ApJ*, 773(2):90, August 2013. .

Philip J. Grylls, F. Shankar, L. Zanisi, and M. Bernardi. A statistical semi-empirical model: satellite galaxies in groups and clusters. *MNRAS*, 483(2):2506–2523, Feb 2019. .

Philip J. Grylls, F. Shankar, and C. J. Conselice. The significant effects of stellar mass estimation on galaxy pair fractions. *MNRAS*, 499(2):2265–2275, December 2020a. .

Philip J. Grylls, F. Shankar, J. Leja, N. Menci, B. Moster, P. Behroozi, and L. Zanisi. Predicting fully self-consistent satellite richness, galaxy growth, and star formation rates from the STatistical sEmi-Empirical modeL STEEL. *MNRAS*, 491(1):634–654, January 2020b. .

Kayhan Gültekin, Douglas O. Richstone, Karl Gebhardt, Tod R. Lauer, Scott Tremaine, M. C. Aller, Ralf Bender, Alan Dressler, S. M. Faber, Alexei V. Filippenko, Richard

Green, Luis C. Ho, John Kormendy, John Magorrian, Jason Pinkney, and Christos Siopis. The M-σ and M-L Relations in Galactic Bulges, and Determinations of Their Intrinsic Scatter. *ApJ*, 698(1):198–221, Jun 2009. .

James E. Gunn and III Gott, J. Richard. On the Infall of Matter Into Clusters of Galaxies and Some Effects on Their Evolution. *ApJ*, 176:1, August 1972. .

Qi Guo, Simon White, Michael Boylan-Kolchin, Gabriella De Lucia, Guinevere Kauffmann, Gerard Lemson, Cheng Li, Volker Springel, and Simone Weinmann. From dwarf spheroidals to cD galaxies: simulating the galaxy population in a ΛCDM cosmology. *MNRAS*, 413(1):101–131, May 2011. .

S. Haan, E. Schinnerer, E. Emsellem, S. García-Burillo, F. Combes, C. G. Mundell, and H.-W. Rix. Dynamical Evolution of AGN Host Galaxies–Gas In/Out-Flow Rates in Seven NUGA Galaxies. *ApJ*, 692:1623–1661, February 2009. .

Mélanie Habouzit, Yuan Li, Rachel S. Somerville, Shy Genel, Annalisa Pillepich, Marta Volonteri, Romeel Davé, Yetli Rosas-Guevara, Stuart McAlpine, Sébastien Peirani, Lars Hernquist, Daniel Anglés-Alcázar, Amy Reines, Richard Bower, Yohan Dubois, Dylan Nelson, Christophe Pichon, and Mark Vogelsberger. Supermassive black holes in cosmological simulations I: M_{BH} - $M_\star$ relation and black hole mass function. *MNRAS*, 503(2):1940–1975, May 2021. .

Nadine Häring and Hans-Walter Rix. On the Black Hole Mass-Bulge Mass Relation. *Apj Letters*, 604(2):L89–L92, Apr 2004. .

C. M. Harrison. Impact of supermassive black hole growth on star formation. *Nature Astronomy*, 1:0165, July 2017. .

Lars Hernquist. Structure of Merger Remnants. I. Bulgeless Progenitors. *ApJ*, 400:460, December 1992. .

Lars Hernquist and Neal Katz. Treesph-a unification of sph with the hierarchical tree method. *The Astrophysical Journal Supplement Series*, 70:419–446, 1989.

John Frederick William Herschel. A General Catalogue of Nebulae and Clusters of Stars. *Philosophical Transactions of the Royal Society of London Series I*, 154:1–137, January 1864.

Gary Hinshaw, JL Weiland, RS Hill, N Odegard, D Larson, CL Bennett, J Dunkley, B Gold, MR Greason, N Jarosik, et al. Five-year wilkinson microwave anisotropy probe* observations: data processing, sky maps, and basic results. *The Astrophysical Journal Supplement Series*, 180(2):225, 2009.

Roger W Hockney and James W Eastwood. *Computer simulation using particles*. crc Press, 1988.

Frank Hohl. Numerical Experiments with a Disk of Stars. *ApJ*, 168:343, September 1971. .

Philip F Hopkins. A general class of lagrangian smoothed particle hydrodynamics methods and implications for fluid mixing problems. *Monthly Notices of the Royal Astronomical Society*, 428(4):2840–2856, 2012.

Philip F. Hopkins and Lars Hernquist. Fueling Low-Level AGN Activity through Stochastic Accretion of Cold Gas. *ApJ Supplement*, 166(1):1–36, September 2006. .

Philip F. Hopkins and Lars Hernquist. Quasars Are Not Light Bulbs: Testing Models of Quasar Lifetimes with the Observed Eddington Ratio Distribution. *ApJ*, 698(2): 1550–1569, June 2009. .

Philip F. Hopkins, Lars Hernquist, Thomas J. Cox, Tiziana Di Matteo, Brant Robertson, and Volker Springel. A Unified, Merger-driven Model of the Origin of Starbursts, Quasars, the Cosmic X-Ray Background, Supermassive Black Holes, and Galaxy Spheroids. *ApJ Supplement*, 163(1):1–49, March 2006. .

Philip F. Hopkins, Lars Hernquist, Thomas J. Cox, Brant Robertson, and Elisabeth Krause. An Observed Fundamental Plane Relation for Supermassive Black Holes. *ApJ*, 669(1):67–73, November 2007. .

Philip F Hopkins, Lars Hernquist, Thomas J Cox, and Dušan Kereš. A cosmological framework for the co-evolution of quasars, supermassive black holes, and elliptical galaxies. i. galaxy mergers and quasar activity. *The Astrophysical Journal Supplement Series*, 175(2):356, 2008.

Philip F. Hopkins, Lars Hernquist, Thomas J. Cox, and Dušan Kereš. A Cosmological Framework for the Co-Evolution of Quasars, Supermassive Black Holes, and Elliptical Galaxies. I. Galaxy Mergers and Quasar Activity. *ApJ Supplement*, 175(2):356–389, April 2008. .

Philip F. Hopkins, Thomas J. Cox, Joshua D. Younger, and Lars Hernquist. How do Disks Survive Mergers? *ApJ*, 691(2):1168–1201, February 2009a. .

Philip F. Hopkins, Lars Hernquist, Thomas J. Cox, Dusan Keres, and Stijn Wuyts. Dissipation and Extra Light in Galactic Nuclei. IV. Evolution in the Scaling Relations of Spheroids. *ApJ*, 691(2):1424–1458, February 2009b. .

Philip F. Hopkins, Kevin Bundy, Darren Croton, Lars Hernquist, Dusan Keres, Sadegh Khochfar, Kyle Stewart, Andrew Wetzel, and Joshua D. Younger. Mergers and Bulge Formation in ΛCDM: Which Mergers Matter? *ApJ*, 715(1):202–229, May 2010. .

Philip F. Hopkins, Eliot Quataert, and Norman Murray. The structure of the interstellar medium of star-forming galaxies. *MNRAS*, 421(4):3488–3521, April 2012. .

Jian Hu. The black hole mass-stellar velocity dispersion correlation: bulges versus pseudo-bulges. *MNRAS*, 386(4):2242–2252, Jun 2008. .

Kuang-Han Huang, S. Michael Fall, Henry C. Ferguson, Arjen van der Wel, Norman Grogin, Anton Koekemoer, Seong-Kook Lee, Pablo G. Pérez-González, and Stijn Wuyts. Relations between the Sizes of Galaxies and Their Dark Matter Halos at Redshifts 0 ¡ z ¡ 3. *ApJ*, 838(1):6, March 2017. .

E. P. Hubble. Extragalactic nebulae. *ApJ*, 64:321–369, December 1926. .

E. P. Hubble. A spiral nebula as a stellar system, Messier 31. *ApJ*, 69:103–158, March 1929a. .

Edwin Hubble. A Relation between Distance and Radial Velocity among Extra-Galactic Nebulae. *Proceedings of the National Academy of Science*, 15(3):168–173, March 1929b. .

M. Huertas-Company, S. Mei, F. Shankar, L. Delaye, A. Raichoor, G. Covone, A. Finoguenov, J. P. Kneib, Fèvre O. Le, and M. Povic. The evolution of the mass-size relation for early-type galaxies from z $\sim$ 1 to the present: dependence on environment, mass range and detailed morphology. *MNRAS*, 428(2):1715–1742, January 2013. .

Joseph B. Hyde and Mariangela Bernardi. The luminosity and stellar mass Fundamental Plane of early-type galaxies. *MNRAS*, 396(2):1171–1185, June 2009. .

Illustris Collaboration. Time evolution of a 10 Mpc (comoving) region within Illustris, 2018. URL https://www.illustris-project.org/media/. [Online; accessed 04-August-2020].

Tomoaki Ishiyama, Francisco Prada, Anatoly A. Klypin, Manodeep Sinha, R. Benton Metcalf, Eric Jullo, Bruno Altieri, Sofía A. Cora, Darren Croton, Sylvain de la Torre, David E. Millán-Calero, Taira Oogi, José Ruedas, and Cristian A. Vega-Martínez. The Uchuu Simulations: Data Release 1 and Dark Matter Halo Concentrations. *arXiv e-prints*, art. arXiv:2007.14720, July 2020.

K. Jahnke and A. V. Macciò. The Non-causal Origin of the Black-hole-galaxy Scaling Relations. *ApJ*, 734:92, June 2011. .

J. H. Jeans. On the theory of star-streaming and the structure of the universe. *MNRAS*, 76:70–84, December 1915. .

Fangzhou Jiang and Frank C. van den Bosch. Generating merger trees for dark matter haloes: a comparison of methods. *MNRAS*, 440(1):193–207, May 2014. .

Fangzhou Jiang and Frank C. van den Bosch. Statistics of dark matter substructure - I. Model and universal fitting functions. *MNRAS*, 458(3):2848–2869, May 2016. .

Lalitwadee Kawinwanichakij, Casey Papovich, Robin Ciardullo, Steven L. Finkelstein, Matthew L. Stevans, Isak G. B. Wold, Shardha Jogee, Sydney Sherman, Jonathan Florez, and Caryl Gronwall. On the (Lack of) Evolution of the Stellar Mass Function of Massive Galaxies from z = 1.5 to 0.4. *ApJ*, 892(1):7, March 2020. .

Jr. Kennicutt, Robert C. Star Formation in Galaxies Along the Hubble Sequence. *Annual Review of Astron and Astrophys*, 36:189–232, January 1998. .

Dušan Kereš, Neal Katz, Romeel Davé, Mark Fardal, and David H. Weinberg. Galaxies in a simulated ΛCDM universe - II. Observable properties and constraints on feedback. *MNRAS*, 396(4):2332–2344, July 2009. .

Juhan Kim, Changbom Park, Graziano Rossi, Sang Min Lee, and J Richard Gott III. The new horizon run cosmological n-body simulations. *arXiv preprint arXiv:1112.1754*, 2011.

Taysun Kimm, Rachel S. Somerville, Sukyoung K. Yi, Frank C. van den Bosch, Samir Salim, Fabio Fontanot, Pierluigi Monaco, Houjun Mo, Anna Pasquali, R. M. Rich, and Xiaohu Yang. The correlation of star formation quenching with internal galaxy properties and environment. *MNRAS*, 394(3):1131–1147, April 2009. .

A. King. Black Holes, Galaxy Formation, and the M_{BH}-σ Relation. *Apj Letters*, 596: L27–L29, October 2003. .

A. King. The AGN-Starburst Connection, Galactic Superwinds, and M_{BH}-σ. *Apj Letters*, 635:L121–L123, December 2005. .

A. King and K. Pounds. Powerful Outflows and Feedback from Active Galactic Nuclei. *Annual Review of Astron and Astrophys*, 53:115–154, August 2015. .

A. R. King. Black hole outflows. *MNRAS*, 402:1516–1522, March 2010a. .

A. R. King. AGN have underweight black holes and reach Eddington. *MNRAS*, 408: L95–L98, October 2010b. .

A. R. King and K. A. Pounds. Black hole winds. *MNRAS*, 345:657–659, October 2003. .

A. R. King, K. Zubovas, and C. Power. Large-scale outflows in galaxies. *MNRAS*, 415: L6–L10, July 2011. .

Andrew King. Supermassive Black Hole Accretion and Feedback. *Saas-Fee Advanced Course*, 48:95, Jan 2019. .

A Klypin, T Primack, and C Henze. Bolshoi Fly-Through, 2011a. URL http://hipacc.ucsc.edu/Bolshoi/Movies.html. [Online; accessed 04-August-2020].

A. A. Klypin and S. F. Shandarin. Three-dimensional numerical model of the formation of large-scale structure in the Universe. *Monthly Notices of the Royal Astronomical Society*, 204:891–907, September 1983. .

Anatoly Klypin, Gustavo Yepes, Stefan Gottlöber, Francisco Prada, and Steffen Heß. MultiDark simulations: the story of dark matter halo concentrations and density profiles. *MNRAS*, 457(4):4340–4359, April 2016. .

Anatoly Klypin, Gustavo Yepes, Stefan Gottlöber, Francisco Prada, and Steffen Heß. MultiDark simulations: the story of dark matter halo concentrations and density profiles. *Monthly Notices of the Royal Astronomical Society*, 457(4):4340–4359, 02 2016.

Anatoly A. Klypin, Sebastian Trujillo-Gomez, and Joel Primack. Dark Matter Halos in the Standard Cosmological Model: Results from the Bolshoi Simulation. *ApJ*, 740(2): 102, October 2011b. .

Anatoly A Klypin, Sebastian Trujillo-Gomez, and Joel Primack. Dark matter halos in the standard cosmological model: Results from the bolshoi simulation. *The Astrophysical Journal*, 740(2):102, 2011.

Dale D. Kocevski, S. M. Faber, Mark Mozena, Anton M. Koekemoer, Kirpal Nandra, Cyprian Rangel, Elise S. Laird, Marcella Brusa, Stijn Wuyts, Jonathan R. Trump, David C. Koo, Rachel S. Somerville, Eric F. Bell, Jennifer M. Lotz, David M. Alexander, Frederic Bournaud, Christopher J. Conselice, Tomas Dahlen, Avishai Dekel, Jennifer L. Donley, James S. Dunlop, Alexis Finoguenov, Antonis Georgakakis, Mauro Giavalisco, Yicheng Guo, Norman A. Grogin, Nimish P. Hathi, Stéphanie Juneau, Jeyhan S. Kartaltepe, Ray A. Lucas, Elizabeth J. McGrath, Daniel H. McIntosh, Bahram Mobasher, Aday R. Robaina, David Rosario, Amber N. Straughn, Arjen van der Wel, and Carolin Villforth. CANDELS: Constraining the AGN-Merger Connection with Host Morphologies at z ~2. *ApJ*, 744(2):148, January 2012. .

J. Kormendy. Kinematics of extragalactic bulges: evidence that some bulges are really disks. In Herwig Dejonghe and Harm Jan Habing, editors, *Galactic Bulges*, volume 153, page 209, January 1993.

John Kormendy and Luis C. Ho. Coevolution (Or Not) of Supermassive Black Holes and Host Galaxies. *Annual Review of Astron and Astrophys*, 51(1):511–653, Aug 2013. .

Marek Kowalski, David Rubin, Greg Aldering, RJ Agostinho, A Amadon, R Amanullah, C Balland, K Barbary, G Blanc, Peter J Challis, et al. Improved cosmological constraints from new, old, and combined supernova data sets. *The Astrophysical Journal*, 686(2):749, 2008.

Michael Kramer and David J. Champion. The European Pulsar Timing Array and the Large European Array for Pulsars. *Classical and Quantum Gravity*, 30(22):224009, Nov 2013. .

Andrey V. Kravtsov. The Size-Virial Radius Relation of Galaxies. *Apj Letters*, 764(2): L31, February 2013. .

Andrey V. Kravtsov, Andreas A. Berlind, Risa H. Wechsler, Anatoly A. Klypin, Stefan Gottlöber, Brandon Allgood, and Joel R. Primack. The Dark Side of the Halo Occupation Distribution. *ApJ*, 609(1):35–49, July 2004. .

Mark R. Krumholz, Avishai Dekel, and Christopher F. McKee. A Universal, Local Star Formation Law in Galactic Clouds, nearby Galaxies, High-redshift Disks, and Starbursts. *ApJ*, 745(1):69, January 2012. .

Mirko Krumpe, Takamitsu Miyaji, Bernd Husemann, Nikos Fanidakis, Alison L. Coil, and Hector Aceves. The Spatial Clustering of ROSAT All-Sky Survey Active Galactic Nuclei. IV. More Massive Black Holes Reside in More Massive Dark Matter Halos. *ApJ*, 815(1):21, December 2015. .

Mirko Krumpe, Takamitsu Miyaji, Alison L. Coil, and Hector Aceves. Spatial clustering and halo occupation distribution modelling of local AGN via cross-correlation measurements with 2MASS galaxies. *MNRAS*, 474(2):1773–1786, February 2018. .

Francesco La Barbera, Alexandre Vazdekis, Ignacio Ferreras, Anna Pasquali, Michele Cappellari, Ignacio Martín-Navarro, Frederik Schönebeck, and Jesús Falcón-Barroso. Radial constraints on the initial mass function from TiO features and Wing-Ford band in early-type galaxies. *MNRAS*, 457(2):1468–1489, April 2016. .

Cedric Lacey and Shaun Cole. Merger rates in hierarchical models of galaxy formation. *Monthly Notices of the Royal Astronomical Society*, 262(3):627–649, 1993.

D. G. Lambas, S. Alonso, V. Mesa, and A. L. O'Mill. Galaxy interactions. I. Major and minor mergers. *A&A*, 539:A45, March 2012. .

A. Lapi, A. Cavaliere, and N. Menci. Intracluster and Intragroup Entropy from Quasar Activity. *ApJ*, 619(1):60–72, Jan 2005. .

A. Lapi, J. González-Nuevo, L. Fan, A. Bressan, G. De Zotti, L. Danese, M. Negrello, L. Dunne, S. Eales, S. Maddox, R. Auld, M. Baes, D. G. Bonfield, S. Buttiglione, A. Cava, D. L. Clements, A. Cooray, A. Dariush, S. Dye, J. Fritz, D. Herranz, R. Hopwood, E. Ibar, R. Ivison, M. J. Jarvis, S. Kaviraj, M. López-Caniego, M. Massardi, M. J. Michałowski, E. Pascale, M. Pohlen, E. Rigby, G. Rodighiero, S. Serjeant, D. J. B. Smith, P. Temi, J. Wardlow, and P. van der Werf. Herschel-ATLAS Galaxy Counts and High-redshift Luminosity Functions: The Formation of Massive Early-type Galaxies. *ApJ*, 742(1):24, November 2011. .

A. Lapi, L. Pantoni, L. Zanisi, J. Shi, C. Mancuso, M. Massardi, F. Shankar, A. Bressan, and L. Danese. The Dramatic Size and Kinematic Evolution of Massive Early-type Galaxies. *ApJ*, 857(1):22, April 2018. .

R. Laureijs, J. Amiaux, S. Arduini, J. L. Augueres, J. Brinchmann, R. Cole, M. Cropper, C. Dabin, L. Duvet, A. Ealet, and et al. Euclid Definition Study Report. *arXiv e-prints*, art. arXiv:1110.3193, October 2011.

Chris Laurel. Celestia [Software Application]. 2001. URL https://celestia.space. [Online; accessed 04-August-2020].

Andy Lawrence, SJ Warren, O Almaini, AC Edge, NC Hambly, RF Jameson, P Lucas, M Casali, A Adamson, S Dye, et al. The ukirt infrared deep sky survey (ukidss). *Monthly Notices of the Royal Astronomical Society*, 379(4):1599–1617, 2007.

Alexie Leauthaud, Andrew J. Benson, Francesca Civano, Alison L. Coil, Kevin Bundy, Richard Massey, Malte Schramm, Andreas Schulze, Peter Capak, Martin Elvis, Andrea Kulier, and Jason Rhodes. The dark matter haloes of moderate luminosity X-ray AGN as determined from weak gravitational lensing and host stellar masses. *MNRAS*, 446(2):1874–1888, January 2015. .

Joel Leja, Benjamin D. Johnson, Charlie Conroy, Pieter van Dokkum, Joshua S. Speagle, Gabriel Brammer, Ivelina Momcheva, Rosalind Skelton, Katherine E. Whitaker, Marijn Franx, and Erica J. Nelson. An Older, More Quiescent Universe from Panchromatic SED Fitting of the 3D-HST Survey. *ApJ*, 877(2):140, June 2019. .

G. Lemaître. Un Univers homogène de masse constante et de rayon croissant rendant compte de la vitesse radiale des nébuleuses extra-galactiques. *Annales de la Société Scientifique de Bruxelles*, 47:49–59, January 1927.

Hongyu Li, Junqiang Ge, Shude Mao, Michele Cappellari, R. J. Long, Ran Li, Eric Emsellem, Aaron A. Dutton, Cheng Li, Kevin Bundy, Daniel Thomas, Niv Drory, and Alexandre Roman Lopes. SDSS-IV MaNGA: Variation of the Stellar Initial Mass Function in Spiral and Early-type Galaxies. *ApJ*, 838(2):77, April 2017. .

Hongyu Li, Shude Mao, Michele Cappellari, Junqiang Ge, R. J. Long, Ran Li, H. J. Mo, Cheng Li, Zheng Zheng, Kevin Bundy, Daniel Thomas, Joel R. Brownstein, Alexandre Roman Lopes, David R. Law, and Niv Drory. SDSS-IV MaNGA: global stellar population and gradients for about 2000 early-type and spiral galaxies on the mass-size plane. *MNRAS*, 476(2):1765–1775, May 2018. .

Yuan Li, Melanie Habouzit, Shy Genel, Rachel Somerville, Bryan A. Terrazas, Eric F. Bell, Annalisa Pillepich, Dylan Nelson, Rainer Weinberger, Vicente Rodriguez-Gomez, Chung-Pei Ma, Ruediger Pakmor, Lars Hernquist, and Mark Vogelsberger. Correlations between Black Holes and Host Galaxies in the Illustris and IllustrisTNG Simulations. *ApJ*, 895(2):102, June 2020. .

LSST Science Collaboration, Paul A. Abell, Julius Allison, Scott F. Anderson, John R. Andrew, J. Roger P. Angel, Lee Armus, David Arnett, S. J. Asztalos, Tim S. Axelrod, Stephen Bailey, D. R. Ballantyne, Justin R. Bankert, Wayne A. Barkhouse, Jeffrey D. Barr, L. Felipe Barrientos, Aaron J. Barth, James G. Bartlett, Andrew C. Becker, Jacek Becla, Timothy C. Beers, Joseph P. Bernstein, Rahul Biswas, Michael R. Blanton, Joshua S. Bloom, John J. Bochanski, Pat Boeshaar, Kirk D. Borne, Marusa Bradac,

W. N. Brandt, Carrie R. Bridge, Michael E. Brown, Robert J. Brunner, James S. Bullock, Adam J. Burgasser, James H. Burge, David L. Burke, Phillip A. Cargile, Srinivasan Chandrasekharan, George Chartas, Steven R. Chesley, You-Hua Chu, David Cinabro, Mark W. Claire, Charles F. Claver, Douglas Clowe, A. J. Connolly, Kem H. Cook, Jeff Cooke, Asantha Cooray, Kevin R. Covey, Christopher S. Culliton, Roelof de Jong, Willem H. de Vries, Victor P. Debattista, Francisco Delgado, Ian P. Dell'Antonio, Saurav Dhital, Rosanne Di Stefano, Mark Dickinson, Benjamin Dilday, S. G. Djorgovski, Gregory Dobler, Ciro Donalek, Gregory Dubois-Felsmann, Josef Durech, Ardis Eliasdottir, Michael Eracleous, Laurent Eyer, Emilio E. Falco, Xiaohui Fan, Christopher D. Fassnacht, Harry C. Ferguson, Yanga R. Fernandez, Brian D. Fields, Douglas Finkbeiner, Eduardo E. Figueroa, Derek B. Fox, Harold Francke, James S. Frank, Josh Frieman, Sebastien Fromenteau, Muhammad Furqan, Gaspar Galaz, A. Gal-Yam, Peter Garnavich, Eric Gawiser, John Geary, Perry Gee, Robert R. Gibson, Kirk Gilmore, Emily A. Grace, Richard F. Green, William J. Gressler, Carl J. Grillmair, Salman Habib, J. S. Haggerty, Mario Hamuy, Alan W. Harris, Suzanne L. Hawley, Alan F. Heavens, Leslie Hebb, Todd J. Henry, Edward Hileman, Eric J. Hilton, Keri Hoadley, J. B. Holberg, Matt J. Holman, Steve B. Howell, Leopoldo Infante, Zeljko Ivezic, Suzanne H. Jacoby, Bhuvnesh Jain, R, Jedicke, M. James Jee, J. Garrett Jernigan, Saurabh W. Jha, Kathryn V. Johnston, R. Lynne Jones, Mario Juric, Mikko Kaasalainen, Styliani, Kafka, Steven M. Kahn, Nathan A. Kaib, Jason Kalirai, Jeff Kantor, Mansi M. Kasliwal, Charles R. Keeton, Richard Kessler, Zoran Knezevic, Adam Kowalski, Victor L. Krabbendam, K. Simon Krughoff, Shrinivas Kulkarni, Stephen Kuhlman, Mark Lacy, Sebastien Lepine, Ming Liang, Amy Lien, Paulina Lira, Knox S. Long, Suzanne Lorenz, Jennifer M. Lotz, R. H. Lupton, Julie Lutz, Lucas M. Macri, Ashish A. Mahabal, Rachel Mandelbaum, Phil Marshall, Morgan May, Peregrine M. McGehee, Brian T. Meadows, Alan Meert, Andrea Milani, Christopher J. Miller, Michelle Miller, David Mills, Dante Minniti, David Monet, Anjum S. Mukadam, Ehud Nakar, Douglas R. Neill, Jeffrey A. Newman, Sergei Nikolaev, Martin Nordby, Paul O'Connor, Masamune Oguri, John Oliver, Scot S. Olivier, Julia K. Olsen, Knut Olsen, Edward W. Olszewski, Hakeem Oluseyi, Nelson D. Padilla, Alex Parker, Joshua Pepper, John R. Peterson, Catherine Petry, Philip A. Pinto, James L. Pizagno, Bogdan Popescu, Andrej Prsa, Veljko Radcka, M. Jordan Raddick, Andrew Rasmussen, Arne Rau, Jeonghee Rho, James E. Rhoads, Gordon T. Richards, Stephen T. Ridgway, Brant E. Robertson, Rok Roskar, Abhijit Saha, Ata Sarajedini, Evan Scannapieco, Terry Schalk, Rafe Schindler, Samuel Schmidt, Sarah Schmidt, Donald P. Schneider, German Schumacher, Ryan Scranton, Jacques Sebag, Lynn G. Seppala, Ohad Shemmer, Joshua D. Simon, M. Sivertz, Howard A. Smith, J. Allyn Smith, Nathan Smith, Anna H. Spitz, Adam Stanford, Keivan G. Stassun, Jay Strader, Michael A. Strauss, Christopher W. Stubbs, Donald W. Sweeney, Alex Szalay, Paula Szkody, Masahiro Takada, Paul Thorman, David E. Trilling, Virginia Trimble, Anthony Tyson, Richard Van Berg, Daniel Vanden Berk, Jake VanderPlas, Licia

Verde, Bojan Vrsnak, Lucianne M. Walkowicz, Benjamin D. Wandelt, Sheng Wang, Yun Wang, Michael Warner, Risa H. Wechsler, Andrew A. West, Oliver Wiecha, Benjamin F. Williams, Beth Willman, David Wittman, Sidney C. Wolff, W. Michael Wood-Vasey, Przemek Wozniak, Patrick Young, Andrew Zentner, and Hu Zhan. LSST Science Book, Version 2.0. *arXiv e-prints*, art. arXiv:0912.0201, December 2009.

M. Lyubenova, I. Martín-Navarro, G. van de Ven, J. Falcón-Barroso, L. Galbany, A. Gallazzi, R. García-Benito, R. González Delgado, B. Husemann, F. La Barbera, R. A. Marino, D. Mast, J. Mendez-Abreu, R. F. P. Peletier, P. Sánchez-Blázquez, S. F. Sánchez, S. C. Trager, R. C. E. van den Bosch, A. Vazdekis, C. J. Walcher, L. Zhu, S. Zibetti, B. Ziegler, J. Bland-Hawthorn, and CALIFA Collaboration. IMF shape constraints from stellar populations and dynamics from CALIFA. *MNRAS*, 463(3): 3220–3225, December 2016. .

Piero Madau and Mark Dickinson. Cosmic star-formation history. *Annual Review of Astronomy and Astrophysics*, 52:415–486, 2014.

John Magorrian, Scott Tremaine, Douglas Richstone, Ralf Bender, Gary Bower, Alan Dressler, S. M. Faber, Karl Gebhardt, Richard Green, Carl Grillmair, John Kormendy, and Tod Lauer. The Demography of Massive Dark Objects in Galaxy Centers. *Astronomical Jmynal*, 115(6):2285–2305, Jun 1998. .

Gary A. Mamon and Ewa L. Łokas. Dark matter in elliptical galaxies - II. Estimating the mass within the virial radius. *MNRAS*, 363(3):705–722, November 2005. .

Gary A. Mamon and Ewa L. Łokas. Erratum: Dark matter in elliptical galaxies - I. Is the total mass density profile of the NFW form or even steeper? *MNRAS*, 370(3): 1581–1581, August 2006. .

A. Marconi, G. Risaliti, R. Gilli, L. K. Hunt, R. Maiolino, and M. Salvati. Local supermassive black holes, relics of active galactic nuclei and the X-ray background. *MNRAS*, 351(1):169–185, Jun 2004. .

Alessandro Marconi and Leslie K. Hunt. The Relation between Black Hole Mass, Bulge Mass, and Near-Infrared Luminosity. *Apj Letters*, 589(1):L21–L24, May 2003. .

Christian Marinoni and Michael J. Hudson. The Mass-to-Light Function of Virialized Systems and the Relationship between Their Optical and X-Ray Properties. *ApJ*, 569 (1):101–111, April 2002. .

Christopher Marsden and Francesco Shankar. Using Unreal Engine to Visualize a Cosmological Volume. *Universe*, 6(10):168, October 2020. .

Christopher Marsden, Francesco Shankar, Mitchele Ginolfi, and Kastytis Zubovas. The case for the fundamental M-sigma. *Frontiers in Physics*, 8:61, March 2020. .

D. Christopher Martin, Ted K. Wyder, David Schiminovich, Tom A. Barlow, Karl Forster, Peter G. Friedman, Patrick Morrissey, Susan G. Neff, Mark Seibert, Todd Small, Barry Y. Welsh, Luciana Bianchi, José Donas, Timothy M. Heckman, Young-Wook Lee, Barry F. Madore, Bruno Milliard, R. Michael Rich, Alex S. Szalay, and Sukyoung K. Yi. The UV-Optical Galaxy Color-Magnitude Diagram. III. Constraints on Evolution from the Blue to the Red Sequence. *ApJ Supplement*, 173(2):342–356, December 2007. .

Ignacio Martín-Navarro, Francesco La Barbera, Alexandre Vazdekis, Jesús Falcón-Barroso, and Ignacio Ferreras. Radial variations in the stellar initial mass function of early-type galaxies. *MNRAS*, 447(2):1033–1048, February 2015. .

Charlotte A. Mason, Tommaso Treu, Kasper B. Schmidt, Thomas E. Collett, Michele Trenti, Philip J. Marshall, Robert Barone-Nugent, Larry D. Bradley, Massimo Stiavelli, and Stuart Wyithe. Correcting the z $\sim$ 8 Galaxy Luminosity Function for Gravitational Lensing Magnification Bias. *ApJ*, 805(1):79, May 2015. .

John C Mather, ES Cheng, David A Cottingham, RE Eplee Jr, Dale J Fixsen, Tilak Hewagama, RB Isaacman, KA Jensen, Stephan S Meyer, Peter D Noerdlinger, et al. Measurement of the cosmic microwave background spectrum by the cobe firas instrument. *The Astrophysical Journal*, 420:439–444, 1994.

Tom McCavana, Miroslav Micic, Geraint F. Lewis, Manodeep Sinha, Sanjib Sharma, Kelly Holley-Bockelmann, and Joss Bland-Hawthorn. The lives of high-redshift mergers. *MNRAS*, 424(1):361–371, July 2012. .

Nicholas J. McConnell and Chung-Pei Ma. Revisiting the Scaling Relations of Black Hole Masses and Host Galaxy Properties. *ApJ*, 764(2):184, Feb 2013. .

Ian D. McGreer, Linhua Jiang, Xiaohui Fan, Gordon T. Richards, Michael A. Strauss, Nicholas P. Ross, Martin White, Yue Shen, Donald P. Schneider, Adam D. Myers, W. Niel Brandt, Colin DeGraf, Eilat Glikman, Jian Ge, and Alina Streblyanska. The z = 5 Quasar Luminosity Function from SDSS Stripe 82. *ApJ*, 768(2):105, May 2013. .

Christopher F McKee and Eve C Ostriker. Theory of star formation. *Annual Review of Astronomy and Astrophysics*, 45, 2007.

B. R. McNamara and P. E. J. Nulsen. Heating Hot Atmospheres with Active Galactic Nuclei. *Annual Review of Astron and Astrophys*, 45:117–175, September 2007. .

Alan Meert, Vinu Vikram, and Mariangela Bernardi. A catalogue of 2d photometric decompositions in the sdss-dr7 spectroscopic main galaxy sample: preferred models and systematics. *Monthly Notices of the Royal Astronomical Society*, 446(4):3943–3974, 2014.

N. Menci, F. Fiore, S. Puccetti, and A. Cavaliere. The Blast Wave Model for AGN Feedback: Effects on AGN Obscuration. *ApJ*, 686(1):219–229, October 2008. .

N. Menci, F. Fiore, C. Feruglio, A. Lamastra, F. Shankar, E. Piconcelli, E. Giallongo, and A. Grazian. Outflows in the Disks of Active Galaxies. *ApJ*, 877(2):74, Jun 2019. .

J. Trevor Mendel, Luc Simard, Michael Palmer, Sara L. Ellison, and David R. Patton. A Catalog of Bulge, Disk, and Total Stellar Mass Estimates for the Sloan Digital Sky Survey. *ApJ Supplement*, 210(1):3, January 2014. .

Andrea Merloni and Sebastian Heinz. Measuring the kinetic power of active galactic nuclei in the radio mode. *MNRAS*, 381:589–601, October 2007. .

David Merritt. *Dynamics and Evolution of Galactic Nuclei*. 2013.

Charles Messier. Catalogue des Nébuleuses et des Amas d'Étoiles (Catalog of Nebulae and Star Clusters). Connoissance des Temps ou des Mouvements Célestes, January 1781.

J. Christopher Mihos and Lars Hernquist. Gasdynamics and Starbursts in Major Mergers. *ApJ*, 464:641, June 1996. .

B. P. Miller, W. N. Brandt, D. P. Schneider, R. R. Gibson, A. T. Steffen, and Jianfeng Wu. X-ray emission from optically selected radio-intermediate and radio-loud quasars. *The Astrophysical Journal*, 726(1):20, Dec 2010. ISSN 1538-4357. . URL http://dx.doi.org/10.1088/0004-637X/726/1/20.

R. Minkowski. Internal Dispersion of Velocities in Other Galaxies. In George Cunliffe McVittie, editor, *Problems of Extra-Galactic Research*, volume 15, page 112, January 1962.

Houjun Mo, Frank C. van den Bosch, and Simon White. *Galaxy Formation and Evolution*. 2010.

Pierluigi Monaco, Tom Theuns, and Giuliano Taffoni. The pinocchio algorithm: pinpointing orbit-crossing collapsed hierarchical objects in a linear density field. *MNRAS*, 331(3):587–608, April 2002. .

Pierluigi Monaco, Fabio Fontanot, and Giuliano Taffoni. The MORGANA model for the rise of galaxies and active nuclei. *MNRAS*, 375(4):1189–1219, March 2007. .

R. Morganti. The Many Routes to AGN Feedback. *ArXiv e-prints*, December 2017.

Donald C. Morton and Roger A. Chevalier. Velocity Dispersions in Galaxies. I. The e7 Galaxy NGC 7332. *ApJ*, 174:489, June 1972. .

Benjamin P. Moster, Andrea V. Macciò, Rachel S. Somerville, Peter H. Johansson, and Thorsten Naab. Can gas prevent the destruction of thin stellar discs by minor mergers? *MNRAS*, 403(2):1009–1019, April 2010a. .

Benjamin P. Moster, Rachel S. Somerville, Christian Maulbetsch, Frank C. van den Bosch, Andrea V. Macciò, Thorsten Naab, and Ludwig Oser. Constraints on the Relationship between Stellar Mass and Halo Mass at Low and High Redshift. *ApJ*, 710(2):903–923, Feb 2010b. .

Benjamin P. Moster, Thorsten Naab, and Simon D. M. White. Galactic star formation and accretion histories from matching galaxies to dark matter haloes. *MNRAS*, 428 (4):3121–3138, February 2013. .

Jeremy Mould. Understanding the Fundamental Plane and the Tully Fisher Relation. *Frontiers in Astronomy and Space Sciences*, 7:21, May 2020. .

Lamiya A. Mowla, Pieter van Dokkum, Gabriel B. Brammer, Ivelina Momcheva, Arjen van der Wel, Katherine Whitaker, Erica Nelson, Rachel Bezanson, Adam Muzzin, Marijn Franx, John MacKenty, Joel Leja, Mariska Kriek, and Danilo Marchesini. COSMOS-DASH: The Evolution of the Galaxy Size-Mass Relation since z $\sim$ 3 from New Wide-field WFC3 Imaging Combined with CANDELS/3D-HST. *ApJ*, 880(1):57, July 2019. .

J. R. Mullaney, D. M. Alexander, J. Aird, E. Bernhard, E. Daddi, A. Del Moro, M. Dickinson, D. Elbaz, C. M. Harrison, S. Juneau, D. Liu, M. Pannella, D. Rosario, P. Santini, M. Sargent, C. Schreiber, J. Simpson, and F. Stanley. ALMA and Herschel reveal that X-ray-selected AGN and main-sequence galaxies have different star formation rate distributions. *MNRAS*, 453(1):L83–L87, October 2015. .

N. Murray, E. Quataert, and T. A. Thompson. On the Maximum Luminosity of Galaxies and Their Central Black Holes: Feedback from Momentum-driven Winds. *ApJ*, 618: 569–585, January 2005. .

Adam Muzzin, Danilo Marchesini, Mauro Stefanon, Marijn Franx, Henry J McCracken, Bo Milvang-Jensen, James S Dunlop, Johan Peter Uldall Fynbo, Gabriel Brammer, Ivo Labbé, et al. The evolution of the stellar mass functions of star-forming and quiescent galaxies to z= 4 from the cosmos/ultravista survey. *The Astrophysical Journal*, 777(1): 18, 2013.

Thorsten Naab, Peter H. Johansson, and Jeremiah P. Ostriker. Minor Mergers and the Size Evolution of Elliptical Galaxies. *Apj Letters*, 699(2):L178–L182, July 2009. .

Julio F. Navarro, Carlos S. Frenk, and Simon D. M. White. The Structure of Cold Dark Matter Halos. *ApJ*, 462:563, May 1996. .

Julio F. Navarro, Carlos S. Frenk, and Simon D. M. White. The structure of cold dark matter halos. *The Astrophysical Journal*, 462:563, May 1996. ISSN 1538-4357. . URL http://dx.doi.org/10.1086/177173.

Dylan Nelson, Annalisa Pillepich, Volker Springel, Rüdiger Pakmor, Rainer Weinberger, Shy Genel, Paul Torrey, Mark Vogelsberger, Federico Marinacci, and Lars Hernquist. First results from the TNG50 simulation: galactic outflows driven by supernovae and black hole feedback. *MNRAS*, 490(3):3234–3261, December 2019a. .

Dylan Nelson, Volker Springel, Annalisa Pillepich, Vicente Rodriguez-Gomez, Paul Torrey, Shy Genel, Mark Vogelsberger, Ruediger Pakmor, Federico Marinacci, Rainer Weinberger, Luke Kelley, Mark Lovell, Benedikt Diemer, and Lars Hernquist. The IllustrisTNG simulations: public data release. *Computational Astrophysics and Cosmology*, 6(1):2, May 2019b. .

Anh Nguyen, Jason Yosinski, Yoshua Bengio, Alexey Dosovitskiy, and Jeff Clune. Plug & play generative networks: Conditional iterative generation of images in latent space. *arXiv preprint arXiv:1612.00005*, 2016.

C. Nipoti, P. Londrillo, and L. Ciotti. Galaxy merging, the fundamental plane of elliptical galaxies and the M_{BH}-σ_0 relation. *MNRAS*, 342(2):501–512, June 2003. .

C. Nipoti, T. Treu, M. W. Auger, and A. S. Bolton. Can Dry Merging Explain the Size Evolution of Early-Type Galaxies? *Apj Letters*, 706(1):L86–L90, November 2009. .

Carlo Nipoti, Tommaso Treu, Alexie Leauthaud, Kevin Bundy, Andrew B. Newman, and Matthew W. Auger. Size and velocity-dispersion evolution of early-type galaxies in a Λ cold dark matter universe. *MNRAS*, 422(2):1714–1731, May 2012. .

K. G. Noeske, B. J. Weiner, S. M. Faber, C. Papovich, D. C. Koo, R. S. Somerville, K. Bundy, C. J. Conselice, J. A. Newman, D. Schiminovich, E. Le Floc'h, A. L. Coil, G. H. Rieke, J. M. Lotz, J. R. Primack, P. Barmby, M. C. Cooper, M. Davis, R. S. Ellis, G. G. Fazio, P. Guhathakurta, J. Huang, S. A. Kassin, D. C. Martin, A. C. Phillips, R. M. Rich, T. A. Small, C. N. A. Willmer, and G. Wilson. Star Formation in AEGIS Field Galaxies since z=1.1: The Dominance of Gradually Declining Star Formation, and the Main Sequence of Star-forming Galaxies. *Apj Letters*, 660(1):L43–L46, May 2007. .

A Nuñez-Castiñeyra, E Nezri, J Devriendt, and R Teyssier. Cosmological simulations of the same spiral galaxy: the impact of baryonic physics. *Monthly Notices of the Royal Astronomical Society*, 501(1):62–77, Oct 2020. ISSN 1365-2966. . URL http://dx.doi.org/10.1093/mnras/staa3233.

P. A. Oesch, G. Brammer, P. G. van Dokkum, G. D. Illingworth, R. J. Bouwens, I. Labbé, M. Franx, I. Momcheva, M. L. N. Ashby, G. G. Fazio, V. Gonzalez, B. Holden, D. Magee, R. E. Skelton, R. Smit, L. R. Spitler, M. Trenti, and S. P. Willner. A Remarkably Luminous Galaxy at z=11.1 Measured with Hubble Space Telescope Grism Spectroscopy. *ApJ*, 819(2):129, March 2016. .

Joseph A. O'Leary, Benjamin P. Moster, and Eva Krämer. EMERGE: Constraining merging probabilities and timescales of close galaxy pairs. *arXiv e-prints*, art. arXiv:2011.05341, November 2020.

Ludwig Oser, Jeremiah P. Ostriker, Thorsten Naab, Peter H. Johansson, and Andreas Burkert. The Two Phases of Galaxy Formation. *ApJ*, 725(2):2312–2323, December 2010. .

Ludwig Oser, Thorsten Naab, Jeremiah P. Ostriker, and Peter H. Johansson. The Cosmological Size and Velocity Dispersion Evolution of Massive Early-type Galaxies. *ApJ*, 744(1):63, January 2012. .

J. P. Ostriker and P. J. E. Peebles. A Numerical Study of the Stability of Flattened Galaxies: or, can Cold Galaxies Survive? *ApJ*, 186:467–480, December 1973. .

Nikhil Padmanabhan, Uroš Seljak, Michael A. Strauss, Michael R. Blanton, Guinevere Kauffmann, David J. Schlegel, Christy Tremonti, Neta A. Bahcall, Mariangela Bernardi, J. Brinkmann, Masataka Fukugita, and Željko Ivezić. Stellar and dynamical masses of ellipticals in the Sloan Digital Sky Survey. *New Astronomy*, 9(5):329–342, June 2004. .

Michael A. Pahre, S. G. Djorgovski, and Reinaldo R. de Carvalho. Near-Infrared Imaging of Early-Type Galaxies. III. The Near-Infrared Fundamental Plane. *Astronomical Jmynal*, 116(4):1591–1605, October 1998. .

Taniya Parikh, Daniel Thomas, Claudia Maraston, Kyle B. Westfall, Daniel Goddard, Jianhui Lian, Sofia Meneses-Goytia, Amy Jones, Sam Vaughan, Brett H. Andrews, Matthew Bershady, Dmitry Bizyaev, Jonathan Brinkmann, Joel R. Brownstein, Kevin Bundy, Niv Drory, Eric Emsellem, David R. Law, Jeffrey A. Newman, Alexandre Roman-Lopes, David Wake, Renbin Yan, and Zheng Zheng. SDSS-IV MaNGA: the spatially resolved stellar initial mass function in $\sim$400 early-type galaxies. *MNRAS*, 477(3):3954–3982, July 2018. .

O. H. Parry, V. R. Eke, and C. S. Frenk. Galaxy morphology in the ΛCDM cosmology. *MNRAS*, 396(4):1972–1984, July 2009. .

John A Peacock, Shaun Cole, Peder Norberg, Carlton M Baugh, Joss Bland-Hawthorn, Terry Bridges, Russell D Cannon, Matthew Colless, Chris Collins, Warrick Couch, et al. A measurement of the cosmological mass density from clustering in the 2df galaxy redshift survey. *Nature*, 410(6825):169, 2001.

P. J. E. Peebles. *The large-scale structure of the universe*. 1980.

P James E Peebles and Bharat Ratra. The cosmological constant and dark energy. *Reviews of modern physics*, 75(2):559, 2003.

Molly S. Peeples and Francesco Shankar. Constraints on star formation driven galaxy winds from the mass-metallicity relation at z= 0. *MNRAS*, 417(4):2962–2981, November 2011. .

C. Y. Peng. How Mergers May Affect the Mass Scaling Relation between Gravitationally Bound Systems. *ApJ*, 671:1098–1107, December 2007. .

Will J Percival, Shaun Cole, Daniel J Eisenstein, Robert C Nichol, John A Peacock, Adrian C Pope, and Alexander S Szalay. Measuring the baryon acoustic oscillation scale using the sloan digital sky survey and 2df galaxy redshift survey. *Monthly Notices of the Royal Astronomical Society*, 381(3):1053–1066, 2007.

Bradley M. Peterson. Reverberation Mapping of Active Galactic Nuclei. *Publications of the ASP*, 105:247, March 1993. .

Bradley M. Peterson. *An Introduction to Active Galactic Nuclei*. 1997.

Annalisa Pillepich, Dylan Nelson, Volker Springel, Rüdiger Pakmor, Paul Torrey, Rainer Weinberger, Mark Vogelsberger, Federico Marinacci, Shy Genel, Arjen van der Wel, and Lars Hernquist. First results from the TNG50 simulation: the evolution of stellar and gaseous discs across cosmic time. *MNRAS*, 490(3):3196–3233, December 2019. .

L. A. Porter, R. S. Somerville, J. R. Primack, and P. H. Johansson. Understanding the structural scaling relations of early-type galaxies. *MNRAS*, 444(1):942–960, October 2014. .

Douglas Potter, Joachim Stadel, and Romain Teyssier. Pkdgrav3: beyond trillion particle cosmological simulations for the next era of galaxy surveys. *Computational Astrophysics and Cosmology*, 4(1):2, 2017.

M. C. Powell, N. Cappelluti, C. M. Urry, M. Koss, A. Finoguenov, C. Ricci, B. Trakhtenbrot, V. Allevato, M. Ajello, K. Oh, K. Schawinski, and N. Secrest. The Swift/BAT AGN Spectroscopic Survey. IX. The Clustering Environments of an Unbiased Sample of Local AGNs. *ApJ*, 858(2):110, May 2018. .

Joel R Primack. Precision cosmology. *New Astronomy Reviews*, 49(2):25–34, 2005.

P. Prugniel and F. Simien. The fundamental plane of early-type galaxies: non-homology of the spatial structure. *Astronomy and Astrophysics*, 321:111–122, May 1997.

Cinthia Ragone-Figueroa and Gian Luigi Granato. Puffing up early-type galaxies by baryonic mass loss: numerical experiments. *MNRAS*, 414(4):3690–3698, July 2011. .

JI Read and T Hayfield. Sphs: smoothed particle hydrodynamics with a higher order dissipation switch. *Monthly Notices of the Royal Astronomical Society*, 422(4):3037–3055, 2012.

Alexandre Refregier. Weak gravitational lensing by large-scale structure. *Annual Review of Astronomy and Astrophysics*, 41(1):645–668, 2003.

Amy E. Reines and Marta Volonteri. Relations between Central Black Hole Mass and Total Galaxy Stellar Mass in the Local Universe. *ApJ*, 813(2):82, Nov 2015. .

Angelo Ricarte and Priyamvada Natarajan. Exploring SMBH assembly with semi-analytic modelling. *MNRAS*, 474(2):1995–2011, February 2018. .

Lewis Fry Richardson. Ix. the approximate arithmetical solution by finite differences of physical problems involving differential equations, with an application to the stresses in a masonry dam. *Philosophical Transactions of the Royal Society of London. Series A, Containing Papers of a Mathematical or Physical Character*, 210(459-470):307–357, 1911.

Douglas Richstone and Wallace L. W. Sargent. A New Determination of the Mass of M32. *ApJ*, 176:91, August 1972. .

K. Riebe, A. M. Partl, H. Enke, J. Forero-Romero, S. Gottlöber, A. Klypin, G. Lemson, F. Prada, J. R. Primack, M. Steinmetz, and V. Turchaninov. The MultiDark Database: Release of the Bolshoi and MultiDark cosmological simulations. *Astronomische Nachrichten*, 334(7):691–708, August 2013. .

Hans-Walter Rix and Simon D. M. White. Optimal estimates of line-of-sight velocity distributions from absorptionline spectra of galaxies : nuclear discs in elliptical galaxies. *MNRAS*, 254:389–403, February 1992. .

Brant Robertson, James S. Bullock, Thomas J. Cox, Tiziana Di Matteo, Lars Hernquist, Volker Springel, and Naoki Yoshida. A Merger-driven Scenario for Cosmological Disk Galaxy Formation. *ApJ*, 645(2):986–1000, July 2006a. .

Brant Robertson, Thomas J. Cox, Lars Hernquist, Marijn Franx, Philip F. Hopkins, Paul Martini, and Volker Springel. The Fundamental Scaling Relations of Elliptical Galaxies. *ApJ*, 641(1):21–40, April 2006b. .

Vladimir Romanyuk. Space engine [Software Application]. *Space Engine Developers*, 2010. URL https://www.http://spaceengine.org/. [Online; accessed 04-August-2020].

Pablo A. Rosado, Alberto Sesana, and Jonathan Gair. Expected properties of the first gravitational wave signal detected with pulsar timing arrays. *MNRAS*, 451(3):2417–2433, Aug 2015. .

D. J. Rosario, B. Trakhtenbrot, D. Lutz, H. Netzer, J. R. Trump, J. D. Silverman, M. Schramm, E. Lusso, S. Berta, A. Bongiorno, M. Brusa, N. M. Förster-Schreiber, R. Genzel, S. Lilly, B. Magnelli, V. Mainieri, R. Maiolino, A. Merloni, M. Mignoli,

R. Nordon, P. Popesso, M. Salvato, P. Santini, L. J. Tacconi, and G. Zamorani. The mean star-forming properties of QSO host galaxies. *A&A*, 560:A72, December 2013. .

Nicholas P. Ross, Ian D. McGreer, Martin White, Gordon T. Richards, Adam D. Myers, Nathalie Palanque-Delabrouille, Michael A. Strauss, Scott F. Anderson, Yue Shen, W. N. Brandt, Christophe Yèche, Molly E. C. Swanson, Éric Aubourg, Stephen Bailey, Dmitry Bizyaev, Jo Bovy, Howard Brewington, J. Brinkmann, Colin DeGraf, Tiziana Di Matteo, Garrett Ebelke, Xiaohui Fan, Jian Ge, Elena Malanushenko, Viktor Malanushenko, Rachel Mandelbaum, Claudia Maraston, Demitri Muna, Daniel Oravetz, Kaike Pan, Isabelle Pâris, Patrick Petitjean, Kevin Schawinski, David J. Schlegel, Donald P. Schneider, John D. Silverman, Audrey Simmons, Stephanie Snedden, Alina Streblyanska, Nao Suzuki, David H. Weinberg, and Donald York. The SDSS-III Baryon Oscillation Spectroscopic Survey: The Quasar Luminosity Function from Data Release Nine. *ApJ*, 773(1):14, August 2013. .

R. P. Saglia, M. Opitsch, P. Erwin, J. Thomas, A. Beifiori, M. Fabricius, X. Mazzalay, N. Nowak, S. P. Rusli, and R. Bender. The SINFONI Black Hole Survey: The Black Hole Fundamental Plane Revisited and the Paths of (Co)evolution of Supermassive Black Holes and Bulges. *ApJ*, 818(1):47, Feb 2016. .

Samir Salim, R. Michael Rich, Stéphane Charlot, Jarle Brinchmann, Benjamin D. Johnson, David Schiminovich, Mark Seibert, Ryan Mallery, Timothy M. Heckman, Karl Forster, Peter G. Friedman, D. Christopher Martin, Patrick Morrissey, Susan G. Neff, Todd Small, Ted K. Wyder, Luciana Bianchi, José Donas, Young-Wook Lee, Barry F. Madore, Bruno Milliard, Alex S. Szalay, Barry Y. Welsh, and Sukyoung K. Yi. UV Star Formation Rates in the Local Universe. *ApJ Supplement*, 173(2):267–292, December 2007. .

Edwin E. Salpeter. The Luminosity Function and Stellar Evolution. *ApJ*, 121:161, January 1955. .

Paolo Salucci, Ewa Szuszkiewicz, Pierluigi Monaco, and Luigi Danese. Mass function of dormant black holes and the evolution of active galactic nuclei. *MNRAS*, 307(3): 637–644, Aug 1999. .

S. Salviander and G. A. Shields. The Black Hole Mass-Stellar Velocity Dispersion Relationship for Quasars in the Sloan Digital Sky Survey Data Release 7. *ApJ*, 764(1):80, Feb 2013. .

D. B. Sanders, B. T. Soifer, J. H. Elias, B. F. Madore, K. Matthews, G. Neugebauer, and N. Z. Scoville. Ultraluminous Infrared Galaxies and the Origin of Quasars. *ApJ*, 325: 74, February 1988. .

P. Santini, D. J. Rosario, L. Shao, D. Lutz, R. Maiolino, D. M. Alexander, B. Altieri, P. Andreani, H. Aussel, F. E. Bauer, S. Berta, A. Bongiovanni, W. N. Brandt, M. Brusa,

J. Cepa, A. Cimatti, E. Daddi, D. Elbaz, A. Fontana, N. M. Förster Schreiber, R. Genzel, A. Grazian, E. Le Floc'h, B. Magnelli, V. Mainieri, R. Nordon, A. M. Pérez Garcia, A. Poglitsch, P. Popesso, F. Pozzi, L. Riguccini, G. Rodighiero, M. Salvato, M. Sanchez-Portal, E. Sturm, L. J. Tacconi, I. Valtchanov, and S. Wuyts. Enhanced star formation rates in AGN hosts with respect to inactive galaxies from PEP-Herschel observations. *A&A*, 540:A109, April 2012. .

W. L. W. Sargent, P. L. Schechter, A. Boksenberg, and K. Shortridge. Velocity dispersions for 13 galaxies. *ApJ*, 212:326–334, March 1977. .

Giulia A. D. Savorgnan and Alister W. Graham. Overmassive black holes in the M_{BH}-σ diagram do not belong to over (dry) merged galaxies. *MNRAS*, 446(3):2330–2336, Jan 2015. .

Giulia A. D. Savorgnan and Alister W. Graham. Explaining the reportedly overmassive black holes in early-type galaxies with intermediate-scale discs. *MNRAS*, 457(1):320–327, Mar 2016. .

C. Scannapieco, M. Wadepuhl, O. H. Parry, J. F. Navarro, A. Jenkins, V. Springel, R. Teyssier, E. Carlson, H. M. P. Couchman, R. A. Crain, C. Dalla Vecchia, C. S. Frenk, C. Kobayashi, P. Monaco, G. Murante, T. Okamoto, T. Quinn, J. Schaye, G. S. Stinson, T. Theuns, J. Wadsley, S. D. M. White, and R. Woods. The Aquila comparison project: the effects of feedback and numerical methods on simulations of galaxy formation. *MNRAS*, 423(2):1726–1749, June 2012. .

Kevin Schawinski, C. Megan Urry, Brooke D. Simmons, Lucy Fortson, Sugata Kaviraj, William C. Keel, Chris J. Lintott, Karen L. Masters, Robert C. Nichol, Marc Sarzi, and et al. The green valley is a red herring: Galaxy zoo reveals two evolutionary pathways towards quenching of star formation in early- and late-type galaxies. *Monthly Notices of the Royal Astronomical Society*, 440(1):889–907, Mar 2014. ISSN 0035-8711. . URL http://dx.doi.org/10.1093/mnras/stu327.

Paul Schechter. An analytic expression for the luminosity function for galaxies. *The Astrophysical Journal*, 203:297–306, 1976.

David Schiminovich, Ted K. Wyder, D. Christopher Martin, Benjamin. D. Johnson, Samir Salim, Mark Seibert, Marie A. Treyer, Tamás Budavári, Charles Hoopes, Michel Zamojski, Tom A. Barlow, Karl G. Forster, Peter G. Friedman, Patrick Morrissey, Susan G. Neff, Todd A. Small, Luciana Bianchi, José Donas, Timothy M. Heckman, Young-Wook Lee, Barry F. Madore, Bruno Milliard, R. Michael Rich, Alex. S. Szalay, Barry Y. Welsh, and Sukyoung Yi. The UV-Optical Color Magnitude Diagram. II. Physical Properties and Morphological Evolution On and Off of a Star-forming Sequence. *ApJ Supplement*, 173(2):315–341, December 2007. .

A. Schulze and L. Wisotzki. Low redshift AGN in the Hamburg/ESO Survey . II. The active black hole mass function and the distribution function of Eddington ratios. *A&A*, 516:A87, June 2010. .

A. Sesana, A. Vecchio, and C. N. Colacino. The stochastic gravitational-wave background from massive black hole binary systems: implications for observations with Pulsar Timing Arrays. *MNRAS*, 390(1):192–209, Oct 2008. .

F. Shankar, P. Salucci, G. L. Granato, G. De Zotti, and L. Danese. Supermassive black hole demography: the match between the local and accreted mass functions. *MNRAS*, 354(4):1020–1030, Nov 2004. .

F. Shankar, A. Lapi, P. Salucci, G. De Zotti, and L. Danese. New Relationships between Galaxy Properties and Host Halo Mass, and the Role of Feedbacks in Galaxy Formation. *ApJ*, 643(1):14–25, May 2006. .

Francesco Shankar, Mariangela Bernardi, and Zoltán Haiman. The Evolution of the M_{BH}-σ Relation Inferred from the Age Distribution of Local Early-Type Galaxies and Active Galactic Nuclei Evolution. *ApJ*, 694(2):867–878, Apr 2009. .

Francesco Shankar, Federico Marulli, Mariangela Bernardi, Michael Boylan-Kolchin, Xinyu Dai, and Sadegh Khochfar. Further constraining galaxy evolution models through the size function of SDSS early-type galaxies. *MNRAS*, 405(2):948–960, June 2010a. .

Francesco Shankar, Federico Marulli, Mariangela Bernardi, Xinyu Dai, Joseph B. Hyde, and Ravi K. Sheth. Sizes and ages of SDSS ellipticals: comparison with hierarchical galaxy formation models. *MNRAS*, 403(1):117–128, March 2010b. .

Francesco Shankar, Federico Marulli, Mariangela Bernardi, Simona Mei, Alan Meert, and Vinu Vikram. Size evolution of spheroids in a hierarchical Universe. *MNRAS*, 428(1):109–128, January 2013a. .

Francesco Shankar, David H. Weinberg, and Jordi Miralda-Escudé. Accretion-driven evolution of black holes: Eddington ratios, duty cycles and active galaxy fractions. *MNRAS*, 428(1):421–446, January 2013b. .

Francesco Shankar, Simona Mei, Marc Huertas-Company, Jorge Moreno, Fabio Fontanot, Pierluigi Monaco, Mariangela Bernardi, Andrea Cattaneo, Ravi Sheth, Rossella Licitra, Lauriane Delaye, and Anand Raichoor. Environmental dependence of bulge-dominated galaxy sizes in hierarchical models of galaxy formation. Comparison with the local Universe. *MNRAS*, 439(4):3189–3212, Apr 2014. .

Francesco Shankar, Stewart Buchan, Alessandro Rettura, Vincent R. Bouillot, Jorge Moreno, Rossella Licitra, Mariangela Bernardi, Marc Huertas-Company, Simona Mei, Begoña Ascaso, Ravi Sheth, Lauriane Delaye, and Anand Raichoor. Avoiding

Progenitor Bias: The Structural and Mass Evolution of Brightest Group and Cluster Galaxies in Hierarchical Models since z ¡~1. *ApJ*, 802(2):73, April 2015. .

Francesco Shankar, Mariangela Bernardi, Ravi K. Sheth, Laura Ferrarese, Alister W. Graham, Giulia Savorgnan, Viola Allevato, Alessandro Marconi, Ronald Läsker, and Andrea Lapi. Selection bias in dynamically measured supermassive black hole samples: its consequences and the quest for the most fundamental relation. *MNRAS*, 460 (3):3119–3142, Aug 2016. .

Francesco Shankar, Mariangela Bernardi, and Ravi K. Sheth. Selection bias in dynamically measured supermassive black hole samples: dynamical masses and dependence on Sérsic index. *MNRAS*, 466(4):4029–4039, Apr 2017a. .

Francesco Shankar, Alessandro Sonnenfeld, Gary A. Mamon, Kyu-Hyun Chae, Raphael Gavazzi, Tommaso Treu, Benedikt Diemer, Carlo Nipoti, Stewart Buchan, Mariangela Bernardi, Ravi Sheth, and Marc Huertas-Company. Revisiting the Bulge-Halo Conspiracy. I. Dependence on Galaxy Properties and Halo Mass. *ApJ*, 840(1):34, May 2017b. .

Francesco Shankar, Viola Allevato, Mariangela Bernardi, Christopher Marsden, Andrea Lapi, Nicola Menci, Philip J. Grylls, Mirko Krumpe, Lorenzo Zanisi, Federica Ricci, Fabio La Franca, Ranieri D. Baldi, Jorge Moreno, and Ravi K. Sheth. Constraining black hole-galaxy scaling relations from the large-scale clustering of Active Galactic Nuclei and implied mean radiative efficiency. *arXiv e-prints*, art. arXiv:1910.10175, Oct 2019a.

Francesco Shankar, Mariangela Bernardi, Kayleigh Richardson, Christopher Marsden, Ravi K. Sheth, Viola Allevato, Luca Graziani, Mar Mezcua, Federica Ricci, Samantha J. Penny, Fabio La Franca, and Fabio Pacucci. Black hole scaling relations of active and quiescent galaxies: Addressing selection effects and constraining virial factors. *MNRAS*, 485(1):1278–1292, May 2019b. .

Francesco Shankar, David H. Weinberg, Christopher Marsden, Philip J. Grylls, Mariangela Bernardi, Guang Yang, Benjamin Moster, Hao Fu, Rosamaria Carraro, David M. Alexander, Viola Allevato, Tonima T. Ananna, Angela Bongiorno, Giorgio Calderone, Francesca Civano, Emanuele Daddi, Ivan Delvecchio, Federica Duras, Fabio La Franca, Andrea Lapi, Youjun Lu, Nicola Menci, Mar Mezcua, Federica Ricci, Giulia Rodighiero, Ravi K. Sheth, Hyewon Suh, Carolin Villforth, and Lorenzo Zanisi. Probing black hole accretion tracks, scaling relations, and radiative efficiencies from stacked X-ray active galactic nuclei. *MNRAS*, 493(1):1500–1511, March 2020a. .

Francesco Shankar, David H. Weinberg, Christopher Marsden, Philip J. Grylls, Mariangela Bernardi, Guang Yang, Benjamin Moster, Hao Fu, Rosamaria Carraro, David M. Alexander, Viola Allevato, Tonima T. Ananna, Angela Bongiorno, Giorgio Calderone, Francesca Civano, Emanuele Daddi, Ivan Delvecchio, Federica Duras, Fabio La

Franca, Andrea Lapi, Youjun Lu, Nicola Menci, Mar Mezcua, Federica Ricci, Giulia Rodighiero, Ravi K. Sheth, Hyewon Suh, Carolin Villforth, and Lorenzo Zanisi. Probing black hole accretion tracks, scaling relations, and radiative efficiencies from stacked X-ray active galactic nuclei. *MNRAS*, 493(1):1500–1511, March 2020b. .

Yue Shen, Jenny E. Greene, Luis C. Ho, W. N. Brand t, Kelly D. Denney, Keith Horne, Linhua Jiang, Christopher S. Kochanek, Ian D. McGreer, Andrea Merloni, Bradley M. Peterson, Patrick Petitjean, Donald P. Schneider, Andreas Schulze, Michael A. Strauss, Charling Tao, Jonathan R. Trump, Kaike Pan, and Dmitry Bizyaev. The Sloan Digital Sky Survey Reverberation Mapping Project: No Evidence for Evolution in the M• -σ_* Relation to $z \sim 1$. *ApJ*, 805(2):96, Jun 2015. .

Ravi K. Sheth and Mariangela Bernardi. Plain fundamentals of Fundamental Planes: analytics and algorithms. *MNRAS*, 422(3):1825–1834, May 2012. .

Ravi K. Sheth and Giuseppe Tormen. Large-scale bias and the peak background split. *MNRAS*, 308(1):119–126, September 1999. .

Joseph Silk and Gary A. Mamon. The current status of galaxy formation. *Research in Astronomy and Astrophysics*, 12(8):917–946, August 2012. .

Joseph Silk and Martin J. Rees. Quasars and galaxy formation. *A&A*, 331:L1–L4, Mar 1998.

S. M. Simkin. Measurements of Velocity Dispersions and Doppler Shifts from Digitized Optical Spectra. *A&A*, 31:129, March 1974.

A. Soltan. Masses of quasars. *MNRAS*, 200:115–122, July 1982. .

Rachel S Somerville and Romeel Davé. Physical models of galaxy formation in a cosmological framework. *Annual Review of Astronomy and Astrophysics*, 53:51–113, 2015.

Rachel S. Somerville, Philip F. Hopkins, Thomas J. Cox, Brant E. Robertson, and Lars Hernquist. A semi-analytic model for the co-evolution of galaxies, black holes and active galactic nuclei. *MNRAS*, 391(2):481–506, December 2008. .

Rachel S. Somerville, Peter Behroozi, Viraj Pandya, Avishai Dekel, S. M. Faber, Adriano Fontana, Anton M. Koekemoer, David C. Koo, P. G. Pérez-González, Joel R. Primack, Paola Santini, Edward N. Taylor, and Arjen van der Wel. The relationship between galaxy and dark matter halo size from z ˜ 3 to the present. *MNRAS*, 473(2):2714–2736, January 2018. .

Volker Springel. The cosmological simulation code gadget-2. *Monthly notices of the royal astronomical society*, 364(4):1105–1134, 2005.

Volker Springel. E pur si muove: Galilean-invariant cosmological hydrodynamical simulations on a moving mesh. *Monthly Notices of the Royal Astronomical Society*, 401(2): 791–851, 2010.

Volker Springel, Tiziana Di Matteo, and Lars Hernquist. Modelling feedback from stars and black holes in galaxy mergers. *Monthly Notices of the Royal Astronomical Society*, 361(3):776–794, 2005.

Volker Springel, Simon D. M. White, Adrian Jenkins, Carlos S. Frenk, Naoki Yoshida, Liang Gao, Julio Navarro, Robert Thacker, Darren Croton, John Helly, John A. Peacock, Shaun Cole, Peter Thomas, Hugh Couchman, August Evrard, Jörg Colberg, and Frazer Pearce. Simulations of the formation, evolution and clustering of galaxies and quasars. *Nature*, 435(7042):629–636, June 2005. .

Volker Springel, Joel Snape, and Andrew Moore. Milennium Movies, 2011. URL http://icc.dur.ac.uk/~ams/galform_movie/. [Online; accessed 03-September-2020].

Kyle R. Stewart, James S. Bullock, Risa H. Wechsler, and Ariyeh H. Maller. Gas-rich Mergers in LCDM: Disk Survivability and the Baryonic Assembly of Galaxies. *ApJ*, 702(1):307–317, September 2009. .

Iskra Strateva, Željko Ivezić, Gillian R. Knapp, Vijay K. Narayanan, Michael A. Strauss, James E. Gunn, Robert H. Lupton, David Schlegel, Neta A. Bahcall, Jon Brinkmann, Robert J. Brunner, Tamás Budavári, István Csabai, Francisco Javier Castander, Mamoru Doi, Masataka Fukugita, Zsuzsanna Győry, Masaru Hamabe, Greg Hennessy, Takashi Ichikawa, Peter Z. Kunszt, Don Q. Lamb, Timothy A. McKay, Sadanori Okamura, Judith Racusin, Maki Sekiguchi, Donald P. Schneider, Kazuhiro Shimasaku, and Donald York. Color Separation of Galaxy Types in the Sloan Digital Sky Survey Imaging Data. *Astronomical Jmynal*, 122(4):1861–1874, October 2001. .

M. J. Stringer, F. Shankar, G. S. Novak, M. Huertas-Company, F. Combes, and B. P. Moster. Galaxy size trends as a consequence of cosmology. *MNRAS*, 441(2):1570–1583, June 2014. .

Baitian Tang and Guy Worthey. Optical spectroscopy and initial mass function of z = 0.4 red galaxies. *MNRAS*, 467(1):674–683, May 2017. .

AN Taylor, S Dye, Thomas J Broadhurst, N Benitez, and E Van Kampen. Gravitational lens magnification and the mass of abell 1689. *The Astrophysical Journal*, 501(2):539, 1998.

The GIMP Development Team. GNU Image Manipulation Program, 1996. URL https://www.gimp.org/. [Online; accessed 13-September-2018].

Jeremy L. Tinker, Brant E. Robertson, Andrey V. Kravtsov, Anatoly Klypin, Michael S. Warren, Gustavo Yepes, and Stefan Gottlöber. The Large-scale Bias of Dark Matter Halos: Numerical Calibration and Model Tests. *ApJ*, 724(2):878–886, December 2010. .

F. Tombesi, M. Cappi, J. N. Reeves, G. G. C. Palumbo, T. Yaqoob, V. Braito, and M. Dadina. Evidence for ultra-fast outflows in radio-quiet AGNs. I. Detection and statistical incidence of Fe K-shell absorption lines. *A&A*, 521:A57+, October 2010a. .

F. Tombesi, R. M. Sambruna, J. N. Reeves, V. Braito, L. Ballo, J. Gofford, M. Cappi, and R. F. Mushotzky. Discovery of Ultra-fast Outflows in a Sample of Broad-line Radio Galaxies Observed with Suzaku. *ApJ*, 719:700–715, August 2010b. .

C. Tonini, A. Lapi, F. Shankar, and P. Salucci. Measuring the Spin of Spiral Galaxies. *Apj Letters*, 638(1):L13–L16, February 2006. .

A. Toomre. On the gravitational stability of a disk of stars. *ApJ*, 139:1217–1238, May 1964. .

Alar Toomre. Mergers and Some Consequences, January 1977.

Alar Toomre and Juri Toomre. Galactic Bridges and Tails. *ApJ*, 178:623–666, December 1972. .

E. Treister, K. Schawinski, C. M. Urry, and B. D. Simmons. Major Galaxy Mergers Only Trigger the Most Luminous Active Galactic Nuclei. *Apj Letters*, 758(2):L39, October 2012. .

Scott Tremaine, Karl Gebhardt, Ralf Bender, Gary Bower, Alan Dressler, S. M. Faber, Alexei V. Filippenko, Richard Green, Carl Grillmair, Luis C. Ho, John Kormendy, Tod R. Lauer, John Magorrian, Jason Pinkney, and Douglas Richstone. The Slope of the Black Hole Mass versus Velocity Dispersion Correlation. *ApJ*, 574(2):740–753, Aug 2002. .

I. Trujillo, A. Burkert, and Eric F. Bell. The Tilt of the Fundamental Plane: Three-Quarters Structural Nonhomology, One-Quarter Stellar Population. *Apj Letters*, 600 (1):L39–L42, January 2004. .

Ignacio Trujillo, Natascha M. Förster Schreiber, Gregory Rudnick, Marco Barden, Marijn Franx, Hans-Walter Rix, J. A. R. Caldwell, Daniel H. McIntosh, Sune Toft, Boris Häussler, Andrew Zirm, Pieter G. van Dokkum, Ivo Labbé, Alan Moorwood, Huub Röttgering, Arjen van der Wel, Paul van der Werf, and Lottie van Starkenburg. The Size Evolution of Galaxies since z~3: Combining SDSS, GEMS, and FIRES. *ApJ*, 650 (1):18–41, October 2006. .

Shinji Tsujikawa. Introductory review of cosmic inflation. *arXiv preprint hep-ph/0304257*, 2003.

Elena Tundo, Mariangela Bernardi, Joseph B. Hyde, Ravi K. Sheth, and Alessandro Pizzella. On the Inconsistency between the Black Hole Mass Function Inferred from $M_\bullet$-σ and $M_\bullet$-L Correlations. *ApJ*, 663(1):53–60, Jul 2007. .

Yoshihiro Ueda, Masayuki Akiyama, Günther Hasinger, Takamitsu Miyaji, and Michael G Watson. Toward the standard population synthesis model of the x-ray background: Evolution of x-ray luminosity and absorption functions of active galactic nuclei including compton-thick populations. *The Astrophysical Journal*, 786(2):104, 2014.

A. Vale and J. P. Ostriker. Linking halo mass to galaxy luminosity. *MNRAS*, 353(1): 189–200, September 2004. .

Jesse van de Sande, Mariska Kriek, Marijn Franx, Pieter G. van Dokkum, Rachel Bezanson, Katherine E. Whitaker, Gabriel Brammer, Ivo Labbé, Paul J. Groot, and Lex Kaper. The Stellar Velocity Dispersion of a Compact Massive Galaxy at z = 1.80 Using X-Shooter: Confirmation of the Evolution in the Mass-Size and Mass-Dispersion Relations. *Apj Letters*, 736(1):L9, July 2011. .

Frank C. van den Bosch, Giuseppe Tormen, and Carlo Giocoli. The mass function and average mass-loss rate of dark matter subhaloes. *MNRAS*, 359(3):1029–1040, May 2005. .

Frank C. van den Bosch, Fangzhou Jiang, Andrew Hearin, Duncan Campbell, Douglas Watson, and Nikhil Padmanabhan. Coming of age in the dark sector: how dark matter haloes grow their gravitational potential wells. *MNRAS*, 445(2):1713–1730, December 2014. .

Remco C. E. van den Bosch. Unification of the fundamental plane and Super Massive Black Hole Masses. *ApJ*, 831(2):134, Nov 2016. .

Remco C. E. van den Bosch, Karl Gebhardt, Kayhan Gültekin, Glenn van de Ven, Arjen van der Wel, and Jonelle L. Walsh. An over-massive black hole in the compact lenticular galaxy NGC 1277. *Nature*, 491(7426):729–731, Nov 2012. .

Remco C. E. van den Bosch, Karl Gebhardt, Kayhan Gültekin, Akin Yıldırım, and Jonelle L. Walsh. Hunting for Supermassive Black Holes in Nearby Galaxies With the Hobby-Eberly Telescope. *ApJ Supplement*, 218(1):10, May 2015. .

R. P. van der Marel, N. W. Evans, H. W. Rix, S. D. M. White, and T. de Zeeuw. Velocity profiles of galaxies with claimed black holes. II. f(E,L_z) models for M32. *MNRAS*, 271:99–117, November 1994. .

A. van der Wel, M. Franx, P. G. van Dokkum, R. E. Skelton, I. G. Momcheva, K. E. Whitaker, G. B. Brammer, E. F. Bell, H. W. Rix, S. Wuyts, H. C. Ferguson, B. P. Holden, G. Barro, A. M. Koekemoer, Yu-Yen Chang, E. J. McGrath, B. Häussler, A. Dekel, P. Behroozi, M. Fumagalli, J. Leja, B. F. Lundgren, M. V. Maseda, E. J. Nelson, D. A. Wake, S. G. Patel, I. Labbé, S. M. Faber, N. A. Grogin, and D. D. Kocevski. 3D-HST+CANDELS: The Evolution of the Galaxy Size-Mass Distribution since z = 3. *ApJ*, 788(1):28, June 2014. .

Pieter van Dokkum, Charlie Conroy, Alexa Villaume, Jean Brodie, and Aaron J. Romanowsky. The Stellar Initial Mass Function in Early-type Galaxies from Absorption Line Spectroscopy. III. Radial Gradients. *ApJ*, 841(2):68, June 2017. .

Pieter G. van Dokkum, Marijn Franx, Mariska Kriek, Bradford Holden, Garth D. Illingworth, Daniel Magee, Rychard Bouwens, Danilo Marchesini, Ryan Quadri, Greg Rudnick, Edward N. Taylor, and Sune Toft. Confirmation of the Remarkable Compactness of Massive Quiescent Galaxies at z ~2.3: Early-Type Galaxies Did not Form in a Simple Monolithic Collapse. *Apj Letters*, 677(1):L5, April 2008. .

Pieter G. van Dokkum, Katherine E. Whitaker, Gabriel Brammer, Marijn Franx, Mariska Kriek, Ivo Labbé, Danilo Marchesini, Ryan Quadri, Rachel Bezanson, Garth D. Illingworth, Adam Muzzin, Gregory Rudnick, Tomer Tal, and David Wake. The Growth of Massive Galaxies Since z = 2. *ApJ*, 709(2):1018–1041, February 2010. .

Sylvain Veilleux, Gerald Cecil, and Joss Bland-Hawthorn. Galactic Winds. *Annual Review of Astron and Astrophys*, 43(1):769–826, September 2005. .

A. Viitanen, V. Allevato, A. Finoguenov, F. Shankar, and C. Marsden. The role of scatter and satellites in shaping the large-scale clustering of X-ray AGN as a function of host galaxy stellar mass. *MNRAS*, 507(4):6148–6160, November 2021. .

Marta Volonteri. Formation of supermassive black holes. *A&A Reviews*, 18(3):279–315, July 2010. .

Ian R. Walker, J. Christopher Mihos, and Lars Hernquist. Quantifying the Fragility of Galactic Disks in Minor Mergers. *ApJ*, 460:121, March 1996. .

Simon DM White and Carlos S Frenk. Galaxy formation through hierarchical clustering. *The Astrophysical Journal*, 379:52–79, 1991.

Chris J. Willott, Loic Albert, Doris Arzoumanian, Jacqueline Bergeron, David Crampton, Philippe Delorme, John B. Hutchings, Alain Omont, Céline Reylé, and David Schade. Eddington-limited Accretion and the Black Hole Mass Function at Redshift 6. *Astronomical Jmynal*, 140(2):546–560, August 2010. .

Jong-Hak Woo, Tommaso Treu, Matthew A. Malkan, and Roger D. Blandford. Cosmic evolution of black holes and spheroids. iii. the mbh-$\sigma_\star$ relation in the last six billion years. *The Astrophysical Journal*, 681(2):925–930, Jul 2008. ISSN 1538-4357. . URL http://dx.doi.org/10.1086/588804.

J. Stuart B. Wyithe. A log-quadratic relation between the nuclear black hole masses and velocity dispersions of galaxies. *MNRAS*, 365(4):1082–1098, Feb 2006. .

G. Yang, W. N. Brandt, F. Vito, C. T. J. Chen, J. R. Trump, B. Luo, M. Y. Sun, Y. Q. Xue, A. M. Koekemoer, D. P. Schneider, C. Vignali, and J. X. Wang. Linking black

hole growth with host galaxies: the accretion-stellar mass relation and its cosmic evolution. *MNRAS*, 475(2):1887–1911, April 2018. .

G. Yang, W. N. Brandt, D. M. Alexander, C. T. J. Chen, Q. Ni, F. Vito, and F. F. Zhu. Evident black hole-bulge coevolution in the distant universe. *MNRAS*, 485(3):3721–3737, May 2019. .

Qingjuan Yu and Scott Tremaine. Observational constraints on growth of massive black holes. *MNRAS*, 335(4):965–976, Oct 2002. .

H. Jabran Zahid and Margaret J. Geller. Velocity Dispersion, Size, Sérsic Index, and D $_n$4000: The Scaling of Stellar Mass with Dynamical Mass for Quiescent Galaxies. *ApJ*, 841(1):32, May 2017. .

H. Jabran Zahid, Ivana Damjanov, Margaret J. Geller, Ho Seong Hwang, and Daniel G. Fabricant. The Stellar Mass Fundamental Plane and Compact Quiescent Galaxies at z ¡ 0.6. *ApJ*, 821(2):101, April 2016. .

L. Zanisi, F. Shankar, H. Fu, A. Rodriguez-Puebla, V. Avila-Reese, A. Faisst, E. Daddi, L. Boco, A. Lapi, M. Giavalisco, P. Saracco, F. Buitrago, M. Huertas-Company, A. Puglisi, and A. Dekel. The evolution of compact massive quiescent and starforming galaxies derived from the $R_e - R_h$ and $M_{\rm star} - M_h$ relations. *arXiv e-prints*, art. arXiv:2105.09969, May 2021.

Lorenzo Zanisi, Francesco Shankar, Andrea Lapi, Nicola Menci, Mariangela Bernardi, Christopher Duckworth, Marc Huertas-Company, Philip Grylls, and Paolo Salucci. Galaxy sizes and the galaxy-halo connection - I. The remarkable tightness of the size distributions. *MNRAS*, 492(2):1671–1690, February 2020. .

Jesus Zavala, Vladimir Avila-Reese, Claudio Firmani, and Michael Boylan-Kolchin. The growth of galactic bulges through mergers in λ cdm haloes revisited–i. present-day properties. *Monthly Notices of the Royal Astronomical Society*, 427(2):1503–1516, 2012.

Y. B. Zel'Dovich. Reprint of 1970A&A.....5...84Z. Gravitational instability: an approximate theory for large density perturbations. *Astronomy and Astrophysics*, 500:13–18, March 1970.

Xiaoxia Zhang, Youjun Lu, and Qingjuan Yu. The Cosmic Evolution of Massive Black Holes and Galaxy Spheroids: Global Constraints at Redshift z <~1.2. *ApJ*, 761(1):5, Dec 2012. .

Ziwen Zhang, Huiyuan Wang, Wentao Luo, H. J. Mo, Zhixiong Liang, Ran Li, Xiaohu Yang, Tinggui Wang, Hongxin Zhang, Hui Hong, Xiaoyu Wang, Enci Wang, Pengfei Li, and JingJing Shi. Host and Trigger of AGNs in local Universe. *arXiv e-prints*, art. arXiv:2012.10640, December 2020.

K. Zubovas and A. King. Clearing Out a Galaxy. *Apj Letters*, 745:L34, February 2012a. .

K. Zubovas and A. R. King. The M-σ relation in different environments. *MNRAS*, 426: 2751–2757, November 2012b. .

K. Zubovas and S. Nayakshin. Energy- and momentum-conserving AGN feedback outflows. *MNRAS*, 440:2625–2635, May 2014. .

Kastytis Zubovas. Tidal disruption events can power the observed AGN in dwarf galaxies. *MNRAS*, 483(2):1957–1969, Feb 2019. .

Kastytis Zubovas and Andrew King. Slow and massive: low-spin SMBHs can grow more. *MNRAS*, 489(1):1373–1378, Oct 2019. .

Fritz Zwicky. On the masses of nebulae and of clusters of nebulae. *The Astrophysical Journal*, 86:217, 1937.